University of Strathclyde

Department of Physics

Submitted in partial fulfilment of the requirements

for the degree of Doctor of Philosophy

System characterisation under experimental constraints

Author:
Kaila C. S. Hall

Supervisors:
Dr. Daniel K. L. Oi
Dr. John Jeffers

October 1, 2015

Copyright

Signed:

Date:

Thank you to all my family
who helped me on this journey.

Summary

Physically realising quantum computation is our long term goal. Currently characterising and verifying quantum states is a hard problem. Verification is necessary in order to understand and control quantum systems. There are also issues in the physical realisation of these systems, the apparatus used does not match the quantum scale and so produces errors in the measurements. There are many different candidates for physically realising quantum computation, we consider measurement based quantum computation using cluster state systems. We explore the different ways of verifying these systems in the presence of various experimental imperfections and non-idealities.

We present a scheme to reduce the cross-talk found when verifying the state through stabilizer operator measurements. The cross-talk comes from physical constraints on the measurement apparatus. Our scheme reduces the cross-talk to almost 50% of the original value. We consider square, triangular and hexagonal connectivity lattices.

We also use the Clauser-Horne-Shimony-Holt (CHSH) inequality as a way to verify atoms trapped in optical lattices through its entanglement. Imperfections arise in this system through finite entropy in the creation process that leads to vacant lattice sites. By optimising the conventional measurement settings we improve the tolerance of the system to incomplete measurement and vacancies. We find violations of the CHSH inequality for very large vacancy rates. We analyse further errors in the detectors and calculate the tolerance of the system in these cases.

We study the effects of superselection rules and their connection to the single particle entanglement question. We review a system presented by Paterek *et al.* [1] and verify it again using the CHSH inequality. We introduce errors into the measurement process. By optimising the measurement settings we increase the tolerance of the system for four different error models. We also explore how non-ideal state preparation affects the detectable violations.

Contents

List of Figures

CHAPTER 1

Introduction

1.1 Introduction

Research into the possibility of using a quantum system for computation has become increasingly popular over the last few decades. The advantage of using a quantum system compared with a classical one is speed. The concept of superposition allows operations to be performed in parallel which significantly increases the speed of the computation. As consumers we are constantly demanding faster performance from technology, as such, exploring the possibility of quantum computation is a reasonable route of research.

Verification of these quantum states is extremely important. When we create a quantum state we need to be able to check it is the correct state. We also need to ensure that when an operation is performed on a particular state the output state is what we expected. The verification allows us to fully understand the underlying physics of the system, without it we could not begin to use quantum states as a resource. Until we build a quantum computer this verification must be done using direct methods. However, as the number of qubits, N, in our quantum system increases the number of parameters needed to characterise the state increases exponentially as 2^N [2]. This rules out methods such as full quantum state tomography for verification as it soon becomes impossible to write down the state [3]. Verification of quantum states is one of the main themes of this work, in each case we identify a way to characterise the quantum state of interest using a linear number of parameters to avoid the issues associated with quantum state tomography.

There are different ideas of how a quantum computer could be realised [4, 5, 6, 7, 8]. The idea we focus on in this thesis is measurement based quantum computation using

cluster states [8, 9]. Cluster states are fully entangled many body qubit systems. Projective single-qubit measurements are performed in a sequence and the results are read-out by a final single particle measurement. The entanglement of the cluster state is a vital component in its usefulness for quantum computation. Any errors or imperfections in the state and measurements could reduce the accuracy of the results [10, 8, 11, 12].

Broadly speaking our theoretical knowledge of how quantum systems perform is good. We are able to describe the systems mathematically and predict how they will perform. However, there is a problem when we physically try to realise these systems. Many body quantum systems, for example a Bose-Einstein Condensate (BEC) require all the atoms in the system to be at a very low temperature, ideally 0K, this freezes out any classical fluctuations and all the atoms can occupy the lowest quantum state making them indistinguishable. Clearly this is not possible in practice as we are performing the experiment at finite temperatures. By using a BEC where classical fluctuations still remain for any sort of computation has the possibility of errors in the results making the system not reliable. If we want to use quantum information as a resource for computation it is vital that it is robust and reliable.

There are also other issues in putting quantum computation into practice such as size. Many body quantum systems are made up of many atoms, depending on the system, for example cluster states. It can be necessary to address individual atoms using laser beams in order to perform rotations on these individual atoms. Currently the width of the laser beams that we have available is larger than the atom spacing meaning when the target atom is addressed the nearest neighbour atoms also feel the affects of the laser. This again can lead to errors in the results if the system is used for computation.

In this thesis we accept that our apparatus is not yet to the standard necessary to produce reliable quantum computation results. We believe that the apparatus will get there eventually but in the meantime we still want to be able to perform quantum computation. We concentrate on tweaks and changes we can make to the theoretical ideal experimental set-up so that we can reduce the impact of the imperfections caused by the apparatus.

1.2 Thesis outline

The three pieces of work presented here are simple theoretical analyses for optimising the performance of various protocols that take into account the underlying characteristics of the physical systems. We focus on the idea of cluster state quantum computation. Using Bose-Einstein condensates (BECs) in optical lattice setups is a promising candidate for implementing quantum computation [11]. However, there are a number of issues that crop up in this model. We explore three different scenarios and present a scheme for addressing the issue of state verification for each. The solutions generally

present further issues, we address these and optimise the scheme in order to reduce the affects the issues have on the measurement results.

Our first piece of work looks at the issue of cross-talk which occurs during the measurement process [13]. Cross-talk occurs due to the measurement apparatus not matching the scale of the system being measured. It can cause errors in the measurement results. Until we are able to access measurement apparatus more suited to the quantum scale we must address this issue. We aim to reduce the impact of the effect by simple modifications of the measurements themselves.

Our second piece of work looks at incomplete measurement and non-ideal states. Incomplete measurement occurs again due to the inaccuracy of the apparatus. It leads to indistinguishability between two states in the system. The non-ideal states occur due to the finite entropy of the BEC creation process which leads to a non-maximally entangled cluster state [14]. These combined errors cause a reduction in the entanglement of the state to be used for quantum computation. By characterising the entanglement using a Bell inequality we aim to show that by optimising the measurement settings even in highly non-ideal states we can still detect the entanglement in the system.

Our third piece of work considers small margins of error and different error models. We look at the impact of superselection rules on the allowed coherent operations and relate this to the question of single particle entanglement [15, 16]. Similar to the second piece of work we use a Bell inequality to characterise the entanglement of the system and explore different types of error that occur from the measurement apparatus.

CHAPTER 2

Quantum theory basics

We begin by introducing the basic quantum theory and notation that will be used throughout this work. From how to describe a quantum state to tools that are commonly used to measure and interpret the results.

2.1 State vector

Every quantum state is described by a state vector. These state vectors reside in the Hilbert space, $\mathcal{H}$, which is a complex vector space. We use Dirac notation to write the state vector of a system as a ket, $|\psi\rangle$, we call this the state of the system. It is possible for the system to be in a superposition of states, this means that its state can be written in terms of two other states as,

$$|\psi\rangle = a_0 |\psi_0\rangle + a_1 |\psi_1\rangle , \tag{2.1}$$

where a_0 and a_1 are complex numbers that are associated with the amplitudes of the system being in one state or the other ($P_j = |a_j|^2$ if $|\psi_0\rangle$ and $|\psi_1\rangle$ are orthonormal, definition follows later). A two-state system is commonly called a qubit, it is the smallest unit of quantum information and lies in a two-dimensional Hilbert space. It can also be represented using a column vector

$$|\psi\rangle = \begin{pmatrix} a_0 \\ a_1 \end{pmatrix} . \tag{2.2}$$

The conjugate transpose of $|\psi\rangle$ is a bra,

$$\langle\psi| = a_0^* \langle\psi_0| + a_1^* \langle\psi_1| = \begin{pmatrix} a_0^* & a_1^* \end{pmatrix} , \tag{2.3}$$

where a_0^* and a_1^* are the complex conjugates of a_0 and a_1. Similar to vectors the inner product of two states shows the overlap between them, for example, the overlap between $|\psi\rangle$ and $|\phi\rangle$ is written as $\langle\phi|\,\psi\rangle$. If the inner product value is zero then the states are orthogonal, the same as two vectors with a zero scalar product would be perpendicular. A state is said to be normalised if the inner product of itself with itself is one,

$$\langle\psi|\,\psi\rangle = 1. \tag{2.4}$$

When the state is not normalised the inner product is strictly positive,

$$|\,\langle\psi|\,\psi\rangle| > 0. \tag{2.5}$$

When a set of states is normalised and orthogonal it is called orthonormal. We can access the probability amplitudes by looking at the overlap between particular states,

$$\begin{aligned} \langle\psi_0|\,\psi\rangle &= a_0 = \langle\psi|\,\psi_0\rangle^*, \\ \langle\psi_1|\,\psi\rangle &= a_1 = \langle\psi|\,\psi_1\rangle^*, \end{aligned} \tag{2.6}$$

where $\{|\psi_0\rangle\,, |\psi_1\rangle\}$ is an orthonormal basis.

In the case where $|\psi\rangle$ is normalised, then $|a_0|^2 + |a_1|^2 = 1$, where $|a_0|^2$ is the probability of measuring the state to be $|\psi_0\rangle$ and $|a_1|^2$ is the probability of measuring the state to be in $|\psi_1\rangle$. A state can be a superposition of many other states,

$$|\psi\rangle = \sum_n a_n\,|\psi_n\rangle\,. \tag{2.7}$$

If $|\psi\rangle$ is normalised and $\{|\psi_n\rangle\}$ are orthonormal then,

$$\sum_n |a_n|^2 = 1. \tag{2.8}$$

2.2 Observables

For each measurable parameter or observable there is an associated Hermitian linear operator, $\hat{A}$. This operator acts upon a state and transforms it into another state

$$\hat{A}\,|\psi\rangle = |\phi\rangle\,. \tag{2.9}$$

The operator can be written as a matrix and is described as Hermitian if $\hat{A} = \hat{A}^\dagger$,

$$\hat{A} = \begin{pmatrix} a_{00} & a_{01} \\ a_{10} & a_{11} \end{pmatrix}, \qquad \hat{A}^\dagger = \begin{pmatrix} a_{00}^* & a_{10}^* \\ a_{01}^* & a_{11}^* \end{pmatrix}, \tag{2.10}$$

where $\hat{A}^\dagger$ is the Hermitian conjugate of $\hat{A}$ defined by

$$\begin{aligned} \langle\psi|\,\hat{A}^\dagger\,|\phi\rangle &= \langle\phi|\hat{A}\,|\psi\rangle^*\,\forall\,|\psi\rangle\,,|\phi\rangle\,, \\ \Rightarrow \begin{pmatrix}\psi_0 & \psi_1\end{pmatrix}\begin{pmatrix}a_{00} & a_{01}\\ a_{10} & a_{11}\end{pmatrix}\begin{pmatrix}\phi_0\\ \phi_1\end{pmatrix} &= \begin{pmatrix}\phi_0 & \phi_1\end{pmatrix}\begin{pmatrix}a_{00}^* & a_{10}^*\\ a_{01}^* & a_{11}^*\end{pmatrix}\begin{pmatrix}\psi_0\\ \psi_1\end{pmatrix} \\ = \begin{pmatrix}\psi_0 a_{00}\phi_0 + \psi_0 a_{01}\phi_1\\ \psi_1 a_{10}\phi_0 + \psi_1 a_{11}\phi_1\end{pmatrix} &= \begin{pmatrix}\phi_0 a_{00}^*\psi_0 + \phi_0 a_{01}^*\psi_1\\ \phi_1 a_{10}^*\psi_0 + \phi_1 a_{11}^*\psi_1,\end{pmatrix} \end{aligned} \tag{2.11}$$

as $\hat{A}$ is hermitian the coefficients a_{00} and a_{11} are real, $a_{01} = a_{10}^*$ and $a_{10} = a_{01}^*$ making Eq. (2.11) true.

2.3 Eigenvalues and Eigenvectors

Eigenvalues are the possible results from an ideal operator measurement. If the operator $\hat{A}$ is Hermitian then the eigenvalue equation is given by,

$$\hat{A}\,|\lambda_n\rangle = \lambda_n\,|\lambda_n\rangle\,, \tag{2.12}$$

where $|\lambda_n\rangle$ are eigenstates and λ_n are eigenvalues. The conjugate of Eq. (2.12) is shown with λ_n replaced with λ_m

$$\langle\lambda_m|\,\hat{A}^\dagger = \langle\lambda_m|\,\hat{A} = \lambda_m^*\,\langle\lambda_m|\,. \tag{2.13}$$

The eigenvalues can be shown to be real and the eigenvectors, corresponding to distinct λ_j, orthonormal using the following equations. Taking the overlap of the conjugate, Eq. (2.13) with $|\lambda_n\rangle$,

$$\langle\lambda_m|\,\hat{A}\,|\lambda_n\rangle = \lambda_m^*\,\langle\lambda_m|\,\lambda_n\rangle, \tag{2.14}$$

and taking the conjugate of Eq. (2.12) with $\langle\lambda_m|$,

$$\langle\lambda_m|\,\hat{A}\,|\lambda_n\rangle = \lambda_n\,\langle\lambda_m|\,\lambda_n\rangle, \tag{2.15}$$

and finally taking Eq. (2.15) from Eq. (2.14),

$$(\lambda_m^* - \lambda_n)\,\langle\lambda_m|\,\lambda_n\rangle = 0, \tag{2.16}$$

if $m = n$, the two states are the same and the eigenvalues must be real to satisfy Eq. (2.5). But if the two states are not the same, $n \neq m$, then the overlap is zero and the states must be orthogonal. This is summarised using the Kronecker delta, δ_{mn},

$$\langle\lambda_m|\,\lambda_n\rangle = \delta_{mn}, \tag{2.17}$$

δ_{mn} has value 1 when $m = n$ otherwise 0. If the state to be measured is normalised and written as

$$|\psi\rangle = \sum_n a_n |\lambda_n\rangle , \tag{2.18}$$

when the measurement of observable A is performed using operator $\hat{A}$ the result will be the eigenvalue λ_n with probability $|a_n|^2$. It is possible for two orthonormal states, $|\lambda_j\rangle$ and $|\lambda_k\rangle$ to have the same eigenvalue, $\lambda_j = \lambda_k$, in this case the state is degenerate and the probability of getting result $\lambda_j = |a_j|^2 + |a_k|^2$. The set of eigenvectors, $\{|\lambda_n\rangle\}$ is complete if all the possible states of the system can be written in the form of Eq. (2.18).

2.4 Expectation value

By performing the same measurement using operator $\hat{A}$ on many states prepared using the same process, a mean or expectation value of the result can be found, this is expressed as

$$\langle\psi| \hat{A} |\psi\rangle = \bar{A} = \langle\hat{A}\rangle = \sum_n \lambda_n |a_n|^2. \tag{2.19}$$

The spread of these results is given by the variance,

$$\sigma^2 = (\Delta A)^2 = \langle\psi| (\hat{A} - \langle\hat{A}\rangle)^2 |\psi\rangle = \langle\psi| \hat{A}^2 |\psi\rangle - \langle\psi| \hat{A} |\psi\rangle^2 . \tag{2.20}$$

2.5 Commutators

When performing multiple measurements on a particular state, multiple operators are used. The order that these operators are applied in is very important. Generally operators do not commute.

$$\hat{A}\hat{B} |\psi\rangle \neq \hat{B}\hat{A} |\psi\rangle . \tag{2.21}$$

The commutator or difference of two operators $\hat{A}$ and $\hat{B}$ is given as

$$[\hat{A}, \hat{B}] = \hat{A}\hat{B} - \hat{B}\hat{A}. \tag{2.22}$$

If the operators do commute the value of the commutator is zero, the order is not important and they are simultaneously measurable.

2.6 Outer product

The outer product is a useful alternative representation of an operator. $|\phi_1\rangle \langle\phi_2|$ is the outer product of the two states $|\phi_1\rangle$ and $|\phi_2\rangle$. The Hermitian conjugate of the above operator is $|\phi_2\rangle \langle\phi_1|$. The operator can only be described as Hermitian if $|\phi_1\rangle = |\phi_2\rangle$. As the outer product is an operator it can act upon a state, $|\psi\rangle$, producing $|\phi_1\rangle \langle\phi_2| \psi\rangle = \langle\phi_2| \psi\rangle |\phi_1\rangle$ as $\langle\phi_2| \psi\rangle$ is the inner product (a complex number) and so can be moved

to the front of the expression. We can write any observable in the outer product form in terms of eigenvalues and eigenvectors.

$$\hat{A} = \sum_n \lambda_n \left|\lambda_a\right\rangle \left\langle\lambda_n\right|, \tag{2.23}$$

where $\hat{A}$ is a Hermitian operator and $\{|\lambda_n\rangle\}$ is the complete set of eigenvectors for that operator.

The operator that acts upon any state $|\psi\rangle$ resulting in $|\psi\rangle$ is called the Identity operator, $\hat{\mathbb{I}}$, it is Hermitian and can be written as

$$\hat{\mathbb{I}} = \sum_n \left|\lambda_n\right\rangle \left\langle\lambda_n\right|, \tag{2.24}$$

where $\{|\lambda_n\rangle\}$ is any orthonormal basis. To show that this operator does return to the original state we use Eq. (2.18) as the description of the state and the Kronecker delta,

$$\begin{aligned} \hat{\mathbb{I}}\left|\psi\right\rangle &= \sum_m \left|\lambda_m\right\rangle \left\langle\lambda_m\right| \sum_n a_n \left|\lambda_n\right\rangle \\ &= \sum_n a_n \sum_m \delta_{mn} \left|\lambda_n\right\rangle \\ &= \left|\psi\right\rangle. \end{aligned} \tag{2.25}$$

2.7 Mixed states

Quantum states that are made up of a single state are called pure states. Not all states are pure it is possible to have mixed states, statistical mixtures of pure states. These mixed states are described by density operators

$$\hat{\rho} = \sum_n P_n \left|\psi_n\right\rangle \left\langle\psi_n\right|. \tag{2.26}$$

If only one of the probabilities, $P_n = 1$, or $P_n = \delta_{mn}$, then the density operator can be simplified to a pure state $\hat{\rho} = |\psi_m\rangle \langle\psi_m|$.

The mixture of states in the density operator are not necessarily orthogonal. It is however always possible to write $\hat{\rho}$ in diagonal form due to its Hermiticity. It is also true that for any state, $|\phi\rangle$, the density operator is always positive,

$$\begin{aligned} \left\langle\phi\right| \hat{\rho} \left|\phi\right\rangle &= \sum_n P_n \left\langle\phi\right| \left.\psi_n\right\rangle \left\langle\psi_n\right| \left.\phi\right\rangle \\ &= \sum_n P_n \left|\left\langle\phi\right| \left.\psi_n\right\rangle\right|^2 \geq 0, \end{aligned} \tag{2.27}$$

as each term contains a probability term that must be positive or zero. We can write the density operator in terms of eigenvalues, ρ_m and eigenvectors, $|\rho_m\rangle$,

$$\hat{\rho} = \sum_m \rho_m |\rho_m\rangle \langle\rho_m| . \tag{2.28}$$

The density operator allows us to change the way we write the expectation value

$$\langle \hat{A} \rangle = \mathrm{Tr}(\hat{\rho}\hat{A}), \tag{2.29}$$

where Tr is the trace operation. This operation sums the diagonal elements of the operator $\hat{\rho}\hat{A}$ in any basis that has a complete orthonormal set of states. If $\{|\lambda_m\rangle\}$ is a complete orthonormal set of eigenvalues then Eq. (2.29) equals,

$$\begin{aligned}
\mathrm{Tr}(\hat{\rho}\hat{A}) &= \sum_m \langle\lambda_m| \left(\sum_n P_n |\lambda_n\rangle \langle\lambda_n| \right) \hat{A} |\lambda_m\rangle \\
&= \sum_n P_n \langle\psi_n| \hat{A} \sum_m |\lambda_m\rangle \langle\lambda_m| \psi_n\rangle \\
&= \sum_n P_n \langle\psi_n| \hat{A} |\psi_n\rangle .
\end{aligned} \tag{2.30}$$

The trace operation is cyclic meaning the order can be rotated $\mathrm{Tr}(\hat{\rho}\hat{A}\hat{B}) = \mathrm{Tr}(\hat{A}\hat{B}\hat{\rho}) = \mathrm{Tr}(\hat{B}\hat{\rho}\hat{A})$. The trace is independent of the basis and used to calculate the expectation of $\hat{A}$. By setting $\hat{A}$ to the identity operator we see the trace is simply the sum of all the probabilities,

$$\begin{aligned}
\mathrm{Tr}(\hat{\rho}\hat{\mathbb{I}}) &= \sum_m \langle\lambda_m| \left(\sum_n P_n |\lambda_n\rangle \langle\lambda_n| \right) \hat{\mathbb{I}} |\lambda_m\rangle \\
&= \sum_n P_n \langle\lambda_n| \hat{\mathbb{I}} \sum_m |\lambda_m\rangle \langle\lambda_m| \lambda_n\rangle \\
&= \sum_n P_n \langle\lambda_n| \hat{\mathbb{I}} |\lambda_n\rangle \\
&= \sum_n P_n \langle\lambda_n| \lambda_n\rangle \\
&= \sum_n P_n .
\end{aligned} \tag{2.31}$$

If we calculate the trace of $\hat{\rho}$ in the basis of its eigenvectors (Eq. (2.28)), we see the trace is also the sum of all the eigenvalues,

$$\begin{aligned}
\mathrm{Tr}(\hat{\rho}) &= \sum_m \langle \rho_m | \left(\sum_n \rho_n |\rho_n\rangle \langle \rho_n| \right) |\rho_m\rangle \\
&= \sum_n \rho_n \langle \rho_n | \sum_m |\rho_m\rangle \langle \rho_m | \rho_n\rangle \\
&= \sum_n \rho_n \langle \rho_n | \rho_n\rangle \\
&= \sum_n \rho_n,
\end{aligned} \tag{2.32}$$

making the sum of the eigenvectors 1. By choosing $\hat{A}$ to be $\hat{\rho}$,

$$\begin{aligned}
\mathrm{Tr}(\hat{\rho}^2) &= \sum_m \langle \rho_m | \left(\sum_n \rho_n |\rho_n\rangle \langle \rho_n| \right) \hat{\rho} |\rho_m\rangle \\
&= \sum_n \rho_n \langle \rho_n | \hat{\rho} \sum_m |\rho_m\rangle \langle \rho_m | \rho_n\rangle \\
&= \sum_n \rho_n \langle \rho_n | \hat{\rho} |\rho_n\rangle \\
&= \sum_n \rho_n \langle \rho_n | \hat{\rho} |\rho_n\rangle \\
&= \sum_n \rho_n \rho_n \\
&= \sum_n \rho_n^2.
\end{aligned} \tag{2.33}$$

We can use this measure as a test of the purity of a state. By interpreting the eigenvalues as probabilities we see that

$$\mathrm{Tr}(\hat{\rho}^2) = \sum_n \rho_n^2 \leq \sum_n \sum_m \rho_n \rho_m = 1, \tag{2.34}$$

this can only be 1 if only one value of $\rho_n = 1$ and all the others are zero meaning $\mathrm{Tr}(\hat{\rho}^2) = 1$ for pure states and $\mathrm{Tr}(\hat{\rho}^2) \leq 1$ for mixed states.

The ensemble description of a state is not necessarily unique, if we take this state

$$\hat{\rho} = \frac{1}{2} |0\rangle \langle 0| + \frac{1}{2} |1\rangle \langle 1|, \tag{2.35}$$

where $|0\rangle$ and $|1\rangle$ are orthonormal states. This state is the same as

$$\hat{\rho} = \frac{1}{3} |0\rangle \langle 0| + \frac{1}{3} \frac{(|0\rangle + \sqrt{3}\,|1\rangle)}{2} \frac{(\langle 0| + \sqrt{3}\,\langle 1|)}{2} + \frac{1}{3} \frac{(|0\rangle - \sqrt{3}\,|1\rangle)}{2} \frac{(\langle 0| - \sqrt{3}\,\langle 1|)}{2}, \tag{2.36}$$

it is not possible to distinguish between the ensembles by measurement.

2.8 Reduced density operator

Two separate states that reside in two different state spaces, a and b, can be written as a composite state using the direct product,

$$|\psi\rangle = |\lambda\rangle_a \otimes |\phi\rangle_b \,, \tag{2.37}$$

where $\otimes$ denotes the tensor product of the state spaces. For convenience the $\otimes$ is usually left out. The state in Eq. (5.1) is separable, this means the state can be written as a product of two states. There is another class of states called entangled states, these cannot be written in the form of Eq. (5.1), for example,

$$|\psi\rangle = \sum_n a_n \, |\lambda_n\rangle \otimes |\phi_n\rangle \,. \tag{2.38}$$

When applying operators to composite states (separable and entangled) it is very important to be clear which state spaces the operator acts upon. If operators $\hat{A}$ acts only on system a then the joint operator on both systems is written as $\hat{A} \otimes \hat{\mathbb{I}}$ and the action of the operator only affects the a subsystem.

We can introduce the reduced density operator by calculating the expectation value of a joint operator,

$$\begin{aligned} \langle\psi| \, \hat{A} \, |\psi\rangle &= \sum_m \sum_n a_m^* a_n \, \langle\phi_m| \otimes \langle\lambda_m| \, \hat{A} \otimes \hat{\mathbb{I}} \, |\lambda_n\rangle \otimes |\phi_n\rangle \\ &= \sum_m \sum_n a_m^* a_n \, \langle\phi_m| \, \phi_n\rangle \, \langle\lambda_m| \, \hat{A} \, |\lambda_n\rangle \\ &= \sum_n |a_n|^2 \, \langle\lambda_n| \, \hat{A} \, |\lambda_n\rangle \,, \end{aligned} \tag{2.39}$$

this is the same result as if we had calculated $\mathrm{Tr}(\hat{\rho}_a \hat{A})$, where

$$\hat{\rho}_a = \sum_n |a_n|^2 \, |\lambda_n\rangle \, \langle\lambda_n| \,, \tag{2.40}$$

this is called the reduced density operator, it only describes the part of the joint state that is in the a subspace which is spanned by $\{|\lambda_n\rangle\}$. By using observables that only affect one subspace of the entangled state any correlations between the two systems will not be taken into account. As such, the only result we can gain from these types of operator measurements would be the reduced density operator of that system. This means we can write Eq. (2.39) as

$$\begin{aligned} \langle\hat{A}\rangle &= \mathrm{Tr}(\hat{A} \otimes \hat{\mathbb{I}} \, |\psi\rangle \, \langle\psi|) \\ &= \sum_m \sum_n \langle\phi_m| \otimes \langle\lambda_n| \, (\hat{A} \otimes \hat{\mathbb{I}} \, |\psi\rangle \, \langle\psi|) \, |\lambda_n\rangle \otimes |\phi_m\rangle \\ &= \mathrm{Tr}_a \left[\hat{A} \mathrm{Tr}_b (|\psi\rangle \, \langle\psi|) \right] , \end{aligned} \tag{2.41}$$

where $\mathrm{Tr}_{a(b)}$ is the trace over system $a(b)$ and system a is spanned by basis $\{|\lambda_n\rangle\}$ and system b is spanned by $\{|\phi_m\rangle\}$. $\mathrm{Tr}_b(|\psi\rangle\langle\psi|)$ is the reduced density operator for system a. If the total density operator is $\hat{\rho}_{ab}$ then the reduced density operator for system a is

$$\begin{aligned}\hat{\rho}_a &= \sum_m {}_b\langle\phi_m|\,\hat{\rho}_{ab}\,|\phi_m\rangle_b \\ &= \mathrm{Tr}_b(\hat{\rho}_{ab}).\end{aligned} \tag{2.42}$$

2.9 Unitary operators

A unitary operator, $\hat{U}$ is a special type of operator,

$$\hat{U}\hat{U}^\dagger = \hat{U}^\dagger\hat{U} = \hat{\mathbb{I}}, \tag{2.43}$$

where $\hat{U}^\dagger = \hat{U}^{-1}$. A unitary operator preserves the overlap between states. If a transformed state is $|\psi'\rangle = \hat{U}|\psi\rangle$ then

$$\langle\phi'|\,\psi'\rangle = \langle\phi|\,\hat{U}^\dagger\hat{U}\,|\psi\rangle = \langle\phi|\,\psi\rangle\forall\,|\phi\rangle\,,|\psi\rangle\,, \tag{2.44}$$

the inner product remains the same between the two states. A unitary operator can act on states or operators with equivalent results,

$$(\langle\psi|\,\hat{U}\rangle)\hat{A}(\hat{U}\,|\psi\rangle) = \langle\psi|\,(\hat{U}^\dagger\hat{A}\hat{U})\,|\psi\rangle\,. \tag{2.45}$$

A larger unitary operator can be made up of a sequence of n smaller unitary operators,

$$\hat{U} = \hat{U}_n\cdots\hat{U}_2\hat{U}_1, \qquad\qquad \hat{U}\,|\psi\rangle = \hat{U}_n\cdots\hat{U}_2\hat{U}_1\,|\psi\rangle\,, \tag{2.46}$$

the order of these operators is important as they do not necessarily commute.

2.10 Pauli Operators

Pauli operators are an example of unitary operators on $\mathcal{H}$. The Pauli operators are as follows,

$$\begin{aligned}\hat{\mathbb{I}} &= |0\rangle\langle 0| + |1\rangle\langle 1| = \begin{pmatrix}1 & 0\\ 0 & 1\end{pmatrix},\\ \hat{\sigma}_x &= |0\rangle\langle 1| + |1\rangle\langle 0| = \begin{pmatrix}0 & 1\\ 1 & 0\end{pmatrix},\\ \hat{\sigma}_y &= i(|1\rangle\langle 0| - |0\rangle\langle 1|) = \begin{pmatrix}0 & -i\\ i & 0\end{pmatrix},\\ \hat{\sigma}_z &= |0\rangle\langle 0| - |1\rangle\langle 1| = \begin{pmatrix}1 & 0\\ 0 & -1\end{pmatrix},\end{aligned} \tag{2.47}$$

where $\sigma_j^2 = \mathbb{I}$ and $\sigma_j^\dagger = \sigma_j$. They form a basis for operators on $\mathcal{H}^{\otimes 2}$ but do not commute with each other.

2.11 The Bloch sphere

Qubits are quantum states that have two orthogonal states, for example, $|\psi\rangle = a_0 |0\rangle + a_1 |1\rangle$. The qubits can be represented as points on the Bloch sphere (Fig. 2.1). The Bloch sphere is a sphere of unit radius. A point on the surface of the sphere represents a qubit in a pure state and the points in the interior represent mixed states. Opposite points describe mutually orthogonal states, for example the point at the top of the Bloch sphere represents the $|0\rangle$ state and at the bottom the $|1\rangle$ state. Any qubit state can be defined by the angles θ and ϕ on the Bloch sphere,

$$|\psi\rangle = \cos\left(\frac{\theta}{2}\right)|0\rangle + \exp(i\phi)\sin\left(\frac{\theta}{2}\right)|1\rangle\,. \tag{2.48}$$

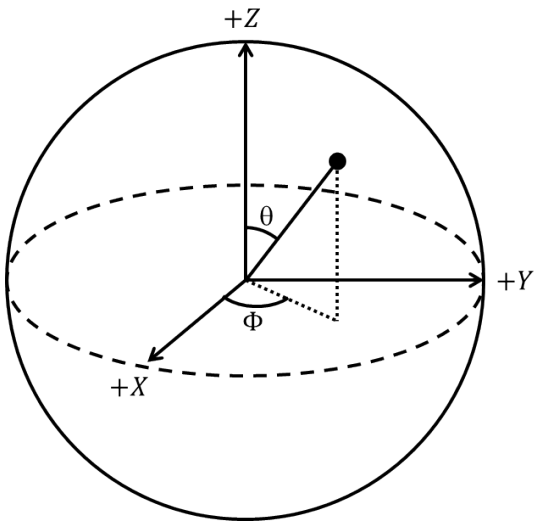

Figure 2.1: Bloch sphere. The angles θ and ϕ are used to define a quantum state on the Bloch sphere.

2.12 Entanglement

A pure state is said to be entangled if it cannot be written as a product of two states

$$\begin{aligned} \text{Non-entangled state:} \quad & |\psi\rangle = |\lambda\rangle_a |\phi\rangle_b\,, \\ \text{Entangled state:} \quad & |\psi\rangle = \frac{1}{\sqrt{2}}(|0\rangle_a |0\rangle_b + |1\rangle_a |1\rangle_b). \end{aligned} \tag{2.49}$$

It is not always clear in which basis a state can be written to show it is separable. When dealing with qubits one way to check if a state is separable is to use the positive

partial transpose, or PPT, criterion. The positive partial transpose is an performs a transpose on only one subsystem of a bipartite system, the state $\rho = |jk\rangle_{AB} \langle lm|$ under the positive partial transpose would become $\rho^{T_B} = |jm\rangle_{AB} \langle lk|$. If the eigenvectors of the partial transpose of the state are positive then the state is definitely separable. For example, if we take the entangled state shown in Eq. (2.49), the positive partial transpose looks like,

$$\begin{aligned} |\psi\rangle \langle\psi| &= \frac{1}{2}(|00\rangle \langle 00| + |00\rangle \langle 11| + |11\rangle \langle 00| + |11\rangle \langle 11|), \\ |\psi\rangle \langle\psi|^{PT} &= \frac{1}{2}(|00\rangle \langle 00| + |01\rangle \langle 10| + |10\rangle \langle 01| + |11\rangle \langle 11|), \end{aligned} \tag{2.50}$$

and the eigenvalues give $-1/2, 1/2, 1/2, 1/2$ so this state is not separable and so must be entangled. The Bell states are a set of maximally entangled two-qubit states

$$\begin{aligned} |\phi^+\rangle &= \frac{1}{\sqrt{2}}(|00\rangle + |11\rangle), \\ |\phi^-\rangle &= \frac{1}{\sqrt{2}}(|00\rangle - |11\rangle), \\ |\psi^+\rangle &= \frac{1}{\sqrt{2}}(|01\rangle + |10\rangle), \\ |\psi^-\rangle &= \frac{1}{\sqrt{2}}(|01\rangle - |10\rangle). \end{aligned} \tag{2.51}$$

These will be useful later. We can also have entangled mixed states, these are states that are not separable and cannot be expressed as a mixture of product states.

2.13 Projective measurements

Simplest form of measurements are von Neumann measurements or projective measurements. We start with an observable that follows the eigenvalue equation

$$\hat{A} |\lambda_n\rangle = \lambda_n |\lambda_n\rangle . \tag{2.52}$$

The eigenstates form a complete orthonormal set so we can write the operator in terms of eigenvalues and vectors,

$$\hat{A} = \sum_n \lambda_n |\lambda_n\rangle \langle\lambda_n| . \tag{2.53}$$

The probability that measurement of A will give λ_n is,

$$P(\lambda_n) = \langle\lambda_n| \hat{\rho} |\lambda_n\rangle = \mathrm{Tr}(\hat{\rho} |\lambda_n\rangle \langle\lambda_n|), \tag{2.54}$$

where $\hat{\rho}$ is the density operator of the system being measured. We introduce the projector $\hat{P}_n = |\lambda_n\rangle \langle\lambda_n|$ and can rewrite the probability as,

$$P(\lambda_n) = \mathrm{Tr}(\hat{\rho}\hat{P}_n), \tag{2.55}$$

this makes dealing with degenerate eigenstates easier. Degenerate eigenstates are those states which have two or more eigenstates that correspond to the same eigenvalue. For example if there are two orthonormal eigenstates $|\lambda_n^1\rangle$ and $|\lambda_n^2\rangle$ that correspond to eigenvalue λ_n can write the probability as,

$$P(\lambda_n) = \sum_{j=1}^{2} \mathrm{Tr}(\hat{\rho}\,|\lambda_n^j\rangle\,\langle\lambda_n^j|), \tag{2.56}$$

the projector here looks like,

$$\hat{P}_n = |\lambda_n^1\rangle\,\langle\lambda_n^1| + |\lambda_n^2\rangle\,\langle\lambda_n^2|\,. \tag{2.57}$$

The projectors in von Neumann measurements have the following properties: they are all Hermitian, $\hat{P}_n^\dagger = \hat{P}_n$, they are all positive, $\hat{P}_n \geq 0$ they are complete $\sum_n \hat{P}_n = \hat{\mathbb{I}}$ and they are all orthonormal $\hat{P}_i\hat{P}_j = \hat{P}_i\delta_{ij}$. We complete the description of the von Neumann measurement by describing the state of the system immediately after the measurement. If a measurement of A gives result λ_n that is associated with a non-degenerate eigenstate $|\lambda_n\rangle$, the post-measurement state is $|\lambda_n\rangle$. So if a measurement of A is performed again straight after the measurement produces the same result. But if the eigenvalue λ_n is associated with more than one eigenstate, the state of the system is changed as,

$$\hat{\rho} \to \hat{\rho}_n = \frac{\hat{P}_n\hat{\rho}\hat{P}_n}{\mathrm{Tr}(\hat{P}_n\hat{\rho}\hat{P}_n)} = \frac{\hat{P}_n\hat{\rho}\hat{P}_n}{P(\lambda_n)}. \tag{2.58}$$

These measurements do not take into account extra noise that may occur in the measurement process. The ideal von Neumann measurement to determine if a qubit is in state $|0\rangle$ or $|1\rangle$ is a pair of projectors,

$$\begin{aligned} \hat{P}_0 &= |0\rangle\,\langle 0|\,, \\ \hat{P}_1 &= |1\rangle\,\langle 1|\,. \end{aligned} \tag{2.59}$$

We can introduce noise using the operators,

$$\begin{aligned} \hat{\pi}_0 &= (1-p)\hat{P}_0 + p\hat{P}_1 = (1-p)\,|0\rangle\,\langle 0| + p\,|1\rangle\,\langle 1|\,, \\ \hat{\pi}_1 &= (1-p)\hat{P}_1 + p\hat{P}_0 = (1-p)\,|1\rangle\,\langle 1| + p\,|0\rangle\,\langle 0|\,. \end{aligned} \tag{2.60}$$

These are not projectors as they are do not obey $P_n^2 = P_n$. They are known as positive operator-values measures (POVMs). As they are not orthonormal the number of elements in the POVM can be larger or smaller then the dimensionality of the system that is measured.

2.14 Measurements in other bases

In many physical systems the natural basis of measurement is the computational basis $\{|0\rangle, |1\rangle\}$. In order to change the basis of measurement from the computation/natural basis to a different one a rotation is required. This can be performed in two different ways, passive or active. A passive rotation is where the axes that define the directions on the Bloch sphere are rotated And an active rotation is where the qubit itself if rotated,

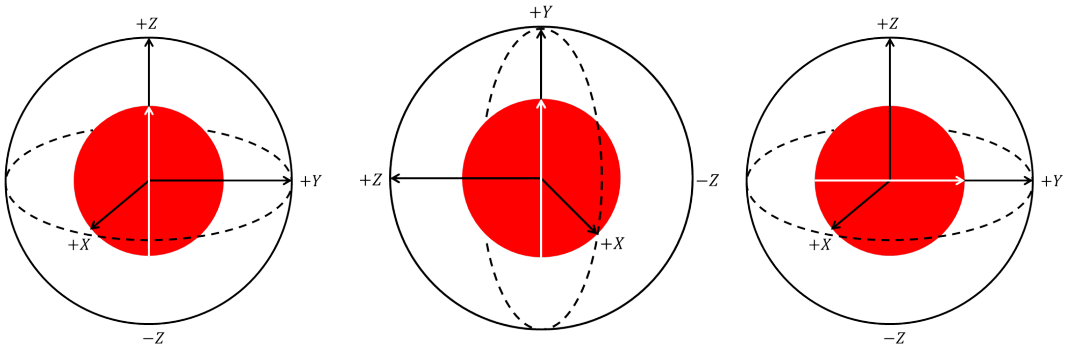

Figure 2.2: Passive versus active rotations. The qubit is shown in red. In (a) the qubit is originally aligned with the Z axes, this the computational basis, indicated by the white arrow. To change the basis we can perform a passive rotation (b) where the axes defining the measurement directions are rotated. Or an active rotation, (c), where the qubit itself is rotated to align with the appropriate measurement axes.

2.15 Quantum circuit

A quantum circuit can be used to describe an experimental set up, here we describe each of the elements in a circuit. A quantum circuit begins with an input and ends with a measurement, it is read from left to right. Each horizontal line represents a wire, this wire does not have to be physical it simply represents a passage of time or a path along which a qubit such as a photon travels along to get to the next element of the circuit. All measurements in a quantum circuit are performed in the computational basis $\{|0\rangle, |1\rangle\}$. The operations in the circuit are performed by quantum gates, these can act on one of more of the channels in the circuit. The single qubit gates we will be concerned with in this work are,

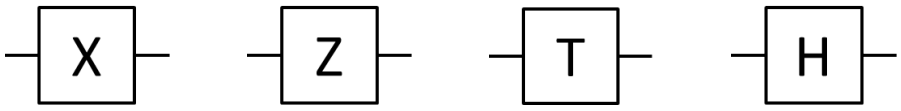

$$\hat{\sigma}_x = \begin{pmatrix} 0 & 1 \\ 1 & 0 \end{pmatrix}, \ \alpha|0\rangle + \beta|1\rangle \rightarrow \beta|0\rangle + \alpha|1\rangle,$$

$$\hat{\sigma}_z = \begin{pmatrix} 1 & 0 \\ 0 & -1 \end{pmatrix}, \ \alpha|0\rangle + \beta|1\rangle \rightarrow \alpha|0\rangle - \beta|1\rangle,$$

$$\hat{T} = \begin{pmatrix} 1 & 0 \\ 0 & e^{i\frac{\pi}{4}} \end{pmatrix}, \ \alpha|0\rangle + \beta|1\rangle \rightarrow \alpha|0\rangle + e^{i\frac{\pi}{4}}\beta|1\rangle,$$

$$\hat{H} = \frac{1}{\sqrt{2}}\begin{pmatrix} 1 & 1 \\ 1 & -1 \end{pmatrix}, \alpha|0\rangle + \beta|1\rangle \rightarrow \alpha\frac{|0\rangle+|1\rangle}{\sqrt{2}} + \beta\frac{|0\rangle-|1\rangle}{\sqrt{2}}.$$

Figure 2.3: Examples of quantum gates used in quantum circuits. The Pauli-X gate, the Pauli-Z gate, the Toffoli gate and the Hadamard gate respectively.

Two-qubit gates are also possible, in these cases the action of the gate is dependent upon the value of one of the qubits. The example here is the Controlled-Z or C-Z gate,

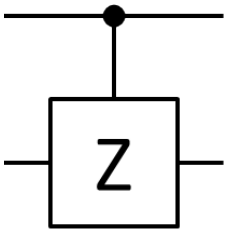

$$|00\rangle \rightarrow |00\rangle$$
$$|01\rangle \rightarrow |01\rangle$$
$$|10\rangle \rightarrow |1(-0)\rangle = |10\rangle$$
$$|11\rangle \rightarrow |1(-1)\rangle = -|11\rangle$$

Figure 2.4: The two-qubit C-Z gate. If the top qubit is in the state $|0\rangle$ then the gate does not act upon the second qubit, however if the first qubit is in the $|1\rangle$ state then the sign is flipped on the second qubit as is shown in the figure.

Putting all these examples together produces an example quantum circuit,

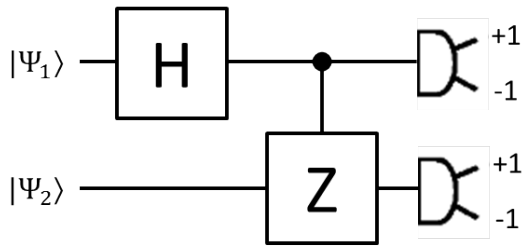

Figure 2.5: Example of a quantum circuit. Two qubits are fed into the circuit. Qubit one is operated on by the Hadamard gate followed by a C-Z operation between the two qubits. Finally the qubits are measured in the computation basis with the result $+1$ corresponding to the $|0\rangle$ state and the -1 result corresponding to the $|1\rangle$ state.

These are the fundamental quantum gates required to perform universal quantum computation. The X, Z and Hadamard gate all lie inside the Clifford group. The Gottesman-Knill theorem states that a set of highly entangled states may be simulated using quantum gates in the Clifford group [2]. By the inclusion of the phase gate, T, we are able to perform universal quantum computation, any unitary operation can be created using this set of gates.

2.16 Clauser-Horne-Shimony-Holt Inequality

Here we show the proof that a violation of the Clauser-Horne-Shimony-Holt (CHSH) inequality is only possible if either the assumption of locality or realism are false. The proof closely follows the arguments shown in [2].

We set up the experiment where Alice and Bob can receive particles prepared by Charlie, they can perform one of two measurements on their particles with equal probability. The result of this measurement will be ± 1. There is not prior knowledge of which measurement will be performed this could be decided using the flip of a coin or a random number generator. Let us call the two possible measurement choices Alice has a and a' each of which will have the result ± 1. Bob also has a choice of two measurements, lets call these b and b'. Fig. 2.6 shows a simple set up of the experiment. We assume these measurements correspond to a physical property of the particle.

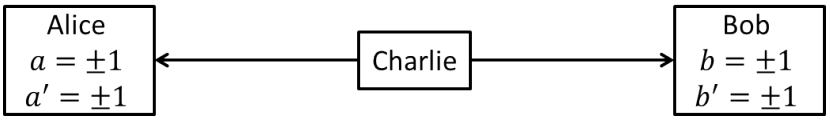

Figure 2.6: CHSH experimental setup. Alice can make one of two measurements a or a' with results ± 1 as can Bob with b or b'.

To ensure there is no information sent between the parties and so one measurement does not affect the other Alice and Bob perform their measurements simultaneously.

Looking at the joint measurement outcomes we use the following expression to find the CHSH inequality

$$ab + a'b + a'b' - ab' = (a + a')b + (a' - a)b', \tag{2.61}$$

as we know $a, a' = \pm 1$ meaning one of the two expressions in Eq. (2.61) must be zero so $ab + a'b + a'b' - ab' = \pm 2$. Now we introduce some probabilities $p(A, A', B, B')$ which denote the probability that the particle was in fact in the state before the measurement was performed, i.e $a = A, a' = A', b = B, b' = B'$. Charlie who prepares the state has control over these values. We can calculate the mean value of Eq. (2.61) using these probabilities

$$\begin{aligned}\mathbf{E}(ab + a'b + a'b' - ab') &= \sum_{AA'BB'} p(A, A', B, B')(AB + A'B' + AB' - AB') \\ &\geq \sum_{AA'BB'} p(A, A', B, B') \times 2 \\ &= 2.\end{aligned} \tag{2.62}$$

We can also write this another way

$$\begin{aligned}\mathbf{E}(ab + a'b + a'b' - ab') = &\sum_{AA'BB'} p(A, A', B, B')AB + \sum_{AA'BB'} p(A, A', B, B')A'B + \\ &\sum_{AA'BB'} p(A, A', B, B')A'B' - \sum_{AA'BB'} p(A, A', B, B')AB' \\ =&\mathbf{E}(ab) + \mathbf{E}(a'b) + \mathbf{E}(a'b') - \mathbf{E}(ab').\end{aligned} \tag{2.63}$$

Joining these two expressions together we see

$$\mathbf{E}(ab) + \mathbf{E}(a'b) + \mathbf{E}(a'b') - \mathbf{E}(ab') \geq 2. \tag{2.64}$$

This is the CHSH inequality.

If Charlie only prepares classical states and sends them to Alice and Bob to measure then the CHSH inequality holds, however if Charlie sends a quantum state then we see a violation. For example, if Charlie sends the Bell state

$$|\psi\rangle = \frac{|01\rangle - |10\rangle}{\sqrt{2}} \tag{2.65}$$

and Alice and Bob perform their measurements using this set of axes

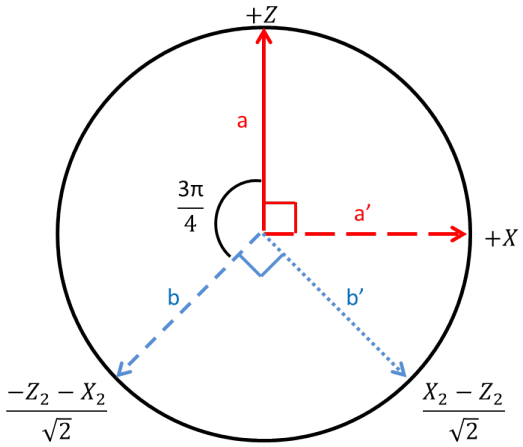

Figure 2.7: Alice and Bob's conventional measurement axes.

The expectation values can now be written using quantum mechanical notation, $\langle \cdot \rangle$

$$\langle ab \rangle = \frac{1}{\sqrt{2}}; \quad \langle a'b \rangle = \frac{1}{\sqrt{2}}; \quad \langle a'b' \rangle = \frac{1}{\sqrt{2}}; \quad \langle ab' \rangle = -\frac{1}{\sqrt{2}}, \tag{2.66}$$

when we put these results into the CHSH inequality we see our violation

$$\langle ab \rangle + \langle a'b \rangle + \langle a'b' \rangle - \langle ab' \rangle = 2\sqrt{2}. \tag{2.67}$$

This violation implies that one of the assumptions in the derivation of the CHSH inequality does not hold. The assumptions we made were that the measurements correspond to a physical property that exists without the measurement taking place, this is called realism. We also assumed that Alice's measurement does not affect Bob's measurement this is known as locality. The violation shows that the quantum state cannot be described using realism or locality. The feature of the quantum state that causes this violation is entanglement, if a state is entangled then it will violate the CHSH inequality and so the inequality can be used as an entanglement witness which is what we will do in this work. It is important to note that the reverse of this statement is not necessarily true, if a state violated the CHSH inequality it is not always entangled.

CHAPTER 3

Cross-talk minimising stabilizer operators

3.1 Introduction

Cluster states are a candidate for measurement-based quantum computation because they are highly entangled multi-party systems. There has been a large amount of research into physically realising cluster states [17, 18, 19, 20, 21, 22, 23]. One example is by trapping single atoms in wells of optical lattices, this set up allows the atoms to be addressed individually which is required for cluster state computation [13].

When creating any type of state it is also important that we are able to verify it. In general, this is a hard problem due to the exponential number of parameters needed to characterise a quantum state. This problem rules out quantum tomography as a resource for verification as it is so inefficient for more than a few qubits [3]. Cluster states are a special class of quantum state that allows simple verification. Each cluster state is associated with a linear set of stabilizer operators. Stabilizer operators are operators that can be used to verify a cluster state with a linear number of measurements.

The physical measurement of the stabilizer operators leads to an issue of cross-talk where adjacent atoms in the lattice may be over or under rotated during measurement leading to errors in the measurement results. By taking advantage of the fact that stabilizer operator sets are not unique, we aim to create equivalent sets of stabilizer operators that have a reduced level of cross-talk.

The chapter is set out as follows, in Sec. 3.2 we introduce the stabilizer operator formalism in cluster states and in Sec. 3.3 show how equivalent sets of stabilizer operators can be created. By defining a cross-talk measure in Sec. 3.4 we will identify the number of times cross-talk affects a cluster state. In Sec. 3.5 explore the ideas of stabilizer operators with no cross-talk in various shaped lattices. In Sec. 3.6 and

Sec. 3.7 we study stabilizer operators in triangular shaped, triangular connectivity and hexagonal cluster states respectively.

This work is available as a preprint article at arXiv:1507.04637 [24].

3.2 Background

It is vital that we are able to verify quantum states that are produced. Usually this is very difficult with many body quantum states as the number of parameters grows exponentially with the number of particles in the state as 2^{2N} where N is the number of qubits in the density operator. However, cluster states provide a solution to this difficulty. A linear number of stabilizer operators, in this case strings of Pauli matrices, can be used to define, and therefore verify a cluster state. Not every quantum state is a cluster state but a large class are. Cluster states are highly entangled and useful for measurement-based computation, they also occur in quantum error correction making them a promising tool for quantum computation. The Gottesman-Knill theorem states that even though the cluster states are highly entangled it is possible to simulate these types of states and the set of Clifford group operators on a classical computer using the Heisenberg representation [2]. The Clifford operators are the Hadamard gate, the phase gate and the CNOT gate, where the CNOT gate is a controlled Pauli X gate. However, although it is easy to describe these specific states and operations, universal measurement-based quantum computation is still difficult. This means that the difficulties in simulating quantum states is not solely down to the entanglement.

In this section we introduce the concept of cluster state computation, describing how stabilizer operators can be used to describe the states. To use these stabilizer operators to verify the state they need to be physically measured, this involves locally addressing certain particles in the cluster state. Due to physical constraints cross-talk can be introduced into the system. This cross-talk can affect the results of our measurements reducing their reliability. We will show how the cross-talk occurs and in the next section suggest ways of reducing and eliminating it.

3.2.1 Cluster states/graph states

A cluster state is a many body quantum system defined as the simultaneous +1 eigen-state of a set, $\mathcal{S}$, of commuting stabilizer operators, $\hat{S}^a$ [25]

$$\hat{S}^a \left|\psi\right\rangle = + \left|\psi\right\rangle, \forall \hat{S}^a \in \mathcal{S}. \tag{3.1}$$

For cluster states the stabilizer operators themselves are constructed using the following equation [25]

$$K^a = \sigma_x^{(a)} \bigotimes_{b \in \text{ neighbour of a}} \sigma_z^{(b)}, \tag{3.2}$$

where σ_x represents a Pauli X operator and σ_z a Pauli Z operator (Eq. (3.3)), a is the initial target qubit and b is all the neighbouring qubits that share an edge with a. An edge is defined as a connection between two qubits signalling there has been an entangling operation between them. Cluster states are a type of graph state and so can be drawn as such. An edge is represented by a line between the two qubits when a cluster state is drawn in its graphical form. Fig. 3.1 shows a square connectivity cluster state that has a stabilizer operator applied to the centre target qubit, a.

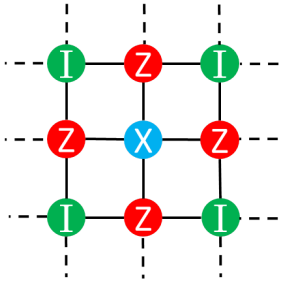

Figure 3.1: Graphical description of a stabilizer operator applied to a central qubit, a, in a infinite square connectivity cluster state. Each node represents a qubit, the letter signifies the type of Pauli operation performed on that qubit and each edge defines an entangling operation between the joined qubits. The Z Pauli operators are applied to, b, the neighbouring qubits. The identity operator is applied to all the qubits not pictured. This labeling format will be used throughout this chapter.

If a cluster state has N qubits we require N linearly independent stabilizer operators to define it. These stabilizer operators can be used to verify the cluster state. When measuring all the N linearly independent stabilizer operators that define a particular cluster state, if all the expectation values are $+1$, we can be certain that the state measured is that particular cluster state [8, 25, 26].

Throughout this chapter when applying a stabilizer operator on qubit "a" we refer to applying the Pauli X operator to qubit a and Z to b, all the neighbours of a. As cluster states come in all shapes and sizes we will also define the shape and connectivity of the cluster state to ensure clarity.

As we know from Eq. (3.2) the stabilizer operators consist of X and Z operators. Measuring the value of the stabilizer operator is measuring the joint expectation value of the string of Pauli operators. The stabilizer operators all commute so in principle it should be possible to measure all of them simultaneously on a single state. However, in practice we construct the stabilizer operators by individual Pauli measurements on each of the separate qubits in the system, then, by combining these results we produce an expectation value of the stabilizer operator measurement. For example, if we take the cluster state shown in Fig. 3.1 and wish to measure the stabilizer operator on the centre qubit we would simultaneously measure each of the qubits in the pattern shown, then by multiplying the ± 1 results of these measurements together we get the expectation value of the stabilizer operator. However if we wish to measure more than one stabilizer at the same time more care must be taken in the measurement pattern

as this will involve measuring both X and Z operators on each qubit individually and these individual Pauli measurements do not commute,

$$X = \begin{pmatrix} 0 & 1 \\ 1 & 0 \end{pmatrix}, \quad Z = \begin{pmatrix} 1 & 0 \\ 0 & -1 \end{pmatrix}, \tag{3.3}$$
$$XZ = -ZX.$$

Given this experimental limitation one way of measuring the expectation value of all the stabilizer operators is to perform two slightly different measurements (Fig. 3.2) on two states prepared in the same way. We measure these patterns many times to build up good statistical values for the expectation of the measurement. The set of stabilizer operators that describe a state is not unique, this is the property that we will exploit later.

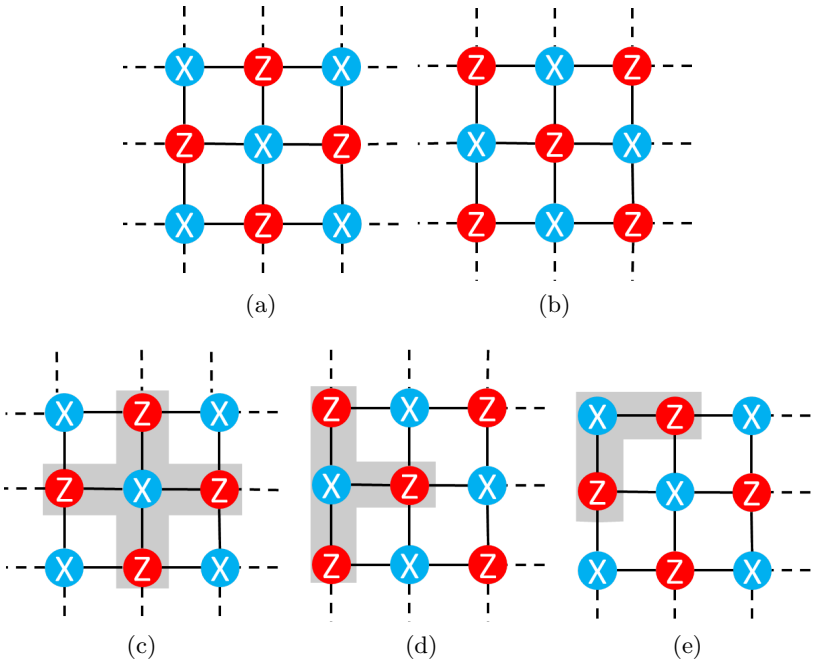

Figure 3.2: Stabilizer operator Pauli measurement patterns. The two patterns of physical measurements performed upon the qubits in the lattice are illustrated in (a) and (b). By multiplying the ± 1 results of these individual operator measurements we can calculate the expectation value of the stabilizer operator applied to any qubit in the lattice. In (c),(d) and (e) the shaded grey areas show the measurement results that are multiplied together to calculate the stabilizer operator on the central, edge and corner qubit respectively.

3.2.2 Fidelity of cluster states

Creating quantum states is a difficult process and many errors in the preparation stages can affect the state produced. It is important to know how close the state produced is

to the ideal state. One way to measure this closeness is using the fidelity measure,

$$\mathcal{F} = \sqrt{\langle\psi|\,\rho\,|\psi\rangle}, \tag{3.4}$$

where $|\psi\rangle$ is the ideal pure state and ρ is the state that has been prepared [2]. Note some authors define the fidelity as $\mathcal{F}' = \mathcal{F}^2$ [27].

In order to calculate the fidelity using Eq. (3.4) a description of ρ is required, this could be done through quantum state tomography [3]. However, the more qubits in the state the more parameters there are and this grows exponentially and becomes too large with more than a few qubits. The number of parameters is 2^N where N is the number of qubits in the system. To counteract this exponential growth it is possible to find a lower bound on $\mathcal{F}$ by using measurements that are linear in N [26].

The operator to calculate the lower bound of fidelity $\hat{S}_\mathcal{S}$ is defined as

$$\hat{S}_\mathcal{S} = \frac{1}{2}[(\sum_{a=1}^{N} \hat{S}^a) - (N-2)\mathbb{I}], \tag{3.5}$$

where $\hat{S}_\mathcal{S} = \pm 1$ meaning $-1 \leq \langle\hat{S}_\mathcal{S}\rangle \leq +1$. Note that when all $\langle\hat{S}_a\rangle = +1, \langle\hat{S}_S\rangle = 1$.

The expectation of this operator gives a lower bound on the fidelity [26],

$$\mathcal{F}^2(\rho,\psi) \geq \langle\hat{S}_\mathcal{S}\rangle_\rho. \tag{3.6}$$

This lower bound is useful as we can be certain that whatever the measurement value of the lower bound is, the actual fidelity of the state will be the same or better $\mathcal{F}^2_{min} \leq \langle\hat{S}_\mathcal{S}\rangle \leq \mathcal{F}^2_{actual}$. This lower bound is a linear function that only needs N expectation values of $\{\hat{S}_\mathcal{S}\}$ to produce a lower bound for $\mathcal{F}$.

3.2.3 Measurement and Cross-talk

To compute the value of the stabilizer operators we need to measure in both the Z and X bases to recreate the patterns shown in Fig. 3.2. The Z basis is the computational basis, the natural basis of measurement, which is not a problem [2]. Measuring in the X basis is more complex, first an active local rotation is applied to the qubit to be measured, this rotates the internal qubit states by $\frac{\pi}{2}$ in the $X-Z$ plane of the Bloch sphere. Then, when a measurement is made on this qubit in the global Z basis the result corresponds to a measurement in the local X basis of the atom (Fig. 3.3).

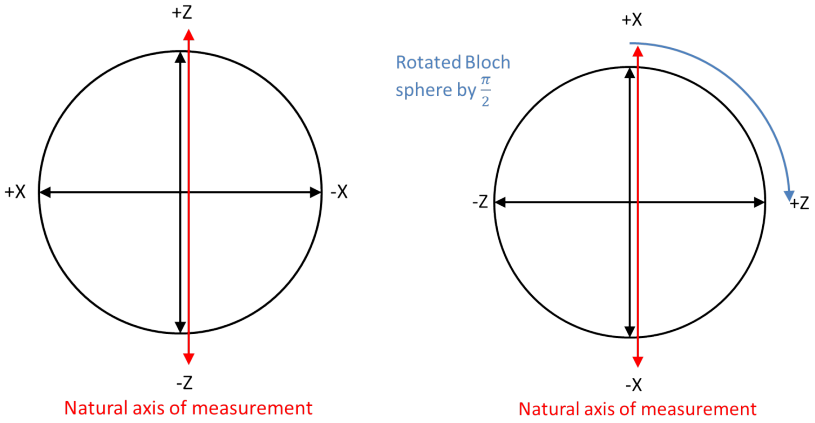

(a) (b)

Figure 3.3: Active rotation of the Bloch sphere. (a) shows the Bloch sphere in its natural orientation, the natural axis of measurement is along the Z axis, actively rotating the sphere by applying a $\frac{\pi}{2}$ pulse to the atom the sphere is rotated meaning the axis of natural measurement is now along what was the X axis. The rotation in this image is just an illustration of types of rotations that could be done, it is not experimentally correct.

This local active rotation of the atom is where we begin to see a problem. To perform the active rotation a global microwave pulse is applied to the entire cluster state that is off-resonant with the energy needed to perform the $\frac{\pi}{2}$ rotation. By locally addressing the individual atoms to be rotated with another off-resonant laser beam that induces the AC Stark effect, the energy levels within the addressed atom shift into resonance with the microwave field which applies a $\frac{\pi}{2}$ pulse, rotating the state [13]. So when the whole lattice is measured in the natural basis of Z, effectively an X measurement is performed on the addressed atoms prior to their rotation. The laser beam that locally addresses the atoms causes our problem. If we look at the experimental set up in Ref. [13] we will see why. Here the atoms are confined in an optical lattice created by counter-propagating laser beams. The addressing laser is a Gaussian beam with a diameter at full-width half-maximum of $\approx 600nm$, the lattice spacing in this experiment is set at $a_{lat} = 532nm$. When the laser addresses an individual atom it is not just the addressed atom that feels its energy (Fig. 3.4). This phenomenon is known as cross-talk. In Ref. [13] an adjacent atom see 10% of the total intensity of the laser, given the centre of the laser hits the exact centre of the target atom. This 10% can lead to the nearest neighbour atoms of the target atom to also be rotated by some amount which will cause error in the measurement results.

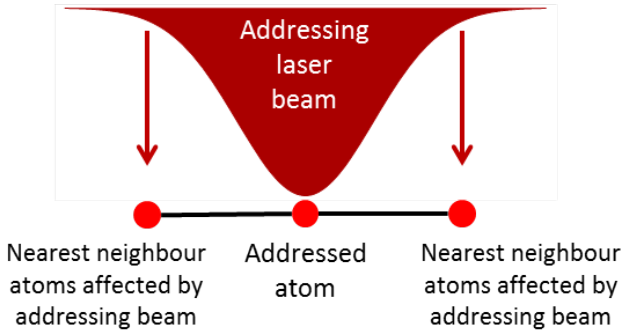

Figure 3.4: Demonstration of how an addressing laser beam can affect nearest neighbour atoms. The width of the beam is larger than the atom spacing and so the nearest neighbour atoms can be affected by the addressing beam.

Effects of this cross-talk could be ameliorated by compensation pulse sequences, this is commonly used in NMR [28]. However, it is desirable to reduce or avoid the overhead incurred by these pulses. Instead, we will be looking at a theoretical way to mitigate this unwanted cross-talk effect. To do this we will explore the manipulation of the stabilizer operators in a way to at least decrease the cross-talk and if possible eradicate it completely.

3.3 Stabilizer operator sets

The set of stabilizer operators that all have expectation value +1 on a particular cluster state form a multiplicative group. This can be shown using the following properties [29];

- The multiplication is associative, $S_1(S_2S_3) = (S_1S_2)S_3$,
- The set has an identity element, this is simply the identity operator applied to all N qubits in the cluster state, $S_{\mathbb{I}} = \mathbb{I}_1 \ldots \mathbb{I}_N$
- Every element has an inverse, the stabilizer operators are made up of Pauli operators which are all their own inverse. Applying a stabilizer operator twice leads to the identity, $S_1S_1 = \mathbb{I}_1 \ldots \mathbb{I}_N$.

This means that the N linearly independent stabilizer operators needed to stabilize a state is not unique. We can use this fact to create equivalent sets with a reduced amount of cross-talk.

3.3.1 Equivalent sets of stabilizer operators

When creating equivalent sets of stabilizer operators it is vital that the new set can reconstruct the canonical set, $\mathcal{S}$, found using Eq. (3.2). $\{\hat{S}^{a'}\}$ is an equivalent set of stabilizer operators if $\hat{S}^a$ is related to $\hat{S}^{a'}$ by a non-singular binary matrix $m = (m_{jk})$ with $m_{jk} = 0$ or 1.

A new equivalent set of stabilizer operators, $\mathcal{S}'$, will stabilize the original cluster state with N stabilizer operators if it follows

$$\hat{S}^{j'} = \prod_{k=1}^{N} (\hat{S}^k)^{m_{jk}}, \tag{3.7}$$

it is also possible to reconstruct the original canonical set, $\mathcal{S}$, found using Eq. (3.2) from this equivalent set.

3.3.1.1 Example of equivalent stabilizer sets

Lets look at an example to see this in action

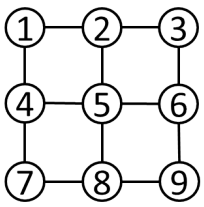

Figure 3.5: A 3×3 cluster state.

Fig. 3.5 shows a 3×3 cluster state with the set canonical stabilizer operators, $\mathcal{S}$ found using Eq. (3.2),

$$\begin{aligned}
s_1 &= X_1 Z_2 \mathbb{I}_3 Z_4 \mathbb{I}_5 \mathbb{I}_6 \mathbb{I}_7 \mathbb{I}_8 \mathbb{I}_9, \\
s_2 &= Z_1 X_2 Z_3 \mathbb{I}_4 Z_5 \mathbb{I}_6 \mathbb{I}_7 \mathbb{I}_8 \mathbb{I}_9, \\
s_3 &= \mathbb{I}_1 Z_2 X_3 \mathbb{I}_4 \mathbb{I}_5 Z_6 \mathbb{I}_7 \mathbb{I}_8 \mathbb{I}_9, \\
s_4 &= Z_1 \mathbb{I}_2 \mathbb{I}_3 X_4 Z_5 \mathbb{I}_6 Z_7 \mathbb{I}_8 \mathbb{I}_9, \\
s_5 &= \mathbb{I}_1 Z_2 \mathbb{I}_3 Z_4 X_5 Z_6 \mathbb{I}_7 Z_8 \mathbb{I}_9, \\
s_6 &= \mathbb{I}_1 \mathbb{I}_2 Z_3 \mathbb{I}_4 Z_5 X_6 \mathbb{I}_7 \mathbb{I}_8 Z_9, \\
s_7 &= \mathbb{I}_1 \mathbb{I}_2 \mathbb{I}_3 Z_4 \mathbb{I}_5 \mathbb{I}_6 X_7 Z_8 \mathbb{I}_9, \\
s_8 &= \mathbb{I}_1 \mathbb{I}_2 \mathbb{I}_3 \mathbb{I}_4 Z_5 \mathbb{I}_6 Z_7 X_8 Z_9, \\
s_9 &= \mathbb{I}_1 \mathbb{I}_2 \mathbb{I}_3 \mathbb{I}_4 \mathbb{I}_5 Z_6 \mathbb{I}_7 Z_8 X_9,
\end{aligned} \tag{3.8}$$

We define our non-singular matrix as

$$m = \begin{pmatrix} 1 & 1 & 0 & 0 & 0 & 0 & 0 & 0 & 0 \\ 0 & 1 & 0 & 0 & 0 & 0 & 0 & 0 & 0 \\ 0 & 0 & 1 & 1 & 0 & 0 & 0 & 0 & 0 \\ 0 & 0 & 0 & 1 & 0 & 0 & 0 & 0 & 0 \\ 0 & 0 & 0 & 0 & 1 & 1 & 0 & 0 & 0 \\ 0 & 0 & 0 & 0 & 0 & 1 & 0 & 0 & 0 \\ 0 & 0 & 0 & 0 & 0 & 0 & 1 & 1 & 0 \\ 0 & 0 & 0 & 0 & 0 & 0 & 0 & 1 & 1 \\ 0 & 0 & 0 & 0 & 0 & 0 & 0 & 0 & 1 \end{pmatrix}. \tag{3.9}$$

Using Eq. (3.7), our new set looks like

$$\begin{aligned} s_{12} &= X_1 Z_1 Z_2 X_2 Z_3 Z_4 Z_5 \mathbb{I}_6 \mathbb{I}_7 \mathbb{I}_8 \mathbb{I}_9, \\ s_2 &= Z_1 X_2 Z_3 \mathbb{I}_4 Z_5 \mathbb{I}_6 \mathbb{I}_7 \mathbb{I}_8 \mathbb{I}_9, \\ s_{34} &= Z_1 Z_2 X_3 X_4 Z_5 Z_6 Z_7 \mathbb{I}_8 \mathbb{I}_9, \\ s_4 &= Z_1 \mathbb{I}_2 \mathbb{I}_3 X_4 Z_5 \mathbb{I}_6 Z_7 \mathbb{I}_8 \mathbb{I}_9, \\ s_{56} &= \mathbb{I}_1 Z_2 Z_3 Z_4 X_5 Z_5 Z_6 X_6 \mathbb{I}_7 Z_8 Z_9, \\ s_6 &= \mathbb{I}_1 \mathbb{I}_2 Z_3 \mathbb{I}_4 Z_5 X_6 \mathbb{I}_7 \mathbb{I}_8 Z_9, \\ s_{78} &= \mathbb{I}_1 \mathbb{I}_2 \mathbb{I}_3 Z_4 Z_5 \mathbb{I}_6 X_7 Z_7 Z_8 X_8 Z_9, \\ s_{89} &= \mathbb{I}_1 \mathbb{I}_2 \mathbb{I}_3 \mathbb{I}_4 Z_5 Z_6 Z_7 X_8 Z_8 Z_9 X_9, \\ s_9 &= \mathbb{I}_1 \mathbb{I}_2 \mathbb{I}_3 \mathbb{I}_4 \mathbb{I}_5 Z_6 \mathbb{I}_7 Z_8 X_9. \end{aligned} \tag{3.10}$$

See Appendix A.1 for the graphical representation of these stabilizer operators. This set still stabilizes the cluster state shown in Fig. 3.5 and can be used to reconstruct the canonical set making it a valid equivalent set.

3.3.2 Construction of cross-talk-free stabilizer operators

The issue of cross-talk arises from having to measure two types of Pauli operator on adjacent qubits. In order to reduce or eradicate the cross-talk in the stabilizer operator we have two choices. The first choice is to create stabilizer operators where the X and Z operators are separated and do not act on adjacent qubits. The second choice is to create stabilizer operators where there is only one type of operator, meaning there is no cross-talk (Fig. 3.6). This operator does not necessarily have to be a Z operator as it is possible to perform a global rotation on all the qubits in the system that avoids the issue of cross-talk. Both these ideas have the potential to create cross-talk-free (CTF) stabilizer operators, we will explore if they are realisable.

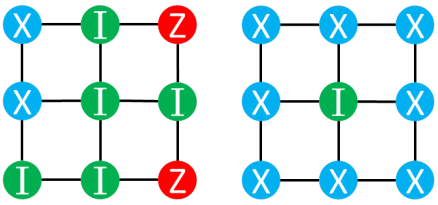

(a) (b)

Figure 3.6: Examples of ideal cross-talk free stabilizer operators. (a) shows the case where the operators are separated. This set up could be physically realised by globally rotating the entire cluster state to the X position, and singly addressing the two qubits that need to be rotated back to their original orientation as these qubits are far enough away from other qubits that require measurement for the cross-talk to not have an effect. (b) is an example of a homogeneous CTF stabilizer operator where only one type of stabilizer is present in the cluster state, found using a global rotation of the entire cluster state.

3.3.2.1 Choice 1: Separating X and Z

We can immediately rule out the first idea of separating the X and Z operators because of the way they are formed using Eq. (3.2). To illustrate this we consider a one dimensional line of N qubits. We wish the X operator to be as far away as possible from the Z operator so the stabilizer operator would look like,

$$X_1\mathbb{I}_2\mathbb{I}_3\ldots\mathbb{I}_{n-2}\mathbb{I}_{N-1}Z_N. \tag{3.11}$$

To create this pattern we follow these steps

$$\begin{aligned} Step\,1 \quad & X_1Z_2\mathbb{I}_3\ldots\mathbb{I}_N, \\ Step\,2 \quad & X_1\mathbb{I}_2X_3Z_4\mathbb{I}_5\ldots\mathbb{I}_N, \\ & \vdots \\ Step\,N_{even} \quad & X_1\mathbb{I}_2X_3\ldots\mathbb{I}_{N-2}X_{N-1}Z_N, \\ Step\,N_{odd} \quad & X_1\mathbb{I}_2X_3\ldots\mathbb{I}_{N-1}X_N. \end{aligned} \tag{3.12}$$

There are two possible endings depending if N is odd or even. When N is even there is no way to eliminate the X that appears on the $(N-1)$th qubit without performing a trivial operation that simply moves the XZ pairing elsewhere in the line. When N is odd all the Z operators are eliminated which is not what we were trying to find, but is a good example of our next idea, homogeneous CTF stabilizer operators.

3.3.2.2 Choice 2: Xs or Zs only

As we have just seen in the previous subsection, it is possible to eliminate all the Z operators from a stabilizer operator. We now see if we can do the same with the X operators.

When we apply Eq. (3.2) to a cluster state, there can only be one X operator applied to each qubit over the whole set of stabilizer operators (See Sec. 3.3.1.1 for a list of stabilizer operators as an example). This means that it cannot be possible to eliminate the X operators as we can only multiply them with a Z or $\mathbb{I}$ operator, neither of which cancel out the X. This leaves us with the conclusion that non-trivial homogeneous cross-talk-free (HCTF) stabilizer operators may only be found using X operators.

In the ideal case, we would like a complete set of HCTF stabilizer operators to define our cluster state, but as any new equivalent set must be able to recreate the canonical set we also see that this will not be possible, as there are no Z operators in the HCTF stabilizer operators. If there are no Z operators in our set and we cannot form them using X and $\mathbb{I}$ operators it will not be possible to recreate the canonical set. This means that in our equivalent set we will have to include some stabilizer operators that contain cross-talk, but we can be clever with this choice and use the stabilizer operators with the least amount of cross-talk to complete the set. We define a measure of cross-talk in a stabilizer operator to aid this choice in Sec. 3.4.

3.4 Minimising cross-talk

As we have seen with a new equivalent set of stabilizer operators we must be able to recreate the canonical set formed using Eq. (3.2). We will not be able to do this just using HCTF stabilizer operators and so we must include cross-talk stabilizer operators. To make the overall cross-talk in the system as low as possible we want to choose the cross-talk stabilizer operators that have the least amount of cross-talk. To quantify cross-talk we introduce a cross-talk penalty, P_{CT}.

3.4.1 Cross-talk penalty

The cross-talk penalty, P_{CT}, describes the number of pairs of XZ operators in any single stabilizer operator, hence the number of times cross-talk will occur in the measurement process,

$$P_{CT}(\hat{S}^a) = Tr[B^\dagger B] = \sum_{jk} x_j^2 z_k^2 A_{jk}^2, \tag{3.13}$$

where $A_{jk}, x_k, z_j = 0, 1$. The elements in this equation are defined as follows,

$$B = A \circ (F_{XZ}), \tag{3.14}$$

this is the Hadamard product or entry wise product where $B_{jk} = A_{jk}(F_{XZ})_{jk}$. A is the adjacency matrix with $A_{jk} = 1$ when qubits j and k share an edge and $A_{jk} = 0$ otherwise,

$$A = \sum_{jk} a_{jk} E_{jk}, \tag{3.15}$$

where E_{jk} is a basis matrix $(E_{jk})_{nm} = \delta_{jm}\delta_{kn}$. F_{XZ} is the outer product of F_X and F_Z,

$$\begin{aligned} F_{XZ} &= \sum_{jk} x_j z_k E_{jk}, \\ F_X = \sum_j x_j E_j, \qquad & F_Z = \sum_k z_k E_k, \end{aligned} \tag{3.16}$$

where x_j is a vector where the element $j = 1$ when an X operator is applied to it and 0 otherwise, same with z_k but with Z operators. E_j and E_k are both basis vectors with the jth and kth element as 1 respectively, otherwise 0.

The total cross-talk in a set of stabilizer operators $\{\hat{S}^a\}$ is characterised as,

$$P_{CT}^{T} = \sum_{1}^{N} P_{CT}(\hat{S}^a). \tag{3.17}$$

3.4.1.1 Example of a set of reduced cross-talk stabilizer operators

If we take the 3×3 cluster state shown in Sec. 3.3.1.1 the canonical set of stabilizer operators has a cross-talk penalty of $P_{CT}^{T_c} = 24$, (See Appendix A.2 for a graphical representation of all nine canonical stabilizer operators). Whereas if we use a set with HCTF stabilizer operators and an intelligent choice of cross-talk stabilizer operators then we can reduce this number to $P_{CT}^{T_{new}} = 13$ (Fig. 3.7). We will show how these HCTF stabilizer operators are constructed in Sec. 3.5.

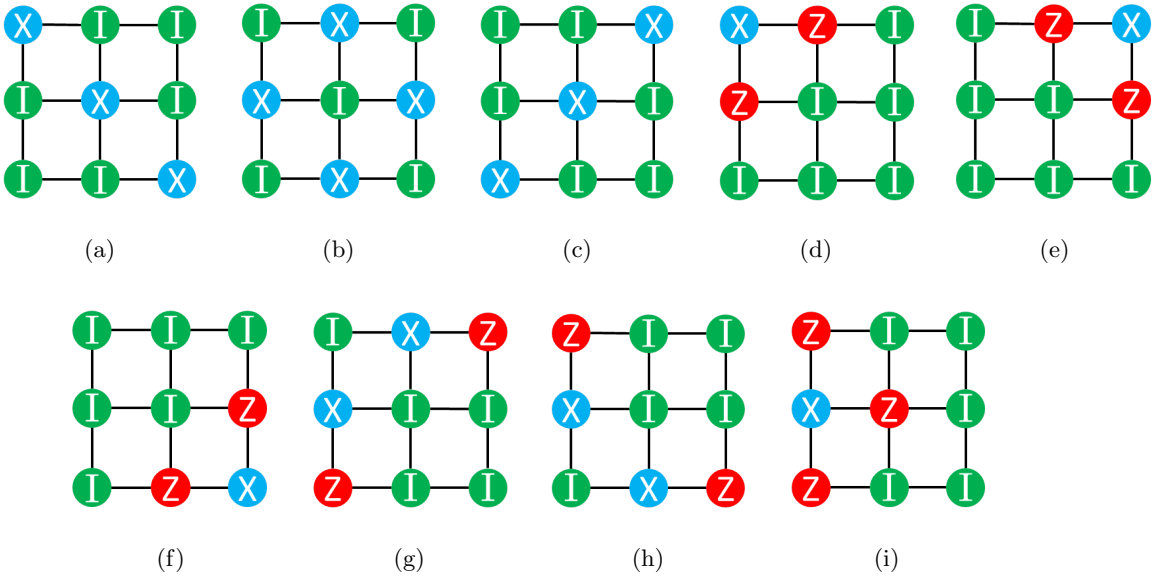

Figure 3.7: Reduced cross-talk set of stabilizers found using a combination of HCTF stabilizer operators and low penalty cross-talk stabilizer operators.

3.4.2 Extending and adapting P_{CT}

This idea can be extended to withstand more complicated definitions of cross-talk and how it affects the system. For example, if the qubits in a cluster state are connected by an edge but the physical distance between them is greater than the range of cross-talk then that XZ pairing should not be included in the cross-talk penalty measure (Fig. 3.8).

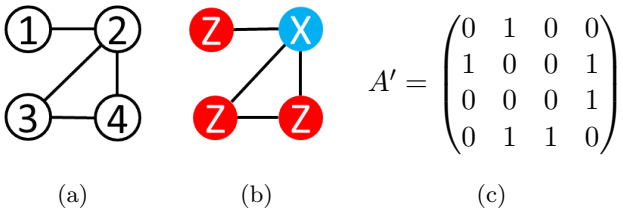

Figure 3.8: A graph state of a modified cluster state. (a) shows a modified cluster state where the edge connecting qubits 2 and 3 is longer than the range of cross-talk in this system. (b) describes the stabilizer operator on qubit 2, although there are three XZ pairings there will only be two counted in the cross-talk penalty. This is highlighted in the modified adjacency matrix in (c).

By adapting the adjacency matrix to reflect the edges in the cluster state that are not long enough to avoid the cross-talk the P_{CT} measure can be used for cluster states with many different types of connectivity.

3.5 Homogenous-cross-talk-free stabilizer operators

Finding shapes in any arbitrary shaped cluster states is a hard problem similar to tiling problems, which are non local and NP complete [30, 31, 32]. Given this issue, we only consider a small number of simple shapes where we have identified patterns and rules in order to find HCTF stabilizer operators. Initially we look at fixed width, square connectivity cluster states, leading on to fixed width triangular connectivity cluster states which have similar properties. We begin by looking at what kinds of shapes and connectivity allow HCTF stabilizer operators to be constructed. Using fixed width, square connectivity cluster states we specify how many HCTF stabilizers can be found in general, we progress this to rectangular and L-shaped, square connectivity cluster states and fixed width triangular connectivity cluster states. We also show two algorithms that find HCTF stabilizer operators from any initial starting row of a constant fixed width cluster state for square connectivity and triangular connectivity.

3.5.1 Shapes of cluster states that allow HCTF stabilizer operators

Cluster states can be created in many shapes and sizes, with lots of different connectivities. It is not possible to create non-trivial HCTF stabilizer operators from all cluster states. This is due to the number of edges connecting each of the nodes in the cluster state. A node with an odd number of edges cannot be surrounded by stabilizer operators as this will lead to Z Pauli operators that cannot be eliminated (Fig. 3.9).

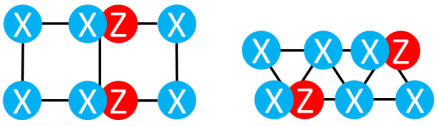

(a) (b)

Figure 3.9: Graphical representation of example cluster states where is it not possible to create non-trivial HCTF stabilizer operators. (a) shows a rectangular shaped, square connectivity cluster state with extra Z operators where there is an odd number of edges hitting a qubit. (b) is the same idea but for a fixed width triangular connectivity cluster state.

3.5.2 HCTF stabilizer operators in fixed width cluster states

To begin to see how the patterns of HCTF stabilizer operators appear we will explore the problem graphically using a step by step intuitive process, then move on to a analytical description once we understand what is happening. To avoid confusion we refer to the lines connecting the qubits as edges and the boundary of the cluster state as the side. We use a trial and error process explicitly manipulating a semi-infinite lattice to find patterns of HCTF stabilizer operators.

Let us imagine that we have a semi-infinite square connectivity cluster state and we have placed a stabilizer operator on the central qubit, graphically this looks like,

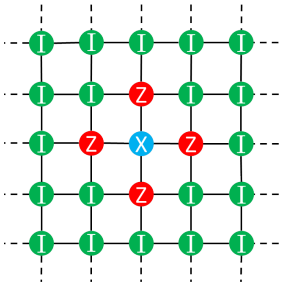

Figure 3.10: Semi-infinite square connectivity cluster state with a stabilizer operator applied to the central qubit.

We are trying to create HCTF stabilizer operators and so must eliminate all the Z operators. To begin this we apply two more stabilizer operators to cancel the four in Fig. 3.10, which however, creates four more (Fig. 3.11).

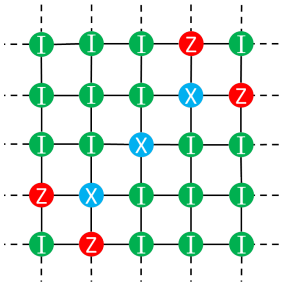

Figure 3.11: Semi-infinite square connectivity cluster state with a further two stabilizer operators applied to eliminate Z operators.

It is obvious that this pattern will continue in the same manner as we eliminate the extra Z operators at each step. Currently there seems no way to eliminate them. Let us now consider what happens if we apply a stabilizer operator to a corner qubit in the cluster state.

3.5.2.1 Corner

We apply a stabilizer operator to a qubit in the corner of our semi-infinite cluster state (Fig. 3.12).

This looks very like the situation we had when we applied a stabilizer operator to the centre qubit, except we only have two Z qubits that we need to eliminate, in which case we can follow the same protocol and apply stabilizer operators in a diagonal line (Fig. 3.13).

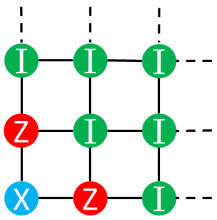

Figure 3.12: Semi-infinite square connectivity cluster state with stabilizer operators applied to the corner qubit.

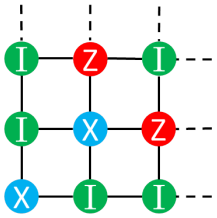

Figure 3.13: Semi-infinite square connectivity cluster state with HCTF stabilizer operator, with diagonal line of stabilizer operators going from corner to corner.

The only way to stop this pattern is to continue to the opposite corner of the cluster state, this is our first HCTF stabilizer operator (Fig. 3.14).

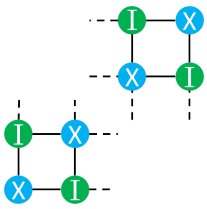

Figure 3.14: HCTF stabilizer operator. Applying stabilizer operators from one corner to the other in a diagonal line eliminates all the Z operators.

A second HCTF stabilizer operator can be found by applying the same principles but in the other corners.

3.5.2.2 Sides

We now look at the case where we start applying stabilizer operators to the side of the cluster state (Fig. 3.15).

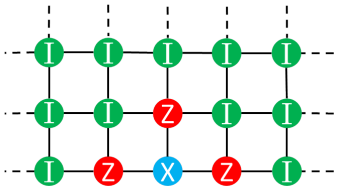

Figure 3.15: Semi-infinite square connectivity cluster state with a stabilizer operator applied to an qubit on a side.

We can see that this is actually the same as the corner qubit but going in two opposite directions (Fig. 3.16).

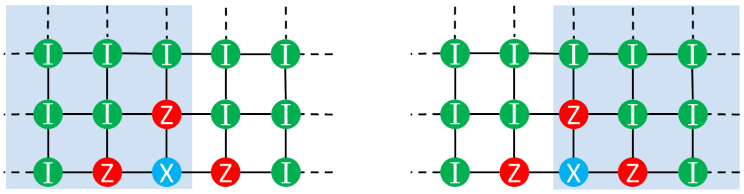

(a) (b)

Figure 3.16: How the stabilizer operator applied to the side qubit can be thought of in the same manner as two corners. (a) shows we can think of the pattern as a stabilizer operator applied to a qubit in the right hand corner of the cluster state shaded in blue. (b) shows the same but for a qubit in the left hand corner.

We follow the same process as previously shown and apply stabilizer operators in diagonal lines to eliminate the Z operators (Fig. 3.17).

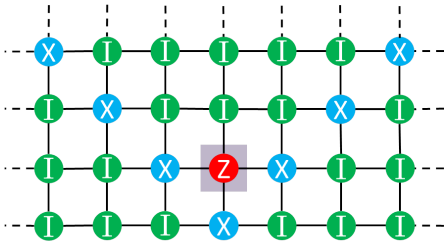

Figure 3.17: Semi-infinite square connectivity cluster state with a stabilizer operator applied to an atom on the side, and diagonal stabilizer operators applied to eliminate Z operators, the remaining problem Z operator is highlighted.

Here we find a problem, there is an extra Z operator, but it is still possible to eliminate this one. We can see from Fig. 3.18 the blue highlighted section is in fact the same as the original pattern applied to the side qubit, so the whole process can just be repeated.

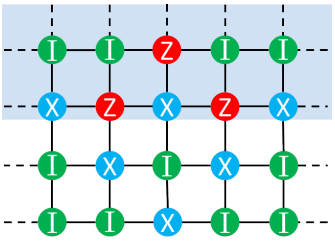

Figure 3.18: Semi-infinite square connectivity cluster state with stabilizer operators applied to eliminate Z operators, the pattern repeats and the blue highlighted section can be addressed in the same way as the original side

3.5.2.3 Shape of cluster state

We can infer from this pattern at the boundary of the cluster state that the only shape this square connectivity cluster state could hold to create HCTF stabilizer operators is a square (Fig. 3.19).

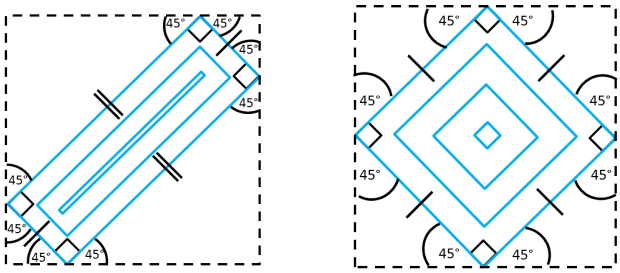

Figure 3.19: How the form of X operators dictates the shape of the cluster state. The only pattern the applied stabilizer operators could make is a square. The bold blue line shows the line of diagonal X operators, the cluster state itself is represented by the dashed line.

It would be possible to have an unconventional shaped cluster state such as those found in Fig. 3.20, but in the following work we will only be considering regular shaped cluster states.

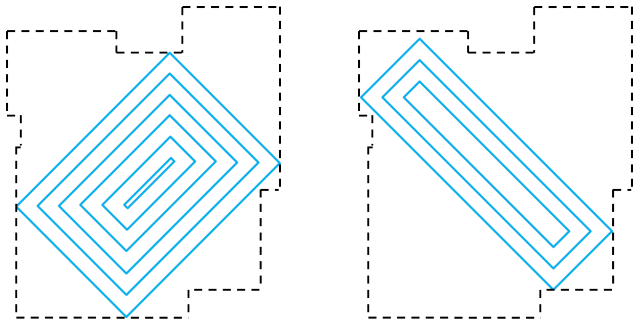

Figure 3.20: Two examples of how a cluster states could be unconventional shapes but still have stabilizer operators constructed in the way we have described

3.5.3 Canonical set of HCTF stabilizer operators

Now that we know how to create HCTF stabilizer operators starting in the corner or on the side of the cluster state, here we approach the cluster state row by row. We suggest the canonical set is found by applying a single stabilizer operator to each of the qubits in the initial row of the cluster state individually. We begin using a fixed width, square connectivity cluster state, creating a system to find the canonical set we look to see if the shape of the cluster state can be extended. We also consider a fixed width, triangular connectivity cluster state as this shows many similarities to the square connectivity cluster state.

3.5.3.1 Fixed width, square connectivity cluster states

To show how the canonical HCTF stabilizer operator set is formed we look at an example of a cluster state that is three qubits wide and begin by placing a stabilizer operator on the first qubit (Fig. 3.21).

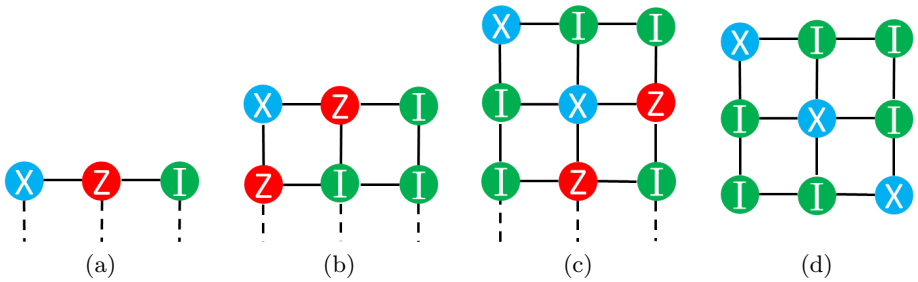

Figure 3.21: How we generate a canonical stabilizer operator, step by step. (d) shows that the HCTF stabilizer operator completed in a square cluster state of 3×3 qubits.

If the cluster state is n qubits wide this gives us n HCTF stabilizer operators, that are all linearly independent as they do not share any qubits in the initial row. This

method also reinforces the square cluster state idea we have seen previously. The complete set of HCTF stabilizer operators for a 3×3 cluster state can be seen in Fig. 3.22.

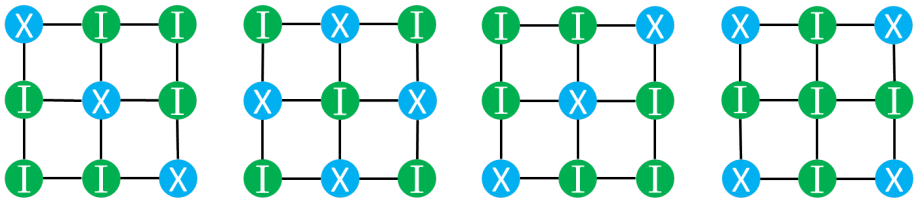

(a) (b) (c) (d)

Figure 3.22: Canonical set of HCTF stabilizer operators. The first three images (a),(b) and (c) show the canonical set of HCTF stabilizer operators found by applying a single qubit to each of the initial starting qubits individually. (d) shows an example of a non-linearly independent HCTF stabilizer operator found by multiplying (a) and (c).

3.5.3.2 Extended square connectivity cluster states

So far we have seen that the HCTF stabilizer operators can be contained within a square cluster state of $n \times n$ qubits, but it is possible to extend the cluster state and add more stabilizer operators below or to the side of the self contained HCTF stabilizer operator pattern.

As long as the cluster state is of the form $(km + (k-1)) \times (lm + (l-1))$ it is possible to find HCTF stabilizer operators. Where m describes the number of qubits in the self contained pattern of the HCTF stabilizer operator to be extended, in the example above $m = 3$. k defines how many of these self-contained patterns there are in rows, each of these patterns are separated by a single row of $\mathbb{I}$ operators and each row is the mirror image of the previous one. l describes how many self-contained patterns there are in columns, once again the patterns are separated by a single column of $\mathbb{I}$ operators and the columns are mirror images of each other. The cluster state can be extended further one way than another as long as each column and row conforms to the equation above (Fig. 3.23). It must be of this form to cancel out unwanted Z operators.

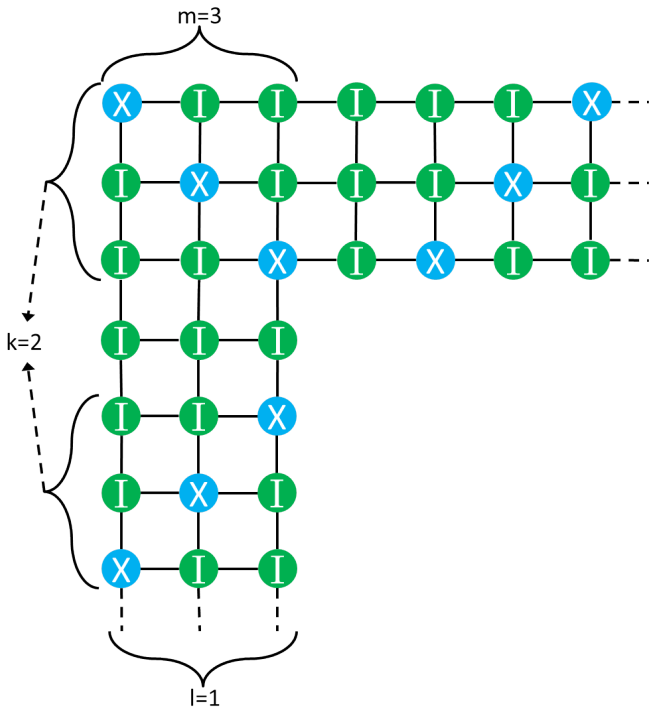

Figure 3.23: The form of an extended cluster state. A cluster state may be extended and still have HCTF stabilizer operators as long as it is of the form $(km + (k - 1)) \times (lm + (l - 1))$.

3.5.3.3 Fixed width, triangular connectivity cluster states

Fixed width, triangular connectivity cluster states have no extra degrees of freedom and so can be treated a lot like the square connectivity cluster states, in the sense of starting at the initial row, with a single stabilizer operator on each qubit (Fig. 3.24).

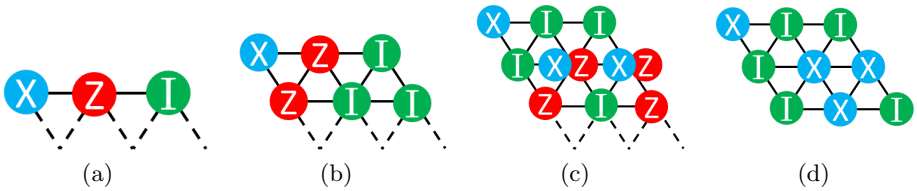

Figure 3.24: Generation of a HCTF stabilizer operator on a fixed width, triangular connectivity cluster state. Found by approaching the lattice row by row.

Due to the differences in connectivity of the cluster state, the canonical set of stabilizer operators look different from that of the squares but we do still find n HCTF stabilizer operators for a cluster state of width n (Fig. 3.25).

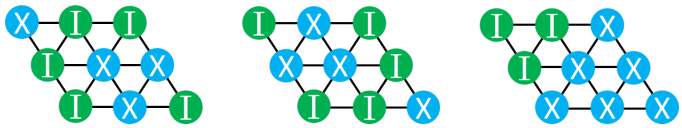

(a) (b) (c)

Figure 3.25: The canonical set of HCTF stabilizer operators for a fixed width, triangular connectivity cluster state. Found by individually applying a single stabilizer operator to each of the initial qubits in the first row.

3.5.3.4 Extended triangular connectivity cluster states

In the same way we could extend the square connectivity cluster states this is also possible with the triangular connectivity lattices. The cluster state must still be of the form $(km+(k-1)) \times (lm+(l-1))$ where, as before, m is the number of qubits in each self contained pattern, k is the number of rows of self contained patterns and l is the number of columns of self contained patterns. In the case of triangular connectivity lattices each additional self contained pattern is not a mirror image of the one before but they still have a row/column of $\mathbb{I}$ operators in between the patterns. Again, as before, the cluster state can be extended further one way than another as long as each row and column of the self contained pattern conform to the structure above.

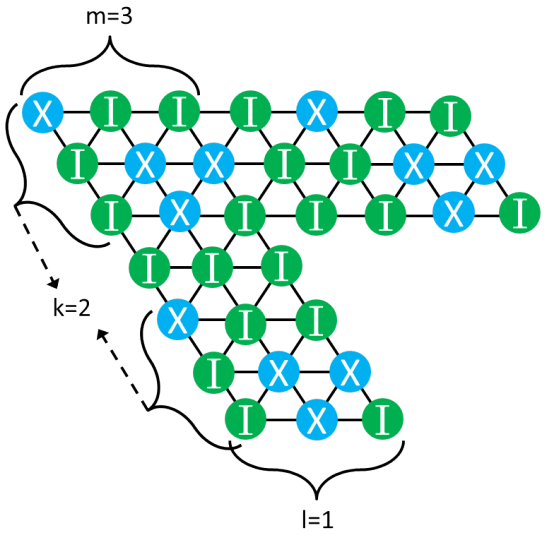

Figure 3.26: The form on an extended cluster state. Extension is possible as long as the cluster state is of the $(km + (k-1)) \times (lm + (l-1))$ form.

3.5.4 Algorithm for finding HCTF stabilizer operators

In this section we present two algorithms for finding HCTF stabilizer operators in fixed width, square and triangular connectivity cluster states.

3.5.4.1 Fixed width, square connectivity cluster states

We have found a simple algorithm that, given an initial starting row, can find the complete HCTF stabilizer operator in a fixed width, square connectivity cluster state.

Data: initial row $a_r = \{0_0, 0_1, \ldots, 1_m, 0_{m+1}\}$,
dummy row $a_{r-1} = \{0_0, \ldots, 0_{m+1}\}$
Result: HCTF Stabilizer Operator
rownumber=3;
while *Number of X operators in the current row* $\neq$ *0* **do**
  $a^c_{r+1} = a^{c-1}_r + a^{c+1}_r + a^c_{r-1} \mod 2$;
  for $c = 2 \ldots m$;
  Print a^c_{r+1} from $c = 2 \ldots m$;
  Count X operators in the row;
  $a_{r+1} = \{0, a^2_{r+1}, a^3_{r+1}, \ldots, a^m_{r+1}, 0\}$;
  rownumber=rownumber+1;
end

Algorithm 1: Algorithm to form HCTF stabilizer operators in a fixed width, square cluster state given an initial first row. a^c_r denotes the qubit in row r, column c. The number of qubits in the initial row is m, we add additional 0 elements at the start and end of the initial row and a dummy row that sits above our initial row to ensure the equation holds. The program finds the configuration of the X operators in each row of the HCTF stabilizer operator and shows how many rows is necessary to complete the HCTF.

3.5.4.2 Fixed width, triangular connectivity cluster states

We have also found another simple algorithm for find HCTF stabilizer operators given an initial row in fixed width, triangular connectivity cluster states.

Data: initial row $= \{0_0, 0_1, \ldots, 1_m, 0_{m+1}\}$,
dummy row $= \{0_0, \ldots, 0_{m+1}\}$
Result: HCTF Stabilizer Operator
rownumber=3;
while *Number of X operators in the current row* $\neq 0$ **do**
    $b^c_{r+1} = b^{c-1}_{r+1} + b^{c-1}_r + b^c_{r-1} + b^{c+1}_{r-1} + b^{c+1}_r \mod 2$;
    for $c = 2 \ldots m$;
    Print b^c_{r+1} from $c = 2 \ldots m$;
    Count X operators in the row;
    $b_{r+1} = \{0, b^2_{r+1}, b^3_{r+1}, \ldots, b^m_{r+1}, 0\}$;
    rownumber=rownumber+1;
end

Algorithm 2: Algorithm to form HCTF stabilizer operators in a fixed width triangular cluster state given an initial row. b^c_r denotes the qubit in row r, column c. The number of qubits in the initial row is m, we add additional 0 elements at the start and end of the initial row and a dummy row that sits above our initial row to ensure the equation holds. The program finds the configuration of the X operators in each row of the HCTF stabilizer operator and shows how many rows is necessary to complete the HCTF.

3.6 Triangle shaped, triangular connectivity cluster states

Finding a deterministic algorithm for cluster states with changing degrees of freedom is not possible because each time we add a new row onto the cluster state, there is a choice of how to cancel out the Z operators leading to different paths not all of which end in a HCTF stabilizer operator (Fig. 3.27).

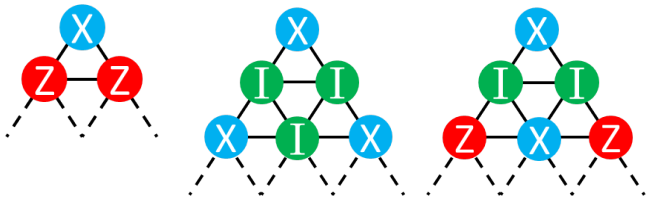

Figure 3.27: Changing degrees of freedom. By changing the number of qubits in each row of the cluster state there is a choice of where to place the stabilizer operators to eliminate the Z operators from the row before. (a) shows the initial pattern with Z operators in row two that we wish to eliminate. (b) is one pattern of stabilizer operators applied to row three that would eliminate the Z operators in row two. However, the pattern in (c) would also eliminate the Z operators. This choice element does not allow for a deterministic algorithm to find the HCTF stabilizer operators.

It is interesting to note that at each new row there is a choice of two patterns of stabilizer operators that are the complement of each other. This means the number of

possible patterns increases very quickly with each new row as 2^r where r is the row number (Fig. 3.28).

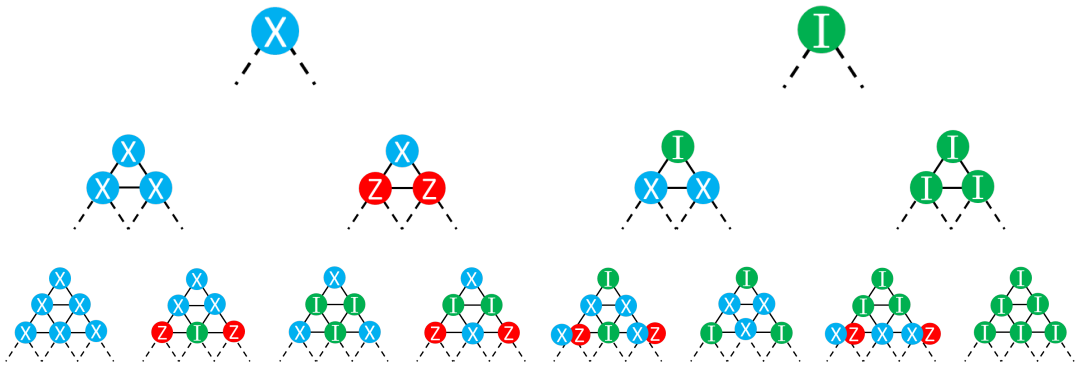

Figure 3.28: Choice of stabilizer operator placement. In each new row there are two options of where to place the stabilizer operators to eliminate the Z operators from the row before. We can see from this figure that the number of possible cluster states increases very quickly.

As there is no simple deterministic algorithm we looked at a brute force approach to find HCTF stabilizer operators. We look at triangle shaped, triangular connectivity cluster states with one qubit all the way up to 45 qubits and notice that there does seem to be a pattern in the number of linearly independent HCTF stabilizer operators that can be found for a cluster state with r qubits along a side.

3.6.1 Canonical HCTF stabilizer operators

In a similar way to how we approached fixed width square and triangle connectivity cluster states we find the canonical set by starting from the outside sides of the cluster state and work in. The first HCTF has stabilizer operators applied to every qubit along the side, this dictates the pattern on the inside of the triangle. The second HCTF stabilizer operator has stabilizer operators applied to all qubits along each side except the first, $r = 1$, and the last, $r = r$. The third HCTF stabilizer operator has stabilizer operators applied to all qubits along each side except the first and second, $r = 1$, $r = 2$, and the second last and last, $r = r - 1$ and $r = r$. This pattern repeats until the centre of the side is reached (Fig. 3.29).

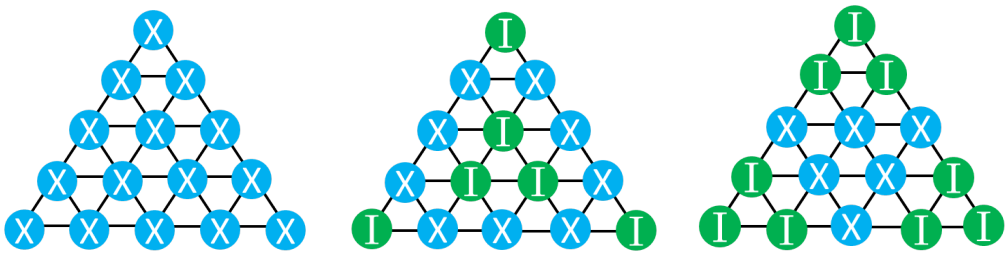

(a) (b) (c)

Figure 3.29: The canonical set of HCTF stabilizer operators for a triangle shaped, triangular connectivity cluster state with $r = 5$.

This way of forming the canonical set leads to a pattern prediction. For a cluster state of side length r qubits we predict the number of HCTF stabilizer operators is $\lfloor \frac{r+1}{2} \rfloor$, i.e. $1, 1, 2, 2, 3, 3..$, where $\lfloor x \rfloor$ denotes a floor function of x which takes x to be the largest integer that is no larger than x, for example, if $x = 4.5$, $\lfloor x \rfloor = 4$.

If we look at how the set of HCTF stabilizer operators change from an odd r to an even r we can understand this floor function. To produce the HCTF stabilizer operator in Fig. 3.30b the first and last qubit along the sides were not acted upon by a stabilizer operator. When we now increase r and perform the same operation (missing the first, $r = 1$, and last qubit, $r = r$) we get Fig. 3.30d. It is clear that it is not possible to produce any more HCTF stabilizer operators in the way we have described as $r = 4$. So we have the same number of HCTF stabilizer operators in the transition from $r = odd$ to $r = even$. However, when we transition to $r = odd$ again, $r = 5$, we see it is now possible to find an additional HCTF stabilizer operator (Fig. 3.30g).

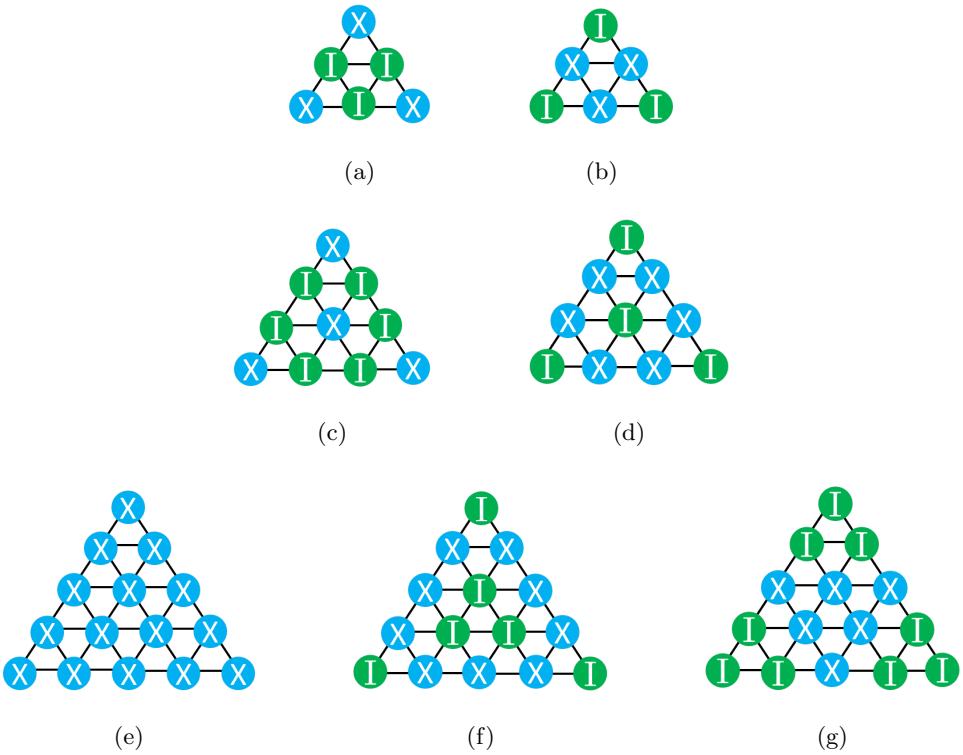

Figure 3.30: The canonical HCTF stabilizer operators for triangle shaped, triangular connectivity cluster states. (a) and (b) for $r = 3$. (c) and (d) for $r = 4$. (e), (f) and (g) for $r = 5$. Note the number of HCTF stabilizer operators does not increase from $r = 3$ to $r = 4$.

This section has not been fully explored as there are too many different avenues and this is left for further research. Perhaps looking at different shaped triangular connectivity cluster states and approaching the application of the stabilizer operators differently could provide other solutions.

3.7 Hexagonal connectivity cluster states

In this section we briefly look at how hexagonal connectivity HCTF stabilizers may be produced. We do not find any definite patterns in this section, but we have found some rules and points of interest that we feel are important to note. We have considered these cluster states in terms of layers, this makes the description of the stabilizer operators simpler (Fig. 3.31).

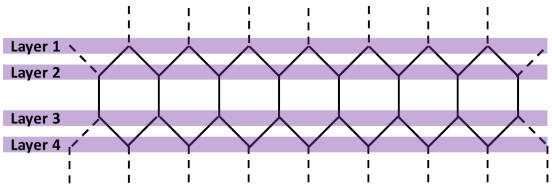

Figure 3.31: Hexagonal cluster state layers. The layers of the semi-infinite hexagonal cluster state are highlighted in purple.

Due to the changing number of qubits in each layer and the connectivity there is a choice of pattern at the widest points of the cluster state but at the thinnest points there is no choice (Fig. 3.32). This choice makes it difficult to find a deterministic algorithm that will find HCTF stabilizer operators.

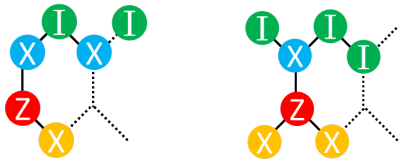

(a) (b)

Figure 3.32: Choice in a hexagonal cluster state. Both images are taken from the left hand boundary of a semi-infinite cluster state. (a) shows there is no choice of where to place the stabilizer operator (shown in orange) in order to cancel the Z operator from the layer before. However, in (b) we see that there is a choice of where to place the stabilizer operator in order to cancel out the Z operator from the layer before.

The goal is to create as many HCTF stabilizer operators as possible, when we think of the cluster state in terms of layers we can see that each layer only depends on the layer before it. This means we only apply stabilizer operators to every other layer. Depending if we start on the initial layer, layer 1, or layer 2 this is likely to produce very different patterns (Fig. 3.33).

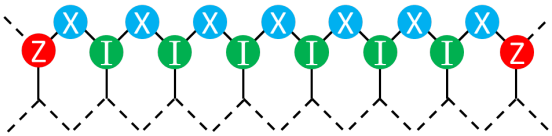

(a)

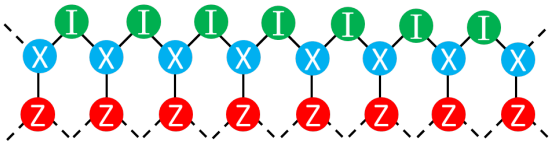

(b)

Figure 3.33: Showing the options of placing the stabilizer operators on the first or second layer of the hexagonal lattice. In (a) the stabilizer operators are placed in the first layer of the hexagonal cluster state. In (b) the stabilizer operators are placed in the second layer of the hexagonal cluster state, this cancels out all the Z operators in the first layer.

If we are applying the stabilizer operators to the even layers in the cluster state it is necessary to apply them to every qubit in the lattice to eradicate all the Z operators from the layer before. However this restriction does not hold when we apply the stabilizer operators to the odd layers, here there are no restrictions on how many we should or should not add. Now we have seen that there are different restrictions depending on where we start in the cluster state we will explore each case individually.

3.7.1 Odd layering

When starting on the odd layer we can see it is not possible to apply stabilizer operators to all the qubits in layer 1 and all the qubits in layer 3 as this will result in a pattern where there is an extra Z operator that cannot be removed (Fig. 3.34).

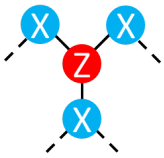

Figure 3.34: This pattern of applied stabilizer operators is not allowed.

We also find that it is necessary for the number of hexagons in the cluster state at its widest point to be odd, otherwise this leads to an extra Z operator that cannot be eliminated (Fig. 3.35).

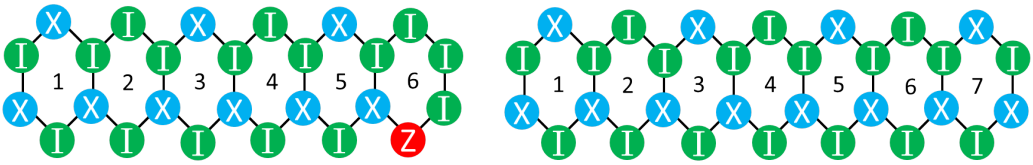

(a) (b)

Figure 3.35: Showing why there must be an odd number of hexagons in the hexagonal cluster state for the pattern to end successfully with no Z operators remaining

If we are applying stabilizer operators to the odd layers we know that the pattern to make a HCTF stabilizer operator will complete in the same way as if we flipped the cluster state and applied them to the even layers. This means that it is only necessary to look at patterns produced by applying stabilizer operators to odd or even layers as they will be the same because it is possible to move up and down the cluster state in both directions.

3.7.2 Choice of pattern

Whichever layer we begin applying stabilizer operators to, we must be careful and consider every possible placing of the stabilizer operators as more than one particular pattern could eliminate Z operators (Fig. 3.36). It is interesting to note that this choice does not present itself until we reach layer 6 of the cluster state. Fig. 3.36 shows an example of a choice, layer 6 in Fig. 3.36a is the complement of Fig. 3.36b. Although we have the choice here, the initial qubit in the layer defines the rest of the pattern and its complement.

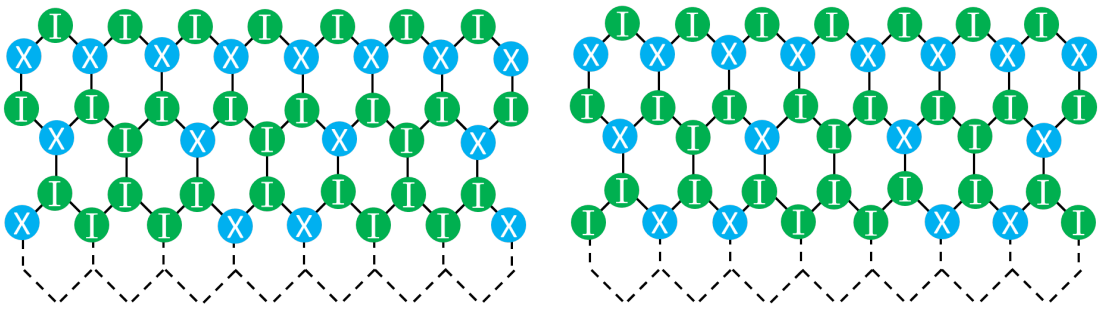

(a) (b)

Figure 3.36: Two different choices of the placement of the stabilizer operators in layer 6 which both result in eliminating the Z operators in layer 5 for a hexagonal cluster state.

3.7.3 Width of lattice

Through trial and error we have found that to create HCTF stabilizer operators it is necessary for the cluster state to be of the form $4m - 1$ full hexagons or $4m$ qubits at the widest point, where m is a positive integer. Patterns not of the form $4m - 1$ full hexagons lead to asymmetric patterns of applied stabilizer operators, these asymmetric patterns cause excess Z operators that cannot be cancelled out (Fig. 3.37).

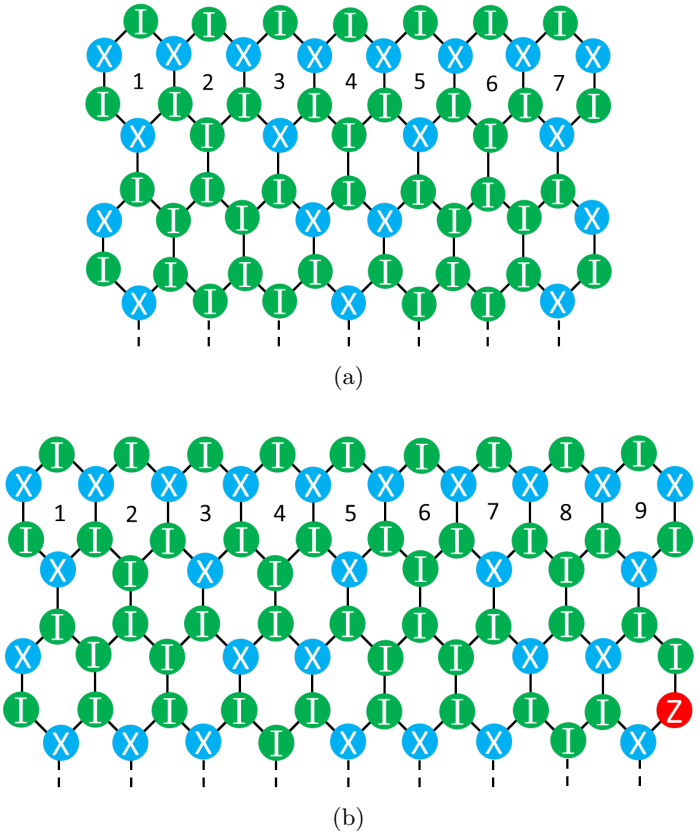

(a)

(b)

Figure 3.37: Example of constraints on the form of cluster states. Unless the cluster state is of the form $4m - 1$ hexagons or $4m$ qubits at its widest point some Z operators will not cancel.

3.7.4 Observations

Although we have not found a conclusive system or algorithm for finding HCTF stabilizers in hexagonal cluster states, we have found some rules that must be followed in order to create them. The main difficulty with finding a deterministic algorithm for HCTF stabilizer operators is the element of choice that is introduced due to the changing number of qubits in each layer and the difference in connectivity. We found it is not important if we start on an odd or even layer as these are rotationally equivalent. We initially noted that the hexagonal cluster state must have an odd number of hexagons width wise in order to cancel all the excess Z operators. Through further investigation

we saw it was vital that the cluster state be of the form $4m - 1$ full hexagons or $4m$ qubits in width at the widest point as any other patterns lead to stray Z operators that destroy the HCTF stabilizer.

Due to the large number of different shapes possible with hexagonal patterns and the different ways to draw the hexagons themselves there are too many ideas for us to cover here. Perhaps looking at hexagonal cluster states in circular formation or by introducing other shapes between the hexagons such as pentagons like a football pattern could prove more fruitful. We leave this section open to further research.

3.8 Conclusion

We began this work with the idea of validating a cluster state with the use of stabilizer operators. By measuring a $+1$ result for all the stabilizer operators defining the cluster state we can be certain that the state we have created is the correct one. However this process of measurement highlights physical problems with the apparatus currently available that lead to cross-talk, which could produce false results. By addressing the form of the stabilizer operators and changing them to reduce the cross-talk we reduce the chance of a false result making the results more reliable.

We considered several different shaped cluster states with different connectivity. We were able to construct simple algorithms to find sets of linearly independent HCTF stabilizer operators for fixed width cluster states. We have shown it is not possible to only use HCTF stabilizer operators to define a cluster state. Given this, we also produced a rating system to help choose the least destructive non-CTF stabilizer operators to complete the set. This allowed us to significantly reduce the overall cross-talk effect on the system.

We briefly explored cluster states that were not of fixed width or consistent connectivity such as triangular shaped, triangular connectivity cluster states and hexagonal connectivity cluster states. The problem with these types of cluster states is by changing the connectivity and number of qubits in each row/layer the degree of freedom changes as we progress though the lattice introducing a choice element of where to place the stabilizer operators to eliminate the Z operators meaning it is not possible to find a deterministic algorithm. We did however find some patterns and rules about how HCTF stabilizer operators could be produced.

Using the algorithms to find the HCTF stabilizer operator set and the rating system to produce a reduced cross-talk set of stabilizer operators for a fixed width, square connectivity cluster state is a positive step to finding more reliable results. The reduction in the cross-talk penalty we found was always one more than half of the original value. Due to the symmetry that is apparent throughout the patterns and relationships between the stabilizer operators we believe that there is scope to either prove that this is the largest reduction or show that we can indeed half the original cross-talk penalty.

Reducing the cross-talk penalty is a significant result, by simply changing the set of stabilizer operators used we have reduced the risk of the cross-talk affecting the nearest neighbour atoms by almost 50%, but it is vital that we consider the cost of these improvements. We highlight this point using an example of a 3×3 cluster state. Before any reduction in the cross-talk a 3×3 lattice would require two patterns of Pauli operators to be measured to reconstruct all the stabilizer operators (Fig. 3.2a, Fig. 3.2b) where $P_{CT}^{T} = 24$. These patterns are measured many times in order to build up statistics for the result. By finding a new improved set of stabilizer operators that have a reduced cross-talk effect we now require three patterns of measurement (Fig. 3.38).

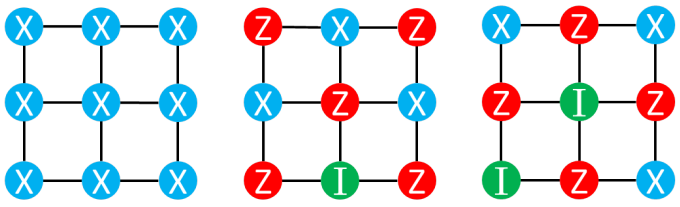

(a) (b) (c)

Figure 3.38: New patterns of measurement. The three patterns of measurement now required to find the reduced cross-talk set of stabilizer operators to define the cluster state. This new set of stabilizer operators has $P_{CT}^{T} = 15$. This set is not the only one we could have chosen, but each set has three patterns and we show this one as an example.

Again these measurements would need to be performed many times to build up good statistics of the results. As there are now three measurement patterns we will incur a time or precision cost. If we were to repeat each measurement pattern the same number of times as the initial ones, then this will take 150% the original time to perform the measurements. Or to save time we could reduce the number of repetitions, however this will also reduce the precision of the result. This balance of time and precision is an issue that must be addressed by the experimentalist.

In this chapter we have only looked at modifying the stabilizer operators construction to reduce the cross-talk in the system. Another route to the reduction could be to physically construct the cluster states in a different way making the qubits that are connected by a edge, creating a pair of X and Z operators, far enough away that the cross-talk created by the active rotation would not affect them (Fig. 3.39).

This idea also introduces some other complexities into the problem, the entangling operations in this case will be much more difficult than a regular square connectivity cluster states making the shape harder to make.

Through our analysis of this work, we have manually found the set of stabilizer operators the reduces the cross-talk penalty but is still equivalent to the canonical set.

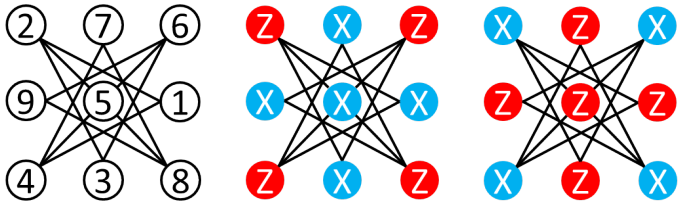

(a) (b) (c)

Figure 3.39: Rearranged cluster state. In (a) the qubits that share an edge have been physically moved to ensure the distance between them is larger than the range of cross-talk. (b) and (c) show the modified checkerboard patterns needed to reconstruct the stabilizer operators to define the cluster state. Here $P_{CT}^{T} = 16$.

This process is time-consuming and it is likely it could be automated. This process if left for further work.

We can relate this work to that done in the next chapter. However the cluster state is created, for example using an optical lattice, there is always a possibility of vacancies in the system. If we take the optical lattice example, a vacancy would be described as a well without a particle, this particle is lost during the creation and loading of the optical lattice due to finite temperatures in the cooling process. Vacancies lead to an incomplete measurement process, one where we cannot tell the difference between a vacancy and a particular measurement result, $|0\rangle$ or $|1\rangle$. When we are considering stabilizer operator measurements on the system with vacancies it is vital we really think about which measurement result to assign to the vacancy measurement. This choice is dependent on the number of Pauli operators in the stabilizer operator. To understand this we use our example of a 3×3 square connectivity cluster state. The canonical set of HCTF for this cluster state were shown early in the chapter but are repeated here for clarity (Fig. 3.40).

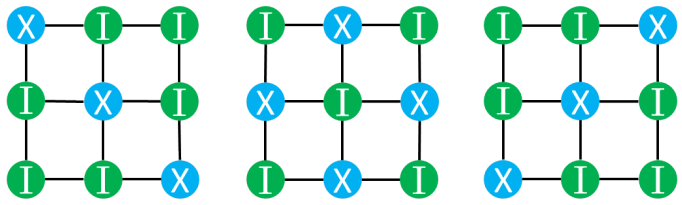

(a) (b) (c)

Figure 3.40: The canonical set of HCTF stabilizer operators for a square connectivity 3×3 cluster state.

Say we have assigned the vacancy result $+1$ and we measure the HCTF stabilizer operator shown in Fig. 3.40a and it just so happens that qubits 1, 5 and 9 are missing due to vacancies in the system. The expectation value result we get is $+1$ which

according to Eq. (3.2) means we have the ideal state when in fact we do not. It is better to assign the vacancy result to -1 and attempt to use as many HCTF stabilizer operators that contain an odd number of Pauli operators so if there are lots of vacancies this can be caught by the measurement result. Obviously this is not a fool-proof system as the pattern of vacancies will be random but in the worst case scenario where there are vacancies where the qubits requiring X operators are, the result will be -1 highlighting that the state is not ideal.

CHAPTER 4

Bell inequality violation, vacancies and incomplete measurements

4.1 Introduction

In this chapter we consider trapping cluster states in optical lattices as a candidate for measurement-based quantum computation. Errors in the process of loading the lattice can lead to a non-ideal state. Fluorescence imaging, used to measure the cluster state, creates an incomplete measurement process. By using entanglement as a verification tool we will perform an optimisation process to maximise the detectable entanglement in these non-ideal states. We will also include various other errors in the measurement process and find limits at which entanglement can not longer be detected.

The chapter is set out as follows, Sec. 4.2 introduces cluster states in optical lattices and briefly describes how they are formed. Sec. 4.3 defines the system we will use for our investigation. Sec. 4.4 describes how we will measure the entanglement of the system. In Sec. 4.5 we perform the optimisation processes to maximise the detectable entanglement. And finally in Sec. 4.6 we introduce further errors into the measurement process.

This work is available as a preprint article at arXiv:1412.7502 [33].

4.2 Background

The motivation behind this problem comes from optical lattice experiments, where neutral atoms are trapped in standing waves created by counter-propagating laser beams [34]. This set-up is a candidate for measurement-based quantum computation and relies on all the atoms in the system being entangled [9]. To set the scene for the issue of vacancies in the system we will briefly cover how an optical lattice is loaded ready to be used for quantum computation.

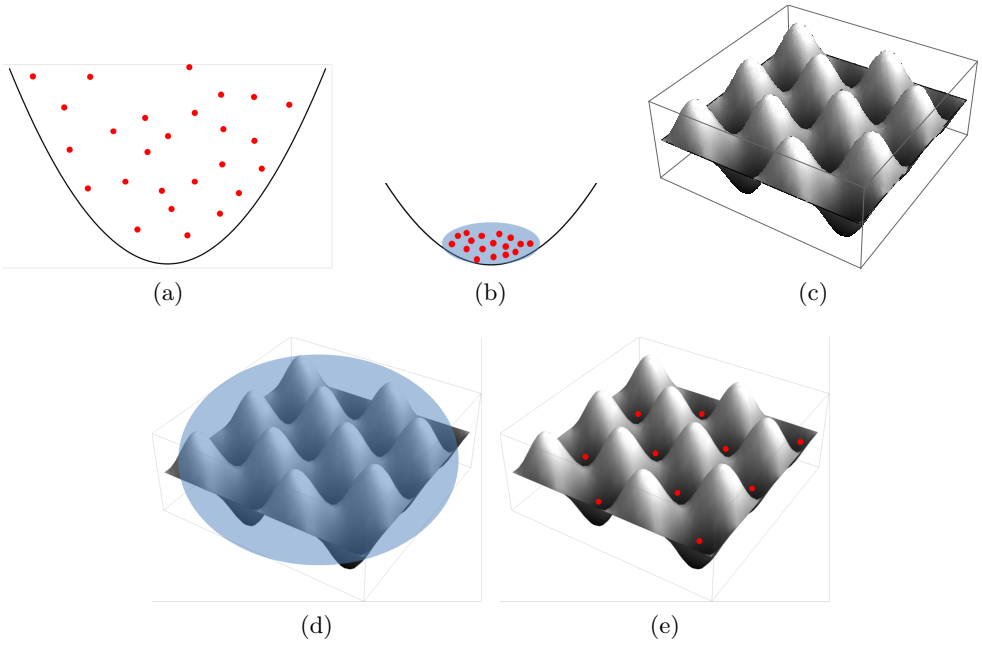

Figure 4.1: Process of creating a cluster state for quantum computation using an optical lattice. (a) a gas of bosonic atoms is trapped. (b) the gas is cooled to a sufficiently low temperature that a Bose-Einstein condensate (BEC) forms. (c) meanwhile an optical lattice is formed. (d) the BEC is then loaded onto the optical lattice. (e) the BEC becomes a Mott insulator with an equal number of atoms at each site.

Process of creating a cluster state for quantum computation using an optical lattice,

- A gas of bosonic atoms in trapped in a magneto optical trap (MOT) [35].
- The gas is cooled using various techniques such as laser and evaporative cooling [36, 37, 38]. This causes a phase transition and the gas becomes a Bose-Einstein condensate (BEC). At this point all the atoms in the system are in the ground state and act as a single identical quantum state of many atoms which can be described by a single wavefunction.
- An optical lattice is formed using counter propagating laser beams [34]
- The BEC is then loaded onto this optical lattice. The condensate can be described as a superfluid if the tunneling or hopping rate, j, of the atoms in the lattice is far greater than the on-site interactions, u. This means the wavefunction has

long-range phase coherence [39] and the atoms are able to tunnel from site to site, making the number of atoms per site undetermined.

- The potential in the lattice is then raised adiabatically changing the balance between j and u to $j << u$. This induces a quantum phase transition and fixes the number of atoms per site, the state is now a Mott Insulator (Fig. 4.1e) [40, 41, 42, 43, 44].

- For cluster state generation the number of atoms per site required is 1, this can be achieved in two ways. Firstly by defining the filling fraction, $\zeta = 1$, this ensures there are only enough atoms to have one per site. Secondly, photo-assisted light collisions can be used in a lattice with filling fraction $\zeta > 1$ to kick-out pairs of atoms in the wells leaving a single atoms at each site if the initial number was odd [45, 46, 47, 48].

- Once the optical lattice has a single atom at each site, collisional gates are used to entangle the atoms in the system. The system is now a cluster state and is ready for quantum information processing [49]. For details of how the collisional gates create entanglement see Appendix B.

Due to finite entropy in the BEC or an increase of temperature at the Mott insulator stage some atoms in the system will have more energy than others and will be able to escape from the wells in the lattice. This leads to non-perfect filling of the lattice [46]. We call the sites in the lattice that have no atoms vacancies. These vacancies create problems when we use the collisional gates to create entanglement in the lattice [49, 50, 51]. The entanglement is created by colliding the internal states of atoms. If there is a vacancy at a particular site, this collision will not happen so the atom hitting the vacancy cannot become entangled with the vacancy and so the overall entanglement of the system will be reduced compared with that of a fully entangled perfectly filled lattice.

We will be using the CHSH inequality to quantify the entanglement in our system [52]. We have chosen to only compare the entanglement of an ideal system compared with the entanglement of a defective one.

As a preliminary investigation we will only consider a one-dimensional two-well system. By only considering a bipartite system we avoid all the complications associated with multi-partite entanglement, entanglement with more than two systems [53]. For example showing that a multipartite system is entangled is not a simple task, using the PPT criterion for these multipartite systems is not as simple for bipartite states and becomes an NP hard problem especially for states with small level of entanglement.

The aim of this chapter is to see if having vacancies in the system affects the detectable level of entanglement. This restricted system will illustrate how these vacancies impact the system, whilst keeping the calculations and measurements relatively simple. Depending on the results it may then be possible to scale up our method to include

more sites, increasing the dimensionality of the state. This of course will require much more complicated measurements and it will be more difficult to show the level of the entanglement in the system.

4.3 System

Due to the complexities of working with a large 3 dimensional lattices we focus on a one-dimensional two-well system. The imperfections in the state preparation mean there is some probability that one or both particles are missing. We ignore the possibility of two or more particles in a single site. This can be guaranteed by photo-assisted collisions as mentioned previously. This gives us four possible starting states prior to the collisional entangling gates (Fig. 4.2). After the entangling operation only the ideal case, where both sites have a particle, will be entangled as the collisional gates will have no effect on the other cases. To aid our explanation of the two lattice sites we introduce two fictitious people, Alice and Bob. Alice controls the first lattice site and cannot access the second site. Bob controls the second lattice site and cannot access the first. This is a convention that is used throughout quantum information.

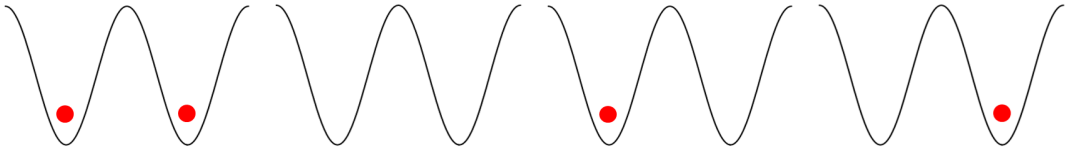

Figure 4.2: The four possible starting systems. The red dot indicates the presence of a particle. (a) shows the ideal case, where both Alice and Bob have a particle, this has probability $(1-p)(1-q)$. (b) shows the state when both sites are vacancies, this occurs with probability p. (c) shows the case where Alice has an atom and Bob a vacancy with probability $(1-p)q\frac{1-r}{2}$ and (d) shows the case when Bob has a particle and Alice has a vacancy with probability $(1-p)q\frac{1+r}{2}$.

The local state space in each lattice site is spanned by the states $\{|v\rangle, |0\rangle, |1\rangle\}$ representing a vacancy (no particle), and the logical states 0 and 1 respectively. The starting states are locally rotated to bring the atoms into the $|+\rangle = \frac{1}{\sqrt{2}}(|0\rangle + |1\rangle)$ and are fed into the quantum circuit where the entangling operation is peformed (Fig. 4.3). We note that the entangling operation used to entangle Alice and Bob's systems is locally equivalent to that used in a cluster state set up but not identical. In cluster states a C-Z gate is used between all the atoms in the state, this creates a maximally entangled state between all the atoms. In our case we perform a controlled-phase gate

between the two sites,

$$C - PHASE = \begin{pmatrix} 1 & 0 & 0 & 0 \\ 0 & 1 & 0 & 0 \\ 0 & 0 & -1 & 0 \\ 0 & 0 & 0 & 1 \end{pmatrix} \tag{4.1}$$

In the ideal case this operation creates $\frac{1}{4}(|00\rangle + |01\rangle - |10\rangle + |11\rangle)$, then by performing a Hadamard gate followed by a Z gate on Alice's subsystem only, we create the maximally entangled singlet state $\frac{1}{\sqrt{2}}(|01\rangle - |10\rangle)$ as required.

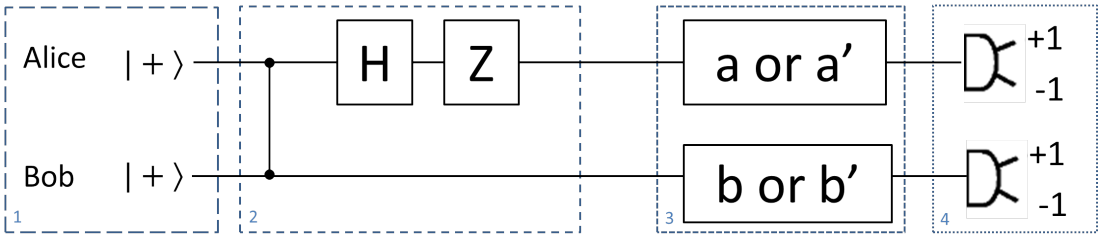

Figure 4.3: Quantum circuit for experimental model.
1: Initial starting state, one of the four possible shown in Fig. 4.2. Here we show the ideal case where $|+\rangle = \frac{|0\rangle+|1\rangle}{\sqrt{2}}$.
2: A C-Z gate between both qubits followed by a Hadamard and Z gate on only Alice's qubit are performed creating the fully entangled Bell state $|\psi^-\rangle = \frac{|01\rangle-|10\rangle}{\sqrt{2}}$.
3: Alice (Bob) choose to measure along axis $a(b)$ or $a'(b')$ on the Bloch sphere independently and at random. These measurements are performed via an active rotation of the state.
4: Read out of measurement results in fixed basis.

We assume that there is no transfer population between the two sites and that the gates are ideal. In order to detect the generation of entanglement, Alice and Bob perform measurements, a or a', b or b'. As is the case in many physical systems, the physical measurement basis is fixed but preceding coherent rotations allow an arbitrary choice of basis of the state [2].

An important feature of our system is an incomplete measurement process meaning it is not possible to differentiate between a vacancy state and one of the logical states e.g. $|v\rangle, |1\rangle$ (Fig. 4.4). This incomplete measurement process arises when using fluorescence detection to measure the state of the qubits [13]. As the logical states $|0\rangle$ and $|1\rangle$ are so close in energy instead of pumping one of the transitions and hoping that the other is not affected, all the atoms in a particular state, say $|1\rangle$, are kicked out of the lattice. The kicking out process is done using a global microwave pulse to induce the AC stark effect on the atoms in $|1\rangle$. If the initial energy required to excite $|1\rangle$ was ω, the global microwave pulse changes this to $\omega + \delta\omega$, then, the entire lattice can be pulsed with a laser of energy $\omega + \delta\omega$ to release all the atoms in $|1\rangle$ leaving those in $|0\rangle$ (and any vacancies that may have been present). Then by fluorescing the $|0\rangle$ transition we can

find all the atoms that were in the $|0\rangle$ state and all those sites that did not fluoresce are assumed to be the $|1\rangle$ state. It is now no longer possible to tell the difference between an atom originally in the state $|1\rangle$ or a vacancy.

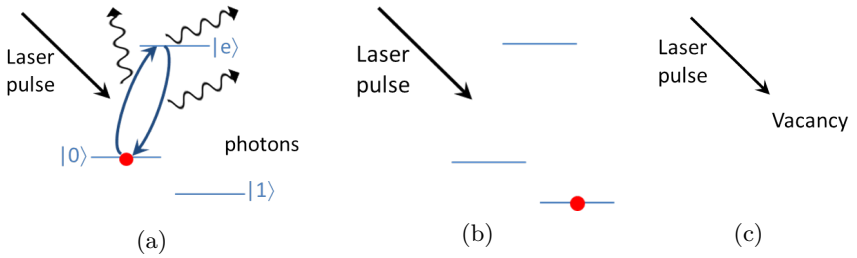

Figure 4.4: Incomplete measurement process. (a) an atom in $|0\rangle$ is excited by the application of a laser pulse with the correct energy. As the atom relaxes back to the ground state it releases photons. These photons are collected by a detector, it is possible to track each photon to the origin site showing which atoms where in $|0\rangle$. (b) if the atom is not in the state being excited, the laser pulse has no effect on the atom and no photons are emitted. In the physical realisation of this process all the atoms in state $|1\rangle$ would have been kicked out of the lattice to avoid accidental excitation due to the closeness of the hyperfine energy levels. (c) when a lattice site that is a vacancy is hit by the laser pulse it also does not release any photons as there is nothing to excite. (b) and (c) produce the same results and it is not possible to differentiate between them.

4.3.1 State description

The four possible states after the entangling operation are as follows

$$\begin{aligned}
\rho_{11} &= |\bullet\bullet\rangle\langle\bullet\bullet|\,, \text{ where } |\bullet\bullet\rangle \to \frac{1}{\sqrt{2}}(|01\rangle - |10\rangle),\\
\rho_{00} &= |vv\rangle\langle vv|\,, \text{ where } |vv\rangle \to |v\rangle|v\rangle\,,\\
\rho_{01} &= |v\bullet\rangle\langle v\bullet|\,, \text{ where } |v\bullet\rangle \to |v\rangle|+\rangle = |v\rangle\frac{1}{\sqrt{2}}(|0\rangle + |1\rangle),\\
\rho_{10} &= |\bullet v\rangle\langle\bullet v|\,, \text{ where } |\bullet v\rangle \to |0\rangle|v\rangle\,,
\end{aligned} \tag{4.2}$$

where $\bullet$ and v denote the presence of a particle and a vacancy respectively. We denote ρ_{11} as the ideal maximally entangled state where both Alice and Bob have a particle in their well, ρ_{00} the non-entangled state where both Alice and Bob do not have particles, ρ_{01} the state where Bob has a particle and Alice does not, and finally ρ_{10} the state where Alice has a particle and Bob does not. By assigning probabilities to each of these possible systems we can describe our two-well system with the following mixed

density operator,

$$\begin{aligned} \rho &= \rho_{01}+\rho_{10}+\rho_{11}, \\ \rho_{AB}(p,q,r) &= p\rho_{00}+(1-p)\rho \\ &= p\rho_{00}+(1-p)\Big(q\Big(\frac{1+r}{2}\rho_{01}+\frac{1-r}{2}\rho_{10}\Big)+(1-q)\rho_{11}\Big), \end{aligned} \tag{4.3}$$

$\{p,q\}$ are probabilities and $-1 \leq r \leq +1$ characterises the asymmetry in the vacancy rates of Alice and Bob. In general we do not initially assume independence of vacancy rates. We note here that any measurements we perform on our system will destroy it. This does not matter as we do not plan to use the state for any computation yet, we perform these measurements to test the creation process and how much entanglement could be detected in the state.

4.4 Detecting entanglement

There are many different ways to test the entanglement of the system, but many of these require us to be able to perform full state tomography on the system and reconstruct a description of the state, for example, concurrence [54, 55]. As we have previously discussed this becomes impossible the more particles there are in the system.

Entanglement witnesses are another tool we could use to test the entanglement of the system. Entanglement witnesses are operators corresponding to observables, $\hat{O}$. For separable states, σ, the expectation of the operator is non-negative. However there exists at least a single entangled state for which the expectation value of the operator is negative. This is possible as the separable states form a convex closed set and an entanglement witness defines the plane that intersects with that set at a single point [53] (Fig. 4.5).

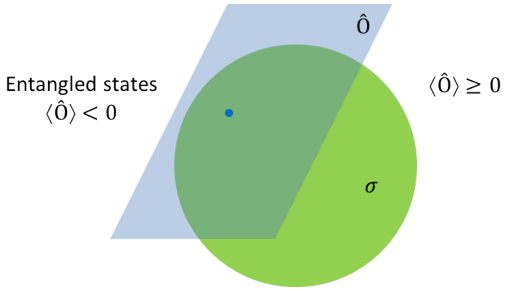

Figure 4.5: Entanglement witness. The green sphere represents the closed convex set of separable states where the expectation value of the entanglement witness is non-negative. The blue plane represents the entanglement witness operators. This plane separates the entangled states from the separable ones, touching only at a single point (the blue dot), this is the density operator that will give a negative expectation value of the entanglement witness.

The problem with using an entanglement witness to detect the entanglement is we need to know the exact state we are trying to test. We also need to know the exact entanglement witness to measure as only one of them will intersect the convex set of separable states at the appropriate point, which leads back to the hard problem of characterising the state. If we did not know the exact entanglement witness associated with the state we are trying to test then instead of the blue plane in Fig. 4.5 resting on a single point in the sphere could cut through the sphere. This complicates the test as if the expectation value of the entanglement witness is negative then it could still lie in the sector of sphere above the plane. There is also the problem that if the expectation value of the entanglement witness is positive then it could lie below the blue plane in Fig. 4.5 but not in the sphere making it entangled. Using an entanglement witness as a test of entanglement only really works if the expectation value is negative, when it is positive then there is the possibility of errors.

Given these difficulties and restrictions we will use a two setting, two outcome CHSH experiment to test the entanglement of our system as it is a sufficient condition for a state to be entangled if it violates this inequality. We have chosen this inequality above the other Bell inequalities as there are minimal assumptions about the form of the measurements or the processes [52, 56]. The only restriction we have on the types of measurements are that the results must be ± 1. This leaves a huge range of options for the experiment, for example, in their paper [52], Clauser, Horne, Shimony and Holt describe the measurement device as a filter then a detector. This detector could be used for the detection or non-detection of particles making the CHSH inequality associated with the counting rate. Or the measurement device could look for the emergence or non-emergence of optical photons from the filter, at the time of the paper it was not possible to detect single photons as the loss rate was too high. Or the filter on the measurement device could be a polarisation filter and the measurement results correspond to the linear polarisation orientation. This huge range of measurement options makes the CHSH measure very useful. The CHSH inequality is a combination of the expectation values of measurements that Alice and Bob are allowed to perform on their parts of the system. Alice has an random, independent choice of two alternative measurements $\{a, a'\}$ and Bob has an random, independent choice of two different measurements $\{b, b'\}$. To ensure that one choice of measurement does not affect the other side's result, the measurements are performed simultaneously. They each assign ± 1 to the possible outcomes. The CHSH value, S, is formed by

$$S = \langle ab \rangle + \langle ab' \rangle + \langle a'b \rangle - \langle a'b' \rangle. \tag{4.4}$$

Under the assumption of local realism,

$$|S| \leq 2, \tag{4.5}$$

which is the CHSH inequality. However, quantum mechanics allows

$$|S| = 2\sqrt{2}, \tag{4.6}$$

for a maximally entangled state of two qubits, see Sec. 2.16 for the proof [2, 57].

In our set up we also have the possibility of there being a vacancy in the system. If Alice or Bob measure a vacancy they always assign the measurement result -1, this means they are unable to distinguish between the logical state $|1\rangle$ and a vacancy, $|v\rangle$. Our measurement is an incomplete projection where

$$\begin{aligned} \pi_{+1} &= |0\rangle\langle 0|, \\ \pi_{-1} &= |1\rangle\langle 1| + |v\rangle\langle v|, \end{aligned} \tag{4.7}$$

where π_{+1} projects on to the subspace $|0\rangle\langle 0|$ and π_{-1} projects onto the degenerate subspace $|1\rangle\langle 1| + |v\rangle\langle v|$. Using these assignments we can represent the measurement settings a, a', b, b' as if we always have a particle but calculate the outcome probabilities to include the effect of vacancies. This addresses the detection loophole problem found in many Bell inequality tests as in our experiment we will always assign a result. We do not need to wait for coincidences as we use all results and do not post-select [58, 59, 60]. We are aiming to find measurement settings that lead to a violation of local realism, i.e. a violation of the CHSH inequality, for the largest range of vacancy probability possible.

4.4.1 Bound on the CHSH value

For our system we can find an upper bound on the CHSH value, S, depending on the vacancy rates by splitting up the components with and without particles, this is what we will be attempting to saturate by optimising Alice and Bob's measurement settings. From the form of the CHSH inequality, the local realism bound of $|S| = 2$ and the Tsirelson bound of $|S| = 2\sqrt{2}$ for a maximally entangled state [57], this leads to

$$|S| \leq 2\alpha + 2\sqrt{2}(1-\alpha), \tag{4.8}$$

where $0 \leq \alpha \leq 1$ is the probability of having a vacancy. Eq. (4.8) will be above 2 if $\alpha \neq 1$ making it possible to violate the CHSH inequality, hence detect entanglement. When $\alpha = 0$, S is at the maximum $2\sqrt{2}$. By using a series of optimisations we will see how closely we can reach this bound. But firstly we explore the analytical expression for S to see if we can reduce the number of parameters to simplify our calculations.

4.4.2 Simplification of the CHSH expression

In the ideal case we can write the measurement settings a, a', b, b' in terms of projectors and their complement on a qubit,

$$\begin{aligned}
&\pi(\theta,\phi) = |\psi\rangle\langle\psi|\,,\\
&\bar{\pi}(\theta,\phi) = |\psi^{\perp}\rangle\langle\psi^{\perp}| + |v\rangle\langle v|\,,\\
&|\psi\rangle = \cos\frac{\theta}{2}|0\rangle + e^{i\phi}\sin\frac{\theta}{2}|1\rangle\,,\\
&|\psi^{\perp}\rangle = \sin\frac{\theta}{2}|0\rangle - e^{i\phi}\cos\frac{\theta}{2}|1\rangle\,,
\end{aligned} \tag{4.9}$$

defining a direction on the Bloch sphere where $0 \leq \theta \leq \pi$ and $0 \leq \phi < 2\pi$ [2]. This is an abuse of notation but throughout this chapter we will treat these measurement settings in the same way we would when performing a CHSH test on qubits.

The physical measurement is always performed along a fixed axis. The measurement settings a, a', b, b' are implemented using unitary rotations that act upon the $|0\rangle$ and $|1\rangle$ components but do not affect $|v\rangle$ this is due to the difficulty of creating superpositions of states with different particle numbers. This inability is governed by superselection rules. We explore the extent of these rules in detail in the next chapter [15, 16]. Each measurement setting is represented by θ and ϕ, for example, measurement setting a has θ_a and ϕ_a. As $|v\rangle$ always gives the result -1, the ρ_{00} component results in the maximum classical correlation independently of the angle θ and ϕ, this gives

$$S = 2p + (1-p)S', \tag{4.10}$$

where p is the probability of ρ_{00} ($|v,v\rangle_{AB}$) occurring, and S' is the state where there is at least one particle. In order for S in Eq. (4.10) to violate the CHSH inequality, ie. be greater than 2, there must be particles in the system ($p < 1$) and there must be some entanglement present in the system ($|S'| > 2$). No matter which measurement settings Alice and Bob use, the double vacancy component of the system will always give the result $S = 2$ as it is a purely classical state. As we are trying to violate the CHSH inequality and exceed 2 we do not need to include the vacancy-vacancy element in our calculations as it does not contribute to the violation. For the purpose of optimisation of the measurement angles we only consider S'.

4.5 Optimising the CHSH value

Explicitly writing S' in the form of differences in measurement angles produces,

$$\begin{aligned} S' &= q\Big((r-1)\cos\theta_a - (r+1)\cos\phi_b \sin\theta_b\Big) \\ +\frac{(q-1)}{2}\Big[&\cos(\theta_a-\theta_b)(1+\cos(\phi_a-\phi_b)) + \cos(\theta_a+\theta_b)(1-\cos(\phi_a-\phi_b)) \\ &+\cos(\theta_a-\theta_{b'})(1+\cos(\phi_a-\phi_{b'})) + \cos(\theta_a+\theta_{b'})(1-\cos(\phi_a-\phi_{b'})) \\ &+\cos(\theta_{a'}-\theta_b)(1+\cos(\phi_{a'}-\phi_b)) + \cos(\theta_{a'}+\theta_b)(1-\cos(\phi_{a'}-\phi_b)) \\ &-\cos(\theta_{a'}-\theta_{b'})(1+\cos(\phi_{a'}-\phi_{b'})) - \cos(\theta_{a'}+\theta_{b'})(1-\cos(\phi_{a'}-\phi_{b'}))\Big]. \end{aligned} \tag{4.11}$$

We are interested in maximising the value of S' to do this we need to find θ's and ϕ's that correspond to the maximum of Eq. (4.11). A local maximum corresponds to the partial derivative equaling zero [61]. Ensuring that a local maximum is the global maxima is, in general, a hard problem. It is possible to get trapped in a local maxima and assume that this is the global maximum (Fig. 4.6).

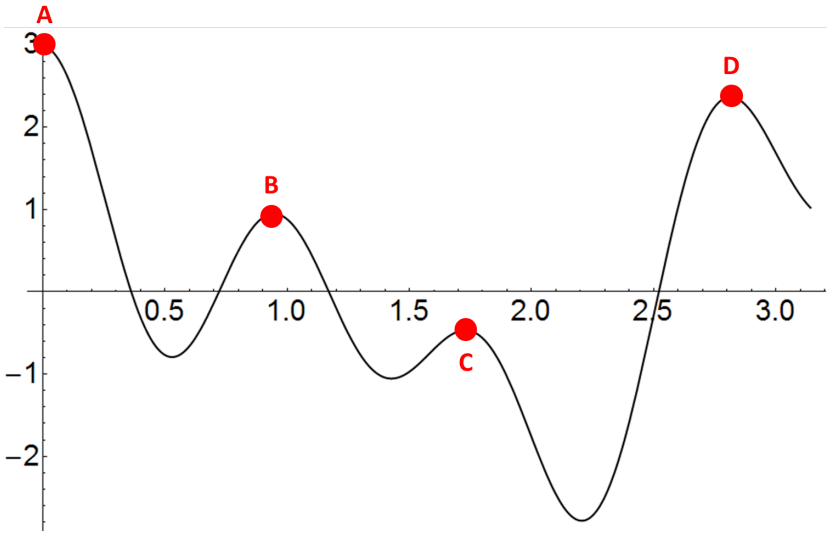

Figure 4.6: Local maxima. A is the global maximum situated at the boundary. B, C and D are all local maxima. It is possible to mistake B, C or D as the global maxima.

In this particular case, the problem is slightly simplier as we do not need to worry about the boundary conditions. The measurements, technically the search space, is compact without boundaries so we do not need to consider the maxima occurring at the boundaries.

To find the maximum of S' we partially differentiate Eq. (4.11) with respect to ϕ_a, $\phi_{a'}$, ϕ_b and $\phi_{b'}$ as follows,

$$\begin{aligned}\frac{\partial S'}{\partial \phi_a} =&\frac{1}{2}(q-1)\Big(\sin(\phi_a-\phi_b)(-\cos(\theta_a-\theta_b)+\cos(\theta_a+\theta_b))\\ &+\sin(\phi_a-\phi_{b'})(-\cos(\theta_a-\theta_{b'})+\cos(\theta_a+\theta_{b'}))\Big),\end{aligned} \tag{4.12}$$

$$\begin{aligned}\frac{\partial S'}{\partial \phi_{a'}} =&\frac{1}{2}(q-1)\Big(\sin(\phi_{a'}-\phi_b)(-\cos(\theta_{a'}-\theta_b)+\cos(\theta_{a'}+\theta_b))\\ &+\sin(\phi_{a'}-\phi_{b'})(\cos(\theta_{a'}-\theta_{b'})-\cos(\theta_{a'}+\theta_{b'}))\Big),\end{aligned} \tag{4.13}$$

$$\begin{aligned}\frac{\partial S'}{\partial \phi_b} =&q(1+r)\sin\theta_b\sin\phi_b+\frac{1}{2}(q-1)\Big(\sin(\phi_a-\phi_b)(\cos(\theta_a-\theta_b)-\cos(\theta_a+\theta_b))\\ &+\sin(\phi_{a'}-\phi_b)(\cos(\theta_{a'}-\theta_b)-\cos(\theta_{a'}+\theta_b))\Big),\end{aligned} \tag{4.14}$$

$$\begin{aligned}\frac{\partial S'}{\partial \phi_{b'}} =&\frac{1}{2}(q-1)\Big(\sin(\phi_a-\phi_{b'})(\cos(\theta_a-\theta_{b'})-\cos(\theta_a+\theta_{b'}))\\ &\sin(\phi_{a'}-\phi_{b'})(-\cos(\theta_{a'}-\theta_{b'})+\cos(\theta_{a'}+\theta_{b'}))\Big).\end{aligned} \tag{4.15}$$

At the local maxima $\frac{\partial S'}{\partial X}=0$, each of the differentials Eq. (4.12)-(4.15) has a $\sin(\phi_j-\phi_k)$ term in each component (highlighted in red). In order to optimise the S we can choose $(\phi_j-\phi_k)=0,\pi \mod 2\pi$ making $\frac{\partial S'}{\partial X}=0$. This forces ϕ_a, $\phi_{a'}$, ϕ_b, $\phi_{b'}=0,\pi \mod 2\pi$, for convenience we set $\phi_a=\phi_{a'}=\phi_b=\phi_{b'}=0$ i.e. the $X-Z$ plane, leading to,

$$\begin{aligned}S' =&q\Big((r-1)\cos\theta_a-(r+1)\sin\theta_b\Big)\\ &+(q-1)\Big(\cos(\theta_a-\theta_b)+\cos(\theta_a-\theta_{b'})+\cos(\theta_{a'}-\theta_b)-\cos(\theta_{a'}-\theta_{b'})\Big).\end{aligned} \tag{4.16}$$

This shows that when Alice and Bob share a symmetric singlet state, $q=0$, then S' is only dependent upon the relative differences of the θ's and so is rotationally invariant. But as soon as $q>0$ the preferred measurement angles are set by the first term in Eq. (4.16) as this part does not just consist of differences of angles, $\cos\theta_a$ and $\sin\theta_b$ need to also be maximised which has a knock on effect on the second component of Eq. (4.16). A balance must be struck between the entangled and separable parts, this is what leads the S' value to decrease as q gets larger.

4.5.1 Optimsation for equal and independent vacancy rate

Now we have fixed the ϕ angles we model a system and attempt to improve the critical limit of vacancy probability that allows a violation of the CHSH inequality. The optimisations in the chapter are numerical and will be performed using Mathematica, by varying the angles along which Alice and Bob perform their measurements we aim to maxmise S. In the model system each site has a equal and independent vacancy

probability, $P_v^A = P_v^B = P_v$. The density operator can be written as,

$$\rho_{AB}\left(P_v^2, \frac{2P_v}{(1+P_v)}, 0\right) = P_v^2\rho_{00} + P_v(1-P_v)\rho_{01} + (1-P_v)P_v\rho_{10} + (1-P_v)^2\rho_{11}, \quad (4.17)$$

where $p = P_v^2, q = \frac{2P_v}{(1+P_v)}$ and $r = 0$. By numerically optimising the measurement settings in three stages we investigate how closely we can reach the bound in Eq. (4.8) (Fig. 4.11, black solid line) for the equal and independent vacancy rate.

4.5.1.1 No Optimisation

We begin by using the conventional measurement settings used in the CHSH test for a singlet state. Here Alice has the choice of measuring along the Z axis of the Bloch sphere or the X axis, whereas Bob has the choice of measuring along the $\frac{-Z-X}{\sqrt{2}}$ axis on the Bloch sphere or the $\frac{X-Z}{\sqrt{2}}$ axis as shown in Fig. 4.7.

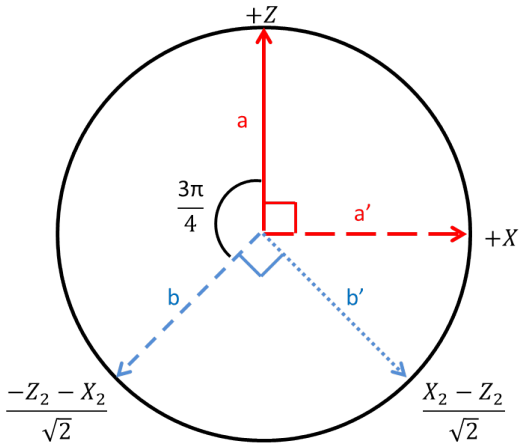

Figure 4.7: Unoptimised measurement settings. The conventional measurement settings that Alice (red) and Bob (blue) use to find the expectation values for the CHSH inequality leading to $S = 2\sqrt{2}$ for an ideal singlet state.

These measurement settings produce the red dashed line in Fig. 4.11. The vacancy probability at which we stop violating the CHSH inequality is $P_{v_{1.1}}^{crit} \approx 0.153$, this is our starting point, we want to try to make this value as large as possible.

4.5.1.2 Step 1: Global rotation around the Y-axis

We now allow Alice and Bob to jointly redefine the $+Z$ direction by rotating their axes around the Y axis of the Bloch sphere keeping the angles between the settings the same (Fig. 4.8)

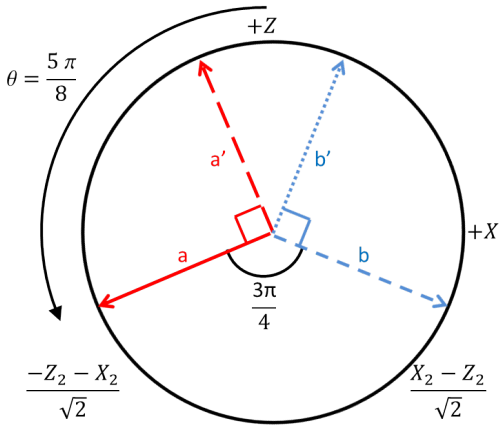

Figure 4.8: Global optimised measurement settings. Alice and Bob's measurement settings when allowed to rotate jointly around the Y axis of the Bloch sphere. The measurement settings shown are the optimal settings for all P_v, where the conventional settings have been rotated by $\frac{5\pi}{8}$.

By rotating the conventional measurement settings by $\frac{5\pi}{8}$ the critical value is raised to $P_{v_{1.2}}^{crit} \approx 0.251$ (Fig. 4.11, orange dashed line). The optimal angle of the bi-local rotations is the same for all P_v. This is because the bi-local rotations optimise the first term of Eq. (4.16) but do not affect the second, as the first term does not depend on the q value the optimal rotation is the same for all P_v. These bi-local rotations do not affect the second term as this part describes the singlet state which is rotationally invariant.

4.5.1.3 Step 2: Bi-local independent rotation about the Y axis

In this step we increase the degrees of freedom and allow Alice and Bob to rotate their local axes individually, but keeping their own settings relative to one another (Fig. 4.9).

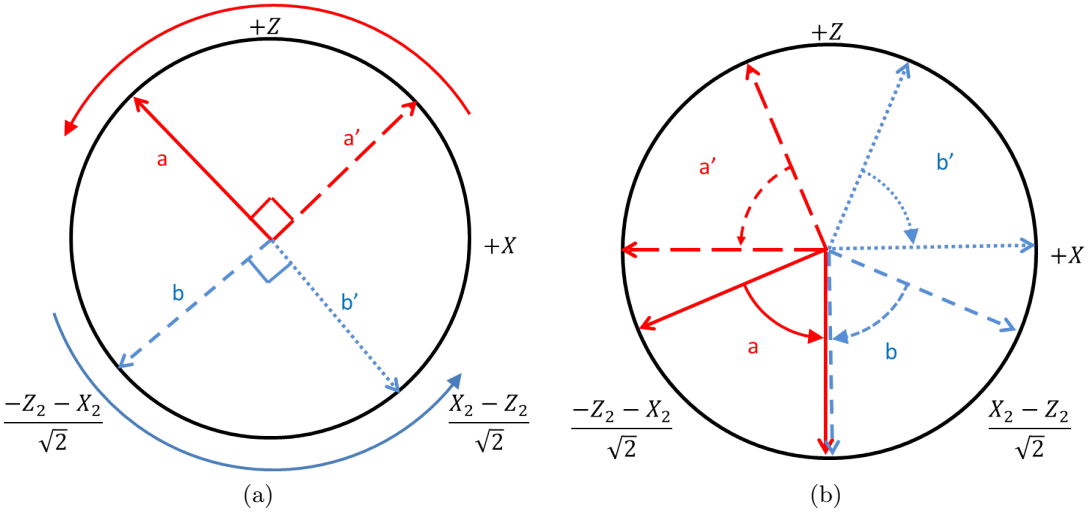

Figure 4.9: Bi-local XZ plane optimised measurement settings. Independent measurement setting rotations. (a) shows how Alice and Bob rotate their settings independently, keeping their individual settings relative to one another. (b) show how the optimal measurement settings change as P_v increases from $P_v = 0.01 \rightarrow 0.99$

The critical value as been increased again to $P_{v_{1.3}}^{crit} \approx 0.269$ (Fig. 4.11, blue dot-dashed line), the optimal rotations for the measurement settings are now different for each value of P_v.

4.5.1.4 Step 3: Individual independent rotation around the Bloch sphere

In the final step we allow Alice and Bob to rotate each of their settings individually around the entire Bloch sphere, Fig. 4.10.

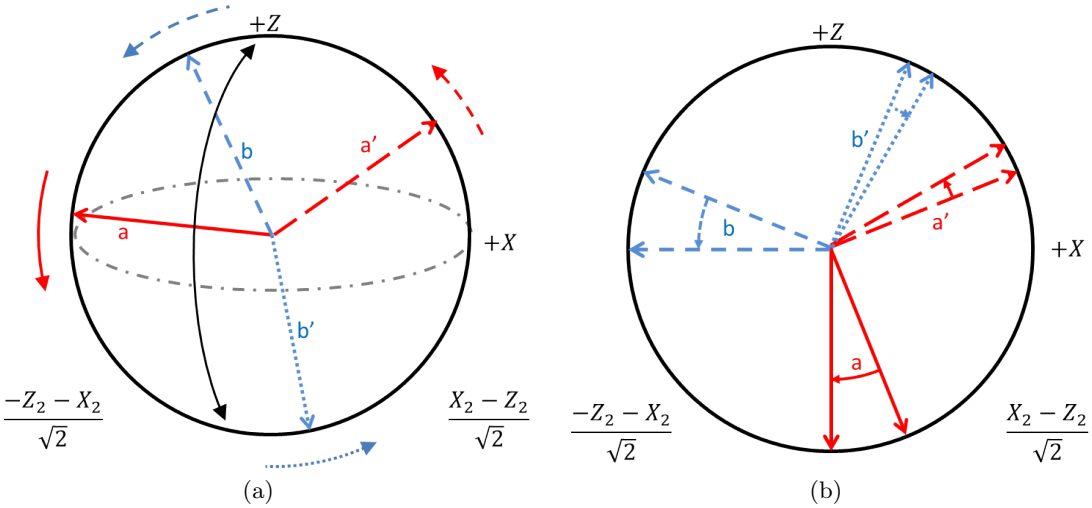

Figure 4.10: Independent local optimised measurement settings. Alice and Bob rotate each setting independently of the other, around the whole Bloch sphere. (a) shows the degrees of freedom Alice and Bob are allowed to rotate their measurement settings. (b) shows the actual measurement settings Alice and Bob choose and how they change from $P_v = 0.01 \rightarrow 0.99$.

This produces a somewhat surprising result, the critical value $P^{crit}_{v_{1.4}}$ is now arbitrarily close to 1 (Fig. 4.11, pink dotted line). Meaning that as long as there are particles in the system, in principle it is possible to violate the CHSH inequality, showing there is entanglement in the system. These measurement settings are different for each value of P_v.

We have also already shown that it was sufficient to search for the optimal measurement settings in the $X - Z$ plane of the Bloch sphere. Other sets of optimal angles do exist in other planes of the Bloch sphere but these sets of angles do not increase the S value and so we can be sure that we only need to consider the sets of angles in the $X - Z$ plane.

4.5.1.5 Comparisons and discussion

Here we show all the optimisations together so a clear comparison can be made, we note that we have not been able to reach the upper bound on S' with this method.

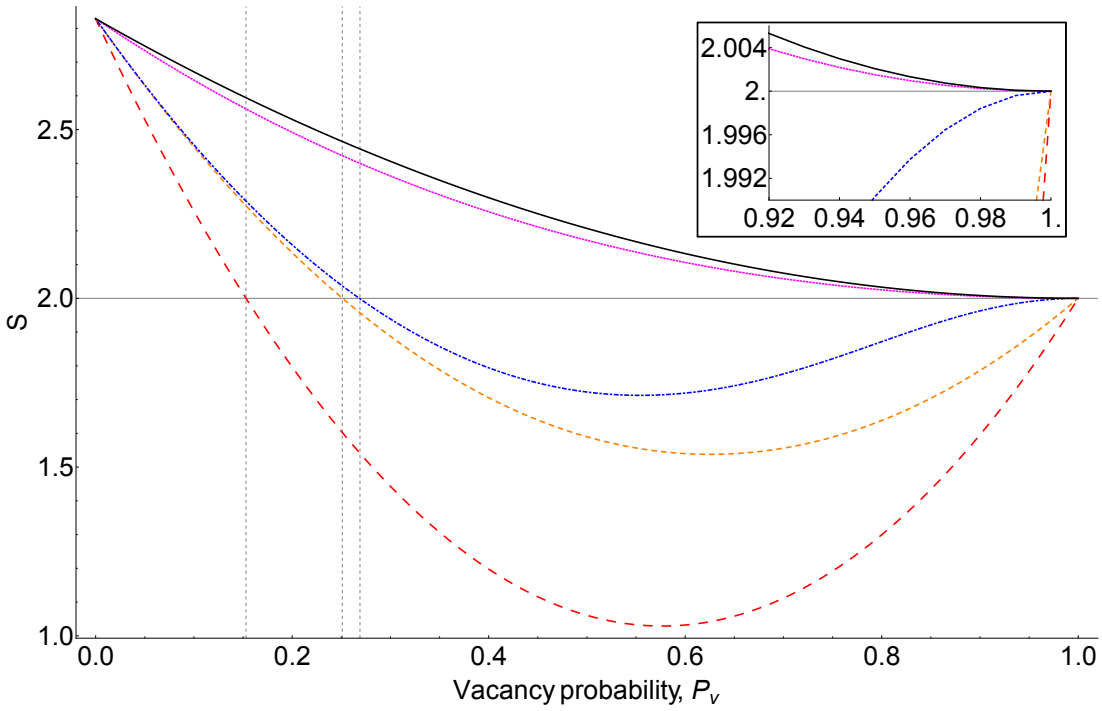

Figure 4.11: The complete optimisation process. Showing how the optimisation steps increase the critical value of P_v
Upper bound (Black solid line) The upper bound given by Eq. (4.8).
No optimisation (Red dashed line) Vacancy probability above which entanglement not detected $P_{v1.1}^{crit} \approx 0.153$.
Step 1 (Orange dashed line) $P_{v1.2}^{crit} \approx 0.251$. The optimal angle of rotation of the measurement settings is $\theta = \frac{5\pi}{8}$ for all P_v.
Step 2 (Blue dot-dashed line) $P_{v1.3}^{crit} \approx 0.269$. The optimal angles of rotation for Alie and Bob's pairs of settings is different for each value of P_v.
Step 3 (Magenta dotted line) $P_{v1.4}^{crit} < 1$. Again the optimal angles of rotation of each of Alice and Bob's measurement settings are different for each value of P_v.

To produce the smooth curves we continuously adjust the search parameters as we vary the vacancy probability. As discussed earlier these optimum settings may describe a local maximum rather than a global maximum, however we can say that the true optimum must be at least as good as the results shown here. By simply changing the measurement settings Alice and Bob use to perform their measurements we are able to detect entanglement in the system the majority of the time except when $p = 1$. To understand why we see this improvement we study how Eq. (4.16) is affected by each optimisation process.

Step 1: Global rotation around the Y-axis - The optimal angle of rotations for all Alice and Bob's measurement settings is the same for all of P_v, which can

be understood by looking at the expression for S' in Eq. (4.16). Rotating all the measurement settings by the same amount will have no effect on the result of the second expression for S as it only contains terms that are differences in settings. If all the settings are rotated by the same amount the result will be the same. The first expression will be affected by the rotation, but, as it is a simple subtraction of two angles it will have a fixed maximum value that is independent of q. This is why we have the optimal rotation angle for the whole range of P_v.

Step 2: Bi-local independent rotation about the Y axis - The optimal angles of rotation stop being the same for all P_v at Step 2. Looking at the second expression in Eq. (4.16), each of the cos terms is made up of subtracting one of Alice's measurement settings from one of Bob's, these measurement settings are rotated independently of one another but a is fixed at $\frac{\pi}{2}$ from a' and the same for Bob's measurement settings. To maximise S' there must be a compromise drawn between the first and second term. For $P_v = 0.01$, $\alpha_{rot} = 1.97, \beta_{rot} = 1.96$ radians (Fig. 4.9) leading to Eq. (4.16) looking like

$$S' = q(-0.537) + (1-q)(2.828), \tag{4.18}$$

as P_v is small, q is small so the second term dominates the equation. But as we increase q the first term will have more of an effect and so a different balance must be struck between the two expressions. For $P_v = 0.26$, $\alpha_{rot} = 2.07, \beta_{rot} = 1.85$ radians leading to

$$S' = q(-0.395) + (1-q)(2.76), \tag{4.19}$$

the angles here produce the best combination of the inputs from the two expressions.

Step 3: Individual independent rotation around the Bloch sphere - Again in Step 3 the optimal measurement settings are different for each P_v looking at the actual measurement settings for when $P_v = 0.01$, $\theta_a = 2.75, \theta_{a'} = 1.18, \theta_b = 5.10$ and $\theta_{b'} = 0.394$ (in the $X-Z$ plane of the Bloch sphere, Fig. 4.10a), this makes Eq. (4.16)

$$S' = q(1.85) + (1-q)(2.828), \tag{4.20}$$

as P_v is small, q is small so the equation is mostly just the second expression but as P_v, hence q, gets larger the input from each expression changes, $P_v = 0.99$, $\theta_a = 3.14, \theta_{a'} = 1.05, \theta_b = 4.71$ and $\theta_{b'} = 0.523$ (in the $X-Z$ plane of the Bloch sphere, Fig. 4.10b), Eq. (4.16) now looks like

$$S' = q(2.0) + (1-q)(2.60), \tag{4.21}$$

where the second expression only contributes a very small amount but is just enough to tip the S' value over 2 to show entanglement in the system.

To check that eliminating p does not affect the value of the CHSH inequality we quickly calculated the optimum measurement settings in both cases (Appendix C.1) and the same optimum measurement settings were found in both cases.

4.5.1.6 More general $\rho(p, q, r)$ states

Up until now we have not been able to saturate the bound shown in Eq. (4.8). In order to saturate this bound we require measurement settings that produce a value of 2 for the non-entangled part of the system in the CHSH inequality and $2\sqrt{2}$ for the entangled part. So far we have only been able to find a balance between the entangled and non-entangled part that jointly violates the CHSH inequality. We now look at more general states to try to create this situation.

We begin by varying r the parameter that controls the symmetry of the vacancy rate of the system,

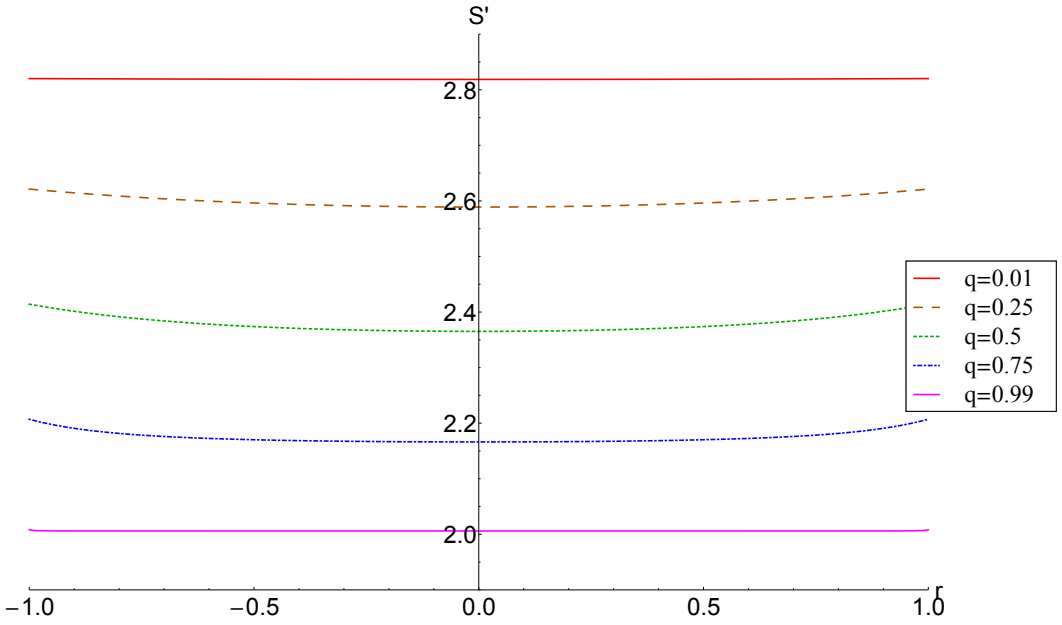

Figure 4.12: S' vs r with fixed q. In each test we fix q then vary r across the range. The value of r does not provide a very significant change in the value of S'. But we can see that the value of S' is largest at the extremes of r. The optimal measurement settings are different for each value of r.

From Fig. 4.12 we can see that it is better to have an asymmetric system, i.e. $r = \pm 1$ to produce a larger S', this can be seen by looking at the density operator. For $r = +1$,

$$\rho_{AB}(0, q, 1) = q\rho_{01} + (1 - q)\rho_{11}. \tag{4.22}$$

We have already seen that bi-local rotations do not affect the entangled part of the system, this allows us to choose measurement settings that produce 2 for the separable part of the state whilst still giving $2\sqrt{2}$ for the entangled part as the angles for the entangled part are rotationally invariant and so can just be matched with the settings that give 2 for the non-entangled part, thus saturating the bound in Eq. (4.8).

The dip that we see as $r \to 1$ is due to the optimum angles for the entangled and non-entangled parts no longer matching, hence a compromise must be made between them leading to a reduced S' value.

By looking at how the individual measurement settings change with r we see that the optimum settings for $r = -1, +1$ are the same for all q as we would expect as this gives us the upper bound on S'.

4.6 Effects of additional imperfections

In the work so far we have not considered any form of error other than the incomplete measurement process. In this section we look at two types of additional error, and see how these affect the detectable entanglement.

4.6.1 Robustness to state knowledge

In most of the optimisation steps we have looked at we must know the true value of p, q and r in order to calculate the optimal measurement settings. Getting these parameters wrong could lead to a reduced violation of the CHSH inequality which could become an issue when close to the boundary. Here we consider the case that our knowledge of q is incorrect but still assume that ρ_{11} is pure and ideal. We need only look at the effects upon S' as previously explained. We also assume that our knowledge of $r = 0$ is correct, we have chosen this r as it produces the smallest optimum of S'. We denote our incorrect estimate of the true q as q'. When $q' \neq q$ then the measurement settings that we choose will not be optimum. To see how much this affects the violation of the CHSH inequality we first find the optimum measurement settings for five estimate q' values, $q' = 0.01, 0.25, 0.5, 0.75, 0.99$, these measurement settings are given in Appendix C.2. By fixing the measurement angles to those for $q' = 0.01$ say, we test how the value of S' is affected over the full range of true q. This is repeated for all five q' settings (Fig. 4.13).

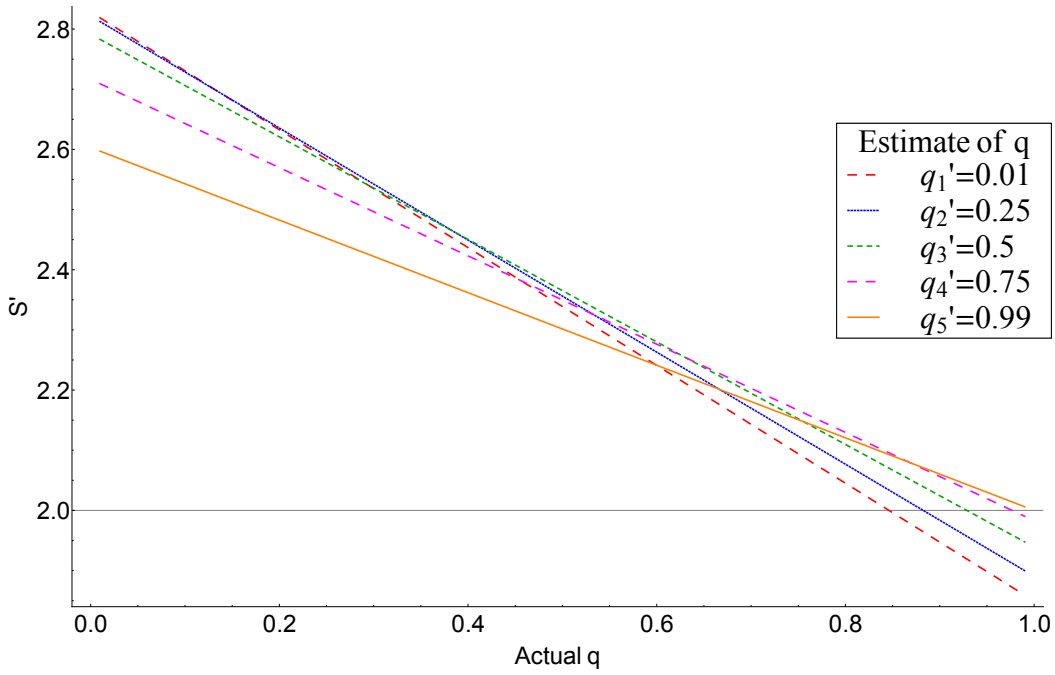

Figure 4.13: S' for estimated q' measurement settings. Using fixed measurement angles found when $q' = 0.01, 0.25, 0.5, 0.75, 0.99$ we test the system over the full range of q to understand how an incorrect estimation affects the S' value.

This test produces an interesting result, the measurement settings for the worst case scenario ($q' = 0.99$) provides a violation for the largest range of true q. This implies that if there is any uncertainty in the true q value then it is better to use the measurement settings calculated from $q' = 0.99$ as this will ensure a violation. Although there is a reduction in the maximum violation of S' this is not significant as the aim of our experiment is to verify the entanglement so any violation is sufficient no matter how small.

4.6.2 Detector error

We have assumed the detection process is ideal with the incomplete measurement process in all the previous work, now we look at two types of error a detector could encounter, inefficiency and dark count.

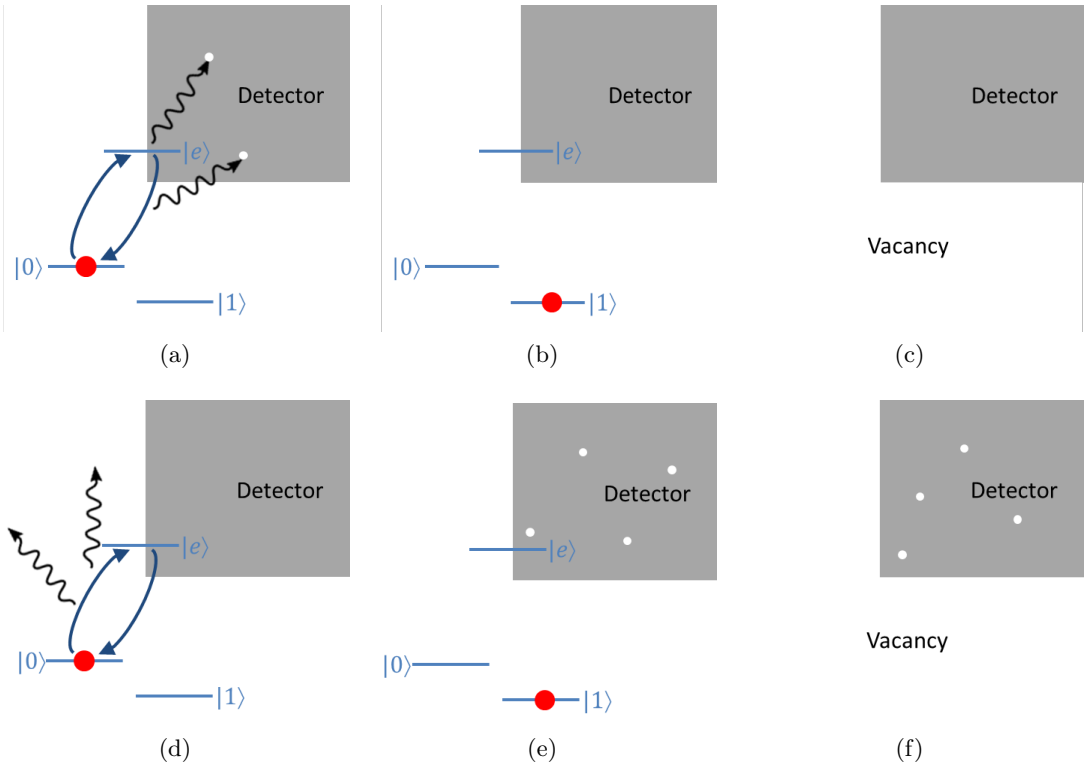

Figure 4.14: Fluorescence measurement outcomes. (a), (b) and (c) show the ideal cases for an atom in $|0\rangle$, an atom in $|1\rangle$ and a vacancy site respectively. The lattice is fluoresced with the $|0\rangle$ transition energy so the atom in $|0\rangle$ is successfully excited and releases photons that are captured by the detector, the white dots indicating a detection. Both the atom in $|1\rangle$ and the vacancy site do not emit photons and the detector is not activated. (d), (e) and (f) show the non ideal cases for an atom in $|0\rangle$, an atom in $|1\rangle$ and a vacancy site respectively. Here, when the lattice is fluoresced the atom in $|0\rangle$ is excited but the photons are released at an angle where they cannot be collected by the detector. In the other cases the atom in state $|1\rangle$ is not excited but stray photons, cosmic rays and trapped charge cause the detector to fire, this is the same for the non-ideal vacancy site.

4.6.2.1 Photons/detector inefficiency

When using fluorescence imaging as a measurement process, there must be efficient capture of all the scattered photons [62, 63, 64]. If all the photons are not captured this could lead to a mis-identification of the state with the dark state or a vacancy (Fig. 4.14). This one-sided measurement error follows the noise model,

$$\begin{aligned} P(+1|\,|0\rangle) &= 1 - P(-1|\,|0\rangle) = \eta, \\ P(-1|\,|1\rangle) &= P(-1|\,|v\rangle) = 1, \end{aligned} \tag{4.23}$$

where $0 \leq (1-\eta) \leq 1$ is the probability of incorrectly identifying the $|0\rangle$ state as the $|1\rangle$ state, with the ideal case as $\eta = 1$ under the equal and independent vacancy rate described in Sec. 4.5.1. We will assume ρ_{11} to be pure and ideal.

The violation of the CHSH inequality decreases as η decreases as we would expect. However, it is always possible to detect entanglement in the system when $0.869 \leq \eta \leq 1$ across the entire range of $0 \leq P_v < 1$ (Fig. 4.15 black dotted line). For $2(\sqrt{2}-1) < \eta \leq 0.869$ it is possible to find a violation for some values of P_v, $\eta = 2(\sqrt{2}-1)$ is the limit of violation and it is only possible to detect a violation if $P_v = 0$ (Fig. 4.15 brown dot-dashed line).

To attempt to beat this limit and reduce η to as small as possible we also performed an optimisation on the input state this is explained in detail later in this section.

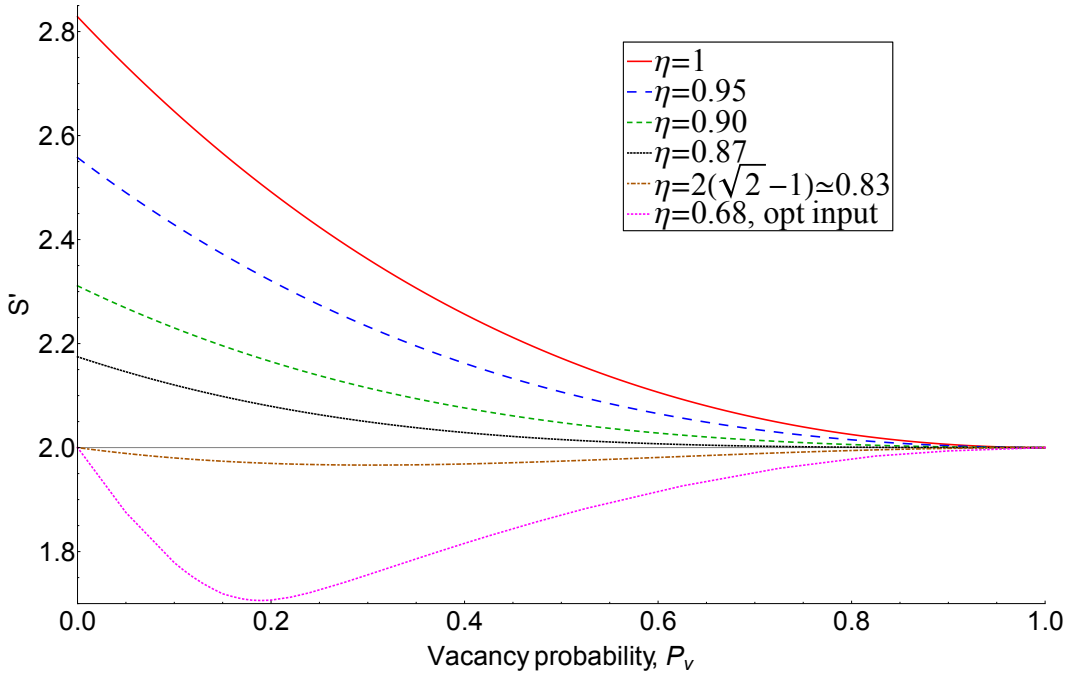

Figure 4.15: S' versus P_v with inefficient detection. By introducing the error η that describes the probability of an atom in the $|0\rangle$ being identified correctly, the S' value is lowered for all $P_v < 1$. The optimal measurement settings are different for each value of P_v.

It is important to have high detection efficiency in post-selection experiments as this closes the detection loophole [65, 66, 67, 68, 69]. The detection loophole is the argument that there could be an underlying hidden variables model that we are unable to detect that explains the non-local behaviour. For example, in a conventional CHSH inequality test Alice and Bob only record their results when both of them have a successful click on their detector, and all the other results are thrown away, i.e. when only one of them gets a click on their detector or neither of them do. We assume that the results that we are able to detect via the coincidences are in line with those that we cannot detect, but if they were not then these hidden results could show a hidden variables model that

we cannot access. Our set up is a bit different as we have an incomplete measurement process meaning that each time Alice and Bob do not detect a particle we assign it that value -1 regardless of the measurement setting so no results are thrown away. Garg and Mermin found that the detection efficiency in their experiment must be higher than $2(\sqrt{2}-1)$, this result matches ours by coincidence as there are various differences in our assumptions and measurement scenarios [67]. We were actually able to better Garg and Mermin's limit by introducing an optimisation on the initial state, Box 1 Fig. 4.3, Sec. 4.3. We do not use post-selection, all of our results are counted in the experiment as due to the incomplete measurement process we are unable to differentiate between a vacancy and a particle in state $|1\rangle$. This means that the detection-loophole does not apply, hence there is no contradiction with the Garg and Mermin result. Instead of Alice and Bob both starting with the $|+\rangle$ state we modified this to be $|\psi_\tau\rangle_A |\psi_\tau\rangle_B$ where $|\psi_\tau\rangle = \cos\tau |0\rangle + \sin\tau |1\rangle$. Using this input state and following the optimisation process in Step 3, we were able to find states and measurement settings that allowed a violation of the CHSH inequality for as low as $\eta = 0.68$ (Fig. 4.15, pink dotted line). We also tested how S' changes with η with an optimised input state and when there is no possibility of vacancies, $P_v = 0$ (Fig. 4.16).

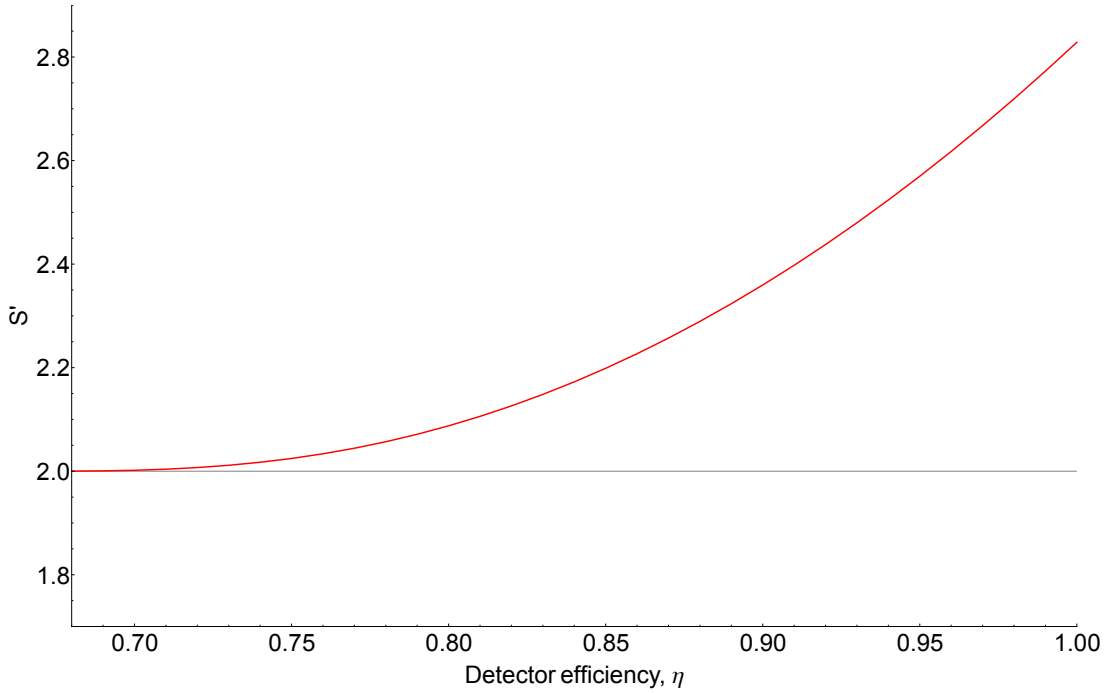

Figure 4.16: S versus η with optimised input state, $P_v = 0$. The limit at which point the system stops violating the CHSH inequality is $\eta = 0.68$.

The optimal measurement settings are no longer in the $X - Z$ plane of the Bloch sphere and are denoted as $[\kappa, \theta, \phi]$, where κ describes the rotation around a specified plane defined by θ and ϕ on the Bloch sphere. For $P_v = 0$ and $\eta = 0.68$ these optimal measurement settings are shown in Fig. 4.17.

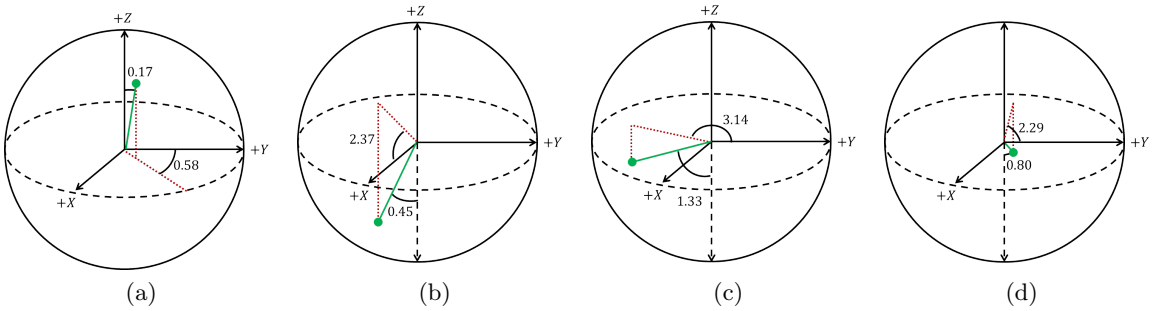

Figure 4.17: Optimum measurement settings for $P_v = 0$ and $\eta = 0.68$. These are a rough representation of the optimum measurement settings on the Bloch sphere where $\tau \approx 6.11$. (a) has settings $a \approx [4.16, 1.95, 4.14]$, (b) has settings $a' \approx [2.21, 1.38, 0.77]$, (c) has settings $b \approx [2.83, 1.56, 1.58]$ and (d) has settings $b' \approx [2.46, 1.48, 0.72]$. As the settings are no long confined to the $X - Z$ plane they are harder to represent.

We have not yet fully explored this avenue for optimisation and leave this open for further work.

4.6.2.2 Error due to dark count

Here we look at the effect of dark counts in the detector, this can lead to the opposite one-sided error. Dark counts arise from thermal activation of avalanche multiplication [70] which can be caused by cosmic rays or trapped charge within the detector [1]. We assume $\eta = 1$, where the dark state $|-1\rangle$ or $|v\rangle$ can be misidentified as $|0\rangle$. The error is modeled as,

$$\begin{aligned} P(+1|\,|0\rangle) &= 1 - P(-1|\,|0\rangle) = 1, \\ P(-1|\,|1\rangle) &= P(-1|\,|v\rangle) = 1 - \epsilon, \end{aligned} \tag{4.24}$$

where $0 \leq \epsilon \leq 1$ is the error due to dark count with the ideal case as $\epsilon = 0$ in the equal and independent vacancy rate model in Sec. 4.5.1.

The dark count error affects the value of S' more significantly than the detector efficiency η. For any $\epsilon > 0$ the range of P_v that violates the CHSH inequality is decreased. As we see in Fig. 4.18, $\epsilon \geq 1 - 2(\sqrt{2} - 1)$ is the limit when we stop being able to violate the CHSH inequality for any value of P_v. Similar to the previous section we found how S' changes with ϵ with an optimised input state with $P_v = 0$ (Fig. 4.19).

[1] The use of cooled detectors [71, 72, 73, 74, 75] should be able to reduce dark counts to negligible levels and so eliminate the effect of this error channel except for extremely high vacancy rates.

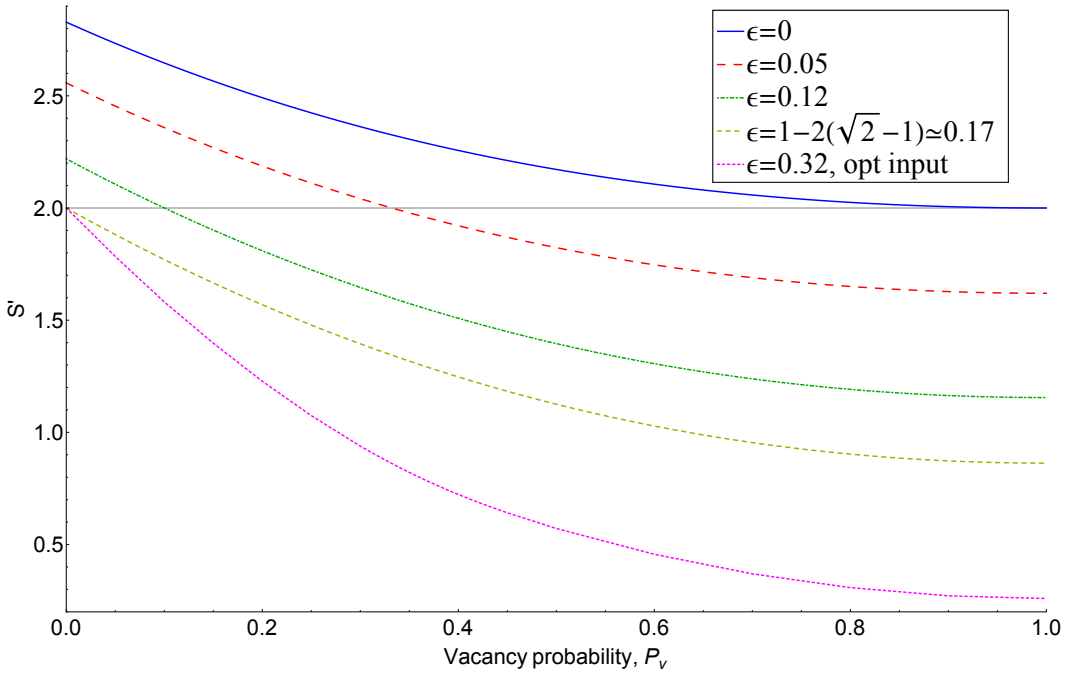

Figure 4.18: Effect of dark count induced error on S'. ϵ is the error that the detector will fire when it should not leading to a false positive result. As soon as this error is incorporated into the system the maximum value of S' is decreased as is the range of P_v that allows a violation of the CHSH inequality.

By optimising the input state as we did for the η error we can increase our dark count error limit to $\epsilon \leq 0.32$ and still obtain a violation when $P_v = 0$, in this case the measurement settings do not sit in the $X - Z$ plane of the Bloch sphere and look like those shown in Fig. 4.20.

The errors η and ϵ seen in Fig. 4.16 and Fig. 4.19 mirror each other as we expect them to as they are opposite one sided errors.

4.6.3 Discussion

The effects of additional imperfections reduces the violation of the CHSH inequality. By optimising the measurement settings Alice and Bob use to calculate the CHSH value the reduction can be minimised.

In the case of imperfect state knowledge, when there is uncertainty in the q value to ensure a violation across the largest range of q it is better to use the measurement settings given for $q = 0.99$ (Details in Appendix C.2).

We also looked at two one-sided errors that mirror each other, detector inefficiency and dark count. As the detector inefficiency increases, the maximum violation of the CHSH inequality decreases as we would expect. By choosing the measurement angles carefully we are able to withstand a detector efficiency of $\eta \approx 0.83$ this can be decreased to $\eta \approx 0.68$ if we also optimise the input state of the system from $|+\rangle$ to $\cos\tau\,|0\rangle +$

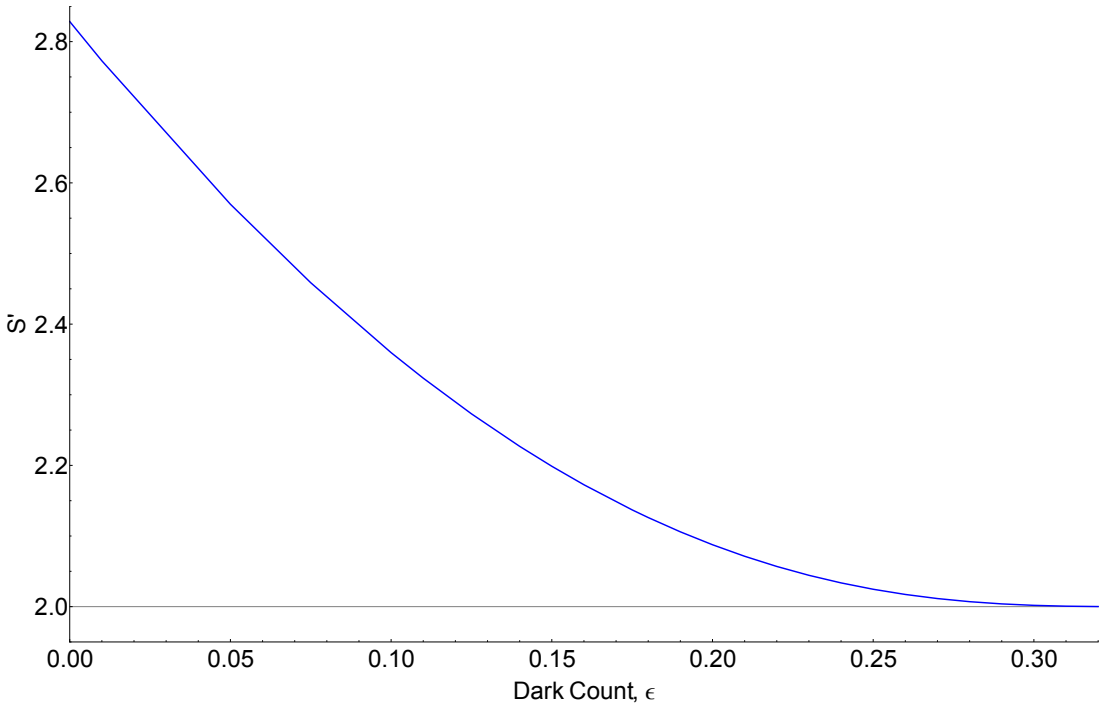

Figure 4.19: S' versus ϵ with optimised input state, $P_v = 0$. The limit at which the system stops violating the CHSH inequality is $\epsilon = 0.32$.

$\sin\tau\,|1\rangle$. The optimum measurement settings no longer lie in the $X - Z$ plane of the Bloch sphere and so the analysis of the problem is much more complicated and time-consuming. We found mirrored results with the dark count error, here the maximum dark count, ϵ, that still provided a violation of the CHSH inequality was $\epsilon \approx 0.17$ which increased to $\epsilon \approx 0.32$ with the optimised input state.

We have shown that even with errors in the system it is possible to detect a violation of the CHSH inequality to conclude that the system is entangled. In practice there would also be errors in the preparation and implementation of the measurement process, in the gate operations and elsewhere in the system which would reduce the detectable violation. However, having these extra errors may not render the experiment useless, we are only interested in witnessing entanglement in the system. This means that even if our results did not show a violation of the CHSH inequality if we knew what the errors were, it would in principle, be possible to undo the errors on the data and revert it back to see if the original error-free state was entangled. This of course would destroy the state but it is a suitable method for characteristion and diagnostics. This process adds an element of complexity that is not ideal. Further exploration of these errors has been left for later work.

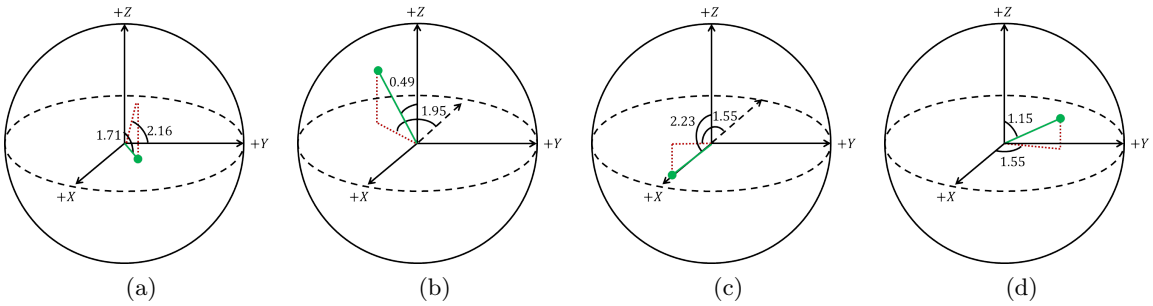

(a) (b) (c) (d)

Figure 4.20: Optimum measurement settings for $P_v = 0$ and $\epsilon = 0.32$. These are a rough representation of the optimum measurement settings on the Bloch sphere where $\tau \approx 3.31$. (a) has settings $a \approx [3.82, 4.18, 3.73]$, (b) has settings $a' \approx [4.18, 1.62, 1.95]$, (c) has settings $b \approx [5.95, 4.39, 1.56]$ and (d) has settings $b' \approx [1.45, 3.68, 4.70]$. As the settings are no long confined to the $X - Z$ plane they are harder to represent.

4.7 Conclusion

In this chapter we began by reviewing how measurement-based quantum computation could be realised using cluster states trapped in optical lattices. By understanding how these lattices are loaded with the atoms we noted that due to finite entropy it is possible to have vacant lattice sites. We investigated the effect these vacancies have on the detectable entanglement in the system. The other important aspect of our system was the incomplete measurement process. This means we could not differentiate between an atom that was in $|1\rangle$ and a vacancy. This is not ideal but it does close the detection loop-hole as we do not post-select our measurement results.

We chose the CHSH inequality to verify the entanglement of the state as this requires a minimum number of assumptions about the measurements and operations. We defined an upper bound on the CHSH value, our aim being to saturate this bound. The system we used in our setup comprised of a bipartite system where due to the possibility of the vacancies there were four possible starting states.

We began by defining a system with an equal and independent vacancy rate. Using the conventional measurement settings used in the CHSH test we found the critical vacancy rate probability that still allowed a CHSH inequality violation. This was not very high and so we performed a three step optimisation processes on the measurement settings in order to increase this critical value as much as possible. In Step 1 we globally rotated the measurement settings around the Y axis and found for the optimum settings the rotation angle was the same for all P_v and the critical value of the vacancy probability increased. Step 2 used bi-local independent rotations around the Y axis where Alice and Bob's measurement settings where rotated independently but keeping their respective set at $\frac{\pi}{2}$ to one another. Again this increased the critical value of the vacancy probability compared with Step 1 and the optimum settings for each P_v were different. Finally, in Step 3 we independently rotated each of Alice and Bob's

measurement settings about the entire Bloch sphere. Again the measurement settings for each value of P_v were different and we were able to find a vast improvement in the critical vacancy probability. A violation was detected for all $P_v < 1$. This means that as long as there is some probability of atoms in the system, e.g. the system is not ρ_{00}, then it would be possible to detect a violation in the CHSH inequality and hence show entanglement.

Although we had found this vast improvement in the critical value of the vacancy probability we had not yet saturated the upper bound. To address this we considered more general states, $\rho(p, q, r)$, and found that when the system is completely asymmetric the bound is saturated (Eq. (4.22)). At these extremes the optimum measurement settings are the same for all q.

So far we assumed that all the measurements and knowledge about the system was ideal, we found we could violate the CHSH inequality for almost all P_v but as $P_v \to 1$ the violation value became smaller and smaller any error in the system is likely to reduce the CHSH value so if the violation is only just above 2 then an error may push this below the boundary. To understand how different types of errors affect the system we considered three different types.

Firstly, error in the knowledge of q when considering a general system $\rho(p, q, r)$. As we have previously stated the optimum measurement settings are different for different values of q. If there is an error in the knowledge of q then incorrect optimum measurement settings could be used which may lead to a failure of violation detection. By testing how different optimum measurement settings perform over the range of q we have shown that even if we use the optimum measurement settings found from the worst system still provides a violation of the CHSH for the whole range of $0.01 \leq q \leq 0.99$. This leads to a decrease in the maximum violation, but, a lower violation for a larger range of q is preferable to a higher violation for a smaller range of q. This is an important result as it makes our system very robust, even if there is a large error in the knowledge of q it would be possible to still detect a violation.

Secondly, we considered the error due to detection inefficiency where there is some probability that not enough photons from an atom in the $|0\rangle$ would be collected and we assume it was actually $|1\rangle$. We found two limits on the error, one where a violation was possible over the whole range of P_v and one where it was possible for $P_v = 0$. At this point we also tested a system with an optimised input state, using this state we were able to better the limits for the detector inefficiency with a non-optimised state.

Finally, we looked at the dark count error, this is effectively the opposite of the detector inefficiency where an atom in $|1\rangle$ or $|v\rangle$ is mistaken for a atom in $|0\rangle$. We found the dark count error to affect the maximum CHSH value more significantly than the detector inefficiency. There is no value of the dark count error that allows for a violation across whole range of P_v. We find the limit at $P_v = 0$ to match $1 - \eta$, the detector error as expected.

Similar to the previous chapter we have shown that simply by changing the measurement we can vastly reduce the effect physical constraints have on the entanglement in the system. By optimising the measurement angles used in the CHSH inequality we have shown that large improvements can be made in the tolerance of the system. In a system with no errors we have shown that even if the probability of any atoms being in the system is almost 0 we can still produce a CHSH inequality violation proving that there is entanglement. This is a powerful result as it shows that the choice of measurement angle is very important, simple changes can maximise the effect of the entangled part of the system no matter how small it is. However, the more errors we include the lower the maximum CHSH value will be. If the maximum value is very close to 2, it is important that we are positive that the violation is from the entanglement in the state and not just the statistical spread of values.

CHAPTER 5

Superselection rules, noise and Bell inequalities

5.1 Introduction

In this chapter we consider the single particle entanglement question. There has been a lot of debate as to whether single particle entanglement actually exists and is meaningful or if it is solely dependent upon the way we write the state. The problem is directly related to superselection rules that restrict the types of states and operations that can be performed on a system. In some cases we can consider the superselection rules to be a useful resource [15]. However, it has been shown there are ways to allow the restricted operations to be performed [1, 15, 16]. This is by the introduction of a reference frame, a separable state shared between the parties before the principal state. Paterek *et al.* have defined the minimum reference frame required to violate the CHSH inequality. We base our work in this chapter on their model [1].

We introduce error into our system in the measurement process. The errors come directly from the apparatus. As in the previous chapter we wish to show detectable entanglement for the largest error possible to make the system more robust. Depending on the placement of the measurement apparatus in the circuit the errors follow different models. By optimising the measurement settings for each of the error models we aim to improve the critical error at which entanglement is no longer possible to be at its maximum.

The chapter is set out as follows, in Sec. 5.2 we review superselection rules and the effects they have on states and operations. We also review the minimum reference frame required to violate the CHSH inequality in a system constrained by superselection rules. In Sec. 5.3 we define the system we will use, taken from [1]. In Sec. 5.4 we describe the error models and optimise the measurement settings to improve the critical value of error. We will check the experimental feasibility of the optimum measurement settings

that we find in Sec. 5.5. In Sec. 5.7 we briefly discuss ideas of how to create the state and in Sec. 5.6 we consider non-ideal state preparation and how this affects the violation of the CHSH inequality in a system with ideal measurements. And finally in Sec. 5.8 we investigate if it is possible to swap the reference frame and principle system to make the state creation process less complex.

In this chapter we are considering a much different system to that which we have covered so far here we change our notation to match that of the literature, to avoid confusion in the rest of the chapter we will be performing measurements in the particle number basis and not considering internal states. Although the following work is different to previous chapters there is a strong link, we have so far looked at optical lattices as a probable candidate for quantum computation exploring the imperfections and errors that occur during its creation, in this chapter we consider another system that could be realised using an optical lattice and we test its robustness again using the CHSH inequality.

5.2 Background

The work in this chapter is based upon a simple question: can a single particle be entangled? This question has lead to many different ideas, and arguments for and against the notion [76, 77, 78, 79, 80, 81, 82, 78, 83, 84, 85, 86, 87].

Given all these contradictory arguments we consider that the single particle entanglement question is actually part of a larger question that concerns the allowed coherent operations that can be performed on quantum states. These restrictions on the coherent operations are called superselection rules. Superselection rules are important as they affect certain types of quantum behaviour such as a reduction in the entanglement of a system [88, 89, 90]. A superselection rule of a particular observable says that it is impossible to prepare a coherent superposition of two eigenstates of a particular observable with different eigenvalues or different conserved quantities, for example, charge conservation [91, 92].

Verstraete and Cirac look into the effect of superselection rules on quantum operations [15]. They look specifically at the particle number superselection rule, this states that the particle number operator commutes with all observables [93]. This means that superpositions of states with different numbers of massive particles cannot be created as this goes against the superselection rule. There are two main points to their paper that are important in this chapter which we will briefly explain. Firstly, superselection rules allow us to create states that are separable but non-local. Secondly, superselection rules allow us to perform perfect data hiding schemes that have previously been proven to be impossible [94, 95] making them a useful resource.

They start with a set of N particles in a Hilbert space and assume that the particle number is a superselection observable, meaning that it is not possible to create a

superposition of two states with different numbers of particles. Any density operator in this setup can be written as

$$\rho = \sum_{N=0}^{\infty} p_N \rho_N, \tag{5.1}$$

where P_N is the probability the state is in ρ_N and ρ_N is the sector of definite particle number N. If we expand the Hilbert space now to two parties, Alice and Bob, still with superselection rules and now with locality rules, Alice and Bob cannot create superpositions of states with different numbers of particles using local operations and classical communication (LOCC). This means we can have states that are separable but non-local. Example 1 of Verstraete and Cirac [] is such a state where ρ_1 is compatible with superselection,

$$\rho_1 = \frac{1}{4}(|0\rangle_A \langle 0| \otimes |0\rangle_B \langle 0| + |1\rangle_A \langle 1| \otimes |1\rangle_B \langle 1|) + \frac{1}{2}(|\psi^+\rangle_{AB} \langle \psi^+|), \tag{5.2}$$

where $|\psi^+\rangle = \frac{1}{\sqrt{2}}(|0\rangle_A |1\rangle_B + |1\rangle_A |0\rangle_B)$. This can be shown to be separable, $\rho_j |a_j\rangle \langle a_j| \otimes |b_j\rangle \langle b_j|$, by looking at the decomposition, $p_k = \frac{1}{4}(k = 1, 2, 3, 4)$,

$$\begin{aligned} |a_{1,2}\rangle = |b_{1,2}\rangle &:= \frac{1}{\sqrt{2}}(|0\rangle \pm |1\rangle), \\ |a_{3,4}\rangle = |b_{3,4}\rangle &:= \frac{1}{\sqrt{2}}(|0\rangle \pm i |1\rangle). \end{aligned} \tag{5.3}$$

These states are not compatible with superselection rules as they are superpositions of states with different numbers of particles. Using this example state Verstraete and Cirac show that they cannot be prepared locally under superselection rules by proving the following: If ρ can be prepared locally, then,

$$\rho = \mathcal{N}(\rho) := \sum_{n_A, n_B = 0}^{\infty} (P_{n_A}^A \otimes P_{n_B}^B) \rho (P_{n_A}^A \otimes P_{n_B}^B), \tag{5.4}$$

and example 1 can be written as,

$$\mathcal{N}(\rho_1) = \frac{1}{4} \sum_{n,m=0}^{1} |n\rangle_A \langle n| \otimes |m\rangle_B \langle m| \neq \rho_1. \tag{5.5}$$

They have shown the state is separable but also cannot be created using LOCC. They also show that the states ρ and $\mathcal{N}(\rho)$ cannot be distinguished using LOCC. This statement is important as it allows a perfect data hiding protocol to be realised showing that the superselection rules can actually be used as a resource. The argument is as follows, Alice and Bob receive a secret bit encoded in state 0 or 1 the state

$$|\pm\rangle := (|0\rangle_1 |1\rangle_2 \pm |1\rangle_1 |0\rangle_2), \tag{5.6}$$

prepared by a third party, Charlie. This preparation is allowed as the global number of particles in both states in the superposition is the same. Alice receives system 1 and Bob system 2. By seeing that $\mathcal{N}(|+\rangle\langle+|) = \mathcal{N}(|-\rangle\langle-|)$ we see that Alice and Bob cannot get any information about the bit using LOCC operations. To access the information they must perform joint operations, which in this case is not allowed. Hence, the secret bit is safe.

Verstraete and Cirac then go on to look at what Alice and Bob would need in order to be able to access secret information. If Alice and Bob share a reference frame of an entangled state prior to receiving the secret bit they are able to infer the value of the hidden bit with probability $\frac{N}{N+1}$. Obviously this is not perfect so they then go on to show that by using the non-local separable states as a reference frame this probability of gaining the value of the bit is arbitrarily close to 1.

Verstraete and Cirac have shown we can create a different type of state that is not entangled but still has non-local properties, for example, sausage states [96]. These states can also be used as a resource and will be useful in our setup in this chapter. They show that the superselection rules can be used as a resource to hide information. They introduce the idea of reference frames that allow us to access this hidden information that we would otherwise not be able to learn. These reference frames are of particular interest as they allow us to bypass the restrictions initially imposed by the superselection rules.

In 1967, Aharonov and Susskind showed that the superpositions that should not be allowed due to superselection rules can be observed if the two parties share the appropriate reference frame, where the reference frame can be used to prepare and measure the system [16]. In their paper, they begin by using an experiment to prepare a coherent superposition of $\sigma_s = +1$ and $\sigma_s = -1$ which under the rules of angular momentum superselection should not be possible. They show that when there is a reference frame between the apparatus of the experiment, i.e. the two magnetic fields are aligned, this coherent superposition is allowed. They set up a magnetic field in the x direction and allow the electron to pass through the field, precessing as expected around the x axis. Due to the setup when the electron leaves the magnetic field it is orientated with the spin in the y direction. This action puts the electron in a coherent superposition of $\sigma = \pm 1$. To prove that the electron is in the coherent superposition Aharonov and Susskind suggest measuring σ_y. If the electron was incoherent this would result in probability $\frac{1}{2}$ that $\sigma_y = \pm 1$, but the coherent results would have probability 1 and 0 for $\sigma_y = +1$ and $\sigma_y = -1$ respectively. How this measurement is done is the key to understanding how reference frames allow these forbidden states, for example it could be done using a second magnetic field. The electron in the superposition $|\sigma = +1\rangle + r\exp(i\theta)|\sigma = -1\rangle$ has a phase, θ, where θ defines the direction of polarisation of the electron. Aharonov and Susskind point out that angles must be measured with respect to a reference frame, in this case they call that the second magnetic field. After the electron has passed through the magnetic fields it is in an eigenstate of L_z,

the component of the angular momentum in the z direction. This means that to an external observer the orientation of the xy planes is uncertain as is the orientation of the electron to the xy plane. But Aharonov and Susskind have already stated that the electron uses the second magnetic field as a reference frame, this is just not accessible to an external observer. It is only important that the two magnetic fields in the system share this reference frame and so have an alignment with respect to each other. The relative phase between the state $|\sigma = \pm\rangle$ is always measured with respect to a reference frame given by one of the magnetic fields, this then gives a reference frame internally for the xy plane.

Aharonov and Susskind then go on to look at another example but this time with charge rather than angular momentum. They start by having two single mode cavities C_1 and C_2 each of which can have an arbitrary number of negatively charged mesons. They prepare a state with Q_1 in C_1 and Q_2 in C_2 where Q_i is the charge in cavity i. Q_1 and Q_2 are uncertain but $Q_1 + Q_2$ is known, this situation could be realised by splitting the mesons before they enter the cavities with the appropriate half-reflecting plate so it is not known how many mesons are in each cavity. Each of the mesons can be described using the wavefunction $\psi_1 + \exp i\phi\psi_2$. If there are enough mesons then the state in the two cavities will have a definite phase of $\phi_1 - \phi_2$ where ϕ_i is the phase conjugate to Q_i. This idea is the same as the last experiment.

Once this setup is prepared a proton is sent into C_1, when it comes out it will be a proton or a neutron when measured (Fig. 5.1a). Aharonov and Susskind's claim is that relative to the reference frame provided by C_1, the nucleon that leaves C_1 is a coherent superposition of zero and plus charge with a definite phase between the proton and neutron components.

They show this by sending the nucleon through C_2 and showing that the emerging state has interference between proton and neutron. They show this by setting up many cavities that could be frames of reference. They randomly pick one to define the zero phase. Using this cavity the superposition of charge states can be prepared and another cavity can be used to check the interference. If a proton passes through cavity C_1 that has state $|Q\theta\rangle$ where θ is the phase then the emerging nucleon has probability $\cos^2(gT\sqrt{q})$ of being a proton and probability $\sin^2(gT\sqrt{q})$ of being a neutron, then when this state is passed through C_2 which is in state $|q'\theta'\rangle$ the relative phase between the neutron and proton is $\theta - \theta'$. If this experiment is repeated lots of times the probabilities of the particle being in one state or the other can be observed as Ramsey fringes, where the probability of the nucleon being a proton say, rises and dips between 0 and 1 (Fig. 5.1b). The ramsey fringe pattern confirms the superposition state, if the state leaving C_1 was simply a mixture of a proton and a neutron ($\frac{1}{2}(|p\rangle\langle p| + |n\rangle\langle n|)$) this fringe pattern would not be observed.

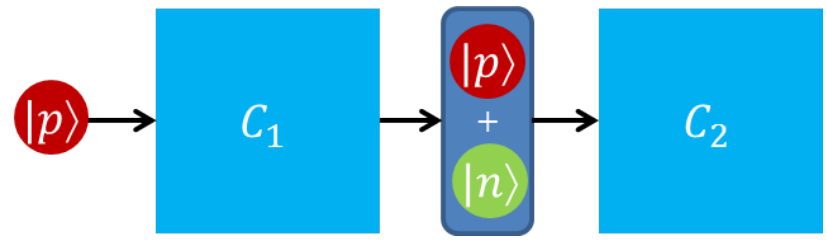

(a)

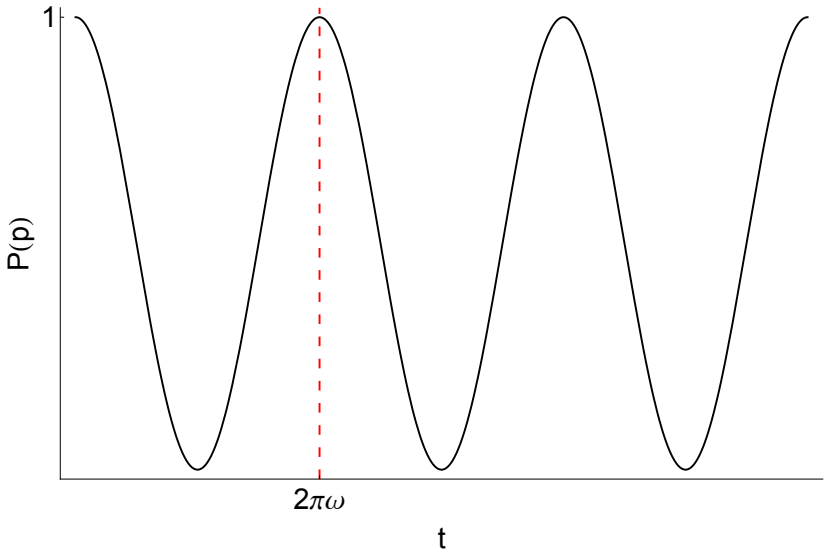

(b)

Figure 5.1: Superposition of a proton and neutron. (a) a proton is sent into C_1, when it emerges it is in a superposition of proton and neutron. To check this the superposition is sent through C_2 then when the probabilities of detecting the particle as a proton is measured, the ramsey fringe pattern is created proving it was in a superposition. (b) Evolution of a coherent superposition. When a coherent superposition is allowed to evolve, the probability of detecting the state in $|p\rangle$, $P(p)$, rises and falls following the graph, repeating every $t = \frac{2\pi}{\omega}$.

The ramsey fringes show that by using a reference frame we can bypass the problem of not having coherent superpositions of two eigenstates of the same observable with different eigenvalues. Using these reference frames they show that we can in fact have single particle entanglement as the superposition of the two eigenstates with different particle number is possible. We will now explore what these reference frames look like and the restrictions on their form. Paterek *et al.* defines the minimum reference frame required to violate a Bell inequality [1]. Their principle system is an entangled state of two and three particles,

$$|\psi\rangle = \frac{1}{\sqrt{2}}(|23\rangle + |32\rangle), \tag{5.7}$$

they show that with the right separable reference frame a Bell inequality can be violated showing that the principle system was in fact entangled, explanation and proof comes later in this section. One way we could create this state is by initially starting with

$|32\rangle$ and allow tunneling between the two parties. Making sure the other states (e.g. $|41\rangle$ and $|50\rangle$ etc.) are energetically unfavoured the principal entangled system could be realised. To link back to the question of single particle entanglement, another way to create the principal system could be to perform coherent operations that obey superselection rules to transform the state $\frac{1}{\sqrt{2}}(|01\rangle + |10\rangle)$ to the principle state this would prove that the single particle system was in fact entangled.

$$\frac{1}{\sqrt{2}}(|01\rangle + |10\rangle) \rightarrow \frac{1}{\sqrt{2}}(|23\rangle + |32\rangle), \tag{5.8}$$

For the rest of this chapter we assume we can perform this transformation and review the results presented in [1] and use them to define our system. The rest of this section follows the arguments in [1] closely.

5.2.1 General description of system that could be used to violate a CHSH inequality

Paterek *et al.* showed that a Bell violation is possible in a system with a principle state and a reference frame if and only if the reference frame has been prepared jointly i.e. a violation is not possible when the reference frame has been created via only local operations that satisfy superselection rules and classical communication (SSR-LOCC) [1]. This is shown by first proving that using a reference frame that is prepared using only SSR-LOCC cannot violate a Bell inequality as it is possible to describe the joint state as separable. Verstraete and Cirac's results agrees with this [15]. This restricts Alice and Bob in their choice of reference frame, in order to have the possibility of detecting a Bell violation they can only use reference frames that cannot be created by only using SSR-LOCC.

Fig. 5.2 shows the system that Alice and Bob share, a reference frame, $\rho_{A'B'}$ and a principal system, ρ_{AB}. Alice has access to the subsystems A and A' and Bob has access to the subsystems B and B', where they can perform measurements with outcomes ± 1. ρ_{AB} is an entangled pure state of N-particles and has the form

$$|\psi\rangle_{AB} = \sum_{n=0}^{N} c_n \, |n\rangle_A \, |N-n\rangle_B \, , \tag{5.9}$$

where $|c_n|^2$ is the probability that Alice has n particles. Particle-number superselection says that all states and measurements commute with the particle-number operator $\hat{N}$. To measure the system Alice and Bob count the number of particles on each of their respective sides.

Using the principal system alone Alice and Bob are not able to violate a Bell inequality as they can only count the particles in their own subsystems so will always get an anticorrelated result, e.g. n_A, $(N-n)_B$. In order to violate a Bell inequality they

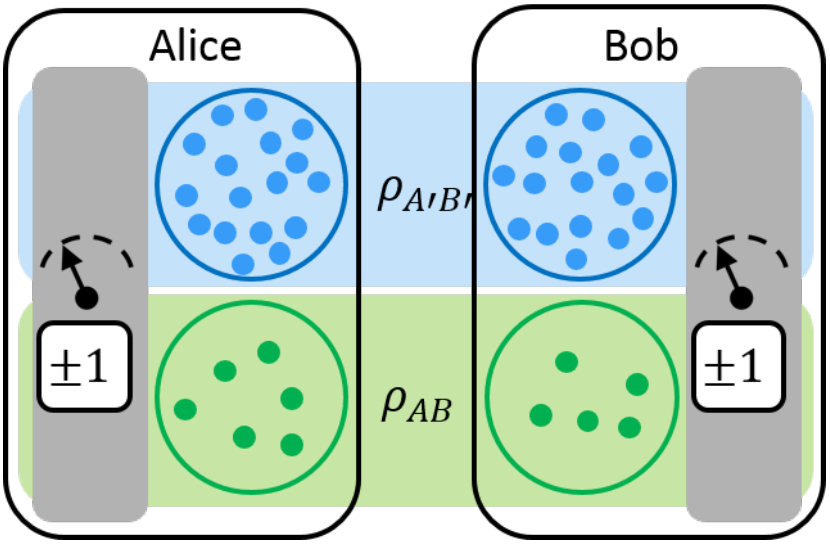

Figure 5.2: The system. Alice and Bob share a reference state $\rho_{A'B'}$. Then they receive the principal system, ρ_{AB}. Alice (Bob) perform a measurement on their subsystems $A(B)$, the result of which is ± 1.

must introduce a reference frame. The form of the reference frame is slightly complicated. To be able to violate a Bell inequality the reference frame they share must be separable. The separable condition comes from that fact that if the CHSH inequality is violated it is important that we are able to say all of the entanglement comes only from the principle system, we can only be certain of this if the reference frame is separable.

Paterek *et al.* showed in order to violate the CHSH inequality the reference frame cannot be formed using SSR-LOCC. Here we follow the argument in their paper. Firstly they show that using a reference frame prepared only using SSR-LOCC cannot lead to a violation in the CHSH inequality as the reference frame can be shown to be equivalent to a general mixed state and as such cannot produce a Bell inequality violation. They then go on to show that by using a reference frame that cannot be prepared using only SSR-LOCC leads to a violation. These arguments follow the paper very closely.

5.2.2 Reference frame prepared using SSR-LOCC

Reference frames prepared using SSR-LOCC commute with local particle-number operators as required by the particle superselection rule and are of the form

$$\rho_{A'B'}^{SSR-LOCC} = \sum_{k,l} p_{kl} \left|k\right\rangle_{A'} \left\langle k\right| \otimes \left|l\right\rangle_{B'} \left\langle l\right|, \tag{5.10}$$

where k is the number of particles in Alice's reference frame and l is the number of particles in Bob's reference frame. Assuming the reference frame is in a pure state, the joint state of the principle system (Eq. (5.9)) and the reference frame (Eq. (5.10)) can

be written as

$$|\psi\phi\rangle_{AA'BB'} = \sum_n c_n |n,k\rangle_{AA'} |N-n,l\rangle_{BB'}, \tag{5.11}$$

grouping subsystems for Alice and Bob together respectively. All the terms in the superposition in Eq. (5.11) have a different number of particles. Superselection rules require that we make measurements that project on to states with a definite number of particles so only one of the expressions in Eq. (5.11) can correspond to any particular result. This situation is exactly the same as having a mixture of $|n,k\rangle_{AA'} |N-n,l\rangle_{BB'}$, and performing a measurement with probability $|c_n|^2$, here the state is separable and so any quantum like effects can be described using a local hidden variables model and will not violate a Bell inequality.

5.2.3 Reference frame prepared not using SSR-LOCC

Now we look at the case where the reference frame is not prepared via SSR-LOCC and see that this produces a joint state that can violate a Bell inequality. The reference frames that allow a violation have the general form

$$\rho_{A'B'} = \sum_{N'} p_{N'} \rho_{N'}, \tag{5.12}$$

where $p_{N'}$ is the probability that the reference frame has N' particles and $\rho_{N'}$ is any arbitrary mixture of pure states of the form $|\phi\rangle_{A'B'} = \sum_{i=0}^{N'} r_i |i\rangle_{A'} |N'-i\rangle_{B'}$ with N' particles. The reference frame cannot be prepared via SSR-LOCC so must have off-diagonal elements in the particle number basis. These types of state have a non vanishing expectation of

$$\nu = \mathrm{Re}[\mathrm{Tr}(R_+ \otimes R_- \rho_{A'B'})], \tag{5.13}$$

where $R_+ = \sum_{a=0}^{N'-\Delta} |a+\Delta\rangle\langle a|$ and $R_- = \sum_{b=\Delta}^{N'} |b-\Delta\rangle\langle b|$ for some $\Delta \geq 1$. ν can be shown to be non-vanishing as it is proportional to the average value of $\sum_{i=0}^{N'-\Delta} r^*_{i+\Delta} r_i$ over all the pure states $|\phi\rangle_{A'B'}$. If the sum $\sum_{i=0}^{N'-\Delta} r^*_{i+\Delta} r_i$ vanishes then ν will vanish. But the sum can only vanish if the signs of $r^*_{i+\Delta} r_i$ alternate leading to cancellations in the terms, when considering pure states that have coherences in the particle number basis. To get around these cancellations it is possible to choose a larger Δ to avoid some of the terms that cause the cancellations. This argument for a non-vanishing ν also backs up our previous statement that useful reference frames cannot be prepared using SSR-LOCC as if the state is prepared using SSR-LOCC then it will not contain any off-diagonal elements, no matter what Δ is and so $\nu = 0$. Paterek *et al.* then go on to show that all reference frames with $\nu \neq 0$ will allow a choice of measurements that produce a violation of CHSH inequality. To show this they start with an entangled principle system of the form,

$$|\psi\rangle_{AB} = \frac{1}{\sqrt{2}}(|2\rangle_A |2+\Delta\rangle_B + |2+\Delta\rangle_A |2\rangle_B). \tag{5.14}$$

The correlation function, the average of Alice and Bob's local results is,

$$E_\phi(\alpha_k, \beta_l) = -\cos 2\alpha_k \cos 2\beta_l + \nu \sin 2\alpha_k \sin 2\beta_l, \tag{5.15}$$

where ν is defined in Eq. (5.13). See Appendix D for details on how the correlation function is calculated. We can now write the CHSH value as

$$S \equiv E(\alpha_1, \beta_1) + E(\alpha_1, \beta_2) + E(\alpha_2, \beta_1) - E(\alpha_2, \beta_2). \tag{5.16}$$

See Appendix **??** for proof of the CHSH.

To find when $S > 2$ we choose $\alpha_1 = 0, \alpha_2 = \frac{\pi}{4}$ and $\beta \equiv \beta_1 = -\beta_2$.

$$S = -2\cos(2\beta) + 2\nu \sin(2\beta). \tag{5.17}$$

We can think of S in terms of the inner product of two vectors $\vec{w} = (-2, 2\nu)$ and an arbitrary normalised vector $\vec{v} = (\cos(2\beta), \sin(2\beta))$. The scalar product between two vectors is given by

$$\vec{a} \cdot \vec{b} = ||a||||b|| \cos\theta, \tag{5.18}$$

where $||a(b)||$ denotes the length of $a(b)$ and θ is the angle between them [97]. By changing the value of β we can find an angle at which $\vec{w}$ and $\vec{v}$ are parallel. Making the scalar product between them

$$\vec{w} \cdot \vec{v} = ||w||, \tag{5.19}$$

as $\vec{v}$ is a normalised vector and so has length 1. The maximum of S is simply given by the length of $\vec{w}$.

$$S_{max} = \sqrt{(-2)^2 + (2\nu)^2} = 2\sqrt{1 + \nu^2}, \tag{5.20}$$

so to lead to a violation of the CHSH inequality

$$S > 2 \,\forall\, \nu \neq 0, \tag{5.21}$$

proving that any reference state where $\nu \neq 0$, which implies it was not created via SSR-LOCC, allows a violate of the CHSH inequality.

5.2.4 Errors in the system

The aim of this work is to test the tolerance of a system under superselection rule restrictions in the presence of errors. Before we define the system we will test, we describe how Alice and Bob measure their system and how the errors we will include could occur in the physical experiment.

The measurements Alice and Bob perform on their subsystems could be done in the same manner as Chapter 4 by applying a timed laser pulse to the subsystem AA' for

Alice and BB' for Bob to perform active rotations. This laser pulse may cause atoms to tunnel from one of Alice's subsystem to the other. Alice's subsystem spans certain states depending on the number of atoms in the system for example,

$$\begin{aligned} &\text{One particle} \left\{ |1,0\rangle, |0,1\rangle \right\}_{AA'}, \\ &\text{Two particles} \left\{ |2,0\rangle, |1,1\rangle, |0,1\rangle \right\}_{AA'}. \end{aligned} \tag{5.22}$$

The measurement applies a fixed measurement basis coherent rotation to measure in the entangled basis, this is seen as a physical movement of one particle from one site to the other (Fig. 5.3). In the one particle case this can be defined as

$$\begin{aligned} (\alpha |1,0\rangle + \beta |0,1\rangle)_{AA'} &\rightarrow |1,0\rangle_{AA'}, \\ (\beta^* |1,0\rangle - \alpha^* |0,1\rangle)_{AA'} &\rightarrow |0,1\rangle_{AA'}. \end{aligned} \tag{5.23}$$

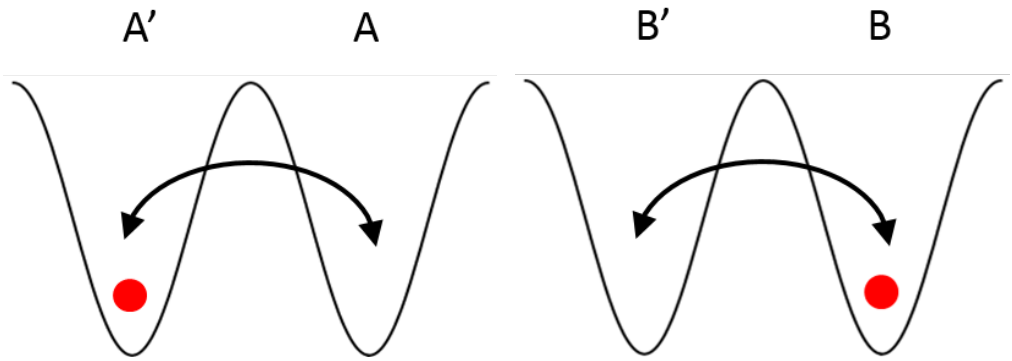

(a) (b)

Figure 5.3: How measurement changes the system

These measurements could be done in a variety of ways, for example by lowering the lattice potential between the two wells will increase the likelihood of the particles tunneling from one site to the other (Fig. 5.4a). The tunneling process is exponential, errors could creep into the system easily. A second way we could envisage the measurement being done is using a Raman transition where a higher energy level is used that is above the well separation (Fig. 5.4). In this case both ω_1 and ω_2 pumps are switched on, this excites the atom to the dummy excited state that is detuned from the actual excited level to ensure the atom does not stay there. Then the atom is pumped by the ω_2 transition down to the ground state in the second well [98].

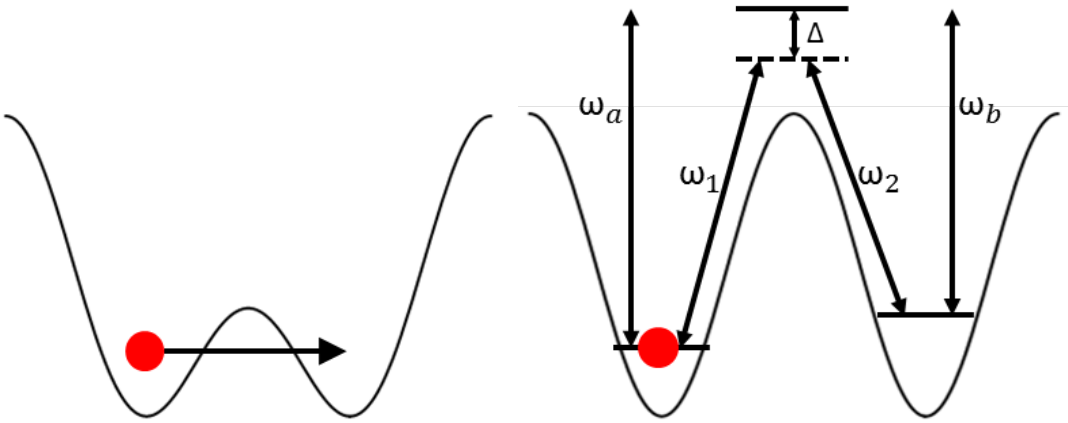

Figure 5.4: Realisation of coherent basis rotations. (a) shows how the barrier between the two wells can be lowered to encourage the likelihood of tunneling between the lattice sites. (b) shows how an intermediate energy level can be used to move an atom from one site to the other where $\omega_a - \omega_b = \omega_1 - \omega_2$ and $\omega_a - \omega_1 = \omega_b - \omega_2 = \Delta$.

The effective operation of either method can be described using the Hamiltonian

$$H = \gamma \frac{\sigma_x}{2}, \tag{5.24}$$

where $\sigma_x = |L\rangle \langle R| + |R\rangle \langle L|$ and γ is the strength of the laser power. This Hamiltonian leads to a rotation of the effective basis of the measurement after particle counting.

In the experiment we are analysing all the noise comes from the electro-optic modulators (EOMs) and is not temporally correlated, though we consider (spatial) correlations between settings on the different sides. The EOMs are used during the measurement to regulate the pulse height and length [99, 100, 101]. Depending where they are placed along the path of the laser beam their effects on Alice and Bob's measurements will be different (Fig. 5.5).

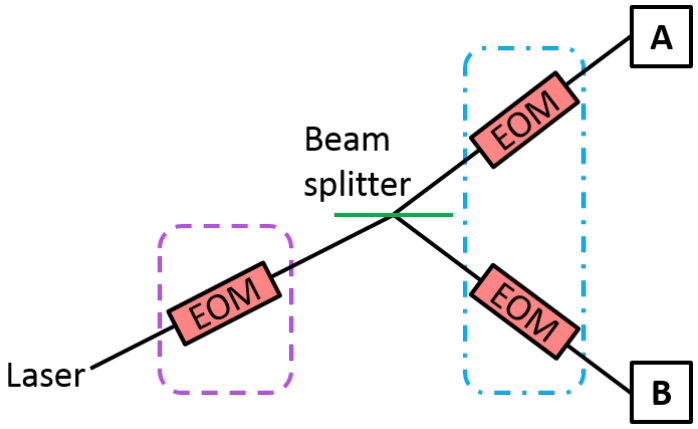

Figure 5.5: Schematic of potential experiment. The first electro-optic modulator (EOM) in the dashed purple box is responsible for all correlated noise as it will affect Alice and Bob's results by the same amount. The second two EOMs in the blue dot-dashed box represent the uncorrelated noise, these two EOMs are independent and so affect Alice and Bob's measurements in different ways.

EOMs use the electro-optic effect to modulate the laser beam. The electro-optic effect is a change the refractive index of a material due to a direct current of low-frequency electric field. By changing the electric field the EOM feels, different phase changes can be achieved [102]. EOMs can also be used to change the measurement basis [101, 103] and control the timing and strength of laser pulses.

The time period for which the EOM is allowed to act will provide a modulation that is characterised by $\tau \propto \gamma t$, if there is some error in the time $t \pm \delta t$, the pulse length will be longer or shorter than expected and the results may not correctly correspond to the measurement. This type of noise is additive as we add or subtract δt to the ideal time period. The additive noise could be uncorrelated or correlated depending on its position in the experiment. If the EOM that is controlling the time period is in the blue dot-dashed box in Fig. 5.5 then the noise is uncorrelated as the EOMs are independent and Alice and Bob could receive different pulse lengths [104]. However if the EOMs controlling the time period are in the purple dashed box in Fig. 5.5 then the noise will be correlated as both Alice and Bob receive the same pulse.

The strength of the laser pulse is characterised by γ and controlled by the EOM, if the strength varies from shot to shot the results may not be accurate [105]. The noise in the strength of the signal is multiplicative as can be seen from Eq. (5.24). Again depending on the position of the EOM the noise is uncorrelated or correlated this is the same as above, in Fig. 5.5 the blue dot-dashed box provides uncorrelated noise and the purple dashed box provides correlated noise.

The joint effects of these two errors can be seen in Fig. 5.6,

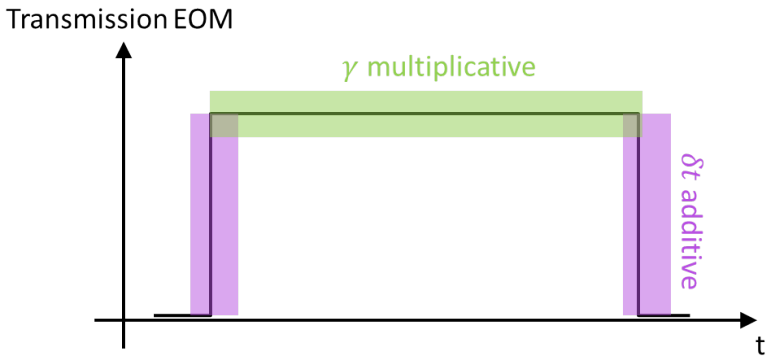

Figure 5.6: Control pulse noise. The results of many runs of the experiment superimposed onto each other, the black line shows the ideal time period and signal strength, the purple areas show the effects of the additive noise from the EOMs in changing the ideal settings and the green areas show the difference in the signal strength due to the multiplicative noise from the EOMs.

5.3 Our system

We know from Paterek *et al.* the form our principle system and reference frame must take to violate a CHSH inequality and the origin of the types of noise that we will include in our analysis.

We consider a specific case of the minimal reference frame from [1] where $\Delta = 1$ and $N' = 1$ and test how the errors affect the CHSH violation. By proper choice of measurement settings we hope to improve this tolerance similar to the process in Chapter 4. Our principal system is defined as,

$$|\psi\rangle_{AB} = \frac{1}{\sqrt{2}}(|2\rangle_A |3\rangle_B + |3\rangle_A |2\rangle_B), \tag{5.25}$$

and the minimal reference frame,

$$|\phi\rangle_{A'B'} = r_0 |0\rangle_{A'} |1\rangle_{B'} + r_1 |1\rangle_{A'} |0\rangle_{B'}, \tag{5.26}$$

where $r_1 r_0^* \neq 0$, ensuring $\nu \neq 0$ meaning the state was not prepared using SSR-LOCC. However before we continue, in Sec. 5.2.1 it was made clear that if entanglement is detected it must be said to come from the principle state and so it is essential that the reference state is separable. Using the PPT criterion for entanglement, Refs. [106, 107] show $|\phi\rangle_{A'B'}$ is entangled for all $r_1 r_0^* \neq 0$ so we need to adapt the reference frame. We could also perform a twirling operation, $\mathcal{T}$, where the twirling operation removes all the coherences that are not compatible with the superselection rules, this operation is explained fully in Sec. 5.5. We now consider a reference frame with at most two

particles as seen in [1],

$$\rho^{'}_{A'B'} = \frac{1}{4}\left(|00\rangle_{A'B'}\langle 00| + |11\rangle_{A'B'}\langle 11|\right) + \frac{1}{4}|\phi\rangle_{A'B'}\langle\phi|, \tag{5.27}$$

we can test that $\rho^{'}_{A'B'}$ is separable using the PPT criterion which says all eigenvalues are positive of the partial transpose of the state if and only if ρ is separable [106, 107]. The partial transpose of $\rho^{'}_{A'B'}$ is as follows

$$\rho^{'T_{B'}}_{A'B'} = \frac{1}{4}(|01\rangle\langle 01| + |00\rangle\langle 11| + |11\rangle\langle 00| + |10\rangle\langle 10|) + \frac{1}{4}|00\rangle\langle 00| + \frac{1}{4}|11\rangle\langle 11|, \tag{5.28}$$

this state has eigenvalues $\frac{1}{2}, \frac{1}{4}, \frac{1}{4}, 0$ meaning that it is separable.

The system we use comprises of the reference frame $\rho^{`}_{A'B'}$, the principal state $|\psi\rangle$ and the measurements defined in Appendix D. Alice's observables look like

$$\begin{aligned}
|\alpha(-1)\rangle &= \cos\alpha\,|1,1\rangle_{AA'} + \sin\alpha\,|2,0\rangle_{AA'} \to +1,\\
|\bar{\alpha}(-1)\rangle &= \sin\alpha\,|1,1\rangle_{AA'} - \cos\alpha\,|2,0\rangle_{AA'} \to -1,\\
|\alpha(0)\rangle &= \cos\alpha\,|3,0\rangle_{AA'} + \sin\alpha\,|2,1\rangle_{AA'} \to +1,\\
|\bar{\alpha}(0)\rangle &= \sin\alpha\,|3,0\rangle_{AA'} - \cos\alpha\,|2,1\rangle_{AA'} \to -1,\\
|\alpha(1)\rangle &= \cos\alpha\,|3,1\rangle_{AA'} + \sin\alpha\,|4,0\rangle_{AA'} \to +1,\\
|\bar{\alpha}(1)\rangle &= \sin\alpha\,|3,1\rangle_{AA'} - \cos\alpha\,|4,0\rangle_{AA'} \to -1,
\end{aligned} \tag{5.29}$$

for Bob's observables, simply swap α for β and AA' for BB'. We assign the eigenvalues ± 1 to the measurement results as shown above. We find the expectation value of one of Alice and Bob's joint measurements to look like

$$\langle\alpha\beta\rangle = -\cos 2\alpha\cos 2\beta + \frac{1}{4}\sin 2\alpha\sin 2\beta, \tag{5.30}$$

where $\nu = \frac{1}{4}$ for $\rho^{'}_{A'B'}$.

Using the trigonometric identities

$$\begin{aligned}
\cos 2\alpha\cos 2\beta &= -\frac{1}{2}(\cos 2(\alpha-\beta) + \cos 2(\alpha+\beta)),\\
\sin 2\alpha\sin 2\beta &= \frac{1}{2}(\cos 2(\alpha-\beta) - \cos 2(\alpha+\beta)),
\end{aligned} \tag{5.31}$$

we can express the expectation value of the joint measurement as a difference of measurement settings which will be more useful for analysis later,

$$\langle\alpha\beta\rangle = -\frac{3}{8}\langle\cos 2(\alpha-\beta)\rangle - \frac{5}{8}\langle\cos 2(\alpha+\beta)\rangle, \tag{5.32}$$

making the whole CHSH value

$$\begin{aligned} S =& \langle\alpha_1\beta_1\rangle + \langle\alpha_1\beta_2\rangle + \langle\alpha_2\beta_1\rangle - \langle\alpha_2\beta_2\rangle \\ =& -\frac{3}{8}\Big(\langle\cos 2(\alpha_1-\beta_1)\rangle + \langle\cos 2(\alpha_1-\beta_2)\rangle + \langle\cos 2(\alpha_2-\beta_1)\rangle - \langle\cos 2(\alpha_2-\beta_2)\rangle\Big) \\ & -\frac{5}{8}\Big(\langle\cos 2(\alpha_1+\beta_1)\rangle + \langle\cos 2(\alpha_1+\beta_2)\rangle + \langle\cos 2(\alpha_2+\beta_1)\rangle - \langle\cos 2(\alpha_2+\beta_2)\rangle\Big). \end{aligned} \tag{5.33}$$

This is the ideal case with no errors in the measurement settings.

We note here that α and β are not real angles, they represent the pulse areas that control the tunneling of atoms from site to site. However analogous to the previous chapter it is useful to consider them as angles in order to visualise the measurement settings and allow us to present them pictorially and in the context of Bell inequalities.

5.4 Optimum measurement settings with additive and multiplicative noise

Experimental imperfection (such as explained in Sec. 5.2.4) can lead to a variation in the actual angles used in the measurement. We model the noise as a random variable, z, with a Gaussian distribution, $\mathcal{N}(\mu, \sigma)$ where μ is the mean of z and σ is the standard deviation. Details of how the expectation value of a random variable is calculated can be seen in Appendix E.

We will calculate S for four different noise models, in each of these we will attempt to increase the tolerance of the system to the noise by changing the measurement settings Alice and Bob use in three stages. The first stage will use an arbitrary set of fixed angles found when the system experiences no noise, this will give a rough idea of how the system performs when we then add noise while modifying our Bell measurements. In the second stage we will set $\alpha_1 = 0$ and optimise the other three measurement settings, this reduces the complexity of the problem but we still hope to improve the tolerance of the system. In the third and final case we optimse over all settings to see if more improvement in the tolerance can be made. At each stage we will review the level of noise that is tolerated to still provide a violation of the CHSH inequality.

5.4.1 Uncorrelated additive noise

As explained in Sec. 5.2.4, uncorrelated additive noise can come from variations in the laser pulse time controlled by the EOM's in the blue dot-dashed box in Fig. 5.5 during the measurement. Eq. (5.32) shows the expectation value of a joint measurement between Alice and Bob, the expressions for the joint measurements follow a normal

distribution and the noise model can be defined as [108]

$$\begin{aligned} 2(\alpha+\beta) &= \mathcal{N}(2(\mu_\alpha + 2\mu_\beta), 2\sqrt{2}\sigma), \\ 2(\alpha-\beta) &= \mathcal{N}(2(\mu_\alpha - \mu_\beta), 2\sqrt{2}\sigma), \end{aligned} \tag{5.34}$$

where μ_x denotes the mean of random variable x and σ is the standard deviation, we assume $\sigma = \sigma_{\alpha_1} = \sigma_{\alpha_2} = \sigma_{\beta_1} = \sigma_{\beta_2}$. Using this we can write the full CHSH value as,

$$\begin{aligned} S = \exp(-4\sigma^2)\Big[&-\frac{3}{8}(\cos 2(\mu_{\alpha_1} - \mu_{\beta_1}) + \cos 2(\mu_{\alpha_1} - \mu_{\beta_2}) \\ &+ \cos 2(\mu_{\alpha_2} - \mu_{\beta_1}) - \cos 2(\mu_{\alpha_2} - \mu_{\beta_2})) \\ &- \frac{5}{8}(\cos 2(\mu_{\alpha_1} + \mu_{\beta_1}) + \cos 2(\mu_{\alpha_1} + \mu_{\beta_2}) \\ &+ \cos 2(\mu_{\alpha_2} + \mu_{\beta_1}) - \cos 2(\mu_{\alpha_2} + \mu_{\beta_2}))\Big]. \end{aligned} \tag{5.35}$$

We begin by using arbitrary fixed optimum angles found when the system has no noise.

5.4.1.1 Fixed angles

As explained in the introduction to this section we use an arbitrary set of angles that produce the maximum S value, $S = 2.0616$, when the system has no noise. These angles are not a unique set, many other sets of angles would produce the same result when the system has no noise, we pick this set at random. The angles we choose are shown in Fig. 5.7,

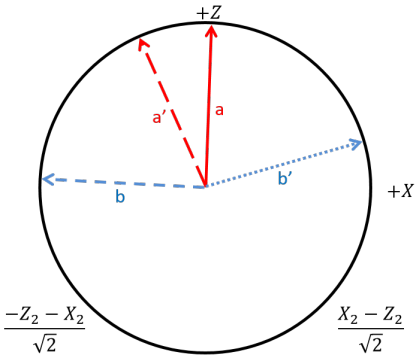

Figure 5.7: Uncorrelated additive noise, arbitrary set of measurement settings, optimised with no noise. $\alpha_1 = 0.0274$, $\alpha_2 = 5.86$, $\beta_1 = 4.76$ and $\beta_2 = 1.30$.

σ_{crit} is the largest error that will allow a violation of the CHSH inequality. By using the angles in Fig. 5.7 over the range of σ we find $\sigma_{1.1}^{crit} = 0.0870$ as shown in Fig. 5.8, we label the σ^{crit} in each optimisation case to match the heading number for clarity.

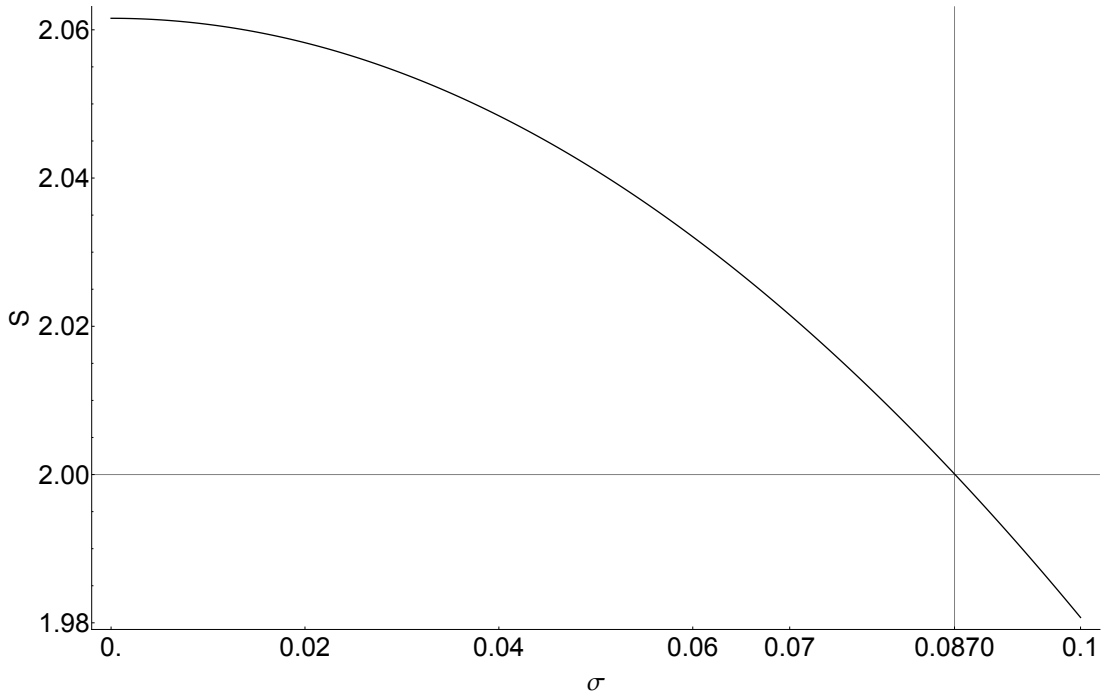

Figure 5.8: Uncorrelated additive noise with fixed angles. Keeping the measurement angles fixed for all σ, the S value steadily decreases and the critical value, $\sigma_{1.1}^{crit} = 0.0870$.

To attempt to increase the limit, σ^{crit}, at which the system ceases to violate the CHSH inequality we will optimise the measurement settings that Alice and Bob use.

5.4.1.2 Optimising measurement settings keeping $\alpha_1 = 0$

By fixing $\alpha_1 = 0$ and optimising α_2, β_1 and β_2 we aim to increase σ^{crit} to show that the system could withstand a larger error and still allow detection of a violation of the CHSH inequality. We expect the angles for each value of σ to be slightly different but restrict them all to be positive in keeping with the interpretation of the pulse areas we use to define them.

However, this optimisation process produces no noticeable increase in the tolerance. We find $\sigma_{1.2}^{crit} = \sigma_{1.1}^{crit} = 0.0870$ to be the limit at which the system is no longer able to violate the CHSH inequality so the graph perfectly matches that seen in Fig. 5.8. The measurement settings at the limit, $\sigma_{1.2}^{crit} = 0.0870$, are shown in Fig. 5.9.

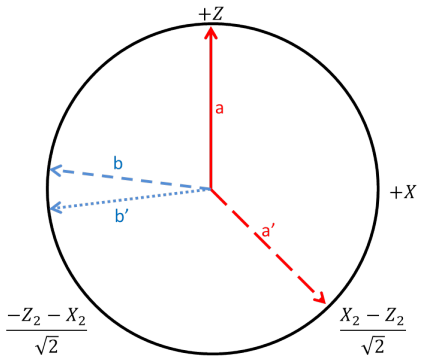

Figure 5.9: Uncorrelated additive noise, optimum measurement settings keeping $\alpha_1 = 0$ when $\sigma_{1.2}^{crit} = 0.870$, $\alpha_2 = 2.36, \beta_1 = 4.83, \beta_2 = 4.59$.

5.4.1.3 Optimising over all angles

We now optimise over all the angles to see if this provides an increase in the tolerance of the system. But in doing so we find no improvement and the results again match the graph in Fig. 5.8, $\sigma_{1.3}^{crit} = \sigma_{1.2}^{crit} = \sigma_{1.1}^{crit} = 0.0870$. Again the measurement settings are different at the limit, $\sigma_{1.3}^{crit} = 0.0870$, and are shown in Fig. 5.10.

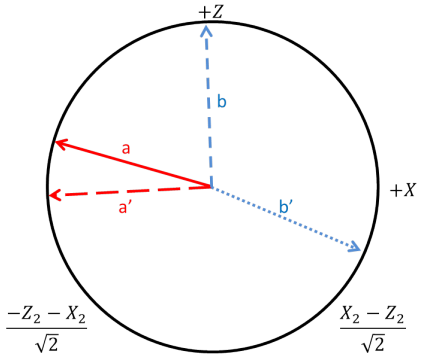

Figure 5.10: Uncorrelated additive noise, optimum measurement settings optimising over all angles when $\sigma_{1.3}^{crit} = 0.870$, $\alpha_1 = 4.99, \alpha_2 = 4.66, \beta_1 = 6.25, \beta_2 = 1.98$.

5.4.1.4 Discussion

We have not been able to find any improvement in the limit of σ^{crit} that produces a violation of the CHSH inequality as we can see in Fig. 5.11.

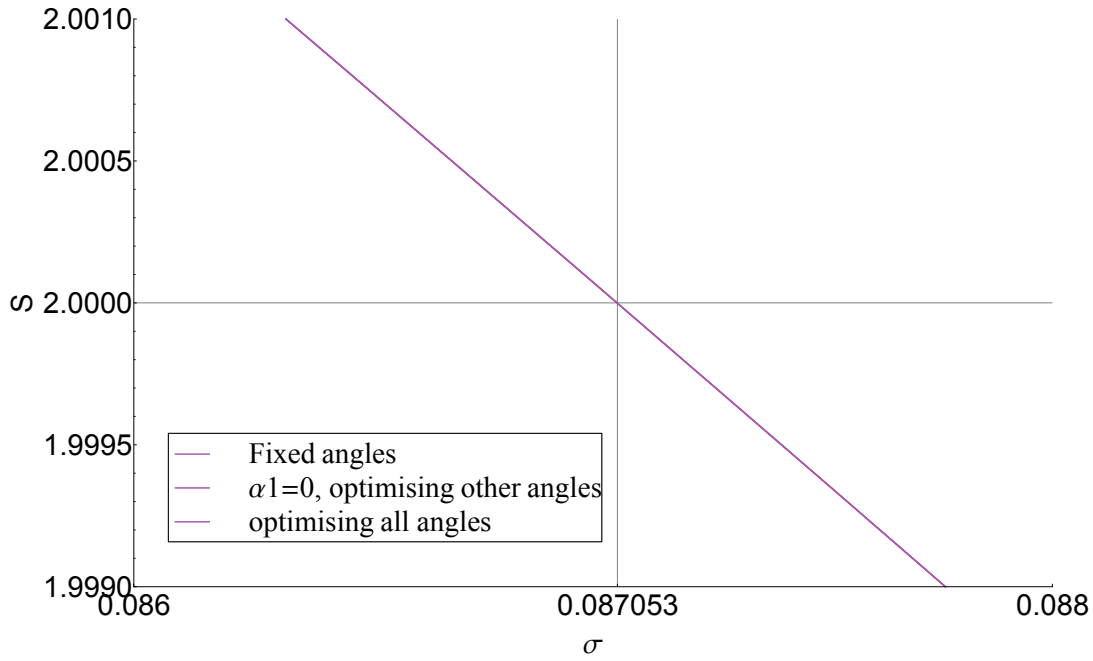

Figure 5.11: Uncorrelated additive noise comparison between the optimisation processes. It is clear to see no improvement in the tolerance but we have found different sets of measurement settings that produce the same results.

For uncorrelated additive noise each set of optimised meaurement settings at each stage give the same $\sigma_{1.3}^{crit} = \sigma_{1.2}^{crit} = \sigma_{1.1}^{crit} = \sigma^{crit}$. We can understand this by studying the expression for S,

$$S = \exp(-4\sigma^2)\Big[-\frac{3}{8}\Big(\cos 2(\alpha_1 - \beta_1) + \cos 2(\alpha_1 - \beta_2) + \cos 2(\alpha_2 - \beta_1) - \cos 2(\alpha_2 - \beta_2)\Big), \\ -\frac{5}{8}\Big(\cos 2(\alpha_1 + \beta_1) + \cos 2(\alpha_1 + \beta_2) + \cos 2(\alpha_2 + \beta_1) - \cos 2(\alpha_2 + \beta_2)\Big)\Big]. \tag{5.36}$$

The noise affects all the terms in the expression, so once we have found the maximum value for the expression in the square brackets we cannot do better as all the measurement settings are suppressed equally by the noise.

In each of the optimisation stages the measurement settings change very slightly as σ is increased, but we are only considering the measurement settings to three significant figures, to this accuracy the measurement settings remain the same throughout the range of σ. This means that it is not important to know what σ is as using any of the optimum set of measurement settings we have found will produce the same results regardless of σ.

5.4.2 Correlated additive noise

As explained in Sec. 5.2.4 correlated additive noise can arise from fluctuations in the length of the laser pulse, this comes from the first EOM in the purple dashed box in

Fig. 5.5. The expectation value of a joint measurement between Alice and Bob is shown in Eq. (5.32). The measurement noises here are correlated meaning β can be written in terms of α, the normal distributions follow

$$\begin{aligned} \alpha &= \mathcal{N}(\mu_\alpha, \sigma_\alpha), \\ \beta &= \mathcal{N}(\mu_\beta + (\alpha - \mu_\alpha), \sigma_\beta), \end{aligned} \tag{5.37}$$

where μ_x is the mean of the random variable x and σ is the standard deviation. We are interested in the addition and subtraction of these angles for the expectation value, they follow,

$$\begin{aligned} 2(\alpha - \beta) &= \mathcal{N}(2(\mu_\alpha - \mu_\beta), 2(\sigma_\alpha - \sigma_\beta)), \\ 2(\alpha + \beta) &= \mathcal{N}(2(\mu_\alpha + \mu_\beta), 2(\sigma_\alpha + \sigma_\beta)). \end{aligned} \tag{5.38}$$

We assume perfect noise correlation. This represents an extreme case and the actual correlation may be less. But this assumption allows us to observe any effects more clearly, $\sigma = \sigma_\alpha = \sigma_\beta$ so

$$\begin{aligned} 2(\alpha - \beta) &= \mathcal{N}(2(\mu_\alpha - \mu_\beta), 0), \\ 2(\alpha + \beta) &= \mathcal{N}(2(\mu_\alpha + \mu_\beta), 4\sigma). \end{aligned} \tag{5.39}$$

Using these definitions we construct the whole CHSH value for correlated additive noise

$$\begin{aligned} S =& \langle \alpha_1 \beta_1 \rangle + \langle \alpha_1 \beta_2 \rangle + \langle \alpha_2 \beta_1 \rangle - \langle \alpha_2 \beta_2 \rangle \\ =& -\frac{3}{8}\Big[\cos 2(\mu_{\alpha_1} - \mu_{\beta_1}) + \cos 2(\mu_{\alpha_1} - \mu_{\beta_2}) \\ &+ \cos 2(\mu_{\alpha_2} - \mu_{\beta_1}) - \cos 2(\mu_{\alpha_2} - \mu_{\beta_2}) \Big] \\ &- \frac{5}{8}\exp(-8\sigma^2)\Big[\cos 2(\mu_{\alpha_1} + \mu_{\beta_1}) + \cos 2(\mu_{\alpha_1} + \mu_{\beta_2}) \\ &+ \cos 2(\mu_{\alpha_2} + \mu_{\beta_1}) - \cos 2(\mu_{\alpha_2} + \mu_{\beta_2}) \Big]. \end{aligned} \tag{5.40}$$

Now we have an expression for S we can start to look at the tolerance of the system

5.4.2.1 Fixed angles

We use the same arbitrary set of fixed angles as in the uncorrelated additive section (Fig. 5.7) because in the case of no noise, $\sigma = 0$, the two expressions for S with uncorrelated and correlated additive noise are the same. Using these fixed angles and varying σ the greatest error the system can experience whilst still violating the CHSH inequality is $\sigma_{2.1}^{crit} = 0.0719$ as shown in Fig. 5.12

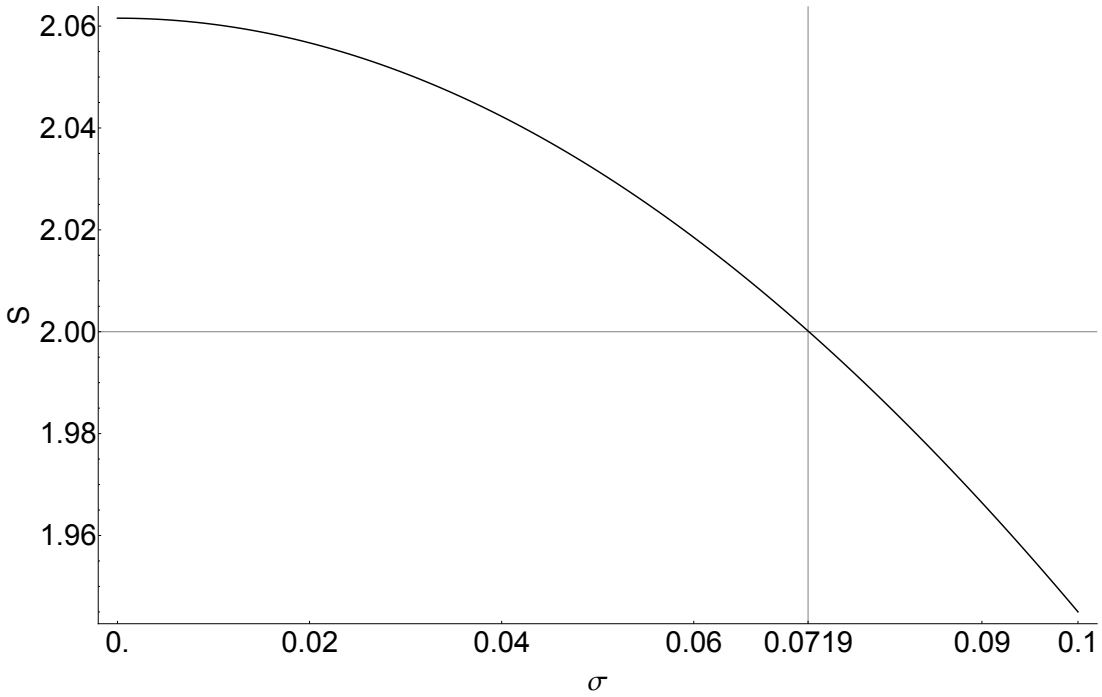

Figure 5.12: Correlated additive noise with fixed angles. Keeping the measurement angles fixed for all σ the S value steadily decreases. The critical value, $\sigma_{1.2}^{crit} = 0.0719$.

In an attempt to improve this tolerance we proceed to the second stage.

5.4.2.2 Optimising angles keeping $\alpha_1 = 0$

As we did in the uncorrelated additive noise process we fix $\alpha_1 = 0$ and optimise α_2, β_1 and β_2 for each value of σ, again we expect the angles to be positive and different depending on the value of σ.

This optimisation produces a very slight improvement on the tolerance taking it up to $\sigma_{2.2}^{crit} = 0.0721$ as shown in Fig. 5.13.

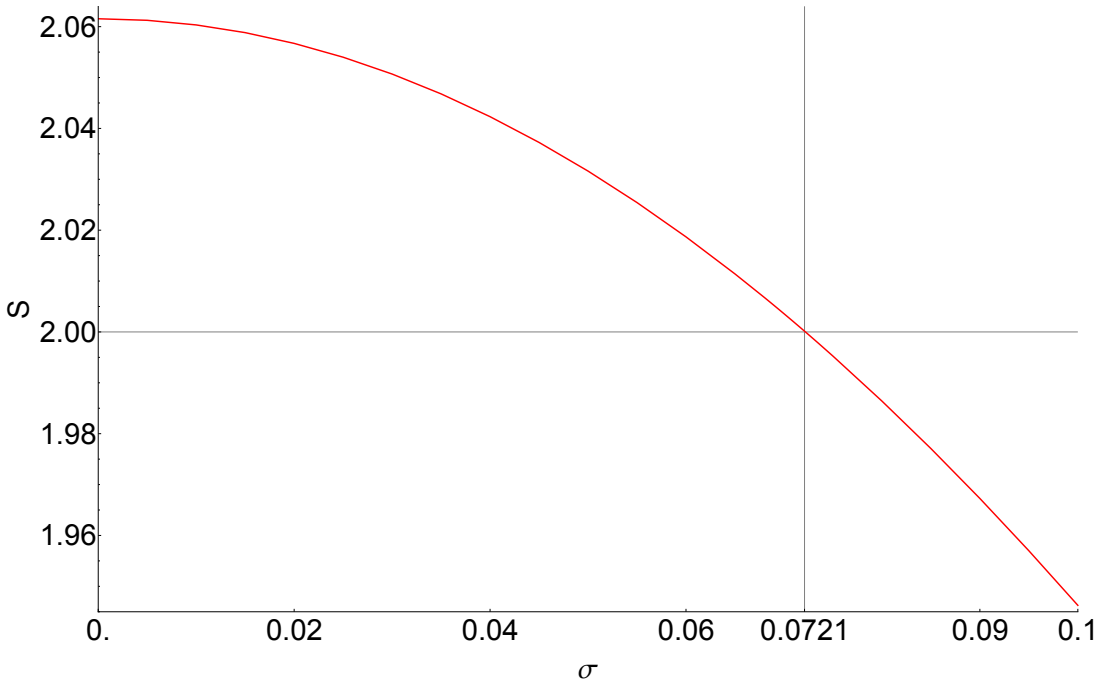

Figure 5.13: Correlated additive noise with $\alpha_1 = 0$ and optimising over the other angles. Fixing $\alpha_1 = 0$ and optimising the other measurement angles for each value of σ we find $\sigma_{1.2}^{crit} = 0.0721$ a slight increase from the fixed angles.

The measurement settings at the limit $\sigma_{2.2}^{crit} = 0.0721$ are shown in Fig. 5.14.

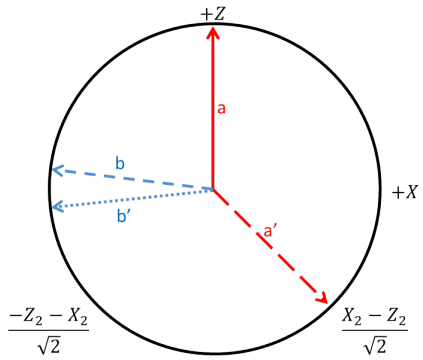

Figure 5.14: Correlated additive noise, optimum measurement settings keeping $\alpha_1 = 0$ when $\sigma_{2.2}^{crit} = 0.0721$, $\alpha_1 = 0$, $\alpha_2 = 2.36$, $\beta_1 = 4.83$, $\beta_2 = 4.60$

To try to push this tolerance even further we now optimise over all the angles.

5.4.2.3 Optimisation over all angles

Optimising over all angles produces the same graph as we found in the previous subsection (Fig. 5.13), where the tolerance is $\sigma_{2.3}^{crit} = \sigma_{2.2}^{crit} = 0.0721$. But again the measurement angles at the limit are different and are shown in Fig. 5.15.

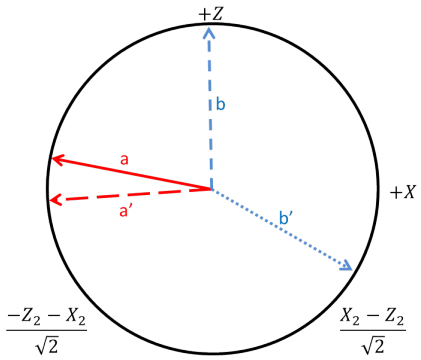

Figure 5.15: Optimum measurement settings optimising over all angles when $\sigma_{2.3}^{crit} = 0.0721, \alpha_1 = 4.91$, $\alpha_2 = 4.65$, $\beta_1 = 6.27$, $\beta_2 = 2.10$.

5.4.2.4 Discussion

Although we have found a very slight improvement we do not think that it is significant we will show why later, however, it is important to understand how this improvement occurs. The graph in Fig. 5.16 indicates a value of $\sigma = 0.0720$ that does not produce a violation in the unoptimised case but in both optimised cases does, to understand why this difference is possible we look at the expression for S. When $\sigma = 0.0720$ using Eq. (5.40) in the unoptimised case,

$$S = 0.546 + 1.52\exp(-8\sigma^2), \tag{5.41}$$

and in both the optimised cases,

$$S = 0.562 + 1.50\exp(-8\sigma^2). \tag{5.42}$$

The reason we are able to improve upon the results is due to the noise only acting on one part of the expressions for S. The optimised cases have found a set of angles that increase the expression that is not affected by the noise but also decrease the expression that is suppressed by the noise, thus leading to an improved S value compared to the unoptimised settings.

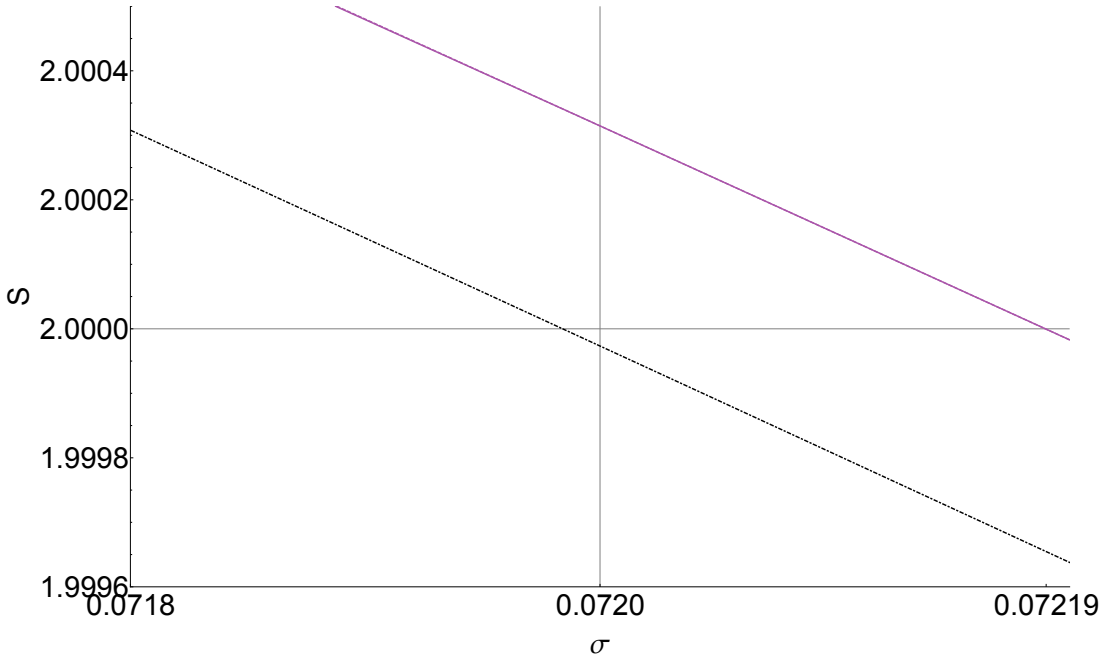

Figure 5.16: Example of a value of σ that produces a violation in the optimised cases but not when the angles are fixed. The black dot-dashed line shows the arbitrary fixed angle case (Sec. 5.4.2.1). The purple solid line shows the two optimisation processes, fixing $\alpha_1 = 0$ (Sec. 5.4.2.2) and optimising over all angles (Sec. 5.4.2.3), these produce the same results and so cannot be distinguished from one another.

As we have stated, we do not believe that the difference in the S value in the unoptimised versus the optimised cases is significant. To test this we use the fully optimised measurement settings (Sec. 5.4.2.3) when $\sigma = 0.035$ as fixed angles and calculate S over the range of σ and compare these to the S values in the unoptimised case (Fig. 5.17). We pick these measurement settings because the optimised measurement settings for each σ change slightly over the range of σ and $\sigma = 0.035$ lies roughly in the middle of the violating range so we take these to be an "average".

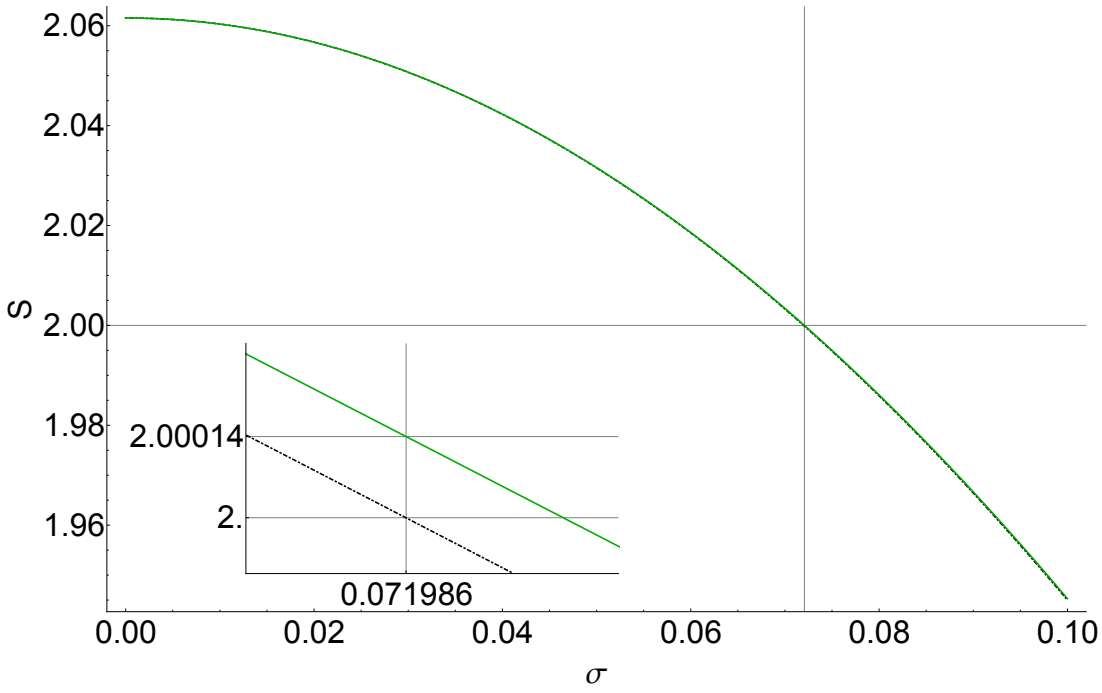

Figure 5.17: Comparing two sets of fixed angles over the range of σ. The black dot-dashed line shows the arbitrary fixed angle case (Sec. 5.4.2.1) and the green solid line is created using the fixed angles found when $\sigma = 0.035$ in the fully optimised case (Sec. 5.4.2.3). The inset shows a highly magnified image of the point at which both sets of angles cease to violation the CHSH inequality.

As we can see from Fig. 5.17 using the arbitrary fixed angles at $\sigma = 0.071986$ the S value is 2 whereas if when we use an optimised set of fixed angles found when $\sigma = 0.035$, $S = 2.00014$ which is an improvement but this is only a 0.014% increase and so we do not consider it to be significant. This means that similar to the uncorrelated additive case, the actual value of σ in the experiment is not so significant, any of the sets of fixed optimised angles will give roughly the same S values.

5.4.3 Uncorrelated multiplicative noise

Uncorrelated multiplicative noise could come from variations in the pulse heights from the secondary EOMs in the blue box in Fig. 5.5. It is uncorrelated as the EOMs are independent. The measurement settings follow these normal distributions,

$$\begin{aligned} \alpha =& \mathcal{N}(\mu_\alpha, f\mu_\alpha), \\ \beta =& \mathcal{N}(\mu_\beta, f\mu_\beta), \end{aligned} \tag{5.43}$$

where f is the multiplicative noise factor. We are interested in the expectation values of joint measurements Alice and Bob perform on their subsystems (Eq. (5.32)), the

normal distribution of the additions and subtractions of α and β are as follows

$$\begin{aligned} 2(\alpha+\beta) &= \mathcal{N}\left(2(\mu_\alpha+\mu_\beta), 2f\sqrt{(\mu_\alpha)^2+(\mu_\beta)^2}\right), \\ 2(\alpha-\beta) &= \mathcal{N}\left(2(\mu_\alpha-\mu_\beta), 2f\sqrt{(\mu_\alpha)^2+(\mu_\beta)^2}\right), \end{aligned} \tag{5.44}$$

making the full CHSH value look like,

$$\begin{aligned} S =& \langle\alpha_1\beta_1\rangle + \langle\alpha_1\beta_2\rangle + \langle\alpha_2\beta_1\rangle - \langle\alpha_2\beta_2\rangle \\ =& -\frac{3}{8}\Big[\exp(-2f^2(\mu_{\alpha_1}^2+\mu_{\beta_1}^2))\cos 2(\mu_{\alpha_1}-\mu_{\beta_1}) + \exp(-2f^2(\mu_{\alpha_1}^2+\mu_{\beta_2}^2))\cos 2(\mu_{\alpha_1}-\mu_{\beta_2}) \\ &+ \exp(-2f^2(\mu_{\alpha_2}^2+\mu_{\beta_1}^2))\cos 2(\mu_{\alpha_2}-\mu_{\beta_1}) - \exp(-2f^2(\mu_{\alpha_2}^2+\mu_{\beta_2}^2))\cos 2(\mu_{\alpha_2}-\mu_{\beta_2})\Big] \\ &-\frac{5}{8}\Big[\exp(-2f^2(\mu_{\alpha_1}^2+\mu_{\beta_1}^2))\cos 2(\mu_{\alpha_1}+\mu_{\beta_1}) + \exp(-2f^2(\mu_{\alpha_1}^2+\mu_{\beta_2}^2))\cos 2(\mu_{\alpha_1}+\mu_{\beta_2}) \\ &+ \exp(-2f^2(\mu_{\alpha_2}^2+\mu_{\beta_1}^2))\cos 2(\mu_{\alpha_2}+\mu_{\beta_1}) - \exp(-2f^2(\mu_{\alpha_2}^2+\mu_{\beta_2}^2))\cos 2(\mu_{\alpha_2}+\mu_{\beta_2})\Big]. \end{aligned} \tag{5.45}$$

We begin by finding fixed angles that maximise this expression with no noise.

5.4.3.1 Fixed angles

The arbitrary set of angles we have chosen that maximise the expression with no noise are shown in Fig. 5.18.

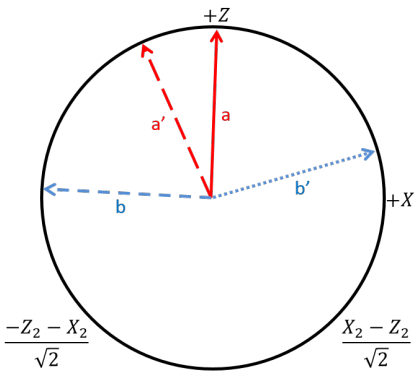

Figure 5.18: Uncorrelated multiplicative noise, arbitrary set of measurement settings, optimised with no noise. $\alpha_1 = 0.0274, \alpha_2 = 5.86, \beta_1 = 4.76, \beta_2 = 1.30$.

Again these measurement settings are not unique and we have picked these particular ones at random. Fixing these angles and varying over f the tolerance of the uncorrelated system is $f_{3.1}^{crit} = 0.0200$ as shown in the black dot-dashed line in Fig. 5.21.

We start our optimisation process again by fixing $\alpha_1 = 0$ and varying the other angles to attempt to increase the tolerance of the system.

5.4.3.2 Optimising angles keeping $\alpha_1 = 0$

By fixing $\alpha_1 = 0$ and varying the other angles for each value of f we find an improvement in the critical value of S where the system will still provide a violation of the CHSH inequality, $f_{3.2}^{crit} = 0.0739$ as shown in the red dashed line in Fig. 5.21.

The optimum measurement settings at this limit, $f_{3.2}^{crit} = 0.0739$, are shown in Fig. 5.19.

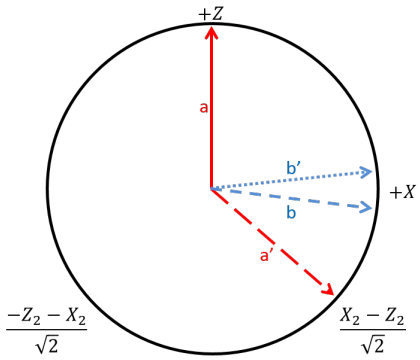

Figure 5.19: Uncorrelated multiplicative noise, optimum measurement settings keeping $\alpha_1 = 0$ when $f_{3.2}^{crit} = 0.0739, \alpha_2 = 2.28, \beta_1 = 1.69, \beta_2 = 1.46$.

We now perform the final optimisation where we vary all angles over the range of f.

5.4.3.3 Optimising over all angles

By optimising all the angles over the range of f we find the tolerance of the system can be improved up to $f_{3.3}^{crit} = 0.190$ as shown in the blue solid line in Fig. 5.21 which is a very good improvement.

The optimum measurement settings at this limit, $f_{3.3}^{crit} = 0.190$, are shown in Fig. 5.20.

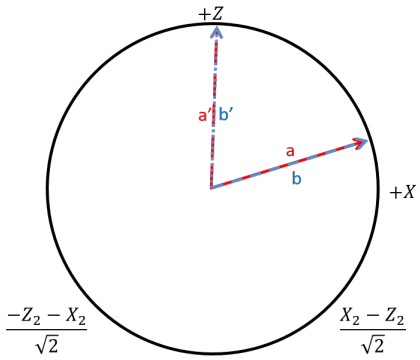

Figure 5.20: Uncorrelated multiplicative noise, optimum measurement settings optimising over all angle when $f_{3.3}^{crit} = 0.190$, $\alpha_1 = 1.28, \alpha_2 = 0.0298, \beta_1 = 1.28, \beta_2 = 0.0298$.

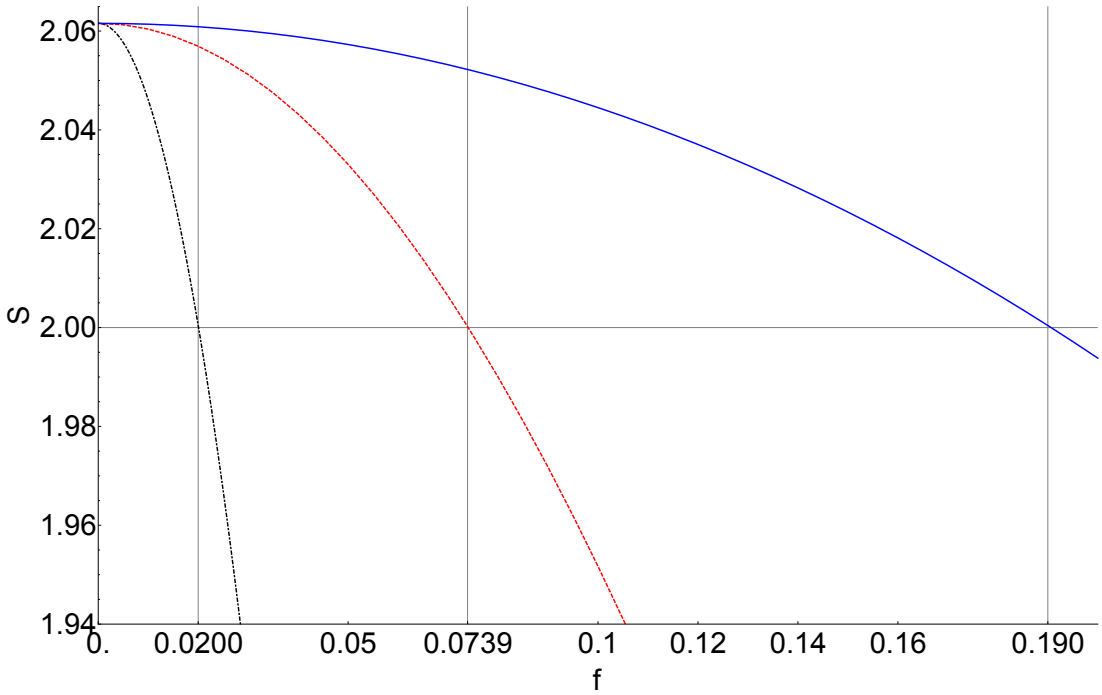

Figure 5.21: Uncorrelated multiplicative noise. By optimising the measurement settings large improvements in the tolerance of the system f^{crit} can be made. The black dot-dashed line represents the fixed angle case where $f_{3.1}^{crit} = 0.200$ (Sec. 5.4.3.1). The red dashed represents the case where $\alpha_1 = 0$ and the other angles are optimised, $f_{3.2}^{crit} = 0.739$ (Sec. 5.4.3.2). The blue solid line shows the fully optimised case where $f_{3.3}^{crit} = 0.190$ (Sec. 5.4.3.3).

See Appendix F for the full range of each of the individual graphs.

5.4.3.4 Discussion

Vast improvements can be made to the tolerance of the system, up to 19%, just by changing the measurement settings Alice and Bob use.

The expression for S in the uncorrelated multiplicative case is much more complicated than the previous additive cases but we can still understand why we are able to find these improvements by looking at the construction. Writing S in a slightly different way we see

$$\begin{aligned} S = &\exp(-2f^2(\mu_{\alpha_1}^2+\mu_{\beta_1}^2))\Big[-\frac{3}{8}\cos 2(\mu_{\alpha_1}-\mu_{\beta_1})-\frac{5}{8}\cos 2(\mu_{\alpha_1}+\mu_{\beta_1})\Big] \\ &+\exp(-2f^2(\mu_{\alpha_1}^2+\mu_{\beta_2}^2))\Big[-\frac{3}{8}\cos 2(\mu_{\alpha_1}-\mu_{\beta_2})-\frac{5}{8}\cos 2(\mu_{\alpha_1}+\mu_{\beta_2})\Big] \\ &+\exp(-2f^2(\mu_{\alpha_2}^2+\mu_{\beta_1}^2))\Big[-\frac{3}{8}\cos 2(\mu_{\alpha_2}-\mu_{\beta_1})-\frac{5}{8}\cos 2(\mu_{\alpha_2}+\mu_{\beta_1})\Big] \\ &+\exp(-2f^2(\mu_{\alpha_2}^2+\mu_{\beta_2}^2))\Big[\frac{3}{8}\cos 2(\mu_{\alpha_2}-\mu_{\beta_2})+\frac{5}{8}\cos 2(\mu_{\alpha_2}+\mu_{\beta_2})\Big]. \end{aligned} \tag{5.46}$$

By choosing the case where $f = 0.18$ as this produces a violation for the fully optimised case but not for the other cases (Fig. 5.22) we look at the numerical expressions for S in the three cases.

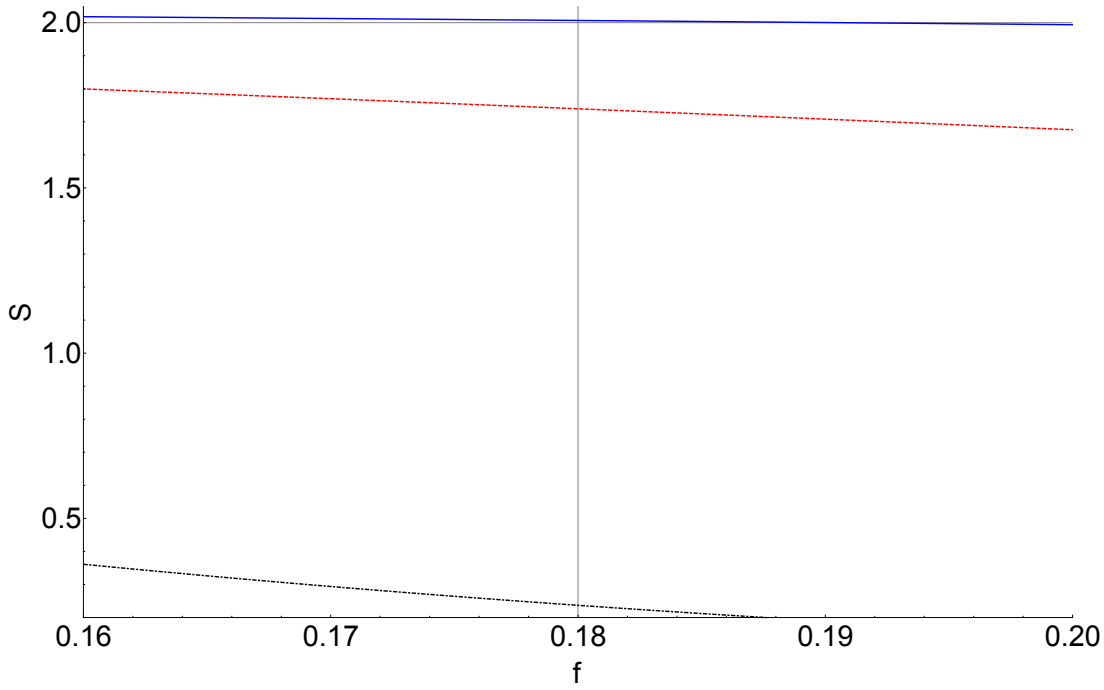

Figure 5.22: Uncorrelated multiplicative noise, example of a value of f that leads to a violation in the fully optimised case but not in the others. The black dot-dashed line shows the optimum values of S found using an arbitrary set of angles (Sec. 5.4.3.1). The red dashed line shows the optimum values of S found when optimising the angles, fixing $\alpha_1 = 0$ (Sec. 5.4.3.2). The blue solid line shows the optimum values of S found optimising over all the angles (Sec. 5.4.3.3).

Using the optimum measurement angles found when $f = 0.180$, in the non-optimised case

$$\begin{aligned} S = &\exp(-133f^2)\Big[0.384\Big] \\ &+ \exp(-81.7f^2)\Big[0.985\Big] \\ &+ \exp(-104f^2)\Big[-0.247\Big] \\ &+ \exp(-52.7f^2)\Big[-0.940\Big], \end{aligned} \tag{5.47}$$

in the partially optimised case

$$\begin{aligned} S = &\exp(-5.29f^2)\Big[0.994\Big] \\ &+ \exp(-4.21f^2)\Big[0.972\Big] \\ &- \exp(-15.1f^2)\Big[-0.247\Big] \\ &+ \exp(-14.0f^2)\Big[-0.324\Big], \end{aligned} \tag{5.48}$$

and in the fully optimised case

$$\begin{aligned} S = &- \exp(-6.49f^2)\Big[-0.609\Big] \\ &+ \exp(-3.25f^2)\Big[0.836\Big] \\ &+ \exp(-3.25f^2)\Big[0.836\Big] \\ &+ \exp(-0.0037f^2)\Big[0.995\Big]. \end{aligned} \tag{5.49}$$

Each of the four parts of the expression, which represent the four expectation values, are affected by a different factor of the noise. By changing the measurement angles a balance can be found producing the maximum value of S. This is why we are able to increase the tolerance of the system by such a large degree by simply changing the measurement angles. This change can be seen by looking at the values in the exponentials, in the unoptimised case the numbers are very large and in each of the following optimisation processes these are significantly reduced.

It is an unexpected result that when optimising over all angles the optimum measurement angles are the same. One way to test to see if this result is valid is to use these optimum angles in a standard CHSH inequality test with no errors. If this provides a violation of the CHSH inequality then we can be sure that the result is correct even if it is surprising, however if there is no violation then there would appear to be something strange going on that would require further investigation.

Unfortunately when we performed this test we found that there was no violation in the standard CHSH inequality test with no errors. There was however a violation when using these errors in the CHSH inequality defined by the expectation values of Cosine defined in Appendix **??** suggesting these are not equivalent. Investigation into these differences in left for further work.

5.4.4 Correlated multiplicative noise

Correlated multiplicative noise can arise from variations in the pulse height of the first EOM in the purple box in Fig. 5.5, it is correlated as Alice and Bob both feel the same effect of the noise.

As α and β are correlated we can write β in terms of α

$$\beta = \mu_\beta + (\alpha - \mu_\alpha)\frac{\mu_\beta}{\mu_\alpha}, \tag{5.50}$$

and the additions and subtractions of the measurement settings in Eq. (5.32) follow the normal distributions

$$\begin{aligned} 2(\alpha+\beta) &= 2\alpha(1+\frac{\mu_\beta}{\mu_\alpha}) = \mathcal{N}(2(\mu_\alpha+\mu_\beta), 2f(\mu_\alpha+\mu_\beta)), \\ 2(\alpha-\beta) &= 2\alpha(1-\frac{\mu_\beta}{\mu_\alpha}) = \mathcal{N}(2(\mu_\alpha-\mu_\beta), 2f(\mu_\alpha-\mu_\beta))), \end{aligned} \tag{5.51}$$

using these distributions the full CHSH value can be written as

$$\begin{aligned}
S &= \langle\alpha_1\beta_1\rangle + \langle\alpha_1\beta_2\rangle + \langle\alpha_2\beta_1\rangle - \langle\alpha_2\beta_2\rangle \\
&= -\frac{3}{8}\Big[\exp(-2(f(\mu_{\alpha_1}-\mu_{\beta_1}))^2)\cos 2(\mu_{\alpha_1}-\mu_{\beta_1}) \\
&\quad + \exp(-2(f(\mu_{\alpha_1}-\mu_{\beta_2}))^2)\cos 2(\mu_{\alpha_1}-\mu_{\beta_2}) \\
&\quad + \exp(-2(f(\mu_{\alpha_2}-\mu_{\beta_1}))^2)\cos 2(\mu_{\alpha_2}-\mu_{\beta_1}) \\
&\quad - \exp(-2(f(\mu_{\alpha_2}-\mu_{\beta_2}))^2)\cos 2(\mu_{\alpha_2}-\mu_{\beta_2})\Big] \\
&\quad -\frac{5}{8}\Big[\exp(-2(f(\mu_{\alpha_1}+\mu_{\beta_1}))^2)\cos 2(\mu_{\alpha_1}+\mu_{\beta_1}) \\
&\quad + \exp(-2(f(\mu_{\alpha_1}+\mu_{\beta_2}))^2)\cos 2(\mu_{\alpha_1}+\mu_{\beta_2}) \\
&\quad + \exp(-2(f(\mu_{\alpha_2}+\mu_{\beta_1}))^2)\cos 2(\mu_{\alpha_2}+\mu_{\beta_1}) \\
&\quad - \exp(-2(f(\mu_{\alpha_2}+\mu_{\beta_2}))^2)\cos 2(\mu_{\alpha_2}+\mu_{\beta_2})\Big].
\end{aligned} \tag{5.52}$$

Using this expression we begin the optimisation process by using arbitrary fixed angles for the system found when the system has no noise.

5.4.4.1 Fixed angles

The arbitrary set of angles we are using that optimise the system with no noise are shown in Fig. 5.23.

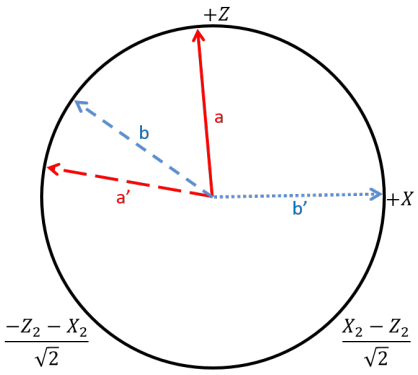

Figure 5.23: Correlated multiplicative noise, arbitrary set of optimum measurement settings with no noise. $\alpha_1 = 6.20$, $\alpha_2 = 4.89$, $\beta_1 = 5.32$, $\beta_2 = 1.56$.

As before, these angles are not unique and we pick them at random. Using these fixed angles over the full range of f we find the maximum tolerance of the system is $f_{4.1}^{crit} = 0.0165$ as shown in the black dot-dashed line in Fig. 5.26. This figure is very low so we move on to the second optimisation process in the hope of increasing it

5.4.4.2 Optimising angles keeping $\alpha_1 = 0$

Here we fix $\alpha_1 = 0$ to reduce the complexity of the problem, expecting the optimum angles for each value of f to differ. This optimisation does increase the tolerance in the

system up to $f_{4.2}^{crit} = 0.0720$ as seen in the red dashed line in Fig. 5.26, which is a big increase from using the fixed angles.

The optimum angles at the limit, $f_{4.2}^{crit} = 0.0720$, are shown in Fig. 5.24.

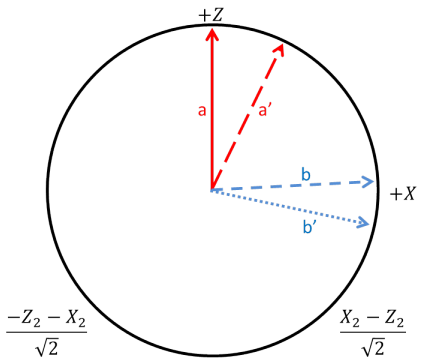

Figure 5.24: Correlated multiplicative noise, optimum measurement settings keeping $\alpha_1 = 0$ when $f_{4.2}^{crit} = 0.0720$, $\alpha_2 = 0.455$, $\beta_1 = 1.751$, $\beta_2 = 1.78$.

To try to push this tolerance further we optimise over all of the angles.

5.4.4.3 Optimising over all angles

Optimising over all the angles makes a huge impact on the tolerance of the system, we are able to find angles which push the tolerance up to $f_{4.3}^{crit} = 0.182$ as seen in Fig. 5.26.

Here the optimum angles at the limit, $f_{4.3}^{crit} = 0.182$, are shown in Fig. 5.25.

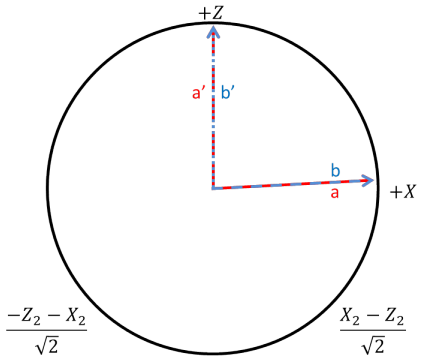

Figure 5.25: Correlated multiplicative noise, optimum measurement settings optimising over all angles when $f_{4.3}^{crit} = 0.182$, $\alpha_1 = 1.52$, $\alpha_2 = 0.000227$, $\beta_1 = 1.52$, $\beta_2 = 0.000227$.

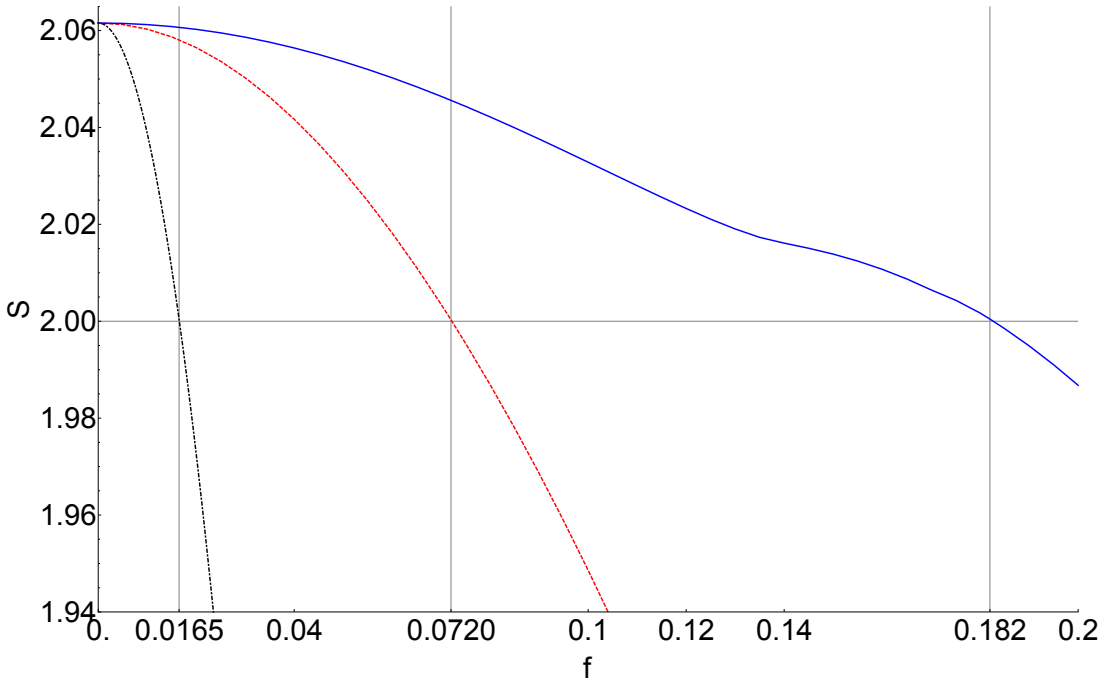

Figure 5.26: Correlated multiplicative noise. By optimising the measurement settings large improvements can be made to the tolerance of the system, f^{crit}. The black dot-dashed line show the case using arbitrary fixed angles, $f^{crit}_{4.1} = 0.0165$ (Sec. 5.4.4.1). The red dashed line shows the case where $\alpha_1 = 0$ and the other angles are optimised, $f^{crit}_{4.2} = 0.0720$ (Sec. 5.4.4.2). The blue solid line shows the fully optimised case where $f^{crit}_{4.3} = 0.182$ (Sec. 5.4.4.3).

5.4.4.4 Discussion

As opposed to the additive noise case, simply by optimising the angles of measurement we can improve the tolerance of the system all the way up to 18% which bodes very well for use in an actual experiment.

To understand why we find this large improvement we look at the expression for S

$$\begin{aligned} S = &-\frac{3}{8}\Big(\cos 2(\alpha_1-\beta_1)+\cos 2(\alpha_1-\beta_2)+\cos 2(\alpha_2-\beta_1)-\cos 2(\alpha_2-\beta_2)\Big) \\ &-\frac{5}{8}\Big(\exp(-2f^2(\alpha_1+\beta_1)^2)\cos 2(\alpha_1+\beta_1)+\exp(-2f^2(\alpha_1+\beta_2)^2)\cos 2(\alpha_1+\beta_2) \\ &+\exp(-2f^2(\alpha_2+\beta_1)^2)\cos 2(\alpha_2+\beta_1)-\exp(-2f^2(\alpha_2+\beta_2)^2)\cos 2(\alpha_2+\beta_2)\Big)\Big]. \end{aligned} \tag{5.53}$$

We look at how the expression for S changes when $f = 0.170$ as this produces a violation in the fully optimised case but not in the other two, Fig. 5.27.

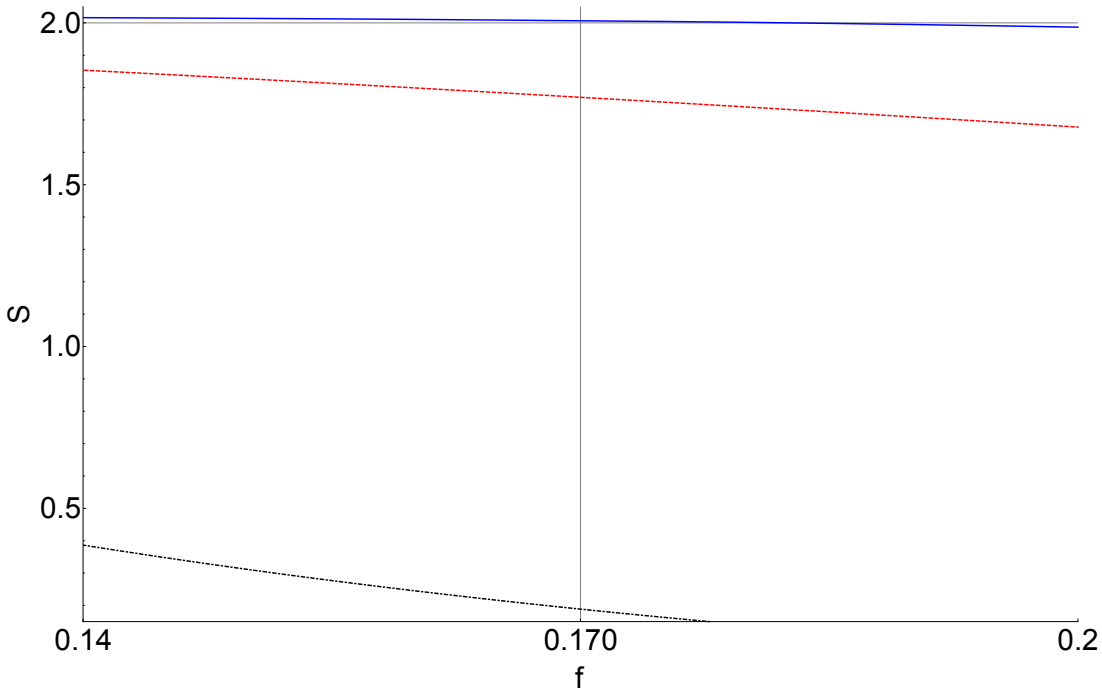

Figure 5.27: Correlated multiplicative noise, example of a value of f that leads to a violation in the fully optimised case but not in the others. The black dot-dashed line shows the optimum values of S found using an arbitrary set of angles (Sec. 5.4.4.1). The red dashed line shows the optimum values of S found when optimising the angles, fixing $\alpha_1 = 0$ (Sec. 5.4.4.2). The blue solid line shows the optimum values of S found optimising over all the angles (Sec. 5.4.4.3).

In the unoptimised case

$$\begin{aligned} S =& 0.313\exp(-265f^2) - 0.00214\exp(-208f^2) + 0.614\exp(-120f^2) \\ &+ 0.591\exp(-83.2f^2) + 0.371\exp(-43.1f^2) + 0.349\exp(-22.2f^2) \\ &+ 0.0706\exp(-1.55f^2) - 0.245\exp(-0.370f^2). \end{aligned} \tag{5.54}$$

In the partially optimised case

$$\begin{aligned} S =& -0.339\exp(-8.57f^2) + 0.849\exp(-6.84f^2) + 0.596\exp(-5.93f^2) \\ &- 0.373\exp(-5.30f^2) + 0.991\exp(-4.51f2) + 0.314\exp(-3.28f^2), \end{aligned} \tag{5.55}$$

and finally in the fully optimised case

$$\begin{aligned} S =& -0.614\exp(-18.6f^2) + 0.622\exp(-4.64f^2) + 0.622\exp(-4.64f^2) \\ &+ 0.373\exp(-4.64f^2) + 0.373\exp(-4.64f^2) + 0.625. \end{aligned} \tag{5.56}$$

Once again through the process of optimisation we are able to find measurement angles that allow a balance to be struck between increasing the part of the expression that is not affected by noise and decreasing the part of the expression that is suppressed by the noise. The value in the exponential decreases through the optimisation process.

As in the previous section the fact the optimum angles are the same is surprising and possibly not reliable.

5.5 Experimental feasibility

We have seen that the tolerance of the system can be improved with some types of errors simply by changing the measurement angles Alice and Bob use. To ensure that this proposal is realistic we look at a reasonable set of errors and calculate the number of trials needed to reproduce these values.

The maximum value of S for our system with a maximum of one particle in the reference frame is $S = 2.0616$. This can be found using the argument in [1]. The argument is structured as follows.

From Eq. (5.13) we can see that ν is maximal for pure product states, $|a'\rangle$ and $|b'\rangle$ for Alice and Bob respectively. As Eq. (5.13) only considers the real parts of the state we only need to worry about the real coefficients of the pure product states which can be written as

$$\begin{aligned} |a'\rangle &= \sum_{n=0}^{N} \mathfrak{a}_n |n\rangle , \\ |b'\rangle &= \sum_{m=0}^{M} \mathfrak{b}_m |m\rangle , \end{aligned} \tag{5.57}$$

where $\mathfrak{a}_n, \mathfrak{b}_m \in \mathbb{R}$. For these types of pure states, setting $\Delta = 1$, we can write the non-vanishing expectation from Eq. (5.13) as,

$$\begin{aligned} \nu =& f_N g_M, \\ f_N \equiv \langle a'| R_+ |a'\rangle &= \sum_{n=0}^{N-1} \mathfrak{a}_n \mathfrak{a}_{n+1}, \\ g_N \equiv \langle b'| R_- |b'\rangle &= \sum_{m=0}^{M-1} \mathfrak{b}_m \mathfrak{b}_{m+1}, \end{aligned} \tag{5.58}$$

where N, M represents the number of particles in Alice and Bobs reference frame respectively. To find the maximum of S it is necessary to maximise ν as can be seen from Eq. (5.20). As f_N and g_M are of the same form, we need only concentrate on f_N. $\langle a'| R_+ |a'\rangle = \langle b'| R_- |b'\rangle$ for states with real coefficients, so $f_N = \frac{1}{2} \langle a'| (R_+ + R_-) |b'\rangle$. As $R_+ + R_-$ is Hermitian the maximum of f_N is found when $|a'\rangle$ is an eigenvector of $R_+ + R_-$ with the highest eigenvalue,

$$\begin{aligned} \max f_N &= \cos\left(\frac{\pi}{N+2}\right), \\ \max g_M &= \cos\left(\frac{\pi}{M+2}\right), \end{aligned} \tag{5.59}$$

in our system $N = M$ as there is at most one particle on each side, making

$$\nu = \cos^2\left(\frac{\pi}{N+2}\right), \tag{5.60}$$

the maximum value of S from Eq. (5.20) is given by,

$$S = 2\sqrt{1+\nu^2} = 2\sqrt{1+\cos^4\left(\frac{\pi}{N+2}\right)}. \tag{5.61}$$

A reference frame with at most one particle on each side, $N = 1$ implies

$$S = 2\sqrt{1+\cos^4\left(\frac{\pi}{3}\right)} = 2.0616. \tag{5.62}$$

As soon as we start to include any type of error this maximum value of S will be decreased. For the experiment to prove that there is entanglement we need to show that the violation of the CHSH inequality is not just due to the spread of values. The mean of the spread must be far enough away from 2 that we be confident it is due to entanglement, not due to random errors.

To see how many trials it would take to safely say the violation is due to entanglement rather than errors, as an example, we set the instrumental noise to be $\sigma_S = 0.01$, taking the value of $S \approx 2.04$ making the mean four standard deviations away from the limit 2 which is far enough to show that the true value of S is above 2 at a 95% confidence level. We know that $S = \langle\alpha_1\beta_1\rangle + \langle\alpha_1\beta_2\rangle + \langle\alpha_2\beta_1\rangle - \langle\alpha_2\beta_2\rangle$, as we want the overall uncertainty of S to be 0.01, the quadrature sum of these individual uncertainties must add up to 0.01 assuming independent errors.

Each of the terms will give a ± 1 result with some probability. The distribution of ± 1 will follow a binomial distribution. In the usual binomial distribution the following formulas hold [61]

$$\begin{aligned} \langle X\rangle &= np, \\ \sigma^2 &= np(1-p), \end{aligned} \tag{5.63}$$

where X is the number of successes in n trials. In our circumstance these are slightly different as our possible results are ± 1 rather than $0, 1$. Our expectation value is the summation of all possible results divided by the number of results. We get $+1$, np times and -1, $n(1-p)$ times

$$\langle\alpha\beta\rangle = \frac{n_{\alpha\beta}p_{\alpha\beta} - n_{\alpha\beta}(1-p_{\alpha\beta})}{n_{\alpha\beta}} = 2p_{\alpha\beta} - 1, \tag{5.64}$$

moving on to the variance again we need to modify the previous result. We have increased the range of the results from $0 \to 1$ to $-1 \to +1$ i.e. doubling it, as the variance is squared this results in multiplying the previous result by 4 so the variance

of our system after n trials looks like

$$\sigma^2_{\alpha\beta(n)} = 4n_{\alpha\beta}p_{\alpha\beta}(1-p_{\alpha\beta}), \tag{5.65}$$

this implies that the average standard deviation is

$$\sigma_{\alpha\beta} = \frac{1}{\sqrt{n_{\alpha\beta}}} 2\sqrt{p_{\alpha\beta}(1-p_{\alpha\beta})}. \tag{5.66}$$

The standard deviation, σ_S, as previously mentioned is the quadrature sum of the individual variances, we assume $n = n_{\alpha_1\beta_1} = n_{\alpha_1\beta_2} = n_{\alpha_2\beta_1} = n_{\alpha_2\beta_2}$.

$$\begin{aligned}\sigma_S &= \sqrt{\sigma^2_{\alpha_1\beta_1} + \sigma^2_{\alpha_1\beta_2} + \sigma^2_{\alpha_2\beta_1} + \sigma^2_{\alpha_2\beta_2}} \\ &= \sqrt{\frac{4}{n}(p_{\alpha_1\beta_1}(1-p_{\alpha_1\beta_1}) + p_{\alpha_1\beta_2}(1-p_{\alpha_1\beta_2}) + p_{\alpha_2\beta_1}(1-p_{\alpha_2\beta_1}) + p_{\alpha_2\beta_2}(1-p_{\alpha_2\beta_2}))},\end{aligned} \tag{5.67}$$

which implies

$$n = \frac{4}{0.01^2}(p_{\alpha_1\beta_1}(1-p_{\alpha_1\beta_1})+p_{\alpha_1\beta_2}(1-p_{\alpha_1\beta_2})+p_{\alpha_2\beta_1}(1-p_{\alpha_2\beta_1})+p_{\alpha_2\beta_2}(1-p_{\alpha_2\beta_2})), \tag{5.68}$$

the total number of runs over the whole experiment will be $n_T = 4n$ as there are four sets of measurements that contribute to the S value. We will calculate the number of runs required for the worst case in both the additive and multiplicative noise models. If $S \approx 2.04$ the measurement settings for this value in the correlated additive noise case are shown in Fig. 5.28.

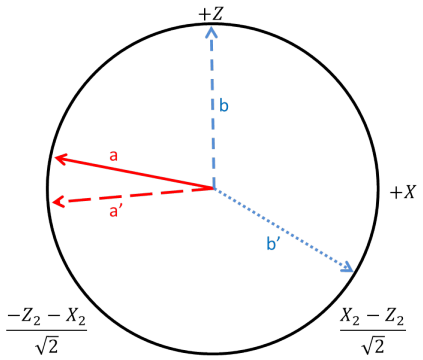

Figure 5.28: Optimised measurement settings when $\sigma = 0.04, \alpha_1 = 4.91, \alpha_2 = 4.64, \beta_1 = 6.27, \beta_2 = 2.11$.

Making

$$\begin{aligned} p_{\alpha_1\beta_1} &= 0.958, \\ p_{\alpha_1\beta_2} &= 0.674, \\ p_{\alpha_2\beta_1} &= 0.990, \\ p_{\alpha_2\beta_2} &= 0.254. \end{aligned} \tag{5.69}$$

Using these values, $n = 18353$ and $n_T = 73413$ assuming it takes approximately 5 seconds per measurement [109] the whole experiment would take almost 102 hours to complete.

Whereas in the correlated multiplicative case

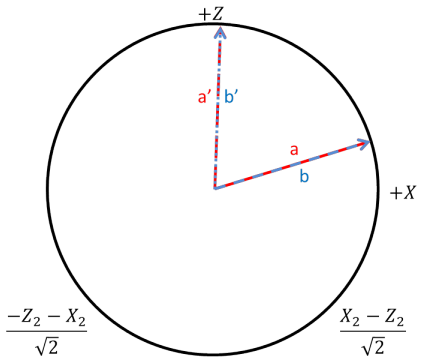

Figure 5.29: Optimised measurement settings when $f = 0.085, \alpha_1 = 1.27, \alpha_2 = 0.0322, \beta_1 = 1.27, \beta_2 = 0.0322$.

making

$$\begin{aligned} p_{\alpha_1\beta_1} &= 0.214, \\ p_{\alpha_1\beta_2} &= 0.0938, \\ p_{\alpha_2\beta_1} &= 0.906, \\ p_{\alpha_2\beta_2} &= 0.00260, \end{aligned} \tag{5.70}$$

using these values $n = 13632$ and $n_T = 54526$ assuming it takes approximately 5 seconds per measurement [109] the whole experiment would take just about 76 hours to complete.

These time periods are reasonable for an experiment of this kind [110]. However to be able to get this sort of result requires a very good experiment which is not impossible but the S value would rely on the actual experimental parameters. As we know the maximum value for S in our example system is $S = 2.06155$ which is very close to 2 so the noise in the system need to be low to allow the violation. If we cannot reach the low noise levels required then the experiment may not detect any violation and hence fail to verify the entanglement. In this case we might consider using a larger reference frame. If we had a reference frame of at most two particles, this state can be found

using the operations described in [1] where first we find a separable state with $N = 2$ using Eq. (5.71) to find the amplitudes of the eigenstates,

$$\mathfrak{a}_n = \sqrt{\frac{2}{N+2}} \sin\left(\frac{\pi(n+1)}{N+2}\right), \tag{5.71}$$

where $n = 0, 1, \ldots, N$. This produces the separable state

$$|\psi_{sep}\rangle = \left(\frac{1}{2}|0\rangle + \frac{1}{\sqrt{2}}|1\rangle + \frac{1}{2}|2\rangle\right)_A \otimes \left(\frac{1}{2}|0\rangle + \frac{1}{\sqrt{2}}|1\rangle + \frac{1}{2}|2\rangle\right)_B, \tag{5.72}$$

This state is separable but it is not compatible with SSR, to make it compatible we perform a twirling operation on it. Twirling removes all the coherences in the state that do not comply with SSR. In the particle number SSR twirling would remove the coherences between states with different numbers of particles. For example, $|11\rangle\langle 20|$ would not be affected as the two states have the same number of particles, however $|20\rangle\langle 10|$ would be removed as there is 2 particles in one state and 1 particle in the other. The formal definition of twirling is written as follows

$$\mathcal{T}(\rho) \equiv \sum_n \prod_n \rho \prod_n, \tag{5.73}$$

where $\prod_n$ is a projector on a subspace with a fixed number of particles n [1]. Taking our separable state $\rho_{sep} = |\psi_{sep}\rangle\langle\psi_{sep}|$ and performing the twirling operation we get

$$\begin{aligned}\mathcal{T}(\rho_{sep}) = &\frac{1}{16}|00\rangle\langle 00| + \frac{1}{8}|01\rangle\langle 01| + \frac{1}{8\sqrt{2}}|01\rangle\langle 10| + \frac{1}{16}|02\rangle\langle 02| + \frac{1}{8}|02\rangle\langle 11| \\ &+ \frac{1}{16}|02\rangle\langle 20| + \frac{1}{8}|10\rangle\langle 01| + \frac{1}{8}|10\rangle\langle 10| + \frac{1}{8}|11\rangle\langle 02| + \frac{1}{4}|11\rangle\langle 11| \\ &+ \frac{1}{8}|11\rangle\langle 20| + \frac{1}{4\sqrt{2}}|12\rangle\langle 12| + \frac{1}{4\sqrt{2}}|12\rangle\langle 21| + \frac{1}{16}|20\rangle\langle 02| \\ &+ \frac{1}{8}|20\rangle\langle 11| + \frac{1}{16}|20\rangle\langle 20| + \frac{1}{8}|21\rangle\langle 12| + \frac{1}{8}|21\rangle\langle 21| + \frac{1}{16}|22\rangle\langle 22|.\end{aligned} \tag{5.74}$$

If we were to use this state in our experiment the maximum S value would be increased

$$N = 2, S = 2\sqrt{1 + \cos^4\frac{\pi}{4}} = 2.23, \tag{5.75}$$

using this reference frame means we are no longer at the limit of violation but comfortably away from 2 allowing some of the other restrictions on the system to relax. However, physically creating this state is more difficult.

5.6 Non-ideal state preparation

In all of the work previously we have assumed that the state preparation has been perfect and consistent. This is unlikely to be the case. In this section we explore

two cases of imperfection in the state preparation. The first case where the principle system is not maximally entangled. And the second case where the reference frame is still separable but not mixed in the same manner.

5.6.1 Principal system not maximally entangled

The principal system when maximally entangled looks like,

$$|\psi\rangle = \frac{1}{\sqrt{2}}(|23\rangle + |32\rangle), \tag{5.76}$$

However, this may not be the case due to errors or imperfections in the creation process. By writing the state in terms of θ we can see what effect this has on the value of S. The principle system is now defined by

$$|\psi'\rangle = \cos\theta\,|23\rangle + \sin\theta\,|32\rangle\,, \tag{5.77}$$

where $0 \leq \theta \leq \frac{\pi}{2}$. Assuming that the measurements are perfect and the rest of the state preparation is perfect we varying only θ, this produces the graph shown in Fig. 5.30.

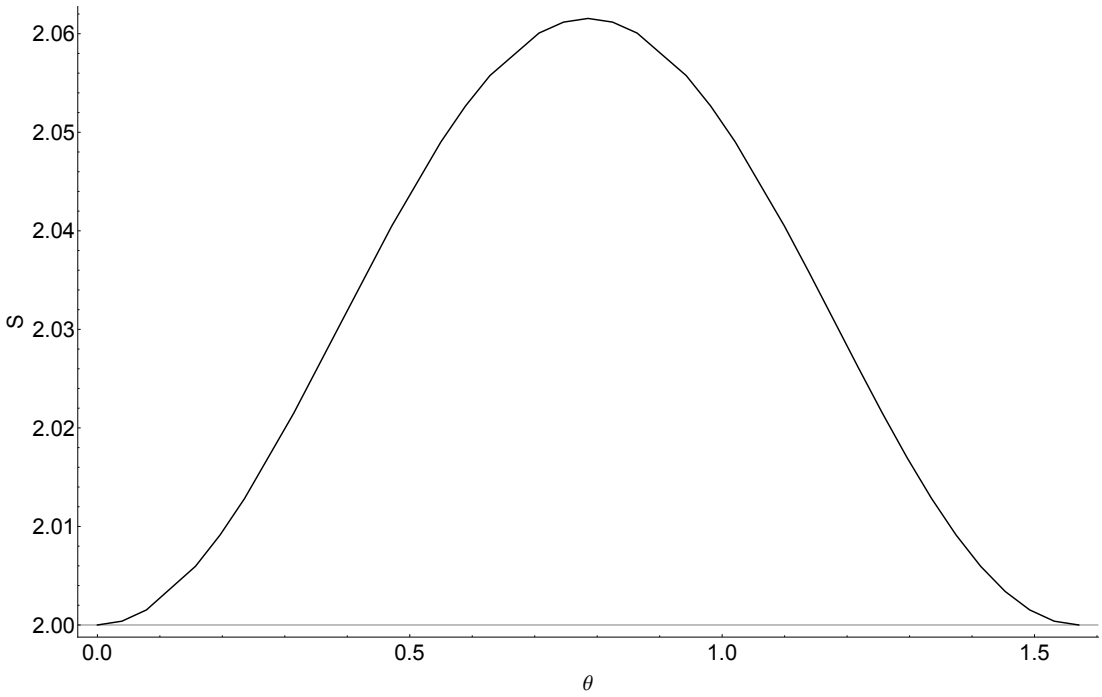

Figure 5.30: Non-ideal principal system. Assuming everything is perfect except the principal system state preparation we see how the S value is affected.

This graph proves that in principle we should always be able to violate the CHSH inequality except in the cases where this principle system contains no entanglement at the extremes of θ.

5.6.2 Variations in the reference frame

We now look at the case where the reference frame changes. Initially it is written as

$$\rho_{ref} = \frac{1}{2}\rho_\phi + \frac{1}{2}(|00\rangle\langle 00| + |11\rangle\langle 11|), \tag{5.78}$$

where $\rho_\phi = \frac{1}{2}(|01\rangle\langle 01| + |01\rangle\langle 10| + |10\rangle\langle 01| + |10\rangle\langle 10|)$ we now write this as

$$\rho'_{ref} = p\left(\frac{1+r}{2}|00\rangle\langle 00| + \frac{1-r}{2}|11\rangle\langle 11|\right) + (1-p)\rho_\phi, \tag{5.79}$$

where $0 \leq p \leq 1, -1 \leq r \leq 1$ this allows us to vary each element.

It is vital that the reference state remains separable so that if any entanglement is detected we can be sure that it came from the principle state and not the reference frame. To ensure that it is separable the eigenvalues of the partial transpose must be positive [106, 107].

The partial transpose of the state in the $\{|00\rangle, |01\rangle, |10\rangle, |11\rangle\}$ basis looks like

$$\begin{pmatrix} p\frac{1+r}{2} & 0 & 0\frac{1-p}{2} & \\ 0 & \frac{1-p}{2} & 0 & 0 \\ 0 & 0 & \frac{1-p}{2} & 0 \\ \frac{1-p}{2} & 0 & 0 & p\frac{1-r}{2} \end{pmatrix}, \tag{5.80}$$

with eigenvalues

$$\frac{1-p}{2}, \frac{1-p}{2}, \frac{1}{2}(p - \sqrt{1-2p+p^2+p^2r^2}), \frac{1}{2}(p + \sqrt{1-2p+p^2+p^2r^2}), \tag{5.81}$$

we can create a region plot that shows the area where p and r would allow for positive eigenvalues, this can be seen in Fig. 5.31

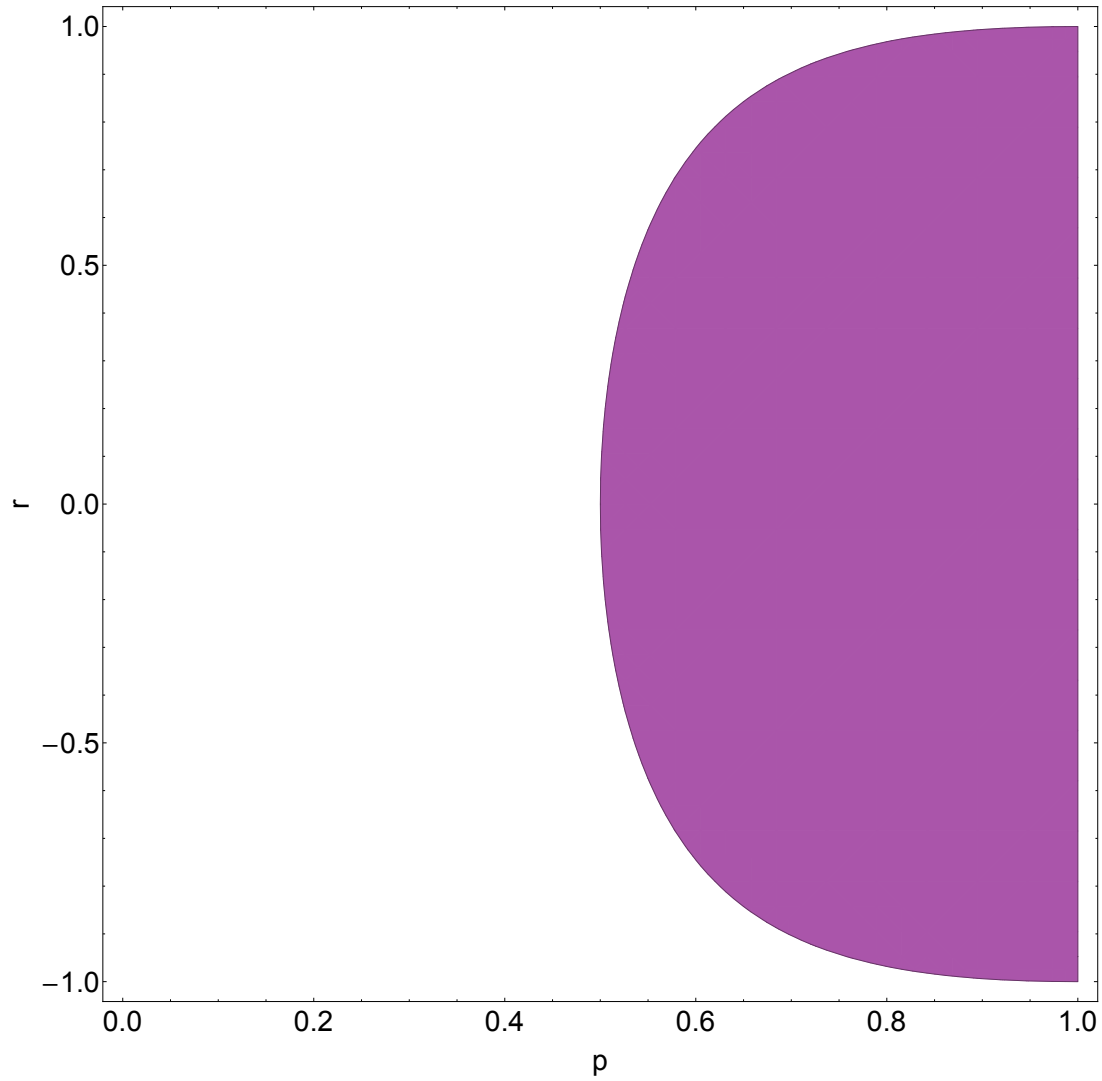

Figure 5.31: Region of separability of reference frame. The shaded area shows the values of p and r that allow a separable reference state.

Now we know the region in which the state is separable we can look at how p and r individually effect the value of S.

5.6.2.1 Effect of r on S

The expression for the expectation value of two measurements α and β in terms of p, r looks like

$$E(\alpha, \beta, p) = -\cos 2\alpha \cos 2\beta - \frac{p-1}{2} \sin 2\alpha \sin 2\beta, \tag{5.82}$$

clearly it does not depend on r so we do not need to worry about r, for simplicity we set it to $r = 0$ and continue to see the effect of p on S.

5.6.2.2 Effect of p on S

By setting $r = 0$ and varying p we assume the principal system is the maximum obtainable and perfectly prepared. We optimise the measurement settings and see a steady decrease in the value of S as p increases (Fig. 5.32). This is to be expected as the reference state itself is not entangled and p controls how much of the ρ_ϕ state, the entangled element, there is in the reference frame.

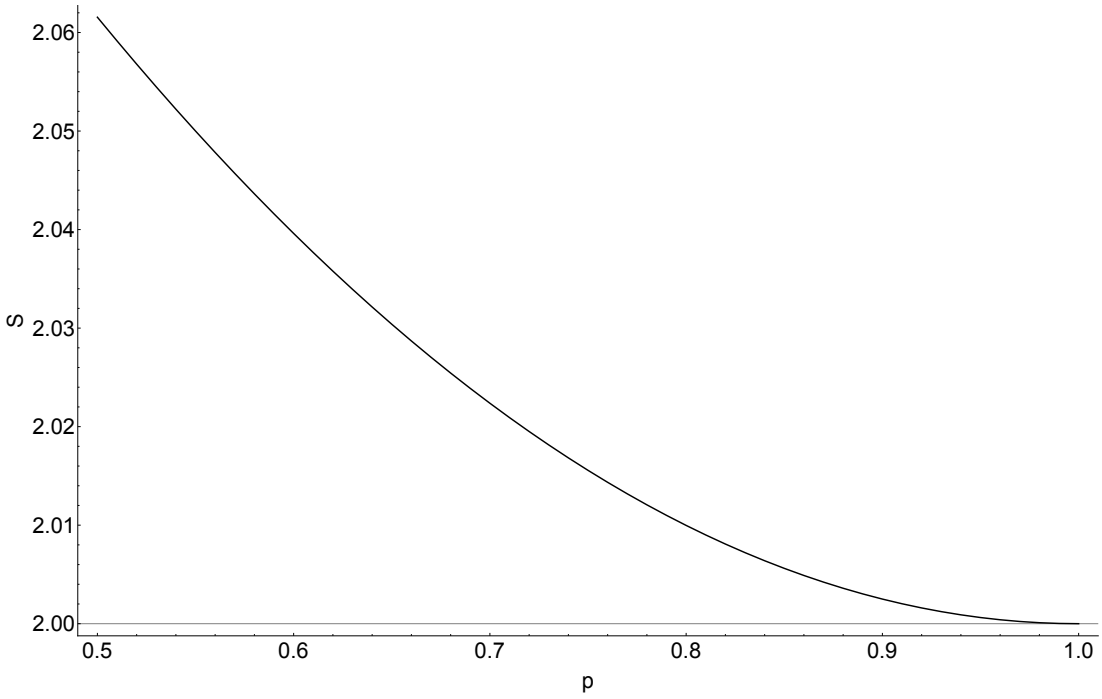

Figure 5.32: Non-ideal reference frame. By varying p, setting $r = 0$ and assuming the principle state preparation is perfect we see the larger the input of p the lower the violation of the CHSH inequality.

5.6.3 Varying both θ and p

We have seen how θ and p both affect the value of S separately but it is likely that these errors causing changes in θ and p will happen simultaneously so we look to see how this affects the value of S in Fig. 5.33.

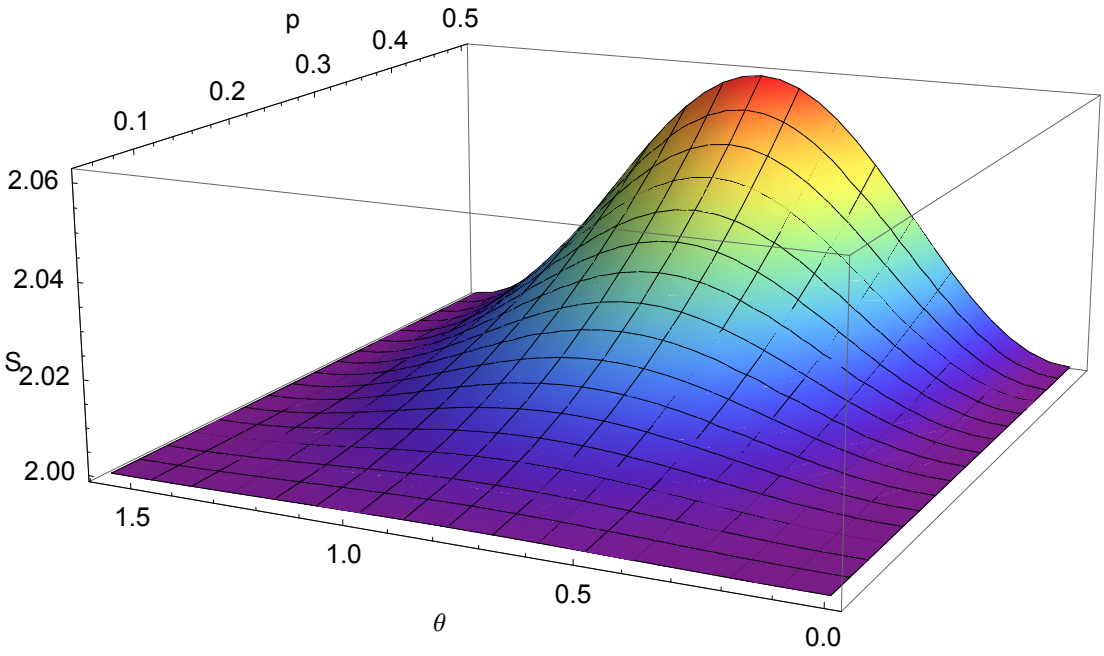

Figure 5.33: Non-ideal principal state and reference frame. We vary θ and p within the parameters in Fig. 5.31 to ensure the reference frame remains separable. It is still possible to violate the CHSH inequality up until the extremes of θ and p.

Once again we can always detect a violation of the CHSH inequality except in the case where $p = 1$ and the state contains no entanglement.

5.7 Creating the state

Although we have a purely theoretical approach to this problem it is important that we take into account how one might go about experimentally realising it. We do not pretend to have a solution to this problem, but suggest possible ideas that could be used in further research.

5.7.1 Reference frame

For the reference frame, Alice and Bob must share the $\frac{1}{\sqrt{2}}(|01\rangle + |10\rangle)$ state this could be realised by adiabatically bringing two wells together, one that has no particles in it and one that has one particle. Bringing them together adiabatically means there is no increase in energy of the system, once they are together and share the same space, they can then be separated again giving Alice and Bob back their wells, this means they

will not know if they have a particle or not [49]. This is a very simplified description of the process.

5.7.2 Principal system

Making the principal system that looks like $\frac{1}{\sqrt{2}}(|23\rangle+|32\rangle)$ could be realised in a similar manner to the reference frame but with wells with 2 and 3 particles ensuring the other states such as $|14\rangle$ and $|50\rangle$ needed more energy and so would not be populated.

Ideally to address the question of single particle entanglement we would like to start with a principle system that just shares 1 particle, $\frac{1}{\sqrt{2}}(|01\rangle + |10\rangle)$, find coherent operations to shift the photon number, then by adding 2 particles to both Alice and Bob's sides we could create the principal state, $\frac{1}{\sqrt{2}}(|23\rangle + |32\rangle)$ that we want. This is preferable as it is easier to make due to only one particle tunneling between the two sites we do not have to worry about making certain states unfavourable. The big question is, can this be done in a coherent manner? If so we can be certain that the single particle state was entangled. Further research will investigate the resources required.

5.7.3 Charge superselection rule

The issues with creating the state link back to the discussions in the introduction regarding single particle entanglement. Creating a system where the entanglement of a single particle can be measured is the ideal goal. In order to realise this we could think about the problem in terms of charge rather than particle number, this allows us to have a principal system that is equivalent to the $\frac{1}{\sqrt{2}}(|01\rangle + |10\rangle)$ state,

$$|\psi\rangle = \frac{1}{\sqrt{2}}(|0, +e\rangle + |+e, 0\rangle), \tag{5.83}$$

where $|0\rangle$ is the state with zero charge and $|+e\rangle$ is the state with positive charge. This state could be easier to physically realise and we can write all the eigenstates as before but with $|j-2, k-2\rangle$ for each state due to the charge number having the possibility of being negative. If we were able to create this state we could repeat the optimisation processes shown in this chapter to test the entanglement of the system.

5.8 Swapping the reference frame and the principle system

Up until now we have been exploring a reference frame and a principle system that we know will allow for a violation of the CHSH inequality and testing how robust this is to various errors that could affect it. However, the principal system, $\frac{1}{\sqrt{2}}(|23\rangle + |32\rangle)$ is difficult to physically construct. Ideally we would like the principal system to look like the reference frame, $\frac{1}{\sqrt{2}}(|01\rangle + |10\rangle)$ as this is much easier to realise. We will now explore how the violation of the CHSH inequality is affected if we swap the principal

system and the reference system. This swap will only mean we swap the state in A for the state in A' and the state in B for the state in B'. Thus making the principle system look like,

$$|\psi\rangle_{AB} = \frac{1}{\sqrt{2}}(|01\rangle + |10\rangle), \tag{5.84}$$

and the reference frame

$$|\phi\rangle_{A'B'} = \frac{1}{2}(\frac{1}{2}(|23\rangle + |32\rangle)(\langle 23| + \langle 32|)) + \frac{1}{4}(|22\rangle\langle 22| + |33\rangle\langle 33|). \tag{5.85}$$

As before it is vital that the reference frame is separable to ensure that we can show that any entanglement in the system is coming purely from the principal system. So before we go on we must check that the reference frame is separable. Using the positive partial transpose [106, 107] to show the separability we see the partial transpose as,

$$\rho_{A'B'}^{T_{B'}} = \frac{1}{4}(|23\rangle\langle 23| + |22\rangle\langle 33| + |33\rangle\langle 22| + |32\rangle\langle 32| + |22\rangle\langle 22| + |33\rangle\langle 33|), \tag{5.86}$$

the eigenvalues of the transposed state are $\frac{1}{2}, \frac{1}{4}, \frac{1}{4}, 0$ as they are all positive we can assume that the state is separable. Now we can check if this state produces a violation. The eigenstates of the swapped system look like,

$$\begin{aligned}
|\alpha(-1)\rangle &= \cos\alpha\,|1,1\rangle_{AA'} + \sin\alpha\,|0,2\rangle_{AA'}\,,\\
|\bar{\alpha}(-1)\rangle &= \sin\alpha\,|1,1\rangle_{AA'} - \cos\alpha\,|0,2\rangle_{AA'}\,,\\
|\alpha(0)\rangle &= \cos\alpha\,|0,3\rangle_{AA'} + \sin\alpha\,|1,2\rangle_{AA'}\,,\\
|\bar{\alpha}(0)\rangle &= \sin\alpha\,|0,3\rangle_{AA'} - \cos\alpha\,|1,2\rangle_{AA'}\,,\\
|\alpha(1)\rangle &= \cos\alpha\,|1,3\rangle_{AA'} + \sin\alpha\,|0,4\rangle_{AA'}\,,\\
|\bar{\alpha}(1)\rangle &= \sin\alpha\,|1,3\rangle_{AA'} - \cos\alpha\,|0,4\rangle_{AA'}\,,\\
|\beta(-1)\rangle &= \cos\beta\,|1,1\rangle_{BB'} + \sin\beta\,|0,2\rangle_{BB'}\,,\\
|\bar{\beta}(-1)\rangle &= \sin\beta\,|1,1\rangle_{BB'} - \cos\beta\,|0,2\rangle_{BB'}\,,\\
|\beta(0)\rangle &= \cos\beta\,|0,3\rangle_{BB'} + \sin\beta\,|1,2\rangle_{BB'}\,,\\
|\bar{\beta}(0)\rangle &= \sin\beta\,|0,3\rangle_{BB'} - \cos\beta\,|1,2\rangle_{BB'}\,,\\
|\beta(1)\rangle &= \cos\beta\,|1,3\rangle_{BB'} + \sin\beta\,|0,4\rangle_{BB'}\,,\\
|\bar{\beta}(1)\rangle &= \sin\beta\,|1,3\rangle_{BB'} - \cos\beta\,|0,4\rangle_{BB'}\,.
\end{aligned} \tag{5.87}$$

However, this set up does not allow a violation of the CHSH inequality, $S = 0.5$ is the greatest value possible. As this principal system and reference frame combination does not allow a violation, we look to find another reference frame that will allow this violation whilst still being separable, to do this we can play around with adding combinations of the states $|22\rangle\langle 22|$, $|33\rangle\langle 33|$, $|23\rangle\langle 23|$ and $|32\rangle\langle 32|$. Let us start by

considering the reference frame,

$$\rho^1_{A'B'} = \frac{1}{4}(|23\rangle + |32\rangle)(\langle 23| + \langle 32|) + \frac{1}{4}|23\rangle\langle 23| + \frac{1}{4}|32\rangle\langle 32|, \tag{5.88}$$

checking first that this state is separable

$$\rho^{1T_{B'}}_{A'B'} = \frac{1}{4}(|23\rangle\langle 23| + |33\rangle\langle 22| + |22\rangle\langle 33| + |32\rangle\langle 32|) + \frac{1}{4}|23\rangle\langle 23| + \frac{1}{4}|32\rangle\langle 32|, \tag{5.89}$$

where the eigenstates of this state are $\frac{1}{2}, \frac{1}{2}, \frac{1}{4}, -\frac{1}{4}$, which are not all positive meaning it is not separable and so not useful for our analysis.

We tried various combinations of each of the additional states with no success, here is a list of combinations of the states that are not separable

$$\begin{aligned}
\rho^2_{A'B'} &= \frac{1}{4}(|23\rangle + |32\rangle)(\langle 23| + \langle 32|) + \frac{1}{4}|23\rangle\langle 23| + \frac{1}{4}|22\rangle\langle 22|, \\
\rho^2_{A'B'} &= \frac{1}{4}(|23\rangle + |32\rangle)(\langle 23| + \langle 32|) + \frac{1}{4}|23\rangle\langle 23| + \frac{1}{4}|33\rangle\langle 33|, \\
\rho^2_{A'B'} &= \frac{1}{4}(|23\rangle + |32\rangle)(\langle 23| + \langle 32|) + \frac{1}{4}|32\rangle\langle 32| + \frac{1}{4}|22\rangle\langle 22|, \\
\rho^2_{A'B'} &= \frac{1}{4}(|23\rangle + |32\rangle)(\langle 23| + \langle 32|) + \frac{1}{4}|32\rangle\langle 32| + \frac{1}{4}|33\rangle\langle 33|, \\
\rho^2_{A'B'} &= \frac{1}{4}(|23\rangle + |32\rangle)(\langle 23| + \langle 32|) + \frac{1}{8}|22\rangle\langle 22| + \frac{1}{8}|33\rangle\langle 33| + \frac{1}{8}|23\rangle\langle 23| + \frac{1}{8}|32\rangle\langle 32|.
\end{aligned} \tag{5.90}$$

None of these states provide a violation of the CHSH inequality either. Going back to the initial state that we tried $\rho^1_{A'B'} = \frac{1}{4}(|23\rangle+|32\rangle)(\langle 23|+\langle 32|)+\frac{1}{4}|23\rangle\langle 23|+\frac{1}{4}|32\rangle\langle 32|$, forgetting for a second that it is not a separable state, this does provide a violation of the CHSH inequality and so perhaps by changing the quantities of each of the elements of the state it would be possible to make it separable.

$$\rho^{1'}_{A'B'} = \frac{X}{2}(|23\rangle\langle 23| + |23\rangle\langle 32| + |32\rangle\langle 23| + |32\rangle\langle 32|) + Y|23\rangle\langle 23| + Z|32\rangle\langle 32|, \tag{5.91}$$

we want this to be separable so take the partial transpose,

$$\rho^{1'T_{B'}}_{A'B'} = \frac{X}{2}(|23\rangle\langle 23| + |22\rangle\langle 33| + |33\rangle\langle 22| + |32\rangle\langle 32|) + Y|23\rangle\langle 23| + Z|32\rangle\langle 32|, \tag{5.92}$$

making the eigenvalues $\frac{-X}{2}, \frac{X}{2}, \frac{X}{2}+Y, \frac{X}{2}+Z$, this shows that there is no way that the eigenvalues of this state could be positive no matter what mixtures of the individual elements were used.

We have not been able to find a way of swapping the reference frame and the principal system to produce a state that violates the CHSH inequality and also has a separable reference frame. We believe there is more to be found down this channel of thought but we leave this open for investigation by somebody else.

5.9 Conclusion

In this work we began by considering whether entanglement of a single particle is possible. This lead to questions about restrictions on coherent operations due to superselection rules. We saw how superselection rules could be used as a resource and how reference frames can be used to get around the restrictions that they impose. We based our work on a system defined by Paterek*et al.* using the minimal reference frame required in order to violate the CHSH inequality. We aimed to show how errors in the measurement apparatus affected the detectable entanglement in the system. By optimising the measurement settings Alice and Bob used to construct the CHSH value we have shown that in a system with certain types of error the critical value of the error at which point the CHSH inequality is no longer violated can be vastly improved.

We assumed the measurements were performed by laser pulses controlled by an EOM. By placing EOMs at different points in the circuit we could have uncorrelated and correlated errors. The EOMs controlled two elements of the laser beam, the strength and the time period these errors are multiplicative and additive respectively. Using the minimal reference frame and ensuring that it was separable so any entanglement detected could be said to have come from the principal system we tested the system with the four different types of noise using the CHSH inequality.

Initially we used an arbitrary set of measurement angles to maximise the CHSH value over the range of the error. We attempted to beat this critical value of error by a series of optimisations of the measurement settings. We fixed $\alpha_1 = 0$ to reduce the complexity of the calculations and optimised the measurement settings for each value of the error. The measurement settings for each value of the error were different. We then optimised the measurement settings with no restrictions on α_1.

For uncorrelated additive error none of the optimisations improved the critical value of the error, the highest error tolerated was $\sigma = 0.0870$. The correlated additive noise provided a very slightly improvement in the error tolerance from $\sigma = 0.0719 \rightarrow 0.0721$ but by closer inspection of the measurement settings we saw they were identical to our level of accuracy. The multiplicative error is where the large improvements were seen. For uncorrelated multiplicative noise the arbitrary angles gave an error tolerance of $f = 0.02$ the first optimisation increased this to $f = 0.0739$ and the second optimisation increased it to $f = 0.190$. The correlated multiplicative noise also improved drastically, the arbitrary angles gave $f = 0.0165$ improved to $f = 0.0720$ by the first optimisation and the to $f = 0.182$ by the second.

Given these vast improvements in the error tolerance we picked a reasonable set of errors and tested how long it would take to perform this type of experiment to ensure it was in line with what could be expected. We saw that in each of the worst cases, where the error tolerance was the lowest for additive and multiplicative errors, the experiment would take around 76 and 102 hours respectively.

We then moved on to look at the impact of errors in the preparation of the state. By changing the principal system from maximally mixed to an entangled state controlled by θ and modifying the reference frame but still ensuring its separability we found it was still possible to always detect entanglement in the system for most values of the variable parameters.

We briefly discussed ideas of how to create the principal system and the reference frame with the possibility of using another basis of measurement such as charge as this allows us to access the superpositions that were previously hard to attain. We also considered the possibility of swapping the reference frame for the principal system but found issues with ensuring the separability of the new reference frame.

We found a surprising result in the multiplicative noise scenarios, the optimum angles for Alice and Bob were found to be the same. Having tested these measurement angles using a standard CHSH inequality set-up and finding that there is no violation in this case we are forced to conclude that there may be something no quite right with our analysis. We leave this for further work.

CHAPTER 6

Conclusion

Our original aim was to identify situations where physical restraints on the apparatus that we might us to realise elements of quantum theory could introduce an error causing our results not to be reliable. As discussed we believe that technology will eventually develop to be at a quantum scale and standard but until that time we want to be able to perform experiments. Instead of trying to change the apparatus to fit the theory we look at the problem from the opposite way around and focus on the changes we can make to the theory given these physical restraints.

We focused on cluster states as a good candidate for quantum computation and identified the following errors that arise from the physical constraints of the apparatus, cross-talk, incomplete measurement, non-ideal states and superselection rules.

The main conclusion to be drawn from this work is that it is possible to perform a better measurement simply by a simple optimisation. In each case we successfully reduced the effects of the physical constraints.

We began by considering stabilizer operators in Chapter 3 we predicted that by modifying the stabilizer operators used to characterise a cluster state we would be able to reduce or eradicate the level of cross-talk in the measurement process. In this case the cross-talk arises from the fact the width of the laser beam is larger than the atom spacing in the cluster state. Although we were able to reduce the cross-talk in the system we found that we could not eradicate it completely as the sets of HCTF stabilizer operators were not able to reconstruct the canonical set of stabilizer operators. But by combining the set of HCTF stabilizer operators with a careful choice of CT-stabilizer operators the effect of cross-talk can be significantly reduced, almost by half. The fact we could not find a way to get this reduction down to a half was very frustrating. The patterns of HCTF stabilizer operators are very symmetrical and we believe there is

a high probability that we were just unable to find the right pattern to get the 50% reduction and would encourage further work on this section.

We also defined algorithms to find the set of HCTF stabilizer operators in fixed width, square and triangle connectivity cluster states. As yet we have not found an automated way using the HCTF and CT stabilizer operators to find the new equivalent set, in our work we performed this task manually which is very time consuming and an automated system would be very helpful. The whole process of finding the reduced cross-talk set of stabilizer operators is very simple and until measurement apparatus that match the quantum scale are available our solution provides a large improvement in the effect of cross-talk on the system.

We then moved on to how a cluster state is formed by cooling a Bose-Einstein Condensate in Chapter 4 and identified incomplete measurement and non-ideal states in these systems. We did not attempt to characterise the state using processes such as full state quantum tomography as, although this would not be such an issue for the two-party system we examine, there would be no hope of scaling our solution to a multipartite system due to the exponential numbers of parameters. Instead, we used a single parameter to examine the impact of incomplete measurement and non-ideal states, the entanglement.

We began by using the conventional measurement settings in the CHSH inequality test and found how well the system performed in the presence of the errors caused by the physical constraints of the system. Using this as a base we optimised the measurement settings over the error range and found a surprising result. We were able to show that there is detectable entanglement in the system as long as there are particles in the system, even if the proportion with the particles is very very small. This result shows that when there is very small entanglement component we are able to tune the measurement settings to pick this part out producing the violation in the Bell inequality, hence detect entanglement. By knowing the errors that affect the system a simple change in the measurement settings can vastly improve the detectable entanglement.

Using these optimum measurement settings to vastly improve the detectable entanglement is very successful but each of the optimum measurement settings are different depending on how large the error in the system is, we went on to explore how robust our discovery was to any uncertainty in the knowledge of the error. We found that even in the very worst case where we assume our system to have an extremely small proportion of an entangled state the optimum measurement settings still provide detectable entanglement for all values of the error making our solution completely robust.

In Chapter 5 we also considered the question of single particle entanglement that has caused great debate. We explain how we believe this to be part of a larger question about allowed coherent operations. We discuss how superselection rules constrain the types of coherent operations that are allowed to be performed on our state and describe how Paterek *et al.* have shown the minimum reference frame required to get around

these superselection rules to perform the operations we require. Using the joint system including a reference frame we focused on the types of errors that can be introduced from the measurement process due to the apparatus used. Similar to the previous chapter we optimised the measurement settings in order to increase the tolerance of the system. Depending on the type of error, we were able to find large improvements in the tolerance showing that this is a worthwhile process. We did produce an unexpected result where the measurement angles Alice and Bob use to perform their measurements are in fact the same. We believe it is worth looking into the definition of the system to fully understand why this result has occurred. We also looked at non-ideal states and found that in the case of no error we are still about to detect entanglement even if the entanglement component approaches zero. We propose that if coherent operations can be found to transform the $\frac{1}{\sqrt{2}}(|01\rangle + |10\rangle)$ to $\frac{1}{\sqrt{2}}(|23\rangle + |32\rangle)$ then the ideas presented here will show that the single particle system is indeed entangled.

All our optimisation processes have produced improvements in the tolerance of the system to various errors. There are elements throughout the thesis that would benefit from further investigation. Further work could be done to increase the numbers of errors considered or to scale up the number of qubits in the system. We suggest that increasing the number of errors would be the most promising area of research at this stage as this will give a greater understanding of the impact of these errors on the tolerance of the system.

APPENDIX A

Graphical representation of stabilizer operator sets

A.1 Equivalent set of stabilizer operators

In Sec. 3.3.1.1 we calculate an example of an equivalent set of stabilizer operators. Here we show this set in graphical form.

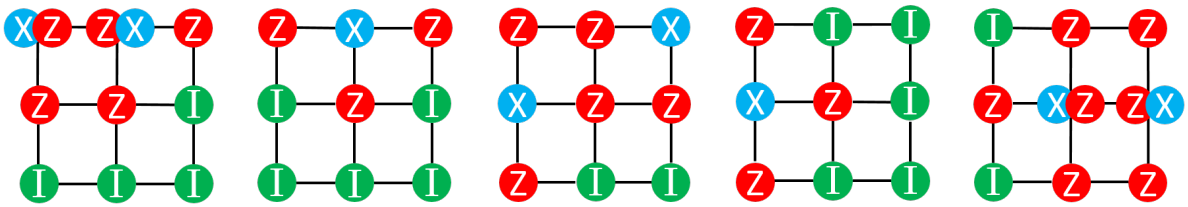

(a) s_{12} (b) s_2 (c) s_{34} (d) s_4 (e) s_{56}

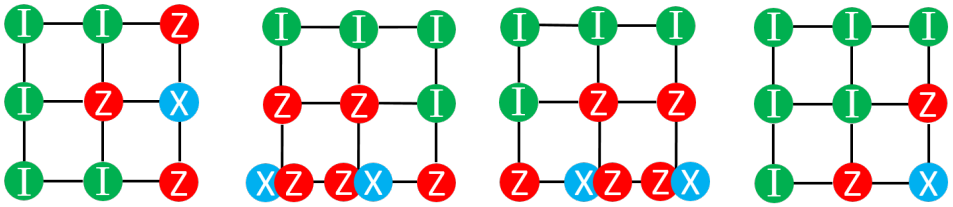

(f) s_6 (g) s_{78} (h) s_{89} (i) s_9

Figure A.1: An equivalent set of stabilizer operators. Found using the a non-singular matrix applied to the canonical set of stabilizer operators in Sec. 3.3.1.1. The order in which the stabilizer operators are applied is very important as the Pauli operators X and Z do not commute on the individual qubits. The ordering of the stabilizer operators correspond to their labeling i.e. s_{12} corresponds to applying stabilizer operator s_1 followed by stabilizer operator s_2.

A.2 Canonical set of stabilizer operators

The canonical set of stabilizer operators for a 3×3 cluster state (Fig. 3.5) are:

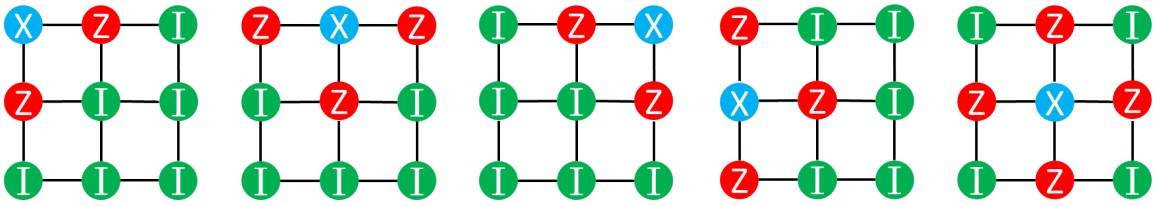

(a) $P_{CT} = 2$ (b) $P_{CT} = 3$ (c) $P_{CT} = 2$ (d) $P_{CT} = 3$ (e) $P_{CT} = 4$

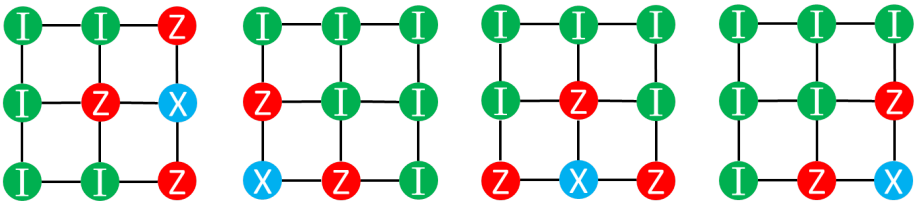

(f) $P_{CT} = 3$ (g) $P_{CT} = 2$ (h) $P_{CT} = 3$ (i) $P_{CT} = 2$

Figure A.2: The nine canonical stabilizer operators found by applying Eq. (3.2) to each qubit in the cluster state. $P_{CT}^{T} = 4.2 + 4.3 + 1.4 = 24$.

APPENDIX B

Entanglement via collisional gates

To understand how the collisional gates create the entanglement we look at an example of two neighbouring atoms in the lattice [51], both atoms on the jth and $(j+1)$th sites are in the $|0\rangle$ state,

$$|\psi\rangle = |0\rangle_j |0\rangle_{j+1}, \tag{B.1}$$

a $\frac{\pi}{2}$ pulse is used on both the atoms to bring them into a superposition of $|0\rangle$ and $|1\rangle$,

$$|\psi\rangle = (|0\rangle_j + |1\rangle_j)(|0\rangle_{j+1} + |1\rangle_{j+1})/2, \tag{B.2}$$

then the internal states of the atoms are split and moved in opposite directions [111], the $|0\rangle$ state moves to the left and the $|1\rangle$ state moves to the right making the joint state look like,

$$|\psi\rangle = (|0\rangle_j |0\rangle_{j+1} + |0\rangle_j |1\rangle_{j+2} + |1\rangle_{j+1} |0\rangle_{j+1} + |1\rangle_{j+1} |1\rangle_{j+2})/2. \tag{B.3}$$

Here we have left $|0\rangle$ in its original position and moved the $|1\rangle$ state a full lattice site, this is the same as moving both half a lattice site in opposite directions. When both atoms occupy the same lattice site $j+1$ there is a phase shift after a time, t [49, 112, 113],

$$|\psi\rangle = (|0\rangle_j |0\rangle_{j+1} + |0\rangle_j |1\rangle_{j+2} + \exp(-i\phi) |1\rangle_{j+1} |0\rangle_{j+1} + |1\rangle_{j+1} |1\rangle_{j+2})/2, \tag{B.4}$$

then the atoms are brought back to their original lattice sites using another $\frac{\pi}{2}$ pulse,

$$\begin{aligned} |\psi\rangle =& (1 + \exp(-i\phi))/2 \, |1\rangle_j |1\rangle_{j+1} \\ &+ (1 - \exp(-i\phi))/2(|0\rangle_j (|0\rangle_{j+1} - |1\rangle_{j+1}) + |1\rangle_j (|0\rangle_{j+1} + |1\rangle_{j+1}))/2, \end{aligned} \tag{B.5}$$

which is the entangled state (Fig. B.1). The problem arises when there is no atom in one of the lattice sites as the phase shift will not occur meaning the atom will not be entangled, reducing the overall entanglement of the system.

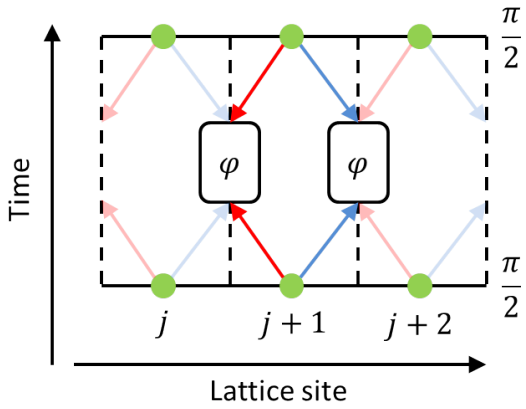

Figure B.1: Entangling operation via collisional gates. Atoms shown in green, $|0\rangle$ spin-state in red and $|1\rangle$ in blue. Coherent superposition of $|0\rangle$ and $|1\rangle$ created by the initial $\frac{\pi}{2}$. The spin states are then separated and moved in opposite directions to collide with spin states from different lattice sites. The states are brought back together and a further $\frac{\pi}{2}$ pulse is applied creating the entangled state.

APPENDIX C

Measurement Angles

C.1 Measurement angles for S versus S'

In Sec. 4.5 we only consider S' in our optimisation process due to the "vacancy-vacancy" (ρ_{00}) element of the system not contributing to the violation of the CHSH inequality. To double check that this is true and the same optimum measurement settings are found in both cases we explicitly show the measurement angles for a handful of cases.

$q = 0.01$						
	S			S'		
	$r=-1$	$r=0$	$r=1$	$r=-1$	$r=0$	$r=1$
θ_a	π	2.75	2.36	π	2.75	2.36
$\theta_{a'}$	1.57	1.18	0.785	1.57	1.18	0.785
θ_b	0.785	1.18	$\frac{\pi}{2}$	0.785	1.18	$\frac{\pi}{2}$
$\theta_{b'}$	0.785	0.393	0	0.785	0.393	0

$q = 0.25$						
	S			S'		
	$r=-1$	$r=0$	$r=1$	$r=-1$	$r=0$	$r=1$
θ_a	3.14	2.81	2.36	3.14	2.81	2.36
$\theta_{a'}$	$\frac{\pi}{2}$	1.16	0.785	$\frac{\pi}{2}$	1.16	0.785
θ_b	0.785	1.24	$\frac{\pi}{2}$	0.785	1.24	$\frac{\pi}{2}$
$\theta_{b'}$	0.785	0.412	0	0.785	0.412	0

$q = 0.5$						
	S			S'		
	$r=-1$	$r=0$	$r=1$	$r=-1$	$r=0$	$r=1$
θ_a	π	2.89	2.36	π	2.89	2.36
$\theta_{a'}$	$\frac{\pi}{2}$	1.13	0.785	$\frac{\pi}{2}$	1.13	0.785
θ_b	0.785	1.32	$\frac{\pi}{2}$	0.785	1.32	$\frac{\pi}{2}$
$\theta_{b'}$	0.785	0.441	0	0.785	0.441	0

$q = 0.75$						
	S			S'		
	$r=-1$	$r=0$	$r=1$	$r=-1$	$r=0$	$r=1$
θ_a	π	3.01	2.36	π	3.01	2.36
$\theta_{a'}$	$\frac{\pi}{2}$	1.09	0.785	$\frac{\pi}{2}$	1.09	0.785
θ_b	0.785	1.44	$\frac{\pi}{2}$	0.785	1.44	$\frac{\pi}{2}$
$\theta_{b'}$	0.785	0.480	0	0.785	0.480	0

$q = 0.99$						
	S			S'		
	$r=-1$	$r=0$	$r=1$	$r=-1$	$r=0$	$r=1$
θ_a	π	3.14	2.36	π	3.14	2.36
$\theta_{a'}$	$\frac{\pi}{2}$	1.05	0.785	$\frac{\pi}{2}$	1.05	0.785
θ_b	0.785	1.57	$\frac{\pi}{2}$	0.785	1.57	$\frac{\pi}{2}$
$\theta_{b'}$	0.785	0.522	0	0.785	0.522	0

C.2 Measurement angles for q' settings

In Sec. 4.6.1 we use the optimum measurement settings for five values of q' as the fixed measurement settings when testing the robustness to state knowledge. These measurement settings are given here for clarity.

$q' = 0.01$	
θ_a	2.75
ϕ_a	0
$\theta_{a'}$	1.18
$\phi_{a'}$	0
θ_b	5.10
ϕ_b	0
$\theta_{b'}$	0.393
$\phi_{b'}$	0

$q' = 0.25$	
θ_a	2.81
ϕ_a	0
$\theta_{a'}$	1.16
$\phi_{a'}$	0
θ_b	5.04
ϕ_b	0
$\theta_{b'}$	0.41
$\phi_{b'}$	0

$q' = 0.5$	
θ_a	2.89
ϕ_a	0
$\theta_{a'}$	1.13
$\phi_{a'}$	0
θ_b	4.96
ϕ_b	0
$\theta_{b'}$	0.44
$\phi_{b'}$	0

$q' = 0.75$	
θ_a	3.01
ϕ_a	0
$\theta_{a'}$	1.09
$\phi_{a'}$	0
θ_b	4.84
ϕ_b	0
$\theta_{b'}$	0.48
$\phi_{b'}$	0

$q' = 0.99$	
θ_a	3.14
ϕ_a	0
$\theta_{a'}$	1.05
$\phi_{a'}$	0
θ_b	4.72
ϕ_b	0
$\theta_{b'}$	0.522
$\phi_{b'}$	0

Table C.1: Fixed angles for when $q' = 0.01, q' = 0.25, q' = 0.5, q' = 0.75$ and $q' = 0.99$. (All angles in radians)

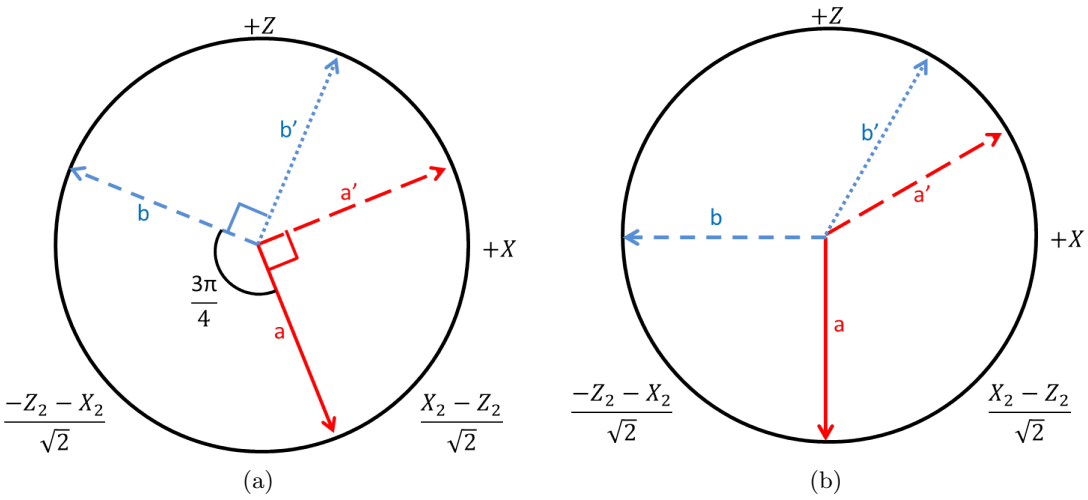

Figure C.1: Fixed angles for q' measurement settings. As the angles do not change very much only the first and last settings are shown. (a) shows the fixed measurement settings for $q' = 0.01$ and (b) shows the fixed measurement settings for $q = 0.99$

APPENDIX D

Correlations formula

The principle system must be of the form

$$|\psi\rangle_{AB} = \frac{1}{\sqrt{2}}(|2\rangle_A |2+\Delta\rangle_B + |2+\Delta\rangle_A |2\rangle_B), \tag{D.1}$$

where $\Delta \geq 1$, and the reference system must be of the form

$$|\phi\rangle_{A'B'} = \sum_{i=0}^{N'} r_i |i\rangle_{A'} |N'-i\rangle_{B'}, \tag{D.2}$$

where $r^*_{i+\Delta} r_i \neq 0$. This leads to a joint state of

$$|\psi\phi\rangle = \sum_i \frac{r_i}{\sqrt{2}}(|2,i\rangle_{AA'} |2+\Delta, N'-i\rangle_{BB'} + |2+\Delta, i\rangle_{AA'} |2, N'-i\rangle_{BB'}). \tag{D.3}$$

The local dichotomic measurements for Alice and Bob that are compatible with particle-number superselection rule look like

$$\begin{aligned} \mathcal{A} &= \sum_{a=-\Delta}^{N'} = |\alpha(a)\rangle \langle\alpha(a)| = \sum_{a=-\Delta}^{N'} |\bar{\alpha}(a)\rangle \langle\bar{\alpha}(a)|, \\ \mathcal{B} &= \sum_{b=-\Delta}^{N'} = |\beta(b)\rangle \langle\beta(b)| = \sum_{b=-\Delta}^{N'} |\bar{\beta}(b)\rangle \langle\bar{\beta}(b)|, \end{aligned} \tag{D.4}$$

where $\mathcal{A}$ describes the measurements Alice can perform on her system defined by the angle α and $\mathcal{B}$ describes the measurements Bob can perform on his system defined by the angle β. The eigenstates of these measurements are defined as follows;

for $a/b = -\Delta, \ldots, -1$

$$\begin{aligned}
|\alpha(a)\rangle &= \cos\alpha\,|1, a+\Delta+1\rangle_{AA'} + \sin\alpha\,|2, a+\Delta\rangle_{AA'}\,,\\
|\bar{\alpha}(a)\rangle &= \sin\alpha\,|1, a+\Delta+1\rangle_{AA'} - \cos\alpha\,|2, a+\Delta\rangle_{AA'}\,,\\
|\beta(b)\rangle &= \cos\beta\,|1, a+\Delta+1\rangle_{BB'} + \sin\beta\,|2, a+\Delta\rangle_{BB'}\,,\\
|\bar{\beta}(b)\rangle &= \sin\beta\,|1, a+\Delta+1\rangle_{BB'} - \cos\beta\,|2, a+\Delta\rangle_{BB'}\,.
\end{aligned} \tag{D.5}$$

For $a/b = 0, \ldots, N' - \Delta$

$$\begin{aligned}
|\alpha(a)\rangle &= \cos\alpha\,|2_\Delta, a\rangle_{AA'} + \sin\alpha\,|2, a+\Delta\rangle_{AA'}\,,\\
|\bar{\alpha}(a)\rangle &= \sin\alpha\,|2+\Delta, a\rangle_{AA'} - \cos\alpha\,|2, a+\Delta\rangle_{AA'}\,,\\
|\beta(b)\rangle &= \cos\beta\,|2+\Delta, a\rangle_{BB'} + \sin\beta\,|2, a+\Delta\rangle_{BB'}\,,\\
|\bar{\beta}(b)\rangle &= \sin\beta\,|2+\Delta, a\rangle_{BB'} - \cos\beta\,|2, a+\Delta\rangle_{BB'}\,.
\end{aligned} \tag{D.6}$$

For $a/b = N' - \Delta + 1, \ldots, N'$

$$\begin{aligned}
|\alpha(a)\rangle &= \cos\alpha\,|2+\Delta, a\rangle_{AA'} + \sin\alpha\,|3+\Delta, a-1\rangle_{AA'}\,,\\
|\bar{\alpha}(a)\rangle &= \sin\alpha\,|2+\Delta, a\rangle_{AA'} - \cos\alpha\,|3+\Delta, a-1\rangle_{AA'}\,,\\
|\beta(b)\rangle &= \cos\beta\,|2+\Delta, a\rangle_{BB'} + \sin\beta\,|3+\Delta, a-1\rangle_{BB'}\,,\\
|\bar{\beta}(b)\rangle &= \sin\beta\,|2+\Delta, a\rangle_{BB'} - \cos\beta\,|3+\Delta, a-1\rangle_{BB'}\,.
\end{aligned} \tag{D.7}$$

Using these eigenstates we can rewrite the state in the eigenstate basis

$$\begin{aligned}
|\psi\phi\rangle = \sum_i \frac{r_i}{\sqrt{2}}\Big(&(\sin\alpha\,|\alpha_{i-\Delta}\rangle - \cos\alpha\,|\bar{\alpha}_{i-\Delta}\rangle)(\cos\beta\,|\beta_{N'-i}\rangle + \sin\beta\,|\bar{\beta}_{N'-i}\rangle)\\
&+ (\cos\alpha\,|\alpha_i\rangle + \sin\alpha\,|\bar{\alpha}_{i-\Delta}\rangle)(\sin\beta\,|\beta_{N'-i-\Delta}\rangle - \cos\beta\,|\bar{\beta}_{N'-i-\Delta}\rangle)\Big).
\end{aligned} \tag{D.8}$$

The probabilities of results can be seen by

$$\begin{aligned}
P_{ab} &\equiv |\langle\alpha(a)\beta(b)|\,\psi\phi\rangle|^2 = \frac{1}{2}|r_{a+\Delta}\sin\alpha\cos\beta + r_a\cos\alpha\sin\beta|^2\delta_{b,N'-a-\Delta},\\
P_{a\bar{b}} &\equiv |\langle\alpha(a)\bar{\beta}(b)|\,\psi\phi\rangle|^2 = \frac{1}{2}|r_{a+\Delta}\sin\alpha\sin\beta - r_a\cos\alpha\cos\beta|^2\delta_{b,N'-a-\Delta},\\
P_{\bar{a}b} &\equiv |\langle\bar{\alpha}(a)\beta(b)|\,\psi\phi\rangle|^2 = \frac{1}{2}|-r_{a+\Delta}\cos\alpha\cos\beta r_a\sin\alpha\sin\beta|^2\delta_{b,N'-a-\Delta},\\
P_{\bar{a}\bar{b}} &\equiv |\langle\bar{\alpha}(a)\bar{\beta}(b)|\,\psi\phi\rangle|^2 = \frac{1}{2}|-r_{a+\Delta}\cos\alpha\sin\beta - r_a\sin\alpha\cos\beta|^2\delta_{b,N'-a-\Delta}.
\end{aligned} \tag{D.9}$$

APPENDIX E

Expectation value of Cosine

Before we begin our investigation into the different types of noise we first establish how to calculate the expectation value of a random variable as a function of cos as this will come in handy later.

Initially we have a random variable θ which has a normal distribution defined as $\mathcal{N}(0, \sigma^2)$, we would like to calculate $\langle \cos\theta \rangle$.

We note that the exponential of $i\theta$ can be written as

$$\exp(i\theta) = \cos\theta + i\sin\theta, \tag{E.1}$$

and

$$\langle \exp(i\theta) \rangle = \exp(-\frac{\sigma^2}{2}), \tag{E.2}$$

by breaking this into real and imaginary parts we see that

$$\begin{aligned} \langle \cos\theta \rangle &= \exp(-\frac{\sigma^2}{2}), \\ \langle \sin\theta \rangle &= 0. \end{aligned} \tag{E.3}$$

Let us now extend this to the case where the normal distribution is not centred around 0. We now look at a random variable z, where $\theta = z - \mu$ and z follows the normal distribution $\mathcal{N}(\mu, \sigma^2)$. Using the information above and the trigonometric identities

$$\cos\alpha + \beta = \cos\alpha\cos\beta - \sin\alpha\sin\beta, \tag{E.4}$$

we can write the expectation values of the cos of a random variable that is not centred around 0

$$\begin{aligned}\langle \cos z \rangle &= \langle \cos\theta + \mu \rangle = \langle \cos\theta \cos\mu - \sin\theta \sin\mu \rangle = \cos\mu \langle \cos\theta \rangle - \sin\mu \langle \sin\theta \rangle \\ &= \exp(-\frac{\sigma^2}{2}) \cos\mu,\end{aligned} \tag{E.5}$$

.

APPENDIX F

Uncorrelated multiplicative noise graphs

Here we show the full graphs for each of the optimisation processes in the uncorrelated multiplicative noise case, details of the measurement settings can be found in Sec. 5.4.3.

F.0.1 Arbitrary fixed angles

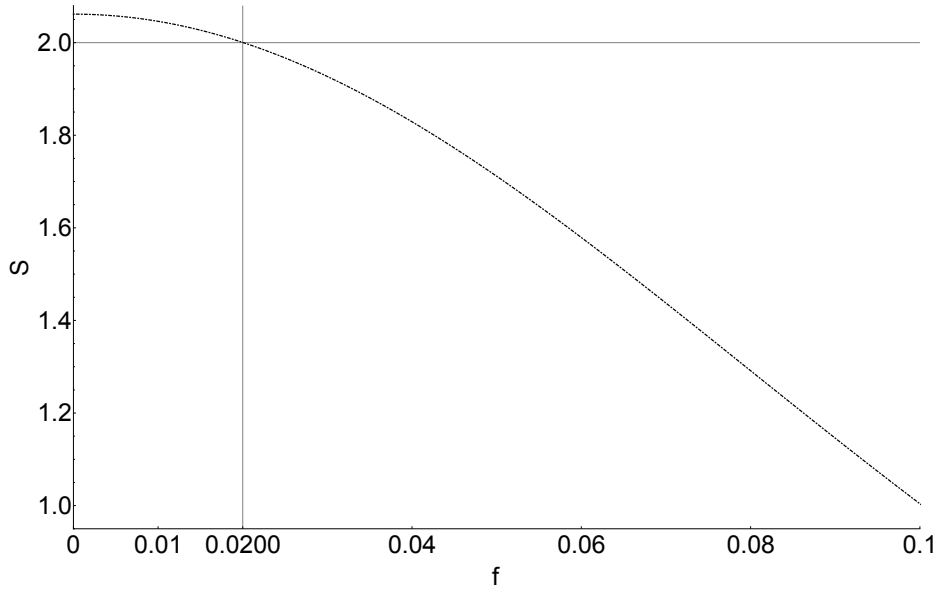

Figure F.1: Non-correlated multiplicative noise with fixed angles. Keeping the measurement angles fixed for all f the S value steadily decreases. The critical value, $f_{3.1}^{crit} = 0.200$.

F.0.2 Optimising angles keeping $\alpha_1 = 0$

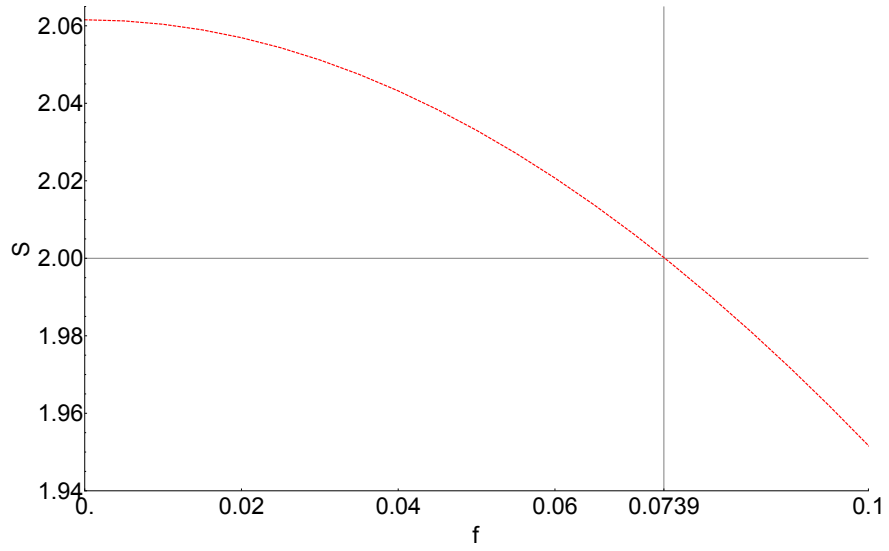

Figure F.2: Non-correlated multiplicative noise setting $\alpha_1 = 0$ and optimising the other angles. Fixing $\alpha_1 = 0$ and optimising the other measurement angles for each value of f we find $f_{3.2}^{crit} = 0.739$.

F.0.3 Optimising over all angles

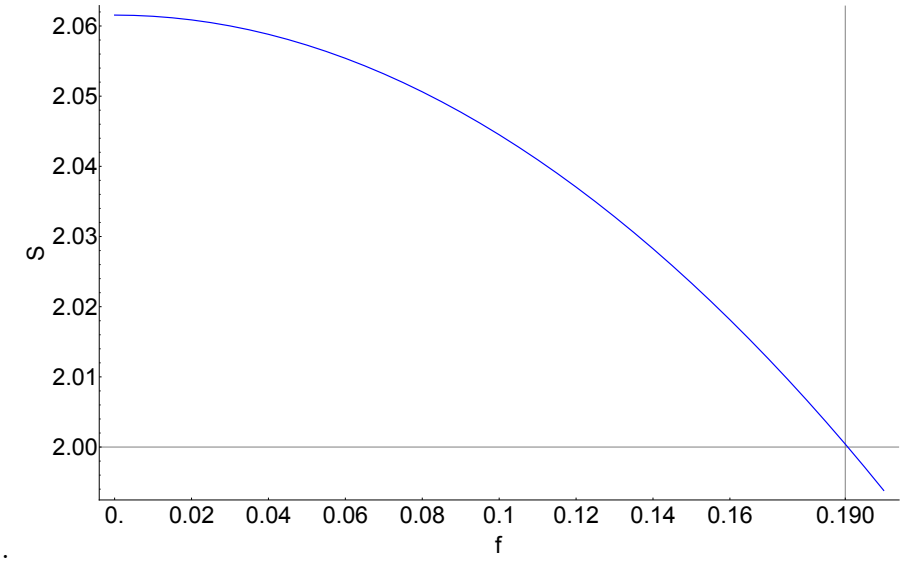

.

Figure F.3: Non-correlated multiplicative noise optimising all the angles. We find $f_{3.3}^{crit} = 0.190$

APPENDIX G

Correlated multiplicative noise graphs

Here we show the full graphs for each of the optimisation processes in the correlated multiplicative noise case, details of the measurement settings can be found in Sec. 5.4.2.

G.0.4 Fixed angles

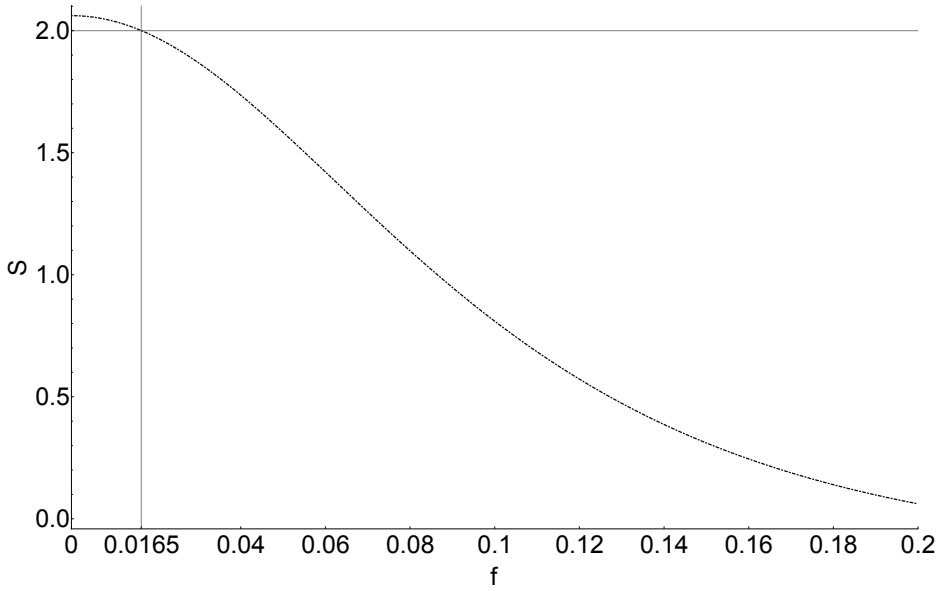

Figure G.1: Correlated mulitplicative noise with fixed angles.

G.0.5 Optimising angles keeping $\alpha_1 = 0$

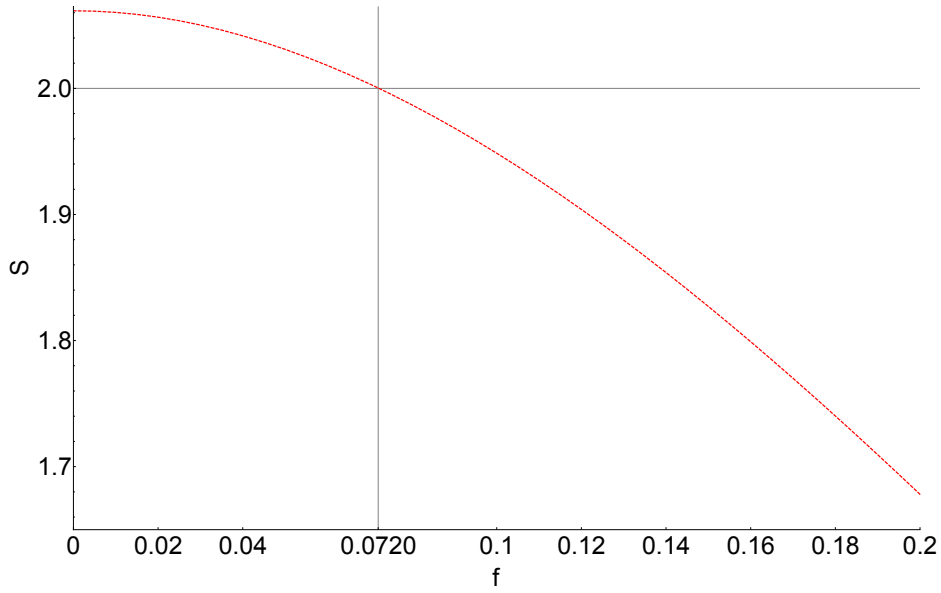

Figure G.2: Correlated multiplicative noise setting $\alpha_1 = 0$ and optimising the other angles.

G.0.6 Optimising over all angles

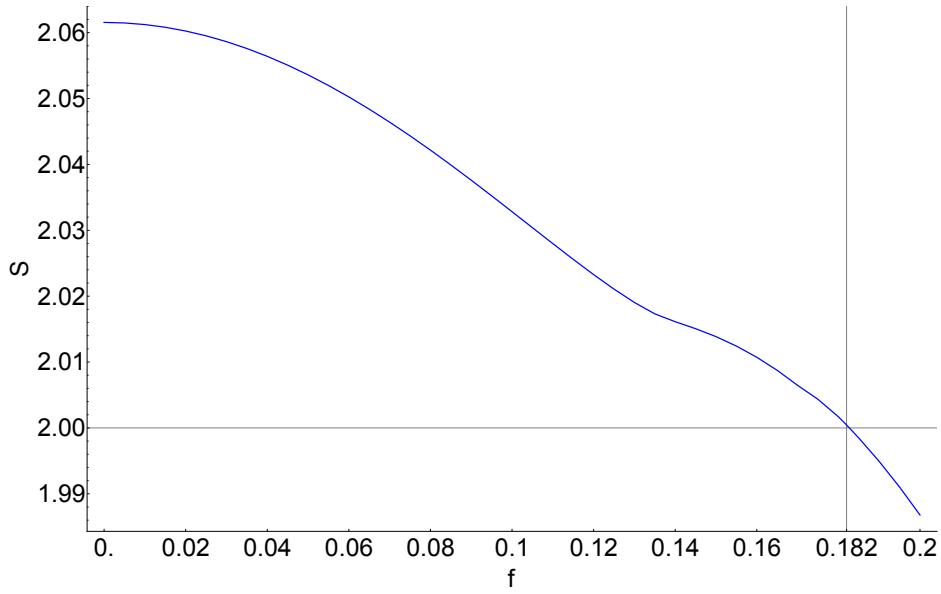

Figure G.3: Correlated multiplicative noise with optimisation of all the angles.

Bibliography

[1] T Paterek, P Kurzyski, D K L Oi, and D Kaszlikowski. Reference frames for Bell inequality violation in the presence of superselection rules. *New Journal of Physics*, 13(4):043027, 2011.

[2] Michael A. Nielsen and Isaac L. Chunag. *Quantum Computation and Quantum Information*. Cambridge University Press, 2000.

[3] A. I. Lvovsky and M. G. Raymer. Continuous-variable optical quantum-state tomography. *Rev. Mod. Phys.*, 81:299–332, Mar 2009.

[4] Warren S Warren. The usefulness of NMR quantum computing. *Science*, 277(5332):1688–1690, 1997.

[5] David Kielpinski, Chris Monroe, and David J Wineland. Architecture for a large-scale ion-trap quantum computer. *Nature*, 417(6890):709–711, 2002.

[6] Daniel Loss and David P DiVincenzo. Quantum computation with quantum dots. *Physical Review A*, 57(1):120, 1998.

[7] Emanuel Knill, Raymond Laflamme, and Gerald J Milburn. A scheme for efficient quantum computation with linear optics. *nature*, 409(6816):46–52, 2001.

[8] Robert Raussendorf and Hans J. Briegel. A one-way quantum computer. *Phys. Rev. Lett.*, 86:5188–5191, May 2001.

[9] Michael A. Nielsen. Cluster-state quantum computation. *Reports on Mathematical Physics*, 57(1):147 – 161, 2006.

[10] Daniel Gottesman and Isaac L. Chuang. Demonstrating the viability of universal quantum computation using teleporation and single-qubit operations. *Nature*, 402:390–393, 1999.

[11] H. J. Brigel, T. Calarco, D. Jaksch, J. I. Cirac, and P. Zoller. Quantum computing with neutral atoms. *Journal of Modern Optics*, 47:415–451, 2000.

[12] Barbara M. Terhal, Michael M. Wolf, and Andrew C. Doherty. Quantum entanglement: A modern perspective. *Physics Today*, 56:46–52, 2003.

[13] Christof Weitenberg, Manuel Endre, Jacob F. Sheron, Marc Chenaeau, Peter Schauss, Takeshi Fukuhara, Immanuel Bloch, and Stefan Kuhr. Single-spin addressing in an atomic Mott insulator. *Nature*, 471:319–324.

[14] Jacob F. Sherson, Christof Weitenberg, Manuel Endres, Marc Cheneau, Bloch Immanuel, and Kuhr Stefan. Single-atom-resolved fluorscence imaging of an atomic Mott insulator, 2010.

[15] F. Verstraete and J. I. Cirac. Quantum nonlocality in the presence of superselection rules and data hiding protocols. *Phys. Rev. Lett.*, 91:010404, Jul 2003.

[16] Yakir Aharonov and Leonard Susskind. Charge superselection rule. *Phys. Rev.*, 155:1428–1431, Mar 1967.

[17] Ping Dong, Zheng-Yuan Xue, Ming Yang, and Zhuo-Liang Cao. Generation of cluster states. *Phys. Rev. A*, 73:033818, Mar 2006.

[18] Harald Wunderlich, Christof Wunderlich, Kilian Singer, and Ferdinand Schmidt-Kaler. Two-dimensional cluster-state preparation with linear ion traps. *Phys. Rev. A*, 79:052324, May 2009.

[19] X.-W. Wang and G.-J. Yang. Schemes for preparing atomic qubit cluster states in cavity QED. *Optics Communications*, 281:5282–5285, October 2008.

[20] M. Cramer, Bernard A., N. Fabbri, L. Fallani, C. Fort, S. Rosi, F. Caruso, M. Inguscio, and M. B. Plenio. Spatial entanglement of bosons in optical lattices. *Nature Communications*, 4:2161, 2013.

[21] Olaf Mandel, Markus Greiner, Artur Widera, Tim Rom, Theodor W. Hänsch, and Immanuel Bloch. Controlled collisions for multi-particle entanglement of optically trapped atoms. *Nature*, 425:937–940, 2003.

[22] P. Walther, K. J. Resch, T. Rudolph, E. Schenck, H. Weinfurter, V. Vedral, M. Aspelmeyer, and A. Zeilinger. Experimental one-way quantum computing. *Nature*, 434:169–176, 2005.

[23] Katherine L. Brown, Clare Horsman, Viv Kendon, and William J. Munro. Layer-by-layer generation of cluster states. *Phys. Rev. A*, 85:052305, May 2012.

[24] K. C. S. Hall and D. L. K. Oi. Cross-talk minimising stabilizers. arXiv:quant-ph/1507.04637.

[25] Robert Raussendorf, Daniel E. Browne, and Hans J. Briegel. Measurement-based quantum computation on cluster states. *Phys. Rev. A*, 68:022312, Aug 2003.

[26] Rolando D. Somma, John Chiaverini, and Dana J. Berkeland. Lower bounds for the fidelity of entangled-state preparation. *Phys. Rev. A*, 74:052302, Nov 2006.

[27] Richard Jozsa. Fidelity of mixed quantum states. *Journal of Modern Optics*, 41(12):2315–2323, 1994.

[28] Holly K. Cummins, Gavin Llewellyn, and Jonathan A. Jones. Tackling systematic errors in quantum logic gates with composite rotations. *Phys. Rev. A*, 67:042308, Apr 2003.

[29] A. Mary Tropper. *Linear Algebra*. Nelson, Bath, 1969.

[30] Harry R. Lewis. Complexity of solvable cases of the decision problem for the predicate calculus. *2013 IEEE 54th Annual Symposium on Foundations of Computer Science*, 0:35–47, 1978.

[31] Raphael M. Robinson. Undecidability and nonperiodicity for tilings of the plane. *Inventiones mathematicae*, 12:177–209, 1971.

[32] Robert Berger. The undecidability of the domino problem. *Memoirs of the American Mathematical Society*, (66), 1966.

[33] K. C. S. Hall and D. L. K. Oi. Bell inequality violation in the presence of vacancies and incomplete measurements. arXiv:quant-ph/1412.7502.

[34] Immanuel Bloch. Ultracold quantum gases in optical lattices. *Nature Physics*, 1:23–30, 2005.

[35] Jérôme Estéve. Cold atoms: Trapped by nanostructures. *Nature Nanotechnology*, 8:317–318, 2013.

[36] C. C. Bradley, C. A. Sackett, J. J. Tollett, and R. G. Hulet. Evidence of Bose-Einstein condensation in an atomic gas with attractive interactions. *Phys. Rev. Lett.*, 75:1687–1690, Aug 1995.

[37] K. B. Davis, M. O. Mewes, M. R. Andrews, N. J. van Druten, D. S. Durfee, D. M. Kurn, and W. Ketterle. Bose-Einstein condensation in a gas of sodium atoms. *Phys. Rev. Lett.*, 75:3969–3973, Nov 1995.

[38] M. H Anderson, J. R. Ensher, M. R. matthews, C. E. Wieman, and E. A. Cornell. Observation of Bose-Einstein condensation in a dilute atomic vapor. *Science*, 269:198–201, 1995.

[39] Sandro Stringari. BoseEinstein condensation and superfluidity in trapped atomic gases. *Comptes Rendus de l'Acadmie des Sciences - Series {IV} - Physics*, 2(3):381 – 397, 2001.

[40] Matthew P. A. Fisher, Peter B. Weichman, G. Grinstein, and Daniel S. Fisher. Boson localization and the superfluid-insulator transition. *Phys. Rev. B*, 40:546–570, Jul 1989.

[41] D. Jaksch, C. Bruder, J. I. Cirac, C. W. Gardiner, and P. Zoller. Cold bosonic atoms in optical lattices. *Phys. Rev. Lett.*, 81:3108–3111, Oct 1998.

[42] Markus Greiner, Olaf Mandel, Tilman Esslinger, Hänsch Theodor W., and Immanuel Bloch. Quantum phase transition from a superfluid to a Mott insulator in a gas of ultracold atoms. *Nature*, 415:39–44, 2001.

[43] I. B. Spielman, W. D. Phillips, and J. V. Porto. Mott-insulator transition in a two-dimensional atomic Bose gas. *Phys. Rev. Lett.*, 98:080404, Feb 2007.

[44] C. Orzel, A. K. Tuchman, M. L. Fenselau, M. Yasuda, and M. A. Kasevich. Squeezed states in a Bose-Einstein condensate. *Science*, 291(5512):2386–2389, 2001.

[45] W. S Bakr, A. Peng, M. E. Tai, R. Ma, J. Simon, J. I. Gillen, S. Fölling, L. Pollet, and M. Greiner. Probing the superfluid-to-Mott insulator transition at the single-atom level. *Science*, 329:547–550, 2010.

[46] Jacob F. Sherson, Christof Weitenberg, Manuel Endres, Marc Cheneau, Bloch Immanuel, and Stefan Kuhr. Single-atom-resolved fluorescence imaging of an atomic Mott insulator. *Nature*, 467:68–72, 2010.

[47] Marshall T. DePue, Colin McCormick, S. Lukman Winoto, Steven Oliver, and David S. Weiss. Unity occupation of sites in a 3d optical lattice. *Phys. Rev. Lett.*, 82:2262–2265, Mar 1999.

[48] W. S. Bakr, A. Peng, M. E. Tai, R. Ma, J. Simon, J. I. Gillen, S. Flling, L. Pollet, and M. Greiner. Probing the superfluidtoMott insulator transition at the single-atom level. *Science*, 329(5991):547–550, 2010.

[49] D. Jaksch, H.-J. Briegel, J. I. Cirac, C. W. Gardiner, and P. Zoller. Entanglement of atoms via cold controlled collisions. *Phys. Rev. Lett.*, 82:1975–1978, Mar 1999.

[50] D. Jaksch and P. Zoller. The cold atom Hubbard toolbox. *Annals of Physics*, 315(1):52 – 79, 2005. Special Issue.

[51] Olaf Madel, Markus Greiner, Artur Widera, Tim Rom, Theodor W. Hänsch, and Immanuel Bloch. Controlled collisions for multi-particle entanglement of optically trapped atoms. *Nature*, 425:937–940, 2003.

[52] John F. Clauser, Michael A. Horne, Abner Shimony, and Richard A. Holt. Proposed experiment to test local hidden-variable theories. *Phys. Rev. Lett.*, 23:880–884, Oct 1969.

[53] Otfried Gühne and Géza Tóth. Entanglement detection. *Physics Reports*, 474(16):1 – 75, 2009.

[54] William K. Wootters. Entanglement of formation of an arbitrary state of two qubits. *Phys. Rev. Lett.*, 80:2245–2248, Mar 1998.

[55] Scott Hill and William K. Wootters. Entanglement of a pair of quantum bits. *Phys. Rev. Lett.*, 78:5022–5025, Jun 1997.

[56] J. S. Bell. On The Einstein Podolsky Rosen Paradox. *Physics*, 1:195–200, 1964.

[57] B. S. Cirel'son. Quantum generalizations of Bell's inequality. *Letters in Mathematical Physics*, 4:93–100, March 1980.

[58] Emilio Santos. Critical analysis of the empirical tests of local hidden-variable theories. *Phys. Rev. A*, 46:3646–3656, Oct 1992.

[59] Paul G. Kwiat, Philippe H. Eberhard, Aephraim M. Steinberg, and Raymond Y. Chiao. Proposal for a loophole-free Bell inequality experiment. *Phys. Rev. A*, 49:3209–3220, May 1994.

[60] M. Ferrero, T. W. Marshall, and E. Santos. Bells theorem: Local realism versus quantum mechanics. *American Journal of Physics*, 58(7), 1990.

[61] K. F. Riley, M. P. Hobson, and S. J. Bence. *Mathematical Methods for Physics and Engineering*. Cambridge University Press, 3 edition, March 2006.

[62] D. J. Wineland and H. Dehmelt. *Bull. Am. Phys. Soc.*, 20:637, 1975.

[63] J. C. Bergquist Wayne M. Intano and D. J. Wineland. Laser spectroscopy of trapped atomic ions. *Science*, 237:612–617, 1987.

[64] D. J. Wineland, J. C. Bergquist, Wayne M. Itano, and R. E. Drullinger. Double-resonance and optical-pumping experiments on electromagnetically confined, laser-cooled ions. *Opt. Lett.*, 5(6):245–247, Jun 1980.

[65] Philip M. Pearle. Hidden-variable example based upon data rejection. *Phys. Rev. D*, 2:1418–1425, Oct 1970.

[66] T. K. Lo and A. Shimony. Proposed molecular test of local hidden-variables theories. *Phys. Rev. A*, 23:3003–3012, Jun 1981.

[67] Anupam Garg and N. D. Mermin. Detector inefficiencies in the Einstein-Podolsky-Rosen experiment. *Phys. Rev. D*, 35:3831–3835, Jun 1987.

[68] Jan-Åke Larsson. Bell's inequality and detector inefficiency. *Phys. Rev. A*, 57:3304–3308, May 1998.

[69] Jan ke Larsson. Loopholes in Bell inequality tests of local realism. *Journal of Physics A: Mathematical and Theoretical*, 47(42):424003, 2014.

[70] Sudhir K. Madan, Basabi Bhaqumi, and Juzer M. Vasi. Experimental observation of avalanche multiplication in charge-coupled devices. *IEEE Transactions on Electron Devices*, ED-30:694–699, 1983.

[71] R.D. McGrath, J. Doty, G. Lupino, G. Ricker, and J. Vallerga. Counting of deep-level traps using a charge-coupled device. *Electron Devices, IEEE Transactions on*, 34(12):2555–2557, Dec 1987.

[72] W.C. McColgin, J.P. Lavine, J. Kyan, D.N. Nichols, and C.V. Stancampiano. Dark current quantization in CCD image sensors. In *Electron Devices Meeting, 1992. IEDM '92. Technical Digest., International*, pages 113–116, Dec 1992.

[73] William C. McColgin, J. P. Lavine, and C. V. Stancampiano. Probing metal defects in CCD image sensors. In *Symposium B Defect and Impurity-Engineered Semiconductors and Devices*, volume 378 of *MRS Online Proceedings Library*, 1995.

[74] William C. Mccolgin, James P. Lavine, Charles V. Stancampiano, and Jeffrey B. Russell. Deep-level traps in CCD image sensors. In *Symposium D Defect and Impurity Engineered Semiconductors and Devices II*, volume 510 of *MRS Online Proceedings Library*, 1998.

[75] Ralf Widenhorn, Morley M. Blouke, Alexander Weber, Armin Rest, and Erik Bodegom. Temperature dependence of dark current in a CCD, 2002.

[76] S. M. Tan, D. F. Walls, and M. J. Collett. Nonlocality of a single photon. *Phys. Rev. Lett.*, 66:252–255, Jan 1991.

[77] Lucien Hardy. Nonlocality of a single photon revisited. *Phys. Rev. Lett.*, 73:2279–2283, Oct 1994.

[78] D. M. Greenberger, M. A. Horne, and A. Zeilinger. Nonlocality of a single photon? *Phys. Rev. Lett.*, 75:2064–2064, Sep 1995.

[79] Emilio Santos. Comment on "nonlocality of a single photon". *Phys. Rev. Lett.*, 68:894–894, Feb 1992.

[80] Lev Vaidman. Nonlocality of a single photon revisited again. *Phys. Rev. Lett.*, 75:2063–2063, Sep 1995.

[81] Lucien Hardy. Hardy replies:. *Phys. Rev. Lett.*, 75:2065–2066, Sep 1995.

[82] Marek Czachor. Bell theorem without inequalities: A single-particle formulation. *Phys. Rev. A*, 49:2231–2240, Apr 1994.

[83] Dipankar Home and Girish S. Agarwal. Quantum nonlocality of single photon states. *Physics Letters A*, 209:1–5, 1995.

[84] Christopher C. Gerry. Nonlocality of a single photon in cavity qed. *Phys. Rev. A*, 53:4583–4586, Jun 1996.

[85] Asher Peres. Nonlocal effects in Fock space. *Phys. Rev. Lett.*, 74:4571–4571, Jun 1995.

[86] S. J. van Enk. Single-particle entanglement. *Phys. Rev. A*, 72:064306, Dec 2005.

[87] Marcin Pawlowski and Marek Czachor. On entanglement with vacuum. arXiv:quant-ph/0507151.

[88] Stephen D. Bartlett and H. M. Wiseman. Entanglement constrained by superselection rules. *Phys. Rev. Lett.*, 91:097903, Aug 2003.

[89] N. Schuch, F. Verstraete, and J. I. Cirac. Nonlocal resources in the presence of superselection rules. *Phys. Rev. Lett.*, 92:087904, Feb 2004.

[90] Norbert Schuch, Frank Verstraete, and J. Ignacio Cirac. Quantum entanglement theory in the presence of superselection rules. *Phys. Rev. A*, 70:042310, Oct 2004.

[91] Stephen D. Bartlett, Terry Rudolph, and Robert W. Spekkens. Reference frames, superselection rules, and quantum information. *Rev. Mod. Phys.*, 79:555–609, Apr 2007.

[92] Mark R. Dowling, Stephen D. Bartlett, Terry Rudolph, and Robert W. Spekkens. Observing a coherent superposition of an atom and a molecule. *Phys. Rev. A*, 74:052113, Nov 2006.

[93] A. Galindo and P. Pascual. *Quantum Mechanics I.* Springer-Verlag, Berlin, 1990.

[94] Barbara M. Terhal, David P. DiVincenzo, and Debbie W. Leung. Hiding bits in Bell states. *Phys. Rev. Lett.*, 86:5807–5810, Jun 2001.

[95] David P. DiVincenzo, Debbie W. Leung, and Barbara M. Terhal. Quantum data hiding. *IEEE Transaction on Information Theory*, 48:580–598, 2002.

[96] Charles H. Bennett, David P. DiVincenzo, Christopher A. Fuchs, Tal Mor, Eric Rains, Peter W. Shor, John A. Smolin, and William K. Wootters. Quantum nonlocality without entanglement. *Phys. Rev. A*, 59:1070–1091, Feb 1999.

[97] M. Spiegel, S. Lipschutz, and D. Spellman. *Schaum's Outline of Vector Analysis.* McGraw-ill Education, 2 edition, 2009.

[98] C. J. Foot. *Atomic Physics*. Oxford Master Series in Physics. Oxford University Press, Oxford, 2005.

[99] Hannes Pichler, Johannes Schachenmayer, Andrew J. Daley, and Peter Zoller. Heating dynamics of bosonic atoms in a noisy optical lattice. *Phys. Rev. A*, 87:033606, Mar 2013.

[100] W. B. Gao, P. Fallahi, E. Togan, J. Miguel-Sanchez, and A. Imamoglu. Observation of entanglement between a quantum dot spin and a single photon. *Nature*, 491:426–430, 2012.

[101] Gregor Weihs, Thomas Jennewein, Christoph Simon, Harald Weinfurter, and Anton Zeilinger. Violation of Bell's inequality under strict Einstein locality conditions. *Phys. Rev. Lett.*, 81:5039–5043, Dec 1998.

[102] Bahaa E. A. Saleh and Malvin Carl Teich. *Fundamentals of Photonics*. John Wiley and Sons, 1991.

[103] Peter Shadbolt, Jonathan C. F. Mathews, Anthony Laing, and Jeremy L. O'Brien. Testing the foundations of quantum mechanics with photons. *Nature Physics*, 10:278–286, 2014.

[104] H. Häffner, C.F. Roos, and R. Blatt. Quantum computing with trapped ions. *Physics Reports*, 469(4):155 – 203, 2008.

[105] F. Schnidt-Kaler, S Gulde, M. Riebe, T. Deuschle, A. Kreuter, G. Lancaster, C. Becher, J. Eschner, H. Häffner, and R. Blatt. The coherence of qubits based on single Ca^+ ions. *J. Phys. B: At. Mol. Opt. Phys*, 36.

[106] Asher Peres. Separability criterion for density matrices. *Phys. Rev. Lett.*, 77:1413–1415, Aug 1996.

[107] Michał Horodecki, Paweł Horodecki, and Ryszard Horodecki. Separability of mixed states: necessary and sufficient conditions. *Physics Letters A*, 223:1–8, 1996.

[108] Chris Belsom. *The Normal Distribution*. Cambridge University Press, Cambridge, 1990.

[109] Deny R. Hamel, Lynden K. Shalm, Hannes Hübel, Aaron J. Miler, Francesco Marsili, Varun B. Verma, Richard P. Mirin, Sae Woo Nam, Kevin J. Resch, and Thomas Jennewein. Direct generation of three-photon polarization entanglement. *Nature Photonics*, 8:801–807, 2014.

[110] M. A. Rowe, D. Kielpinksi, V. Meyer, C. A. Sackett, W. M. Itano, C. Monroe, and D. J. Wineland. Experimenal violation of a Bell's inequality with efficient detection. *Nature*, 409:791–794, 2000.

[111] Olaf Mandel, Markus Greiner, Artur Widera, Tim Rom, Theodor W. Hänsch, and Immanuel Bloch. Coherent transport of neutral atoms in spin-dependent optical lattice potentials. *Phys. Rev. Lett.*, 91:010407, Jul 2003.

[112] Anders Sørensen and Klaus Mølmer. Spin-spin interaction and spin squeezing in an optical lattice. *Phys. Rev. Lett.*, 83:2274–2277, Sep 1999.

[113] Markus Greiner, Olaf Mandel, Theodor W. Hänsch, and Immanuel Bloch. Collapse and revival of the matter wave field of a Bose-Einstein condensate. *Nature*, 419:51–54, 2002.